Clemson University
TigerPrints

All Dissertations | Dissertations

August 2020

# Diagnosis, Rupture Risk Evaluation and Therapeutic Intervention of Abdominal Aortic Aneurysms Using Targeted Nanoparticles

Xiaoying Wang
*Clemson University*, xiaoyingw29@hotmail.com

Follow this and additional works at: https://tigerprints.clemson.edu/all_dissertations

## Recommended Citation

Wang, Xiaoying, "Diagnosis, Rupture Risk Evaluation and Therapeutic Intervention of Abdominal Aortic Aneurysms Using Targeted Nanoparticles" (2020). *All Dissertations*. 2672.
https://tigerprints.clemson.edu/all_dissertations/2672

This Dissertation is brought to you for free and open access by the Dissertations at TigerPrints. It has been accepted for inclusion in All Dissertations by an authorized administrator of TigerPrints. For more information, please contact kokeefe@clemson.edu.

# DIAGNOSIS, RUPTURE RISK EVALUATION AND THERAPEUTIC INTERVENTION OF ABDOMINAL AORTIC ANEURYSMS USING TARGETED NANOPARTICLES

---

A Dissertation
Presented to
the Graduate School of
Clemson University

---

In Partial Fulfillment
of the Requirements for the Degree
Doctor of Philosophy
Bioengineering

---

by
Xiaoying Wang
August 2020

---

Accepted by:
Dr. Narendra Vyavahare, Committee Chair
Dr. Jeoung Soo Lee
Dr. Jeffery Anker
Dr. Bruce Gray

# ABSTRACT

Abdominal aortic aneurysm (AAA) disease causes dilation of the aorta that can lead to aortic rupture and death if not treated early. It is the 14th leading cause of death in the U.S. and is cited as the 10th leading cause of death in men over age 55, affecting thousands of patients and their families. To date, AAA patients have minimal access to safe and efficient imaging modalities for diagnosis as well as pharmacotherapies. AAA is usually detected and monitored with ultrasonography or contrast-enhanced computed tomography (C.T.), which doesn't provide biomechanical information of the AAAs that are essential for predicting rupture risks. Furthermore, unfortunately, there is no currently known pharmaceutical treatment to cure the AAAs.

Key pathological processes occurring within AAAs include inflammation, vascular smooth muscle cell apoptosis, and extracellular matrix (ECM) degradation. The deterioration of the elastic lamina in the aneurysmal wall is a consistent feature of AAAs and the fact that the adult elastic lamina does not remodel in aneurysm progression, making it an ideal target for delivering contrast agents and treatments. In this research, we have delivered gold nanoparticles (AuNPs), a commonly used C.T. contrast agent, and pentagalloyl glucose (PGG) loaded nanoparticles to the AAAs in an angiotensin II (AngII) infusion induced mouse model by conjugating the nanoparticles with antibodies that target degraded elastin.

Here, owing to their degraded elastin targeting ability, we have observed a positive correlation between the quantities of the locally accumulated AuNPs in the aneurysmal

tissue in C.T. scans and the elastin damage levels of the AAAs. Furthermore, the AuNPs accumulations were found negatively correlated to the mechanical properties of the AAAs, which makes AuNPs a potential non-invasive surrogate marker of AAA rupture risk. Moreover, we have shown that targeted delivery of PGG could reverse the aortic dilation, ameliorate the inflammation, restore the elastin as well as the AAA mechanical properties of the aneurysmal tissue. Therefore, PGG loaded nanoparticles can be an effective treatment option for early to middle stage aneurysms to prevent disease progression.

# DEDICATION

In memory of my late grandmother Yuehua Wu, for teaching me patience, persistence, kindness and love that made me who I am.

To my parents Tengsheng Wang and Liping Deng, for supporting me in every step of my life and every decision I made. If not for their love and support, I will not be standing where I am now.

# ACKNOWLEDGMENTS

First and foremost, I would like to give my immense gratitude and respect to my advisor Dr. Narendra Vyavahare who has been a great mentor, with his constant guidance and support, throughout my Ph.D. journey. His passion for innovations has been a great inspiration and encouragement for me to proceed as a researcher. His broad knowledge and critical thinking have greatly contributed to the success of this research.

I would also like to extend my appreciation to my committee members Dr. Jeoung Soo Lee, Dr. Bruce Grey, and Dr. Jeffery Anker for their valuable insights, ideas, and advice on this project.

A significant part of my dissertation comes from animal studies. For all the help I have gotten during my numerous visits to Godley Snell Research Center, I would like to thank Dr. John Parrish, Jessica Privett, Travis Pruitt, Tina Parker, Cynthia Nigro, Melody Willey, and everyone at the facility.

Another important part of my study comes from biomechanical tests. I would like to thank Dr. John Eberth, Dr. Brooks Lane, Shahd Hasanain and Liya Du for all the help and advice they gave me on mechanical studies to complete this research.

I would like to acknowledge my fellow lab members for their contributions to this research and their support in life. Dr. Vaideesh Parasaram, Dr. Saketh Karamched, Tyler Gibson, Dipasha Sinha, Fatema-Tuj Zohora, and Nicholas Bain are the ones who made some of the work in this dissertation possible with their inputs, guidance, and motivation.

I would like to thank Dr. Guzeliya Korneva for all the discussions and insights she had to offer me apart from her invaluable help with HPLC. I thank Dr. Saphala Dhital for her help in flow cytometry and Dr. Agnes Nagy-Mehesz for all her help and advice with Immunohistochemistry. I would like to thank Clemson Light and Imaging Facility staff for their help in darkfield microscopy.

I am also grateful to Dr. Laberge and the Department of Bioengineering at Clemson University for giving me an opportunity as a graduate student and especially to Maria Torres for all the help she has provided right from the day I started. I extend my thanks to all the administrative staff of the department who made things easy for me.

I would like to say a huge thank you to all my friends in the United States and China who have been an inseparable part of my life. I would like to give special thanks to Yingying Xia, Erwan Bounin, and Dr. Anastasia Frank-Kamenetskii for always supporting and believing in me.

I would also like to acknowledge the financial support provided by the National Institutes of Health and the Hunter Endowment to Dr. Vyavahare.

TABLE OF CONTENTS

Page

Table of contents (Continued)

Page

Table of contents (Continued)

Page

LIST OF TABLES

Table Page

LIST OF FIGURES

List of Figures (Continued)

Figure Page

List of Figures (Continued)

Figure Page

List of Figures (Continued)

Figure Page

# LIST OF ABBREVIATIONS

| | |
|---|---|
| AAA | Abdominal aortic aneurysm |
| ACE | Angiotensin-converting enzyme |
| ACTB | Actin-beta |
| AngII | Angiotensin II |
| ANOVA | Analysis of variance |
| ApoE | Apolipoprotein E |
| ARB | Angiotensin receptor blocker |
| AT1a | Angiotensin type 1a |
| AT1R | Angiotensin II type I receptor |
| AuNP | Gold nanoparticle |
| BAPN | 3-aminopropionitrile fumarate salt |
| BB-94 | Batimastat |
| BLN-NP | Blank bovine serum albumin nanoparticle |
| BSA | Bovine serum albumin |
| $CaCl_2$ | Calcium chloride |
| CCR2 | C-C chemokine receptor type 2 |
| CLIO | Cross-linked iron oxide nanoparticles |
| Ct | Cycle threshold |
| CT | Computed tomography |
| CTA | Computed tomography angiography |

| | |
|---|---|
| CVD | Cardiovascular disease |
| DFM | Darkfield microscopy |
| DI | Deionized |
| DiR | 1, 1-dioctadecyl-3, 3, 3, 3- tetramethylindotricarbocyanine iodide |
| DiR-NP | DiR loaded bovine serum albumin nanoparticle |
| DLS | Dynamic light scattering |
| DMAB | Didodecyldimethylammonium bromide |
| EBP | Elastin-binding protein |
| ECG | Electrocardiogram |
| ECM | Extracellular matrix |
| EDC | 1-Ethyl-3-(3-dimethylaminopropyl) cardodiimide |
| EDTA | Ethylenediaminetetraacetic acid |
| EL | Elastin antibody |
| ELN | Elastin gene |
| ELISA | Enzyme-linked immunosorbent assay |
| EDFM | Enhanced darkfield microscopy |
| eNOS | Endothelial nitric oxide synthase |
| EPR | Enhanced permeability and retention |
| ERC | Elastin receptor complex |
| EVAR | Endovascular aneurysm repair |
| FDA | Food and Drug Administration |
| FEA | Fine element analysis |

| | |
|---|---|
| FSI | Fluid-solid interaction |
| GPI | Glycosylphosphatidylinositol |
| G&R | Growing and remodeling |
| H&E | Hemotoxylin and eosin |
| HMG-CoA | 3-3-hydroxy-3-methylglutaryl-coenzyme A |
| HSA | Human serum albumin |
| HSI | Hyperspectral imaging |
| hSMC | Human smooth muscle cell |
| IACUC | Institutional animal care and use committee |
| ICP-MS | Inductively coupled plasma mass spectrometry |
| IFN- γ | Interferon gamma |
| IHC | Immunohistochemistry |
| IL | Interleukin |
| ILT | Intraluminal thrombus |
| JNK | C-Jun N-terminal kinase |
| LDH | Lactate dehydrogenase |
| LDLr | Low density lipoprotein receptor |
| LOX | Lysyl oxidase |
| LPS | Lipopolysaccharide |
| MAPK | Mitogen-activated protein kinase |
| MCP | Monocyte chemoattractant protein |
| MES | 2-(N-morpholino) ethanesulfonic acid |

| | |
|---|---|
| MIP | Maximum intensity projection |
| miR | microRNA |
| MMP | Matrix metalloproteinase |
| MPEG | Methyl polyethylene glycol |
| mPEG-NHS | α-maleimide-ω-Nhydroxysuccinimide ester poly (ethylene glycol) |
| MPS | Mononuclear phagocyte system |
| MRA | Magnetic resonance angiography |
| MRI | Magnetic resonance imaging |
| NF-κB | Nuclear factor-kappa B |
| NHS | N-hydroxysulfosuccinimide |
| NP | Nanoparticle |
| NSF | Nephrogenic systemic fibrosis |
| OCT | Optimal cutting temperature |
| OPN | Osteopontin |
| OR | Open surgery |
| OVA | Ovalbumin |
| PBLG | Poly (γ-benzyl L-glutamate) |
| PBS | Phosphate-buffered saline |
| PdI | Polydispersity index |
| PDTC | Pyrrolidine dithiocarbamate |
| PEI | Polyethyleneimine |
| PEG | Polyethylene glycol |

| | |
|---|---|
| PET | Positron emission tomography |
| PGG | 1,2,3,4,6-pentagalloyl-O-D-glucopyranose |
| PGG-NP | PGG loaded bovine serum albumin nanoparticle |
| PLA | Poly (lactic acid) |
| PLGA | Poly (lactic-co-glycolic acid) |
| PPAR | Peroxisome proliferator-activated receptor |
| PPCA | Protective protein/cathepsin A |
| PPE | Porcine pancreatic elastase |
| PPIA | Peptidylprolyl isomerase |
| PRF | Pulse repetition frequency |
| PSMA | Prostate-specific membrane antigen |
| PWS | Peak wall stress |
| PWRI | Peak wall rupture index |
| PW | Pulse wave |
| PWV | Pulse wave velocity |
| qPCR | Quantitative polymerase chain reaction |
| RAS | Renin-angiotensin system |
| RCAN1 | Regulator of calcineurin activity 1 |
| RECK | Reversion-inducing-cysteine-rich protein with kazal motifs |
| ROS | Reactive oxygen species |
| RT | Reverse transcriptase |
| SDS | Sodium dodecyl sulfate |

| | |
|---|---|
| SMC | Smooth muscle cell |
| SPIO | Superparamagnetic iron oxide |
| $Ta_2O_5$ | Tantalum oxide |
| TAA | Thoracic aortic aneurysm |
| TGF | Transforming growth factor |
| TIMP | Tissue inhibitor of metalloproteinases |
| TNF | Tumor necrosis factor |
| t-PA | Tissue-type plasminogen activator |
| USPIO | Ultra-small superparamagnetic iron oxide |
| VEGF | Vascular endothelial growth factor |
| VSMC | Vascular smooth muscle cell |
| VVG | Verhoeff-van Gieson |
| $^{18}$F-FDG | $^{18}$F-fluorodeoxyglucose |
| 3D | Three dimensional |

# 1. INTRODUCTION

An abdominal aortic aneurysm (AAA) is a cardiovascular disease featured by the abnormal dilation of the abdominal aorta. Male gender, genetic factors, aging, smoking, and other cardiovascular diseases such as atherosclerosis, diabetes, hypercholesterolaemia, and hypertension play as the risk factors of AAA onset [1]. Histologically, AAA is characterized by chronic transmural inflammation [2], resulting in the breakdown and elimination of essential proteins in the connective tissue of the aortic wall. Extensive research about AAAs has revealed that extracellular matrix (ECM) plays a vital role in its pathophysiology [3]. Mounting evidence has suggested that elastin, one of the critical components of ECM, drives this progression of this disease by virtue of its degradation. Among the enzymes that degrade ECM are matrix metalloproteinases (MMPs) and cathepsins, which can breakdown elastin laminae [4]. If not treated early, the weakening of the aorta can progressively worsen and led to aortic rupture and death [5]. In order to reduce the mortality of AAAs, the U.S. Preventive Services Task Force recommends that men aged 65–75 years who have ever smoked should get an ultrasound screening for abdominal aortic aneurysms, even if they have no symptoms [6].

The clinical standard for diagnosing AAA is whether the maximum aortic diameter reached 3cm or aortic dilation reached 1.5-fold [7]. Current imaging methods, such as ultrasound and computed tomography (CT), are excellent to look at the overall growth of aneurysms and can provide the geometrical information needed clinically to make the diagnosis and choose treatment strategies. However, focal aortic wall weakening caused

by ECM degradation and remodeling is generally not precisely detected. Such weak spots exhibit high-stress concentration and can increase the risk of rupture independent of the AAA size, thereby putting even small AAAs at high risk for rupture. In order to identify the AAAs that are in higher rupture risks and decrease mortality in AAA patients, it is desired to develop an imaging modality that could localize vulnerabilities at the aneurysmal site.

Contrast-enhanced CT, an anatomical imaging technique, has been widely used in the diagnosis and long-term follow-up due to its ability to provide precise anatomical and morphological measurements of the AAAs [8, 9]. However, contrast-enhanced CT alone is unable to provide pathological information of the AAAs, such as the extent of ECM degradation and identify rupture-prone AAAs accurately. Moreover, a large dose of iodine- or gadolinium-based contrast agent is required for performing contrast-enhanced CT, the toxicity of which places it at a disadvantage compared to other imaging methods such as magnetic resonance imaging (MRI), nuclear imaging, and optical imaging [9, 10]. Gold nanoparticles (AuNPs) have been investigated for many years as an ideal radiopaque CT contrast agent for its excellent X-ray absorbing ability and low toxicity [10]. PEGylated AuNPs with prolonged blood circulation times were used for imaging of the cardiovascular system [11]. A targeted delivery of surface-modified AuNPs can reduce the dose of contrast agent applied, increase the imaging quality, and provide more information of the AAAs depending on the molecular probe attached to the AuNP surface.

Besides an instructive imaging modality for diagnostic, an efficient treatment strategy can also achieve mortality benefit. To date, the most effective treatment for AAAs

is surgical intervention, and no pharmacological treatment is available on the market. Given the alarming mortality rate of 90% in the case of AAAs [12], and the fact surgical intervention is not possible in all the cases, it brings us to an imminent need for minimally invasive treatment options. Many drugs such as statins and doxycycline have been found to prevent AAA formation and progression in animal models when delivered systemically [13-15]. However, they were not successfully translated into clinical AAA treatment, possibly due to that systemic administration does not provide the necessary therapeutic drug concentration at the site of AAA [16]. A local delivery of the drugs using targeting nanocarriers could improve their therapeutic efficacy and prevent systemic side effects.

Currently, most of the potential drugs focus on reducing the local inflammation in the aneurysmal tissue but not reversing already degraded ECM. An ideal therapeutic intervention would not only prevent further degradation of ECM but also restores the structural integrity, in turn leading to the restoration of aorta's mechanical properties. On multiple occasions, our group has successfully demonstrated the beneficial effects of pentagalloyl glucose (PGG) in stabilizing and regenerating vascular tissue's ECM both *in-vitro* and *in-vivo* [17, 18]. Recently Nosoudi et al. have also demonstrated successful treatment of AAAs induced by a local injury model in rats [19].

In this dissertation research, firstly, we have synthesized and conjugated AuNPs that possess the ability to target AAAs. It has been shown that the systemic delivery of surface-modified AuNPs that bind to degraded elastin in an angiotensin II (AngII) mouse model of AAA provides a unique way to visualize local areas of ECM degradation that are more prone to rupture. Secondly, we present the successful treatment of AAAs in the same

mouse model using targeted nanoparticle delivery. We tested our hypothesis that PGG loaded bovine serum albumin (BSA) nanoparticles can be targeted to damaged elastin in aneurysmal mouse aorta, thereby not only protecting elastin from MMPs but also regenerating elastic fibers. Apart from looking at the structural integrity of ECM, we have studied the ability of the nanoparticles to restore the mechanical properties of the aorta. We have also delved deeper to investigate if PGG treatment can trigger anti-inflammatory signals to understand its extended effects on ECM. Overall, our goal was to present targeted AuNPs delivery as an excellent imaging contrast agent for AAAs and PGG loaded BSA nanoparticles as an alternative therapeutic approach to reverse AAA clinically.

This dissertation is organized as follows:

- In Chapter 2, we presented a comprehensive review of the cardiovascular system and diseases, physiology and histology of abdominal aorta, aortic elastin content, an introduction to AAAs including pathophysiology and biomechanics, the methods used for AAA rupture risk assessment, the animal models used for AAA studies, and the imaging modalities and treatment for AAAs.
- In chapter 3, we provided the specific aims designed for this project as well as a brief description of the approaches we took to achieve these aims.
- In chapter 4, we described the synthesis and characterization (including size, surface charge, cytotoxicity, cellular uptake, *in-vitro* targeting) of elastin antibody conjugated AuNPs.

- In chapter 5, we presented the *in-vivo* targeting studies of the surface-modified AuNPs in the AngII mice model and the correlation between the AuNPs accumulation and the AAA rupture risk.
- In chapter 6, we presented targeted therapy with nanoparticle loaded with PGG to protect the vascular elastic lamina and restore the aortic mechanical properties and showed that it could halt or even reverse the progression of AAAs in the AngII induced mice model.
- In chapter 7, we concluded the whole presented research and discussed future research attempts that needed to be taken to achieve clinical benefits for AAA patients further.

# 2. LITERATURE REVIEW

## 2.1 The cardiovascular system and cardiovascular diseases

The cardiovascular system, also known as the circulatory system for blood, is one of the most important organ systems that facilitates blood circulation and mass transportation [20]. The cardiovascular system consists of two subunits: the heart, which functions as an anatomical pump that pushes the blood through the whole body, and the blood vessels, including arteries, veins, and capillaries that are the conduits carrying the blood [21]. It plays a vital role in maintaining homeostasis by continuously regulating the blood flowing throughout the system, transporting nutrients, electrolytes, gases, and other essential materials into the environment where cells reside in as waste products are removed [22].

Cardiovascular diseases (CVDs) are diseases that involve the heart or blood vessels (Figure 2-1). The physiological disorders of the heart include arrhythmia, carditis and cardiomyopathy, heart valve problems, rheumatic heart disease, and congenital heart disease, and vascular diseases include coronary artery disease, peripheral arterial disease, stroke, aneurysms, arterial calcification and atherosclerosis, deep vein thrombosis, and pulmonary embolism. According to the world health organization, it is the leading cause of death worldwide [23]. CVD accounted for approximately 17.8 million deaths in 2017 globally and this number is expected to grow to more than 22.2 million by 2030, according to a 2014 study [24]. In the United States alone, CVDs have remained the number one

cause of death, responsible for as many as 859,125 deaths in 2017. The annual total cost of CVDs in the US has been estimated at $351.2 billion in 2014 to 15 [25].

### 2.2 The arteries in the cardiovascular system

An artery, which carries blood from the heart to various organs and tissues of the body, contains three tunics in the wall. The innermost layer, the tunica intima, is composed of epithelial and connective tissues that form the continuous endothelial lining of the entire vascular system. The middle layer, known as the tunica media, is a smooth muscular layer

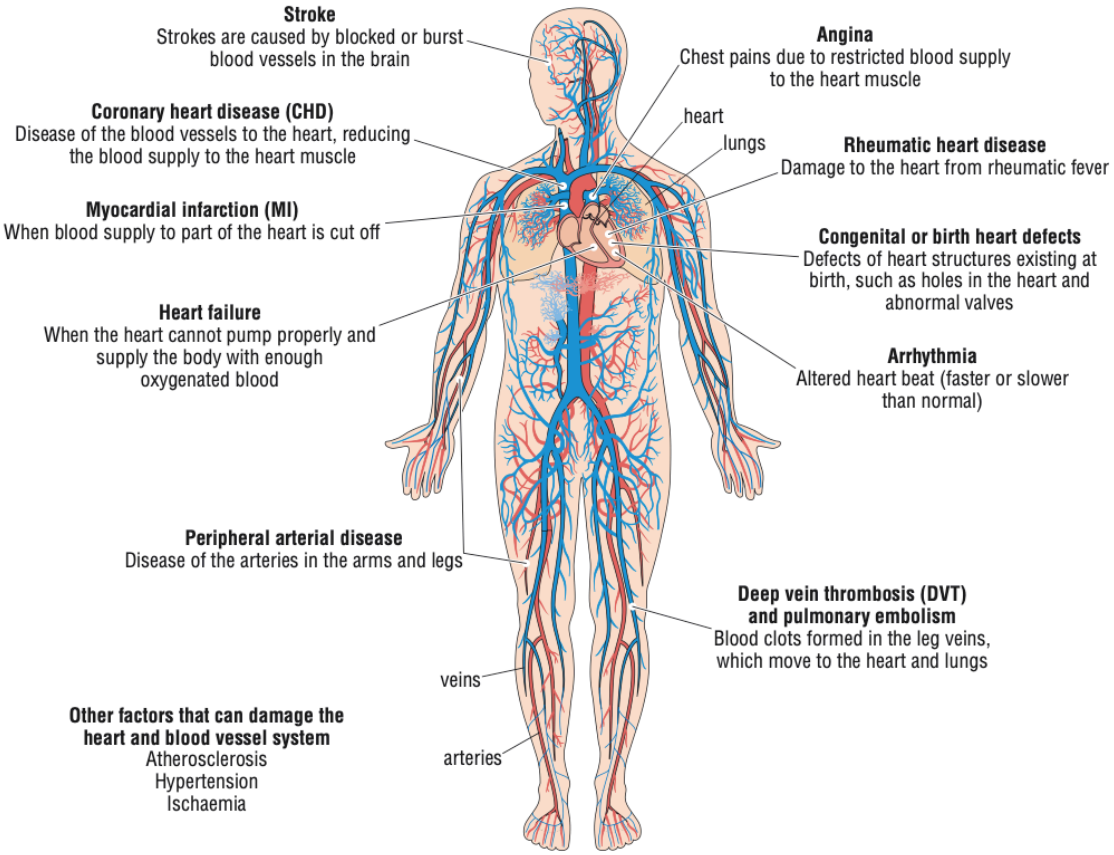


**Figure 2-1.** Human cardiovascular system with the associated various cardiovascular diseases [26].

supported by connective tissue that is primarily made up of elastic fibers and some collagen fibers [27]. It is the essential part of the arteries to regulate blood flow and blood pressure. The tunica externa, also known as the tunica adventitial, is the outermost layer of the vascular wall composed primarily of connective tissue with fibroblasts, helping to hold the vessel in a relative position [28].

According to the various sizes, arteries can be categorized into arterioles (with a diameter below 0.5mm), muscular or distributing arteries (medium-sized), and elastic or conduit arteries (typically with a diameter larger than 10 mm). Although all types of arteries are composed of the three tunics, there are some structural differences between different types of arteries due to their variety of functionalities (Figure 2-2). The arterioles are the primary resistance vessels that distribute blood flow into capillary beds in the organs, featured with only one or two layers of the smooth muscle in the tunica media [29]. The muscular arteries, on the other hand, present a much thicker smooth muscle layer in the tunica media in corresponding to their leading role in vasoconstriction [30]. The elastic arteries such as aorta have the thickest tunica media that contains a high percentage of elastic fibers to withstand the high blood pressure causing by the heart blood ejection [31].

### 2.3 Physiology and histology of abdominal aorta

The abdominal aorta is a part of the aorta that passes through the abdominal cavity, beginning at the level of the diaphragm and ending at the common iliac bifurcation [32]. It supplies all of the abdominal organs such as the liver, stomach, spleen, duodenum with oxygenated blood to maintain their functionality. As a transitional elastic artery, the

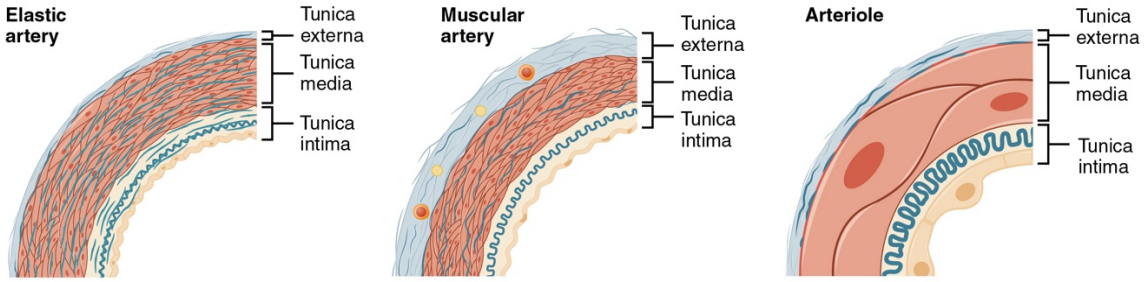


**Figure 2-2.** Types of Arteries and Arterioles. Comparison of the walls of an elastic artery, a muscular artery, and an arteriole is shown. In terms of scale, the diameter of an arteriole is measured in micrometers compared to millimeters for elastic and muscular arteries [30].

abdominal aorta has a monolayer of endothelium and a scant pad of sub-endothelial fibrous connective tissue upon an intact internal elastic lamina, a relatively thick media consists of smooth muscle cells (SMCs) embedded in structural proteins, and an adventitial that contains a network of vasa vasorum [33, 34]. Since the media normally accounts for up 80% of the abdominal aortic wall, the thickness of the abdominal aortic wall nearly linearly relates to the number of the medial lamellar units [34]. For an adult human, the normal abdominal aorta has a media consists of 28 to 30 concentric fibromuscular layers with an average thickness of 0.8 to 1mm [35].

In large arteries like aorta, the network of vasa vasorum plays an important role in the delivery of nutrients and oxygen to and the removal of waste products from the aortic walls. However, it has been demonstrated that the infrarenal abdominal aortic media is vastly avascular because the vasa vasorum has been shown to only penetrate the media of vessels with greater than 29 medial lamellar units [34]. Thus, it is likely that the relatively fewer lamellar units and lower collagen to elastin ratio in the abdominal aortic media

comparing to the theoretic aorta, and the fact that the survival of SMCs in the abdominal aortic media mainly depends on trans-intimal diffusion of nutrients make the abdominal aorta more prone to aneurysmal degeneration [36].

### 2.4 Elastin in the aortic wall

Elastic fiber is the main component that makes up roughly 50% of the arterial extracellular matrix (ECM), and provide the necessary load-bearing ability in low-pressure regions and elasticity for proper cardiovascular function in vertebrate animals [37, 38]. It has two major components: an elastin core that comprises 90% of the fiber, and a scaffold of microfibrils, which are composed mostly of fibrillin-1 and -2 [39]. The synthesis of the elastin fibers can be divided into three stages, known as (a) secretion of the tropoelastin (a ~60 -70 kDa protein) by elastogenic cells, including SMCs, endothelial cells, fibroblasts, and chondroblasts, into the ECM, (b) coacervation that forms self-aggregated tropoelastin spherules, and (c) cross-linking that generates the networks of elastic fibers by depositing the spherules onto microfibrils and forming intramolecular and intermolecular crosslinks with the participation of lysyl oxidase (LOX) enzymes (Figure 2-3) [40].

ELN is the only tropoelastin gene in humans. Most of the elastin synthesis in human bodies happens very early in life. As we age, ELN expression decreases dramatically, resulting in a decrease of elastin product and causing difficulties for elastin damage repair [41]. The elasticity of the elastin fibers is a result of its massive cross-linking network that maintains the mechanical stability when elastic fiber undergoes deformation (Figure 2-4). The reversible elasticity of the aortic elastic fibers plays an important role in maintaining the

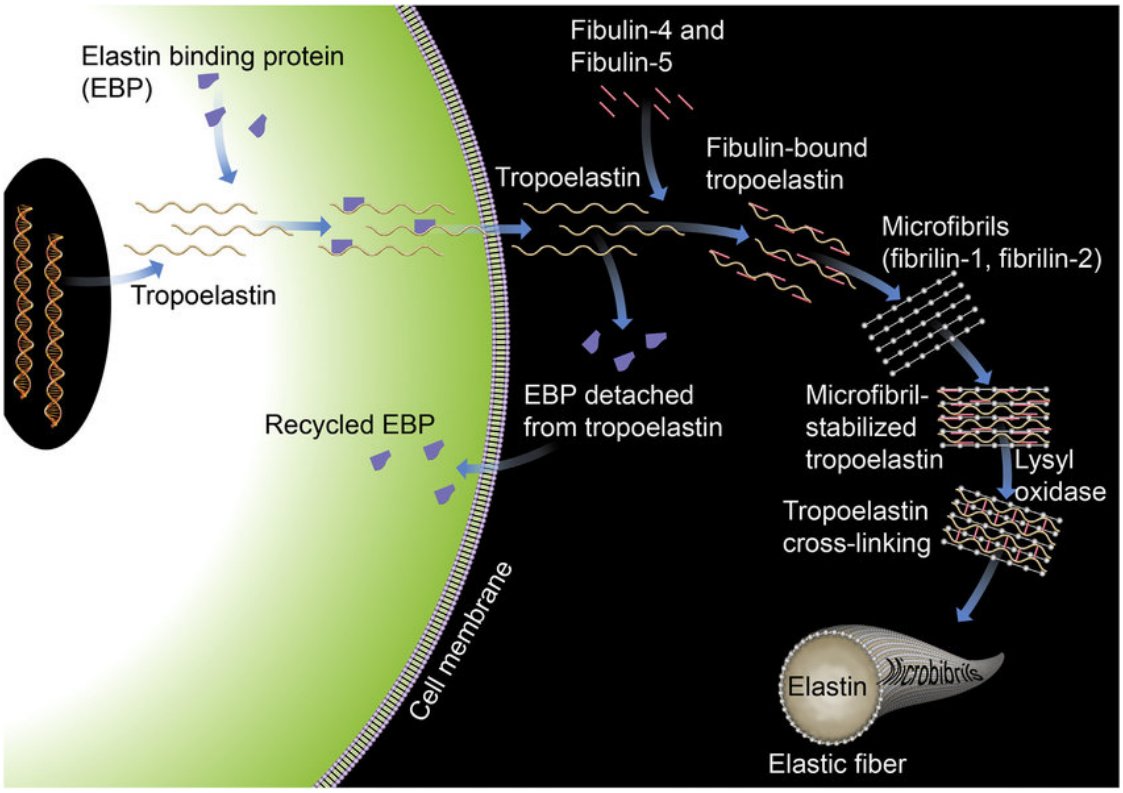


**Figure 2-3.** Elastogenesis: from tropoelastin to elastic fibers; Tropoelastin synthesis, binding with elastin-binding protein (EBP), transport, release of EBP, assembly with fibulins, binding to microfibrils, LOX-mediated cross-linking, and final formation of an elastic fiber [42].

Windkessel effect of the cardiovascular system to allow sufficient blood supply in the distal micro-vasculatures [43].

The amount and organization of the elastic fibers, as well as the collagen fibers in the aortic ECM, dominate the passive mechanical behavior of the large elastic arteries. The arteries underwent elastase treatment in animal models were shown to have a significant increase of the side lengths in both longitudinal and circumferential directions, indicating

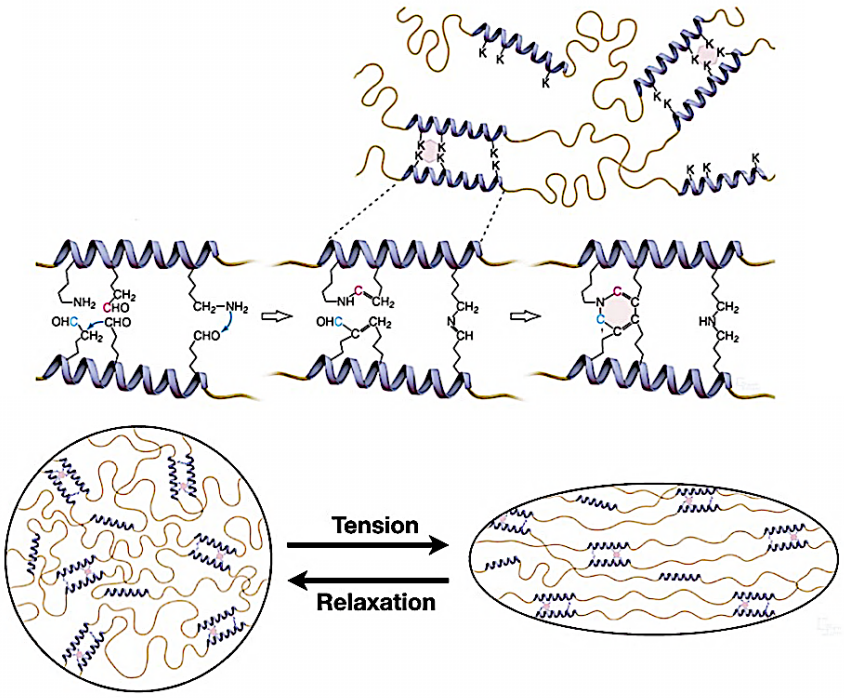


**Figure 2-4.** Crosslinking of elastin and mechanism of elastin stretch and recoil [44].

the weakening of the arterial wall [45, 46]. Experiments on the aorta from mice lacking elastin gene (ELN-/-) have demonstrated a reduction in the circumferential material stiffness at low pressure [47]. Thus, insufficient elastin, improper assembly, disorganization, fragmentation, and remodeling of the elastic fibers change the passive mechanical behavior of the elastic arteries.

Aside from the influence it has in aortic mechanical properties, elastin and its degradation products, resulted from matrix aging and/or cardiovascular diseases, have signaling effects that can lead to pathological changes to the cardiovascular system. In a study on rat aorta, Sauvage M. et al. reported the colocalization of transforming growth factor (TGF) -β1 immunoreactivity and tropoelastin expression in the developing rat aorta

[48]. The accumulation of elastin has been suspected to change the availability of TGF-β indirectly by modulating latent TGF-β binding to microfibrils [49]. And soluble tropoelastin has been demonstrated to regulate the proliferation of VSMCs, as well as to change the stiffness in an *in-vitro* cell culture model [50, 51].

Signaling effects of the elastin degradation products, such as elastin-derived peptides (EDP), a bioactive product of elastic fiber degradation, and fragmentation that retain the VGCAPG peptide sequence, mostly depends on their interaction with elastin receptor complex (ERC) [52, 53]. ECR is a heterotrimeric cellular surface receptor for elastin composed of a peripheral elastin-binding protein (EBP, 67 kDa), a protective protein/cathepsin A (PPCA, 55 kDa) and a membrane-bound neuraminidase, Neu-1 (61 kDa) [54]. The EBP subunit presents two functional-binding sites, including the EDP binding site that induces signaling pathways, and the galactosugars attaching site, which is associated with EDP release and dissociation of the complex [42].

The binding between EDP to EBP is capable of activating several intracellular signaling pathways depending on the cell type (Figure 2-5). EDP can modulate the vascular tone through its ability to influence the vascular endothelial relaxation and the vascular smooth muscle cells (VSMCs) contraction [55, 56]. Moreover, the EDP has been implied to play a crucial role as a chemotaxin in the recruitment of monocytes, neutrophils, macrophages, and fibroblasts, as well as a regulator of VSMCs migration [57-61]. It has also been reported that EDP can modulate the macrophage polarization and the proliferation of fibroblasts and VSMCs [62-64]. The structural and mechanical change in

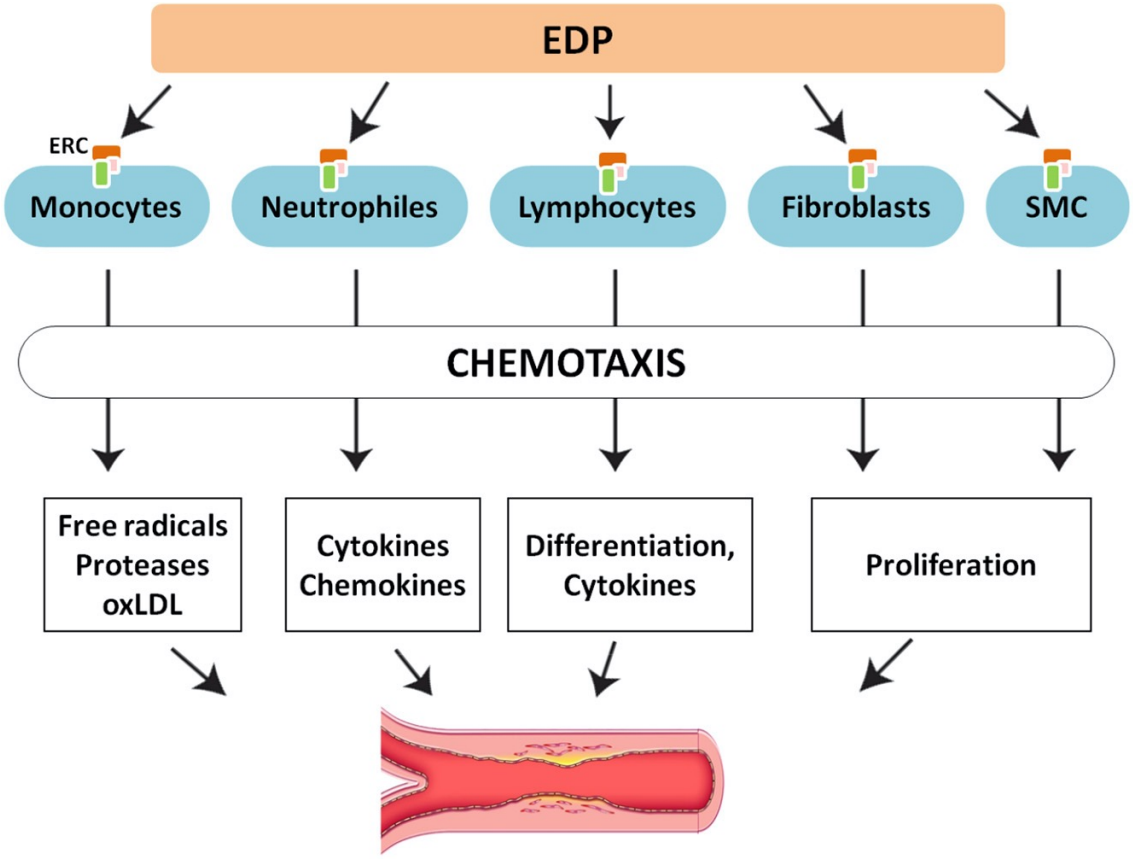


**Figure 2-5.** EDP affect various cell functions through its cognate receptor ERC, playing a crucial role in the development of cardiovascular diseases such as hypertension, atherosclerosis, and aneurysm [53].

the large elastic arteries such as aorta can result in a malfunctional circulatory system that is responsible for many acquired cardiovascular diseases.

Arterial stiffness is one of the structural mechanical properties that depend on the mechanics of elastic fibers in the arterial wall. The assessment of arterial stiffness is usually achieved by measuring the pulse wave velocity (PWV), distensibility characterized by circumferential strain, and Peterson's elastic modulus [47, 65-67]. Due to the limited

synthesis timeframe and low turnover rate, the damage of elastin fibers with aging or disease generally remains unrepaired. Insufficient or destruction of the elastin network initially leads to decreased stiffness in arteries and is characteristic of the first shift in mechanical behavior called the initial-softening phase [46, 68]. Meanwhile, the EDPs induce the local proliferation of VSMCs and fibroblasts and recruit the leukocytes to the remodeling sites, creating a proinflammatory remodeling environment. The remodeling of the ECM after the elastin damage, which is characterized as a deposition of non-organized collagen fibers and proteoglycans, in combination with a change of VSMC plasticity, stiffen the arterial wall and cause a loss in arterial mechanical properties [69, 70].

### 2.5 Abdominal aortic aneurysm (AAA)

An abdominal aortic aneurysm (AAA) is an abnormally widened or bulged area of the abdominal aorta. Depending on the location where the enlargement happens, AAAs can be divided into four main categories, suprarenal AAAs, pararenal AAAs, juxtarenal AAAs, and infrarenal AAAs (Figure 2-6). It is characterized by an impaired vessel wall integrity, which is featured as a progressive disruption and weakening of the ECM, leading to dilation of the aorta that can be fatal if not treated [35].

A human AAA is diagnosed when the aortic diameter is higher than 3.0cm or more than 50% larger than the average diameter [5]. AAA is a common disease that has a prevalence of approximately 4.8% (6.0% for males and 1.6% for females) in the general population [71]. Including patients who die before reaching the hospital, the mortality rate due to abdominal aortic aneurysm rupture is 90%, and the number of deaths attributable to

the AAAs is more than 15,000 per year [72]. It is the 14th leading death cause in the US and is cited as one of the top 10 causes of death among older men [73].

### 2.6 Pathophysiology of AAA

Several biological processes and risk factors, including genetic factors, lifestyle-associated risk factors, and other cardiovascular diseases have been identified to contribute to AAA pathogenesis. AAA is typically associated with aging and atherosclerosis, with attendant risk factors such as hypercholesterolemia, hypertension, and diabetes [74]. Smoking is also a significant risk factor for AAA development. As in a small aneurysm trial, which randomized 1090 patients with AAA with diameters of 4–5.5 cm between immediate repair and surveillance, 91.8% of the patients were former or current smokers [75].

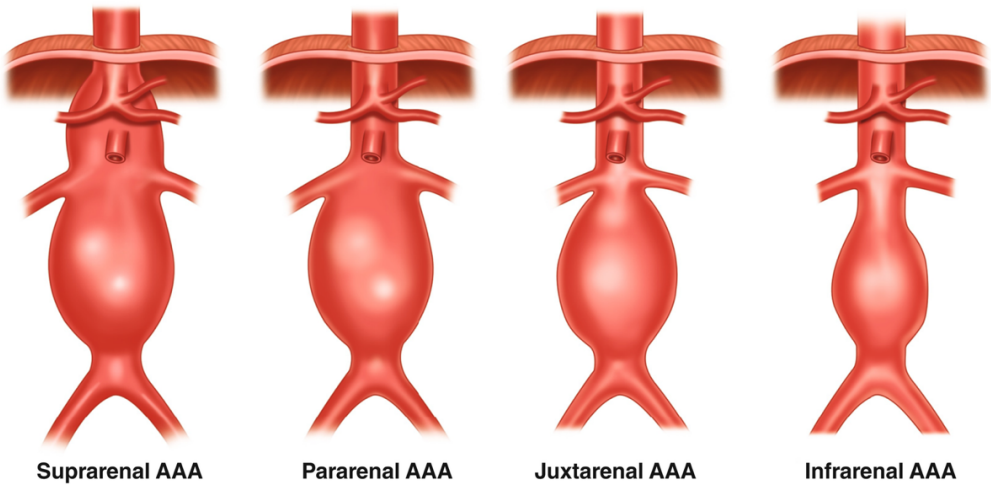


**Figure 2-6.** Crawford's classification of AAAs [76].

The pathophysiology of AAA has been studied on different levels (Figure 2-7) [5]. On the histological level, AAA onset is associated with chronic adventitial and media inflammatory cell infiltration, apoptosis of VSMCs, and ECM degradation, primarily

elastic lamina degradation by proteolytic enzymes such as matrix metalloproteinases (MMPs) and cathepsins[35, 77, 78]. Many inflammatory cells have been detected in the aneurysmal tissue, including macrophages, T lymphocytes subset, B lymphocytes, neutrophils, and mast cells. These cells elevate the inflammation in the aneurysmal tissue and accelerate the degradation of the ECM by influencing the production of multiple inflammatory factors and extracellular proteases [5, 79, 80]. Moreover, a recent study found that the abnormal presence of adipocytes in the aortic adventitial could recruit macrophages; therefore, increase the MMP-2 and MMP-9 levels and degrade collagen fibers surrounding them [81]. Aortic VSMCs in the aneurysmal tissue have been shown to have phenotype changes from a contractile type to synthetic one in consistence with the cytoskeletal rearrangement, which also preceded elastolysis and gross media remodeling [74]. Adventitial fibroblasts are presumed to promote structural repair when the damage is done to the aortic wall. However, the interstitial collagen becomes disorganized and compromises the mechanical properties of the aortic wall.

On the molecular level, many chemokines, cytokines, proteases, microRNAs (miRs) and the renin-angiotensin system (RAS) have been implicated in the formation and progression of AAAs. Some upregulated pro-inflammatory cytokines such as interleukin (IL)-1β, IL-6, IL-17, IL-23 and tumor necrosis factor (TNF)-α, monocyte chemoattractant protein (MCP)-1 have been demonstrated to contribute to the recruitment and differentiation of macrophages at the aneurysmal site [5, 74]. TGF-β, on the other hand, is a critical down-regulated cytokine that plays a protective role in human AAA pathogenesis despite its ability to promote thoracic aortic aneurysm (TAA) formation [82].

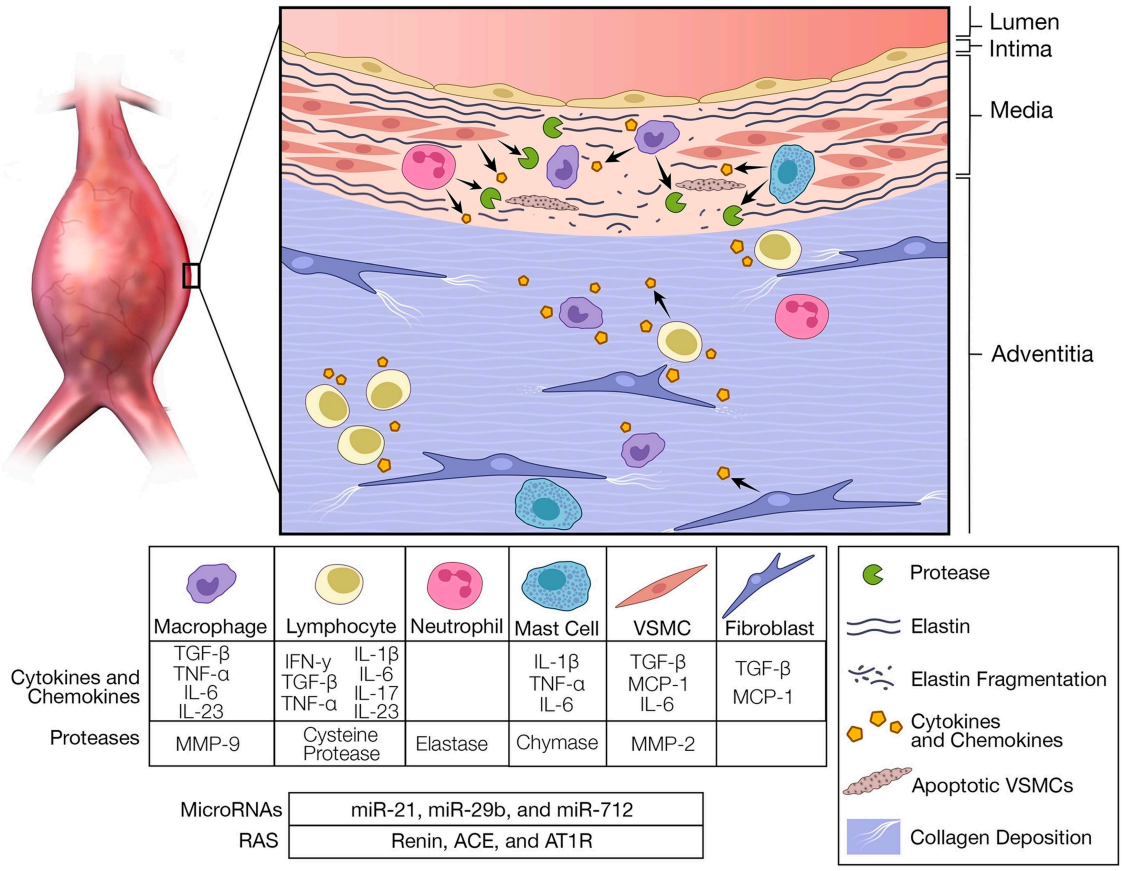


**Figure 2-7.** Pathophysiology of AAA with the table legend that illustrates major cell types, cytokines, protease, miRs. and RAS involved in AAA pathogenesis [5].

Lysyl oxidase (LOX), an oxidase the activity of which also has been found suppressed in the AAA, can stabilize the ECM by crosslinking the collagen and elastin and inhibiting MCP-1 secretion and the subsequent inflammatory responses, and slow down the progression of the AAA [83].

Some proteases and their inhibitors, including MMP, serine proteases, and cysteine proteases, have been involved in the AAA formation and progression by causing structural damage of elastin and collagen in the aortic ECM, which leads to weakening and dilation

of the abdominal aorta [84]. The complementary role of macrophage-derived MMP-9, and MMP-2, an MMP that has a unique ability to degrade both elastin and fibrillar collagen, has been proved critical in the development of AAAs [85]. Cysteine and serine proteases, on the other hand, can activate neutrophil elastase and some other proteases in AAAs, which cause further degradation of the ECM and AAA progression [86].

MiRs are a class of short, well-conserved, non-coding RNAs that play their biological role by influencing the stability and translation of mRNAs [87]. Several miRs have been identified as crucial regulators during the AAA development recently. A decrease of miR-29b has been detected in human AAA tissues due to the aortic damage [86]. However, several studies in mouse models indicated that when the expression of the miR-29b was further suppressed to levels lower than typical pathological decreases, several ECM proteins expression was upregulated and the progression of the AAA was slowed down [88]. The upregulation of murine specific miR-712 and its human/murine homolog miR-205 has been demonstrated to downregulate two key upstream inhibitors of MMPs, tissue inhibitor of metalloproteinases (TIMP)3 and reversion-inducing cysteine-rich protein with kazal motifs (RECK), which leads to ECM degradation and AAA progression [89]. Moreover, it has been pointed out that the overexpression of miR-181b could negatively regulate TIMP3 expression and activity [90]. On the contrary, overexpression of miR-21, a miR that has been identified as a critical mediator for proliferation and apoptosis of VSMCs, can prevent AAA formation [91].

The relationship between RAS and AAA development has been studied in many animal studies. The infusion of angiotensin II (AngII) in mice deficient for apolipoprotein

E (ApoE-/-) or low-density lipoprotein receptor (LDLr-/-) in combine with a high-fat diet can induce aneurysms and dissections at the suprarenal abdominal aorta [92]. AngII infusion in mice was shown to associate with the adventitial accumulation of C-C chemokine receptor type 2 $(CCR2)^{+}$ macrophages specifically at the sites of aneurysm formation and the most prominently at the sites of dissection [93]. AngII also stimulates the angiotensin type 1a (AT1a) receptors to regulate the mitogen-activated protein kinase (MAPK) signaling cascade and enhance the TGF-β signaling, which eventually leads to the production of pro-inflammatory factors [74].

**2.7 Biomechanics of AAAs**

The biomechanics of the aneurysmal aortic wall has been extensively studied to develop a method to predict the rupture risk of the AAAs. The rupture of the AAAs happens when the strength of the wall cannot withhold the blood pressure. Thus, studying the effect of blood pressure on the aortic wall is essential. The aortic wall is a tubular structure that repeatedly deforms under pulsatile blood pressure, which generates forces that can be normalized and translated into radical, circumferential, axial, and wall shear stresses (Figure 2-8) [94].

The formation of the AAAs can significantly change the aortic mechanical properties due to the degradation of the structural proteins such as elastin and collagen fibers [95]. Destructive AAA tissue characterization tests such as uniaxial extension test until failure, biaxial extension tests, and peeling tests were performed for material property data collection. Anisotropic responses with stiffer behavior have been demonstrated in the circumferential direction of AAAs in *ex-vivo* AAA studies [96, 97]. The geometrical

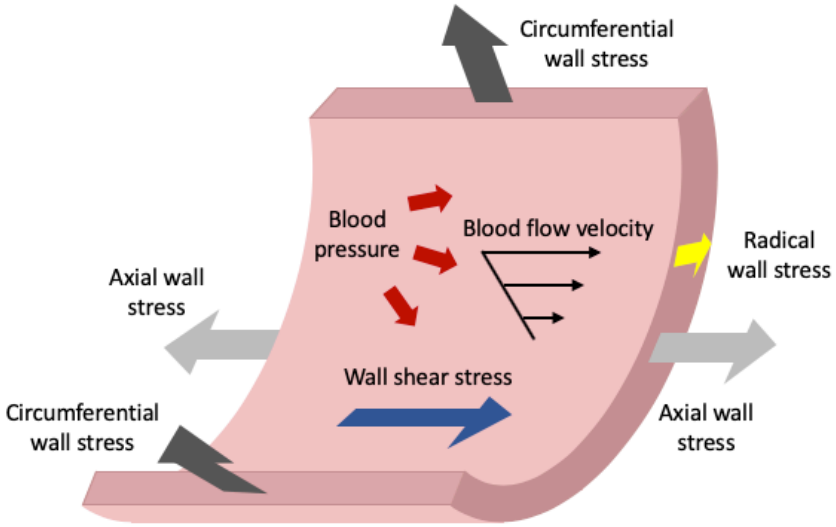


**Figure 2-8**. Mechanical loading state of aortic tissue shows circumferential, axial, radial, and wall shear stresses in the aortic wall.

change of the abdominal aorta and other related pathological changes, including the formation of an intraluminal thrombus (ILT) and the apoptosis of VSMCs, can result in a change in the local fluid dynamics [94]. The combination of a weakened aortic wall and the abnormal fluid dynamics may elevate the mechanical stresses on the aneurysmal aortic wall and lead to rupture.

### 2.8 Rupture risk assessment of AAA

The potential risk of an aneurysm rupture is determined by factors such as evolving geometry, mechanical properties, and hemodynamic loads/perivascular conditions [98]. Nowadays, three major categories of assessment methods have been applied to predict AAA rupture risk: AAA geometrical analysis, local biomechanics analysis, and biomarker analysis.

**AAA geometrical analysis**

Geometrical information such as maximum aortic diameter has been used as the standard clinical criteria for assessing the AAA rupture risk and deciding treatment strategy [99]. Advances in medical imaging, particularly computed tomography angiography (CTA) and magnetic resonance imaging (MRI), provide exquisite data on overall patient-specific geometries. While using the geometric modeling to predict the rupture risk AAAs, at least 40 image-based geometric parameters are correlated with AAA rupture and 15 of the correlates are statistically significant for the predictive model [100]. However, the recommendation of intervention should not only base on the size of the AAA, as many small AAAs ruptured while large AAAs remained stable in clinical cases [101].

AAA geometry is complex and, in most cases, cannot be approximated by a thin-walled cylinder. For example, almost all clinically relevant AAAs contain ILTs composed of fibrin, inflammatory cells, platelets, and red blood cells [99]. The formation of ILT influences the structural and mechanical properties of the AAA. Thus, to predict the patient-specific rupture risk more precisely, fine element analysis (FEA) is used to reconstruct a more accurate 3-dimensional (3D) AAA morphology and to calculate the biomechanical parameters.

**AAA biomechanical analysis**

To understand the biomechanical properties of the aneurysms, computational models have been developed base on the AAA rupture factors (Figure 2-9). These models can be used to find the mechanical weak point of the aneurysm and predict its rupture possibility. FEA for AAA usually incorporates risk factors such as AAA geometry, gender,

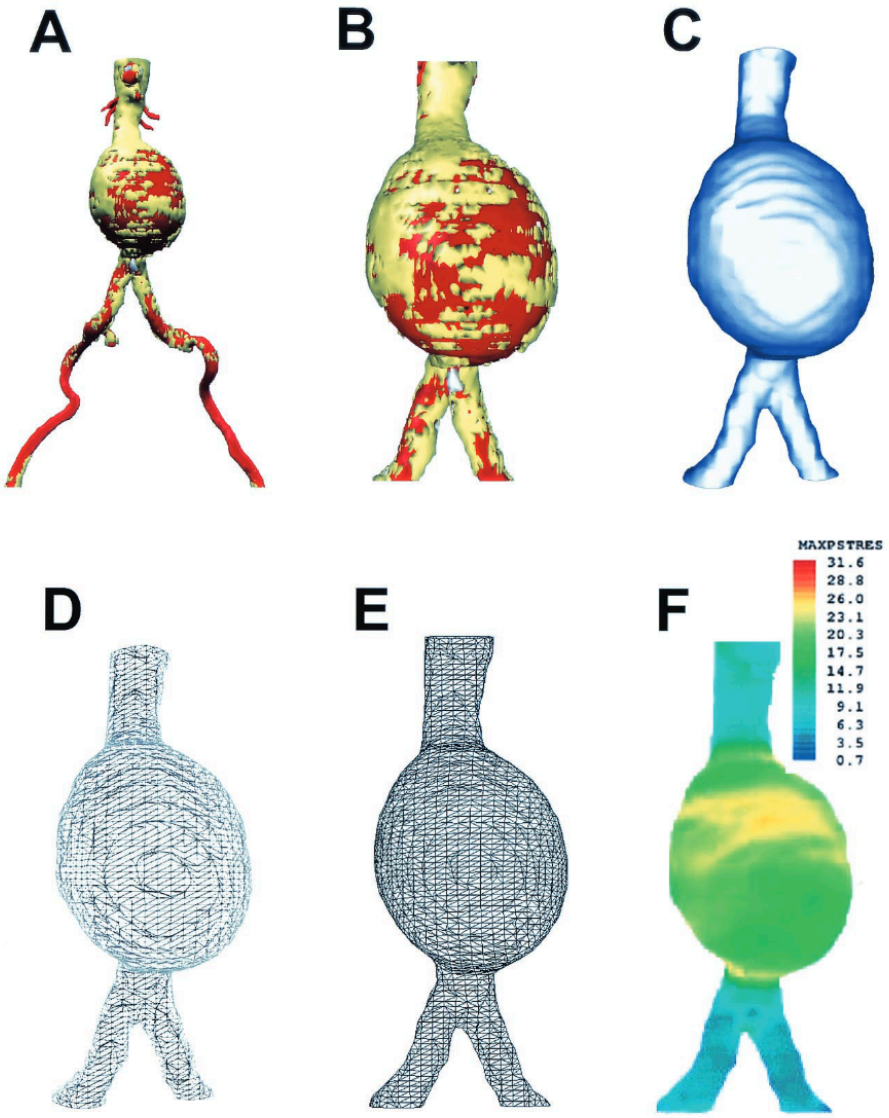


**Figure 2-9.** Process of creation of appropriate 3D reconstruction for stress analysis: A. Initial surface shaded 3D reconstruction; B. Elimination of anatomic elements not pertinent to stress analysis; C. Merged 3D reconstruction to obtain outer boundaries of the aortic wall; D. Initial 3D mesh; E. Refined mesh ready for input into FEA program; and F. Stress analysis with stress mapped onto the surface of 3D reconstruction with color gradients to represent stress gradients [102].

blood pressure, smoking history, and the amount of ILT [103]. Two commonly used biomechanical dices, peak wall stress (PWS) and peak wall rupture index (PWRI), can be calculated using FEA to estimate the future AAA rupture risk. As we mentioned previously, the rupture of AAA happens when the aortic wall stress exceeds the mechanical strength of the wall. Thus, it is feasible to use PWS, the highest von Mises wall stress within an AAA, to predict the potential rupture. PWS calculations are based on blood pressure, aortic wall properties, and the geometry of the 3D AAA model reconstructed from the CTA images [104]. PWRI is a relatively more sophisticated mechanical parameter than PWS. While PWS considers only the stress, PWRI is estimated base on the relationship between the local wall stress and local wall strength, using the following equation:

$$PWRI = \max\left(\frac{Wall\ stress}{Wall\ strength}\right)$$

However, the classic FEA is usually performed base on a fixed AAA geometry. The progression of the AAA with time could greatly change the stress and the strength of the aneurysmal tissue, thus, make the previous rupture risk evaluation less accurate. Computational modeling of vascular growth and remodeling (G&R) provides a tool to model the time evolution of vascular diseases based on the assumption that mechanical hemostasis exists [102]. On the foundation of the FE analysis for stress, G&R modeling adapts the growth stimulation to the configuration by introducing the influence of constituents such as elastin, collagen, and SMCs, to mimic the AAA progression *in-vivo* (Figure 2-10) [105]. Zeinali-Davarani, S. et al developed a computational G&R model by

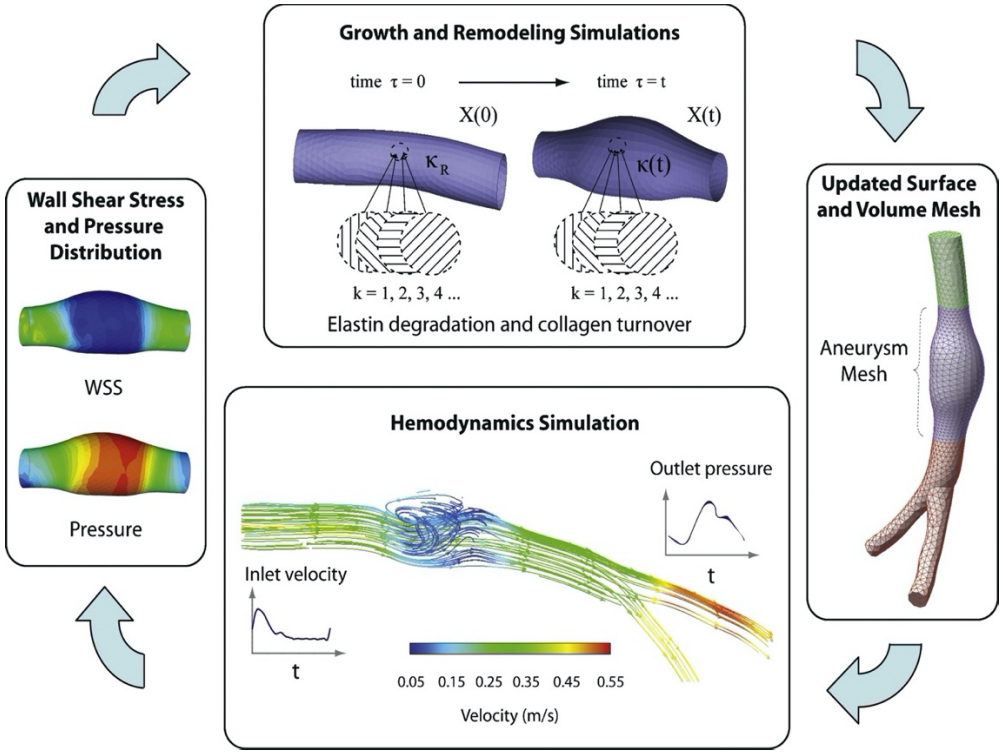


**Figure 2-10.** *In-vivo* configurations for fluid-solid growth simulations, iterative loop, and information transfer in the coupling between the hemodynamics and G&R simulations [106].

applying estimated material parameters as well as the distributions of wall thickness and anisotropy gained from an inverse optimization method to develop the vessel wall model and then introducing spatial elastin degradation as the stimulation to the model [107]. Sheidaei, A. et al. reported a G&R model based on the effect of wall shear stress to understand the progression and rupture mechanism of AAAs [106]. These models provided theoretical frameworks for further developing patient-specific AAA models for clinical use.

Both PWR and PWRI have been reported to be higher in symptomatic or ruptured than in intact AAAs in many independent studies, indicating their potential to be used as AAA rupture risk assessment tools [103, 108, 109]. Moreover, the development of the G&R model provided a tool for studying the rupture risk of AAA in a progression dependent manner. However, the calculations for PWR and PWRI, as well as the establishment of the G&R models are based on some predefined AAA parameters such as the aneurysmal wall thickness, due to the limitation in spatial resolution of imaging. The variety of these parameters between patients can cause inaccuracy of the rupture-predicting capability of the existing computational models.

**AAA biomarkers analysis**

In addition to the biomechanical features, some AAA related biomarkers, including serum EDP concentration, $^{18}$F-fluorodeoxyglucose ($^{18}$F-FDG) uptake, and ILT size can be used to predict the expansion and rupture of AAAs [110]. As the AAA progress, the degradation and fragmentation of elastin in the aneurysmal tissue release EDP into the circulation and can be detected using ELISA method. It has been demonstrated in a five-year human small AAA study that serum EDP level is significantly correlated with AAA expansion in ~90% of the tested cases [111]. The level of the inflammation in the aneurysmal tissue also varies during the progression of the AAAs. The high metabolic activity associated with a severe local inflammation precedes a phase of AAA rapid growth and is then followed by a period of stasis with low metabolic activity [112]. $^{18}$F-FDG uptake increase, featuring an increased metabolic activity in the aneurysmal tissue, can be

detected and quantified using positron emission tomography (PET) and can be used as a reliable marker for AAA expansion [113-115].

Furthermore, the ILT size is also a promising prognostic growth marker for AAAs. A thin ILT layer can function as a protection for the aortic wall because it can buffer the stress and lower the rupture risk for the aneurysm [116]. However, when growing too thick, the ILT layer can cause the aortic wall to weaken, for example, due to hypoxia. ILT is also the source of many pro-proteolytic processes that stimulate aortic wall degradation [117]. A clinical study performed by Haller S.J. et al. pointed out that the protective biomechanical advantage that ILT provided by lowering wall stress seems to be outweighed by the weakening of the AAA wall, particularly in patients with small ruptured AAAs [118].

### 2.9 Animal models for AAA

Animal models of AAA can provide insight into the mechanisms of progression of the human disease based on the assumption that the biochemical, biomechanical, and cellular properties in the animals are comparable to those in humans. However, due to the species-specific variety, there is no perfect animal model for AAAs. Each different experimental model of AAA only presents partially the pathological features that have been discovered in human AAAs. AAA animal models have been developed using genetic manipulation, physical and chemical induction, as well as the combinations of these technics. Different animal species have been used to create *in-vivo* AAA models, including mouse, rat, hamster/guinea pig, rabbit, turkey, dog, sheep, and porcine to study the mechanisms of AAA.

**Rodent AAA models**

Rodents are most wildly used to develop animal models for reasons including the small size, relative cheapness, great accessibility, and the ability to be genetically manipulated. Several different techniques, including elastase treatment, calcium chloride ($CaCl_2$) treatment, AngII infusion, and xenograft transplantation, has successfully induced the formation of AAAs with different characteristics in rodents.

The elastase model in rodents is performed by intraluminal or periarterial application of elastase, usually porcine pancreatic elastase (PPE), via a midline abdominal incision (Figure2-11). Traditionally, to perform intraluminal perfusion of the PPE, the infrarenal abdominal aorta is dissected from the surrounding connective tissue and isolated from the circulation by applying atraumatic clamps. PPE is then injected into the isolated part of the aorta through a catheter. When the perfusion is finished, the catheter and the clamps are removed to restore the blood flow, and the incision is sutured close. This method can be challenging to perform due to the small size of the rodent aorta.

A more straightforward elastase treatment that involves an application of a periadventitial PPE soaked gauze has been developed to introduce elastin damage to the rodent aorta [119]. Moreover, the combined use of 3-aminopropionitrile fumarate salt (BAPN) and periadventitial PPE treatment results in an advanced staged AAA that forms thrombus and can spontaneously rupture [120]. The AAAs developed using the rodent elastase model have multiple pathological features that are similar to human AAAs including the infiltration of the macrophages in the adventitial, degradation of media elastin, apoptosis of VSMCs, and formation of intraluminal thrombus [119, 121].

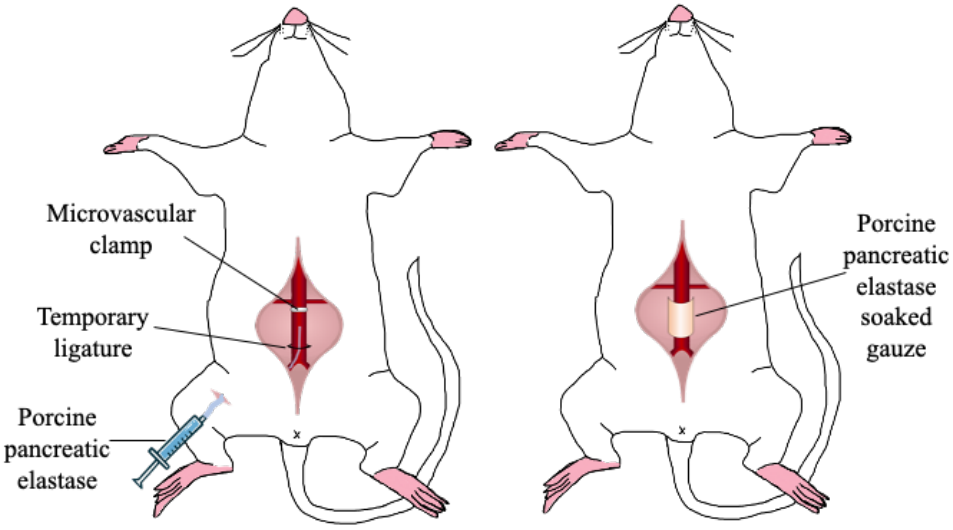


**Figure 2-11.** Intraluminal and periarterial application of elastase on rodent aorta.

Periadventitial administration of calcium chloride at the infrarenal aorta can also induce AAAs in rodents. The surgical protocol for this model is similar to the periarterial PPE treatment model, but a gauze soaked with calcium chloride solution is applied instead of PPE. The expansion of the aorta was mostly reported immediately after the $CaCl_2$ exposure. Increased endothelial permeability and VSMC apoptosis have been documented in $CaCl_2$ treated vasculature, as well as vascular calcification and the infiltration of inflammatory cells in the adventitia and media [122]. This model is developed to closely mimic human AAA pathology in terms of upregulated inflammation, degradation of ECM, neovascularization, increased oxidative stress, VSMC apoptosis, and heavy aortic calcification which has been reported in 80% of human AAAs [123]. The main problem with the $CaCl_2$ AAA model is that there is no evidence of intraluminal thrombus formation and rupture, as is seen in human AAAs.

Ang II infusion via a subcutaneously implanted osmotic pump for 28 days, can induce AAA in wild type C57BL/6 mice or transgenic mice (ApoE-/- or LDLr-/-) (Figure 2-12). Aneurysms in this model are usually observed at the suprarenal abdominal aorta as well as the ascending aorta, making it a proper model for studying both AAAs and TAAs. AngII has been known as a peptide hormone that can increase blood pressure by constricting the blood vessels. Although the infusion of AngII in hyperlipidemic mice can increase mean arterial pressure, it has been demonstrated that the arterial dilation and AAA formation in these models was not related to the increased blood pressure [92, 124]. The upregulation of mRNA expressions of MMP, PPAR-γ, MCP-1, and uPAR in AngII induced AAAs increases the inflammation in the aortic wall in a blood pressure-independent way [125]. AngII promotes the enlargement of the suprarenal aorta accompanied by atherosclerosis, medial hypertrophy, accumulation of macrophages in the external elastic lamina, and thrombosis in ApoE-/- mice, which mimics human AAA development [126].

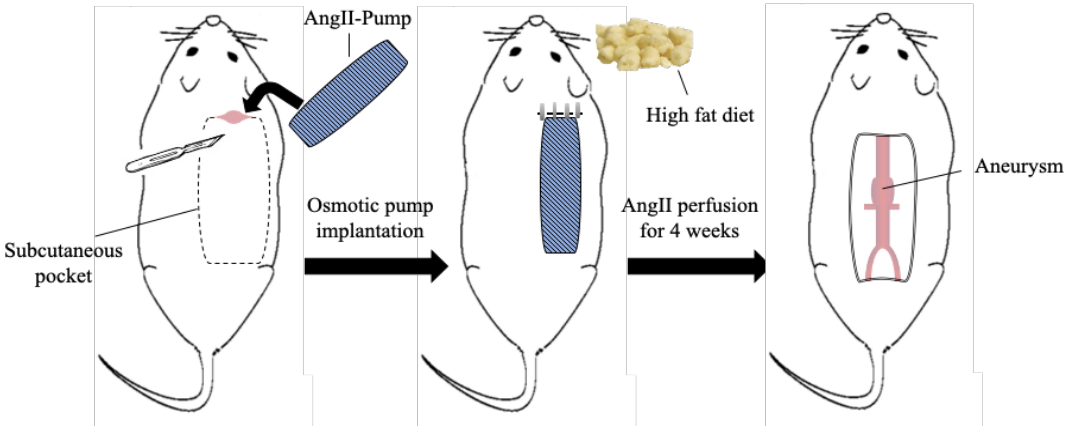


**Figure 2-12.** Development of AngII infused AAA model.

Transplantation of a decellularized xenograft to replace a part of the healthy rodent aorta can also induce aneurysms. Usually, a donor aorta, for example, an aorta from guinea pig, is harvested and decellularized with sodium dodecyl sulfate (SDS) and then transplant into the rodent via major abdominal surgery. The donor aortic ECM induces a chronic interspecies immunological response that causes the destruction and dilation of the xenograft [127]. The infiltration of monocytes and T-lymphocytes has been reported in the intimal of the transplanted graft [128]. The pre-immunization of rodents with donor aortic ECM accelerates xenograft destruction and triggers AAA rupture [129]. This model is not as frequently studied in small animals but can be used to specifically study the roles of the immune system, aortic ECM, and VSMCs in AAA development.

**Non-rodent AAA animal models**

The development of new surgical techniques and new devices for AAAs created a need for animal models that can create AAA with anatomical similarities to humans. Medical devices, such as stents and grafts, need to be tested before incorporation to the clinic, and rodent models failed to translate the experimental findings due to their small size. Thus, increasing efforts have been made to create AAAs in larger species. Chemical induction is one way that has been wildly used in creating AAAs in large animals such as rabbits, dogs, and swine. The application of elastase, collagenase, or $CaCl_2$ alone can induce AAAs in rabbit with a more than 50% dilation [130, 131]. However, for larger animals like dogs and porcine, a combined treatment (elastase, collagenase, and angioplasty) must be applied to generate AAAs that are big enough for further study [132]. A large animal model can also be developed using grafts or patches. In the graft model, a

manufactured graft or a xenograft is interposed into the infrarenal abdominal aorta to induce aneurysms. And in the patch model, instead of a graft, an elliptical patch or a pouch, made out of the vein, prothesis vascular graft, and rectus fascia, is applied through a longitudinal aortotomy [133, 134]. These models which apply biological materials such as abdominal rectus fascia and veins have rupture characteristics that are similar to humans [127].

### 2.10 AAA diagnosis strategies and imaging modalities

When the enlargement of the aorta is greater than 1.5-fold of its normal size, it is considered an aneurysm [73]. Clinical diagnosis of AAAs is most common by ultrasound quantification of aortic diameter. It has been wildly used in the screening program for AAAs in many countries because it is inexpensive, non-invasive, and effective. Men and women, aged 65 years or older with a smoking or family AAA history, are recommended to receive onetime ultrasonography of the infrarenal abdominal aorta even if they have no symptoms [6]. Ultrasound is also used as a monitoring tool for patients with small AAAs to track AAA progression. Although it has been demonstrated to be a relatively accurate imaging modality for AAA screening, obese body habitus, bowel gas, and the observer's skill set can compromise the ultrasound accuracy [135]. Moreover, the imaging accuracy of ultrasound decreases as the size of the aorta increases [136].

When ultrasound images are suboptimal, computed tomography (CT) is used as an alternative imaging method. It is a superior diagnostic modality compared with ultrasonography because it can provide valuable information with high reproducibility, including a more accurate AAA morphology as well as the surrounding anatomy, the

presence of intraluminal thrombus, and calcifications. More advanced CT-based modalities, such as Helical CT and CTA are wildly used as the imaging modalities for the pre-operative AAA evaluation because they can generate a 3D road map of nearby vessels as well for planning surgical repair [137]. Moreover, some findings from the CT imaging render CTA the ability to provide information for assessing the inflammation level and rupture risk of the aneurysms. For example, CT-detected delayed enhancement in the aortic wall represents an increased density of inflammatory cells and neovessels in the aortic adventitial, and the intraluminal crescent sign represents the bleeding in the intraluminal thrombus [138]. However, the ionizing radiation and the contrast agents that are used in CTA can cause adverse effects in cases involving repeated imaging or renal insufficiency.

Magnetic resonance imaging (MRI) is another advanced imaging modality for AAAs with high sensitivity and reproducibility. MRI can provide high resolution 3D anatomical imaging of AAAs, as well as the information about aortic calcification, inflammation, and biomechanics [139, 140]. The advantage of performing magnetic resonance angiography (MRA), comparing to CTA, is that no ionizing radiation and contrast agent exposure is required. Instead of gadolinium contrast agent injection, a longer acquisition time in MRA can also enhance the AAAs [138]. But the use of MRI is limited because of its relatively high cost, patient-related motion artifact, and patient claustrophobia during longer scanning times.

## 2.11 Contrast agent for computed tomography (CT) scan

The X-ray absorption profile of different materials varies with the density and atomic number according to the formula that has been used to estimate the X-ray absorption coefficient under limited conditions:

$$\mu \approx \frac{\rho Z^4}{AE^3}$$

where $\rho$ is the material density, Z is the atomic number, A is the atomic mass and E is the X-ray energy. Different X-ray absorptions of different materials generate contrast in a CT scan. Many bodily tissues including bones and lungs are easily recognized in a CT scan due to their distinct X-ray absorption profile comparing to the soft tissues. However, it remains challenging to identify the interface between two adjacent soft tissues or between soft tissue and physiological fluids such as blood [141]. Contrast imaging agents are often applied to better visualize and differentiate the tissue of interest such as AAA from the surrounding connective tissue, improve the imaging quality, and increase the CT sensitivity. Various contrast media with a sufficient *in-vivo* retention-time has been developed to fulfill the requirement to highlight the tissue of interest in a CT scan.

### Iodine-based contrast agent

Covalently bound iodine has historically been a popular choice for designing CT contrast agent due to the high atomic number of iodine (Z = 53) (Figure 2-13). The iodinated contrast agent can be divided into ionic and non-ionic categories. Ionic contrast agents dissociate into negative and positive ions when dissolved in water while non-ionic contrast agents do not dissociate and contain polar hydroxide groups that confer them their

water solubility [142]. Non-ionic contrast agents comparably present more advantages to be used clinically including lower intrinsic osmolality and lower incidence of adverse health effects [143]. Over the past few decades, efforts have been made to optimize the iodinated contrast agent design by manipulating the functional groups present on the aromatic ring. The purpose of the optimization is to increase the water solubility and bio-tolerability while decreasing the binding to biological receptors and the toxicity of the iodinated contrast agent. Moreover, iodine can be encapsulated into nanoparticles to achieve some additional benefits, including increased blood circulation time, reduced renal clearance rate, and capillary leakage [144]. It is a better choice to enhance CT imaging for the cardiovascular system.

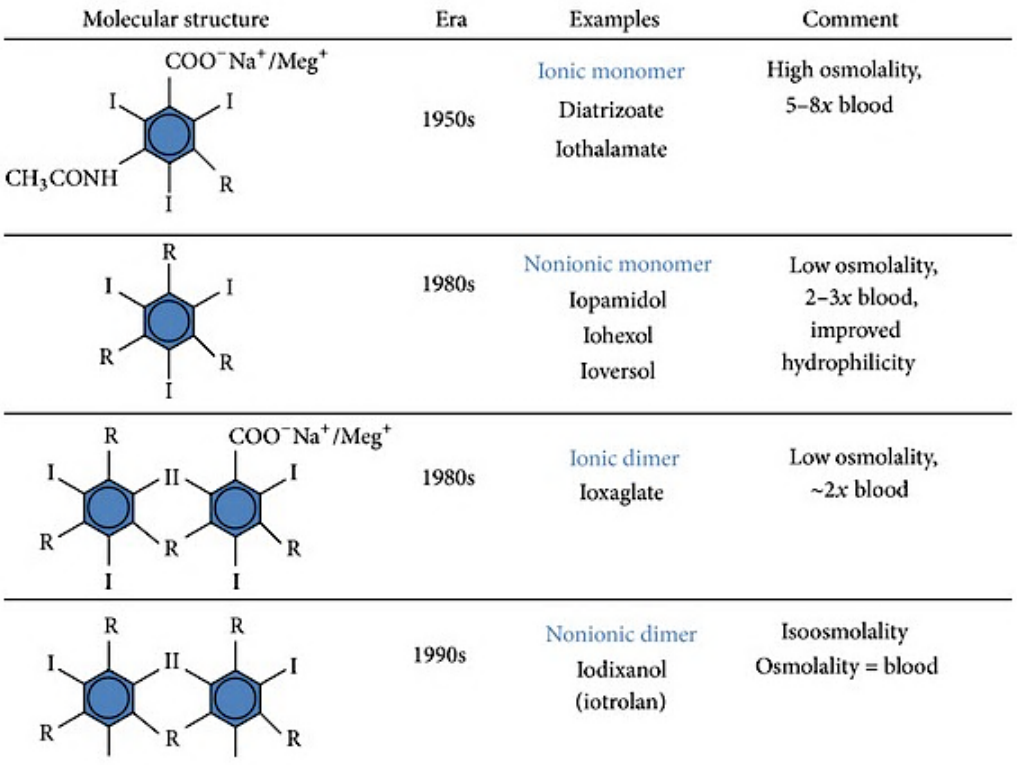


**Figure 2-13.** Different designs of iodinated contrast media [145].

**Lanthanide-based contrast agents**

Given their high atomic numbers, Lanthanide-based contrast agents, which are commonly used in MRI imaging, can also be used as a CT contrast agent for cardiovascular and pulmonary imaging [146, 147]. Although free lanthanide ions are extremely toxic, gadolinium (Z = 64), dysprosium (Z = 66), and ytterbium (Z = 70) form highly thermodynamically stable polyaminocarboxylic acid chelate complexes that make them clinically safe to be used as contrast agent [148, 149]. Since the lanthanide atoms have higher atomic numbers than iodine, they can offer higher X-ray attenuation and CT sensitivity than the equal mole amount of iodine atoms. However, some clinical studies show that gadolinium imaging media can be a cause of pancreatitis and nephrotoxicity that results in nephrogenic systemic fibrosis (NSF) and encephalopathy in certain at-risk patients [150-152]. Lanthanide based contrast agents can be nanoparticulated as well to increase the stability of the contrast agent, minimize the free lanthanide ion release and prolong their circulation time in blood [153].

**The gold nanoparticles-based contrast agent**

Gold nanoparticles (AuNPs) are an ideal radiopaque contrast media because of the following reasons: (a) gold has high density and high atomic number (Z=79), which renders it a high X-ray attenuation; (b) AuNPs have been demonstrated to have good biocompatibility *in-vivo*; (c) physical, chemical and biological properties of the AuNPs can be manipulated by the well-established synthesis and modification chemistry [154]. It has been reported that when the size of the AuNPs falls in a certain range, usually small sizes, AuNPs have a wild biodistribution and exhibit toxicity [155]. This problem can be solved

by controlling the size and shape of the AuNPs during synthesis, and by modifying the surface of the AuNPs with biocompatible molecules such as polyethylene glycol (PEG) and albumin [156, 157].

Surface coated AuNPs have long blood circulating time and can be used as the contrast agent for blood pool imaging. Moreover, the surface-modified AuNPs can be used to image targeted organs. The application of heparin polysaccharides conjugated AuNPs can produce a highly liver-specific contrast in mice [158]. Lisinopril coated AuNPs can be used to target the angiotensin-converting enzyme (ACE) overexpression in lung tissue in-vitro [159]. AuNPs coated with antibodies that can target the pathological biomarkers in cancer, for example, UM-A9 antibodies and Herceptin, have been studied as specific tumor targeting contrast agents for CT imaging [160, 161]. Although AuNPs based contrast agent has been demonstrated to be a great compromise between contrasting properties, physicochemical properties, and biocompatibility, the high cost of gold has been limiting its application in clinical CT imaging [154].

**Other metallic contrast agents**

Other metallic contrast agents such as water-soluble tantalum oxide ($Ta_2O_5$) and bismuth (Z=83) based contrast agents have been studied as inexpensive alternatives for AuNPs. $Ta_2O_5$ nanoparticle is an inexpensive, biocompatible contrast agent that has been used in tracheobronchial and gastrointestinal imaging [162] The sizes of these particles are easily controllable and surfaces of $Ta_2O_5$ nanoparticles can be modified with zwitterionic coatings. It possesses better CT attenuation properties than an iodinated agent on a per-mole basis [141]. Bismuth-based nanoparticles with good X-ray attenuating properties that

exhibit long vascular half-life have been developed and tested in mice as a potential contrast agent [163]. However, the clinical application of bismuth-based contrast agents is confined due to the difficulties in controlling the nanoparticle size and modifying the surfaces, and the lack of toxicity evaluation. As the synthesis and modification of these nanomaterials get optimized, they hold promise in the field of cardiovascular, lymphatic system, and tumor tissue CT imaging.

## 2.12 AAA Treatment Strategies

### Current treatments for AAAs

Currently, AAA patients can be clinically treated with either conservative methods or surgical interventions depending on the absolute/relative size or the growth rate of the aneurysm. Conservative management via regularly repeated ultrasonography for smaller AAAs with diameters vary from 3.0 to 5.4 cm greatly reduced the observed AAA-related mortality [6]. It is also a common treatment strategy for patients whose assessment of surgical risk overweighs the benefits. The medical aim for conservative management is to slow down the growth of AAAs and reduce the rupture risk pharmacologically by treating AAA related cardiovascular disease such as hypertension [164]. In the meantime, patients are recommended to quit the AAA promoting lifestyles such as smoking and unhealthy diets. By limiting the risk factors associated with AAA progression, patients with nonprogressive small aneurysms can get a better benefit from a conservative approach than a surgical treatment that usually has high risks of complications.

However, for patients with (a) AAAs that reach a diameter threshold of 5.5 cm, (b) smaller AAAs of which the diameters grow 1.0 cm per year, or (c) ruptured AAAs, a surgical repair

is usually recommended to diminish the risk of fatal rupture [165]. The two most common and effective interventions for AAAs are traditional open surgery (OR) and abdominal endovascular aneurysm repair (EVAR). OR fix the AAA with a major operation by excluding the aneurysm with a synthetic tube or bifurcated graft while EVAR only requires a small groin incision that allows the placement of a stent-graft in the aneurysm (Figure 2-14) [166]. Although surgical repair can effectively reduce the overall AAA mortality, perioperative mortality remains high because of the risk of operation process including long surgical time and a large surgical incision during an OR surgery, and post-operation complications such as infection, ischemia, thromboembolism, pulmonary insufficiency, and myocadiac dysfunction for both OR and EVAR treatment [167].

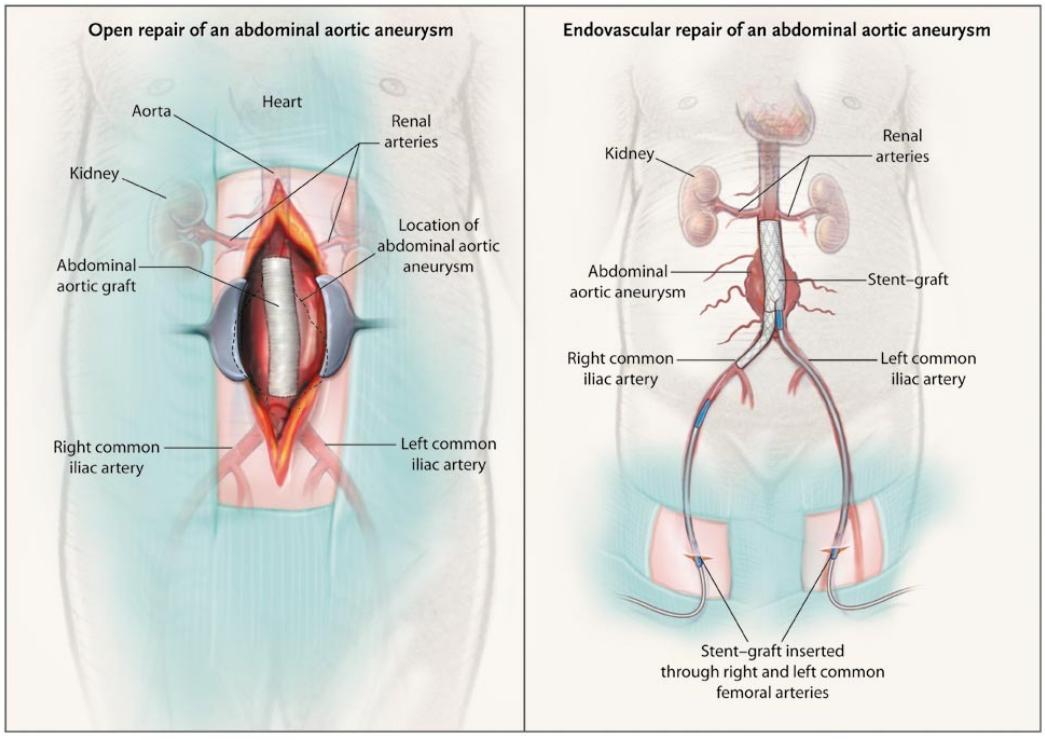


**Figure 2-14.** Open repair and endovascular repair of an infrarenal AAA [166].

### Potential pharmacotherapy for AAAs

A lot of recent studies focused on developing pharmacotherapy for AAA to stop the expansion of AAAs at an early stage or reduce post-operation complications, so the patients can avoid surgical risks. Most of the prospective pharmacotherapies aim to reduce the local inflammatory response in the aneurysmal tissue and stabilize and regenerate the damaged aortic wall. One of the main targets for the AAA pharmacotherapies is the class of MMPs. MMPs are a group of calcium-dependent zinc-containing endopeptidases that play an important role in ECM degradation and tissue remodeling [168]. There are 23 known human MMPs currently (Table 2-1), among which upregulated activities of MMP-2 and MMP-9 in the aneurysmal tissue have been wildly studied in the pathogenesis of AAAs.

MMP inhibitors, including doxycycline and batimastat (BB-94) (Figure 2-15), are the most extensively tested pharmacotherapy for AAA treatment in both animal models and clinical trials. The administration of MMP inhibitors can reduce the production and the activity of MMPs, thus, prevent the destruction of elastic lamellae without decreasing inflammatory cell infiltration [169]. Doxycycline is a synthetic antibiotic derived from tetracycline that has been clinically used to treat many different types of infections. It also has some non-antibiotic properties, including inhiation of inflammation, proteolysis, angiogenesis, and apoptosis [15]. Doxycycline inhibits MMPs via diminishing the activation of pro-MMPs, accelerating the MMP degradation, and loss of enzymatic activity [170].

The inhibition of MMP activity can be also achieved by altering the enzyme structure by chelating the zinc (II) ion of the active site, binding to the backbone of the

**Table 2-1.** Human matrix metalloproteinase

| No. | Class | MMP No. | Trivial name |
|---|---|---|---|
| 1 | Collagenases | MMP-1 | Interstitial collagenase |
| 2 | | MMP-8 | Neutrophil collagenase |
| 3 | | MMP-13 | Collagenase 3 |
| 4 | Gelatinases | MMP-2 | 72 kDa gelatinase A |
| 5 | | MMP-9 | 92 kDa gelatinase B |
| 6 | Stromelysins | MMP-3 | stromelysin-1 |
| 7 | | MMP-10 | stromelysin-2 |
| 8 | | MMP-11 | stromelysin-3 |
| 9 | Matrilysins | MMP-7 | Matrilysin 1 |
| 10 | | MMP-26 | Matrilysin 2 |
| 11 | MT-MMPs | MMP-14 | MT-1 MMP |
| 12 | (Transmembrane) | MMP-15 | MT-2 MMP |
| 13 | | MMP-16 | MT-3 MMP |
| 14 | | MMP-24 | MT-5 MMP |
| 15 | (GPI anchored) | MMP-17 | MT-4 MMP |
| 16 | | MMP-25 | MT-6 MMP |
| 17 | Other enzymes | MMP-12 | Macrophage elastase |
| 18 | | MMP-19 | RASI-1 |
| 19 | | MMP-20 | Enamelysin |
| 20 | | MMP-21 | - |
| 21 | | MMP-23 | CA-MMP |
| 22 | | MMP-27 | - |
| 23 | | MMP-28 | Epilysin |

enzyme, or interacting with subsites of the enzyme [171]. BB-94 is one of the board spectrum MMP inhibitors that has a hydroxamate group which can bind to the active zinc in MMPs [172]. Treatment with a low dose of BB-49 with an aneurysm targeting nanoparticle system has been reported to suppress MMP activity and AAA progression in a $CaCl_2$ induced rat AAA model [169].

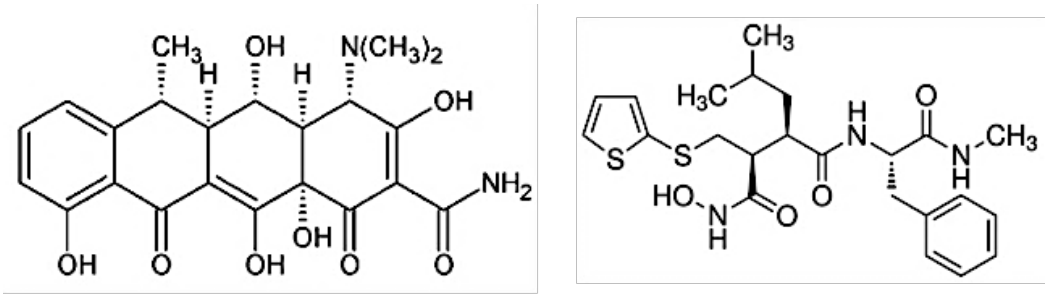


Doxycycline Batimastat

**Figure 2-15.** Structure of doxycycline and batimastat.

Several drugs, such as pyrrolidine dithiocarbamate (PDTC) and statins, were studied for their ability to reduce the inflammatory response in aneurysmal tissue by interacting with pro-inflammatory signaling pathways. Nuclear factor-kappa B (NF-κB) is a transcription factor implicated in the processes of inflammatory responses and oxidative stress. The activation of NF-κB signaling pathway can result in mRNA expressions of the genes for numerous cytokines, growth factors, and adhesion molecules [173]. NF-κB activation is a major early event in the pathogenesis of inflammation-related vascular diseases, making the blockade of endothelial NF-κB signaling a promising strategy for preventing vascular inflammation and dysfunction, especially aneurysm formation [174]. PDTC, an antioxidant, and inhibitor for NF-κB signaling pathway, has been reported to

successfully relieve cancer cachexia and attenuate lipopolysaccharide (LPS) induced injury [175-178]. PDTC can induce the expression of the regulator of calcineurin activity 1 (RCAN1), thus, prevent the activation of NF-κB signaling pathway (Figure 2-16) [179]. Considering the important role NF-κB plays in the AAA pathogenesis, PDTC has also been tested in animal AAA models, and has effectively inhibited AAA progression by modulating the expression of MMPs and proinflammatory cytokines [180-182].

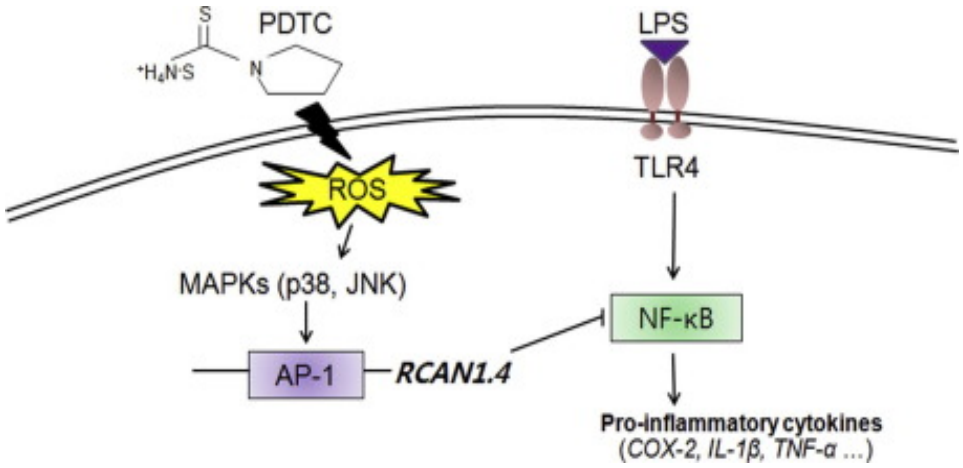


**Figure 2-16.** PDTC inhibits NF-κB signaling via inducing RCAN1 expression [179].

Statins, the inhibitors of 3-3-hydroxy-3-methylglutaryl-coenzyme A (HMG-CoA) reductase, are a class of well-established drugs for lowering the cholesterol level in vascular diseases [183-185]. It has been shown that statins can reduce the secretion of pro-inflammatory proteins such as MMPs and MCPs in *ex-vivo* studies with cultured human AAAs by preferentially inhibit the Rac1/ NF-κB signaling pathway [186, 187]. Further studies on simvastatin and pravastatin (Figure 2-17), two kinds of statins that had the fewest side effects in this class of medications, have demonstrated their ability to increase TIMP-1 production in rodent models [13, 14]. Statin treatment not only attenuates the AAA

progression in animal models but also in clinical studies. In a study of 130 patients with AAAs not treated surgically, the group of patients who were received statins treatment showed significantly smaller AAA sizes and lowered mortality comparing to the group of patients not treated with statins [188].

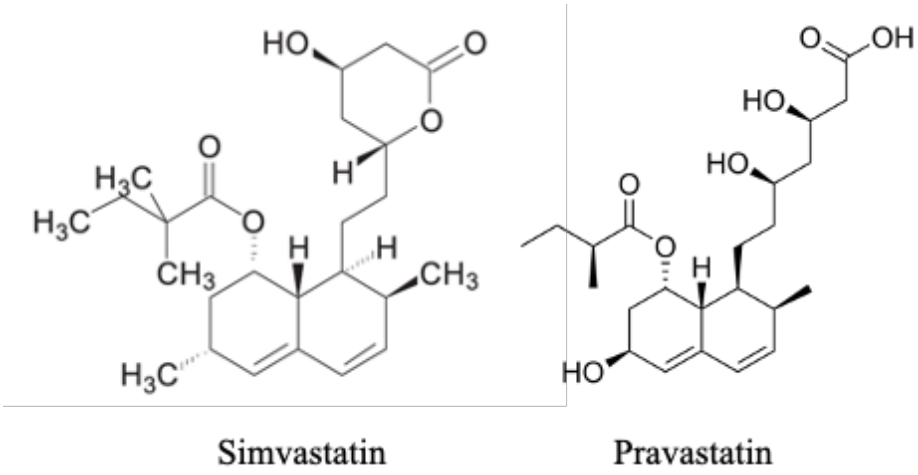


**Figure 2-17.** Structures of simvastatin and pravastatin.

The development of AAA is associated with increased oxidative stress in the aortic wall. Overproduction of reactive oxygen species (ROS) as a result of the change in aortic mechanical stress and expression of cytokines can subsequently induce vascular inflammation, increased MMP activity, SMCs apoptosis, and change in collagen properties [189]. α-tocopherol, known as vitamin E, is a dietary antioxidant that has been demonstrated to reduce macrophage infiltration, osteopontin (OPN) expression and ROS activity in an AngII induced ApoE-/- mouse AAA model [190]. The size and weight of these AAAs were both decreased, indicating that vitamin E has the potential to slow down AAA progression. β-carotene is another antioxidant that has been reported to attenuate the

AAA formation. β-carotene may activate RAR/RXR pathway and dimerize with peroxisome proliferator-activated receptors (PPARs) to repress the target genes, regulate inflammatory reactions, alleviate macrophage recruitment and resolve atheromatous plaques in the ApoE-/- mice model [125].

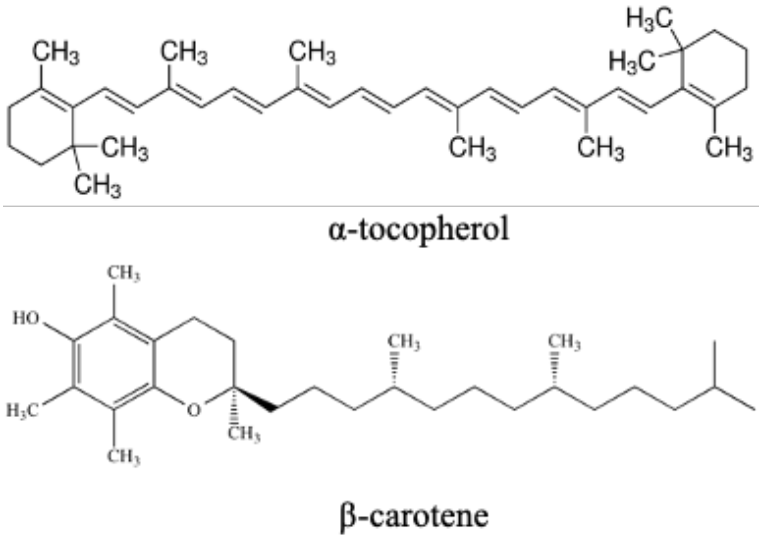


**Figure 2-18.** Structures of α-tocopherol and β-carotene.

Given the fact that RAS participates in several pro-AAA mechanisms, ACE inhibitors, and angiotensin receptor blockers (ARB) have been studied as pharmacological treatments for AAAs [191]. It has been well established that the clinical application of ACE inhibitors and ARBs can regulate the blood pressure in patients with hypertension [192]. The decrease in blood pressure lowers the aortic wall stress, thus decrease the rupture risk of AAAs. Moreover, ACE inhibitors and ARBs have anti-inflammatory effects on the aneurysm wall by suppressing the NF- κB pathway and TGF-β/SMAD signaling [193]. ACE inhibitors such as captopril, lisinopril, and enalapril prevented the development of AAA and attenuated the degradation of media elastin in an elastase infusion model [194].

ARBs such as telmisartan and valsartan limit the progression of AAAs by inhibiting the angiotensin II type I receptor (AT1R) cascade [195-197].

**Table 2-2.** Potential pharmacotherapy for abdominal aortic aneurysms

| Drugs | Known mechanisms | Effects |
|---|---|---|
| Doxycycline | Pro-MMPs activation ↓ | MMP-9 ↓, MMP-2 ↓, preserved elastin |
| BB-94 | Zinc (II) ion chelation | MMP-9 ↓, MMP-2 ↓, preserved elastin |
| PDTC | NF-κB pathway ↓, Notch pathway ↓ | Cellular infiltration ↓, MMP-9 ↓, IL-1β ↓, IL-6 ↓, preserved elastin |
| statins (simvastatin and atorvastatin) | Rac1/NF-κB pathway ↓ | Macrophage infiltration ↓, MMP-9 ↓, MCP-1 ↓, MCP-2 ↓, epithelial neutrophil-activating peptide (CXCL5) ↓, TIMP-1 ↑, preserved elastin |
| α-tocopherol | Oxidative stress ↓ | Macrophage infiltration ↓, ROS ↓, OPN ↓ |
| β-carotene | Oxidative stress ↓, RAR/RXR pathway ↑ | Macrophage infiltration ↓, ROS ↓, Atheromatous plaques ↓ |
| ACE inhibitors | AT1R ↓, AT2R ↓, NF-κB pathway ↓, TGF-β/SMAD ↓ | Blood pressure ↓, MMP-9 ↓, preserved elastin |
| ARBs | AT1R ↓, ERK ↓, NF-κB pathway ↓ | Blood pressure ↓, MMP-9 ↓, Bcl-2/Bax ↑, preserved elastin |

All the drugs that can be used as a pharmacotherapy for AAA mentioned above are summarized in Table 2-2.

Polyphenols are a large and varied family of natural compounds that consist of a hydrophobic core surrounded by phenolic (-OH) groups on the exterior. Pentagalloyl glucose (β-1,2,3,4,6-Pentagalloyl-O-D-Glucopyranose, PGG) is one of the tannic acid derivatives that contain five identical gallic acid ester linkages involving the aliphatic hydroxyl groups in the sugar core (Figure 2-19) [198]. It has gained a lot of scientific attention recently because of its potential use as an antimicrobial, anti-inflammatory, anticarcinogenic, antidiabetic, and antioxidant agent [199].

Studies indicated that PGG could be used as an ECM stabilizer due to its capability to bind to structural fibers in the ECM and, in doing so, render them resistant to enzymatic degradation. Periarterial treatment with PGG preserved elastin fiber integrity and hindered aneurysmal dilatation of the abdominal aorta in clinically relevant calcium chloride and elastase-induced animal injury model of AAA [200, 201]. More interestingly, enhancement of ECM biosynthetic enzymes such as LOX can not only stabilize the ECM but also reduced inflammatory responses, including MCP-1 secretion, macrophage infiltration, and c-Jun N-terminal kinase (JNK) pathway activation, thereby preventing AAA progression in mice [83].

Most of the pharmacotherapies mentioned above were tested in animal models. To translate the research findings into clinical practice, further studies need to focus on how these drugs interact with human AAA *in-vivo*. In the established human AAA treatment

clinical trials, drugs were usually administrated systemically. Although systemic pharmacologic treatments have shown effectiveness in animal models, they did not bring many benefits to the AAA patients due to either low local drug concentration or severe

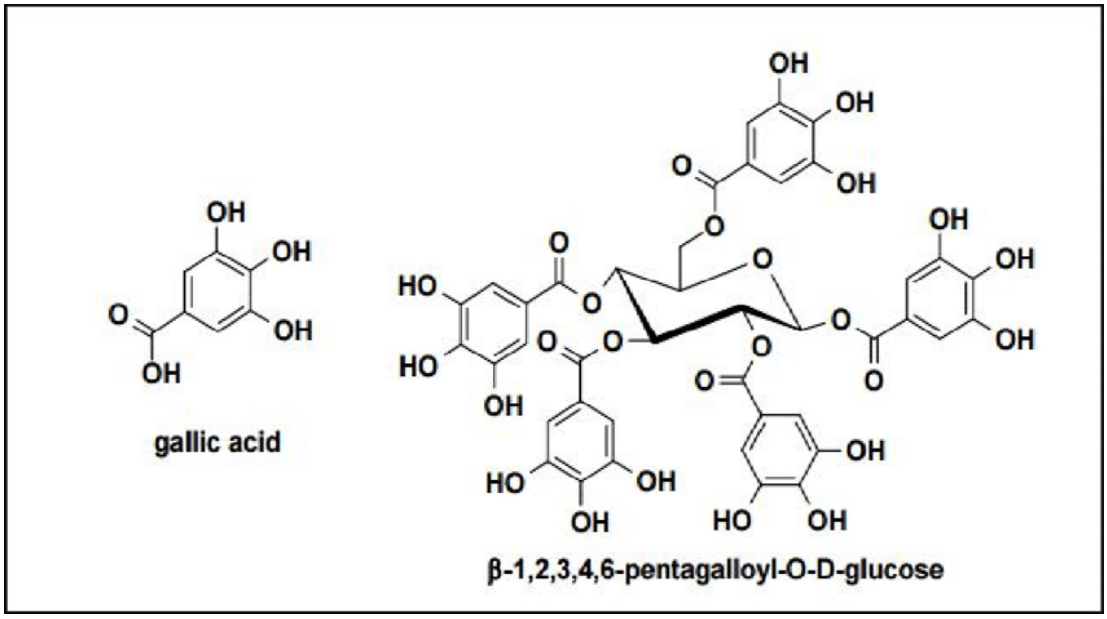


**Figure 2-19.** Gallic acid and PGG structure [202].

systemic side-effects. For instance, systemic delivery can cause off-target inhibition of the MMP activities that are essential for normal homeostasis [203]. Since AAA is predominately localized to a limited area on the aorta, targeted delivery of pharmacologic agents is a tempting approach to increase therapeutic efficacy and reduce systemic side effects. Local drug delivery can be achieved by establishing a nanoparticle system that targets pathological biomarkers located in the aneurysmal tissue or combining the drugs with medical devices such as grafts or endovascular stents via surface coating.

## 2.13 Targeting nanoparticles (NP) systems

Nanotechnology is a powerful tool that has been wildly used in developing and optimizing novel diagnostic strategies and pharmacotherapies in many fields. The physiological and chemical properties of the materials change drastically in nanoscale. It provides a possibility to make the synthesized materials less toxic and more biocompatible for *in-vivo* use by making them into size-controlled and surface-modified NPs. NPs are relatively stable in biological systems, characterized by a long blood half-life and their ability to evade elimination by the reticuloendothelial system [204]. The surface modification also can render NPs certain unique features that enable them to target specific tissues or organs to maximize the beneficial effects of the loaded chemicals by improving local availability and lower off-target complications.

Many types of nanosystems, including dendrimers, quantum dots, micelles, liposomes, polymeric nanoparticles, carbon nanotubes, albumin, and metallic nanoparticles such as gold and iron oxide, have been studied in a range of diseases. The nanosystem is usually selected base on the applications. For example, self-assembling peptide amphiphile nanofibers are being investigated as treatments to modify stem cell proliferation and differentiation in regenerative medicine [205]. Gold nanoparticles, magnetic iron oxide nanoparticles, and quantum dots can be used directly for targeted bioimaging [206-208]. Moreover, drugs can be loaded to the surface of these nanosystems via surface modifications to achieve both diagnostic and treatment capabilities at the same time [209-211]. Dendrimers, polymeric, liposomal, and albumin nanoparticles have been extensively

studied as *in-vivo* drug delivery nanocarriers because of their high biocompatibility, biodegradability, and high dug payload [212-214].

To date, the targeting of AAAs for therapeutic and imaging purposes remains significantly challenging because of the limited number of viable targets and a relatively

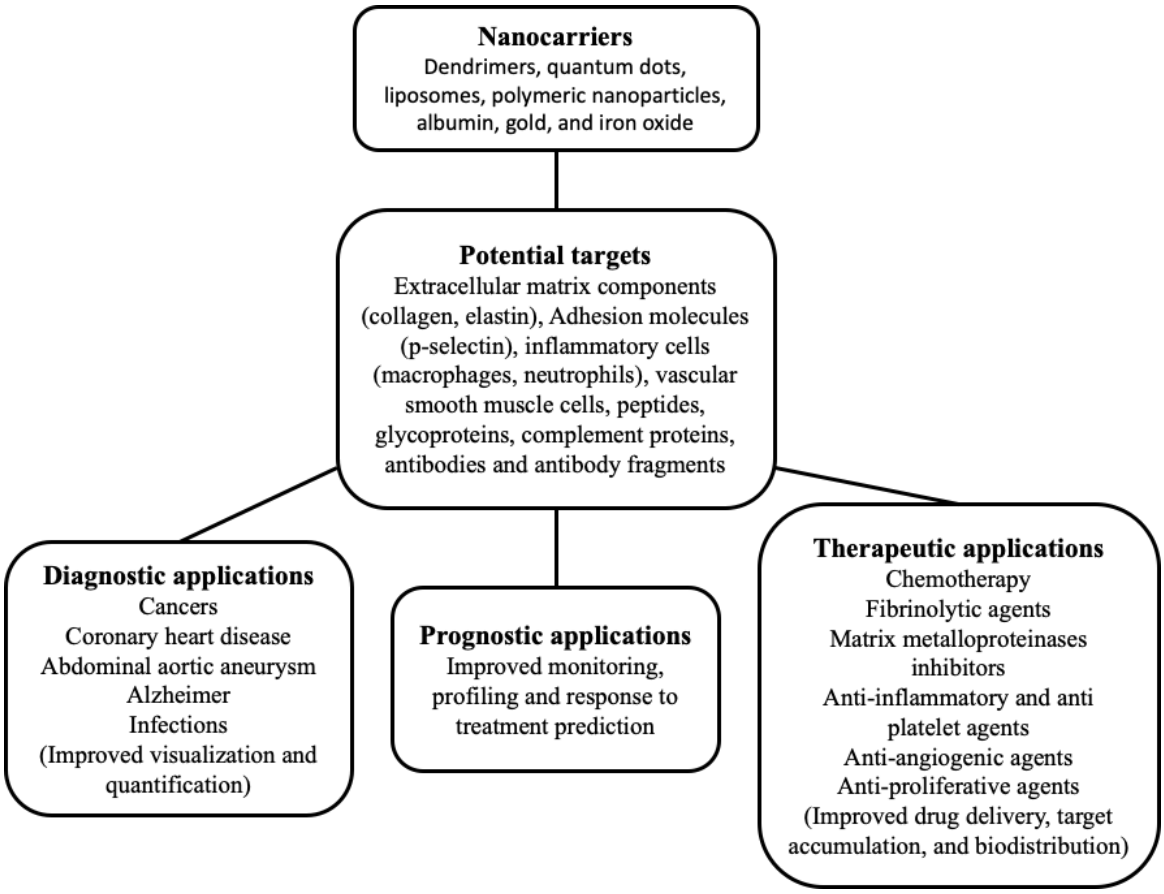


**Figure 2-20.** Schematic diagram of nanocarriers, potential targets, and potential applications in medicine [215].

low hemodynamic residence time in the diseased aorta. As NPs have to be administered intravenously into circulation to target vascular disease, an immune response, known as opsonization, to the blood proteins that are absorbed onto the particle surface will occur

[216]. Opsonization will result in the particles being quickly eliminated from circulation by the mononuclear phagocyte system (MPS), and the desired imaging and therapeutic effect would not be achieved [217]. Yet, despite the difficulties in designing targeting systems for vascular diseases, some surface-modified nanosystems have been developed to successfully target AAAs.

**Metallic nanoparticles**

Ultra-small SPIO (USPIO) nanoparticles are a novel category of MRI contrast agents that play a crucial role in the imaging of AAAs. USPIO nanoparticles include ferumoxtran-10 and ferumoxytol with a diameter of <50 nm. They can be used as a blood pool contrast agent but also can be taken up by tissue-resident macrophages and can be used to identify cellular inflammation within tissues [218]. In several rodent animal models, marked accumulation of USPIO-labeled macrophages was found within the aneurysmal aorta that could be identified by MRI and was confirmed by immunohistochemistry [219-221]. Preliminary evidence of USPIO uptake in human abdominal aortic aneurysms (AAA) has been described by Sadat U. et al in a 14 patient study [222]. Thus, USPIO enhanced MRI can be potentially effective in the quantification of the AAA associated inflammatory processes.

Cross-linked iron oxide nanoparticles (CLIO) also have been reported to possess the ability to target the monocytes/ macrophages in the aneurysmal tissue. A recent study performed in ApoE-/- mice indicated that dextran-coated iron oxide nanoparticles could be labeled with fluorine-18 ($^{18}F$) and could provide a specific signal intensity enhancement in the aneurysmal wall in PET -CT scans [223]. In this reported AAA targeting NP system,

CLIO was avidly internalized by phagocytic cells in the aneurysmal tissue to achieve targeting and $^{18}F$ functioned as the PET scan tracer to visualize the inflammatory level of the AAAs.

**Polymeric nanoparticles**

Biodegradable polymeric NPs have shown significant therapeutic potential for controlled drug delivery. Nanoparticles made of polymers, such as poly (lactic acid) (PLA), poly-lactic-co-glycolic acid (PLGA), polyethylene glycol (PEG), and their copolymers, present themselves as lucrative options for drug delivery owing to the possibility to tailor their physical, surface, and degradation characteristics. Drugs that are enclosed within the polymeric NPs would be protected from potential degradation by enzymes or hydrolysis, and the encapsulation would allow for developing more flexible and patient-friendly delivery techniques [224]. Most of the drug-loaded polymeric NPs can be obtained using an emulsification-solvent evaporation technique [225, 226].

PLA is biocompatible, biodegradable by hydrolysis and enzymatic activity. It has low immunogenicity, as well as a broad range of mechanical and physical properties that can be engineered appropriately to suit different applications [227]. The matrix of PLA-NP allows the control of drug release kinetics, offering PLA-NP based drug carriers the benefit of sustainable therapeutic drug release over prolonged periods [228]. The United States Food and Drug Administration (FDA) has approved the use of PLA-NPs in humans, which makes PLA-NPs suitable for expedited clinical translation. Previous studies from our lab have demonstrated the ability of the antibody conjugated PLA-NPs to target aneurysmal tissue and slowly release therapeutic drugs [169, 229].

PLGA is a co-polymer with physicochemical characteristics that vary with the lactic to glycolic ratio. Its application in humans has also been approved by the FDA [230]. Surface modified PLGA NPs have been used for AAA therapeutic and imaging purposes. Surface functionalization of PLGA NPs with a cationic amphiphile, such as didodecyldimethylammonium bromide (DMAB), endows the NPs with the ability to bind fibrin clots [231]. When loaded with fibrinolytic drugs, the NPs have been shown to slowly cause clot lysis and attenuate the proteolytic loss of vascular elastic matrix. Moreover, hyaluronan oligomers loaded PLGA NPs have been reported to have a controlled and sustained drug delivery profile and elastogenic induction property when added into cultured aneurysmal rat aortic SMCs [232]. PLGA NPs have also been used to encapsulate contrast agents such as iron oxide and gadolinium, and modified to target thrombosis to enhance the AAA MRI signal intensity [233, 234].

**Albumin based nanoparticles**

Albumin, a major transport protein component in blood plasma, has been commonly used for drug delivery because it is known to be non-toxic, non-immunogenic, biocompatible, and biodegradable. Albumin in its monomeric formula and albumin-based nanoparticles have emerged as attractive drug carriers, owing to its promising intrinsic binding capability of a significant amount of drug molecules [235]. According to the sources, albumin can be divided into three major types: ovalbumin (OVA) from egg white, bovine serum albumin (BSA), and human serum albumin (HSA). BSA is a type of albumin that is wildly accepted in the pharmaceutical industry because of its medical importance, low cost, and ease of purification. HSA could be used to substitute BSA in *in-vivo*

applications to avoid a possible immunologic response [236]. Registered HSA-based particles such as Albunex™ and Abraxane™ presented high *in-vivo* tolerance and great drug delivery profile in clinical studies [237, 238].

NPs that are made out of albumin have been studied for targeting several vascular diseases. Apatinib-loaded HSA NPs have been used to inhibit vascular endothelial growth factor (VEGF) induced retinal vascular leakage both *in vitro* and *in vivo* in a study performed by Jeong J. H. et al. [239]. Piceatannol-loaded BSA NPs have been studied to prevent vascular inflammation by blocking β2 integrin signaling in leukocytes and detaching the adherent neutrophils on vascular endothelial cells [240]. Ji, J. et al have reported a method to crosslink albumin NPs crosslinked into albumin ultrasound microbubbles. A highly expressive tissue-type plasminogen activator gene (t-PA) plasmid was packaged inside to prevent the formation of thrombosis in a dog model of coronary bypass [241]. More importantly, according to the previous research from our lab, an antibody conjugated BSA-NPs drug delivery system loaded with PGG has been shown to be capable of targeting AAA in a $CaCl_2$ induced rat model and an elastase-induced mouse model [169, 201]. And ethylenediaminetetraacetic acid (EDTA)-loaded BSA NPs conjugated with the same antibodies have been reported to successfully target chronic kidney disease-induced arterial calcification in a rat model and achieve therapeutic purposes [242]

Albumin nanoparticles can be prepared using techniques including coacervation, emulsification, thermal gelation, and nanospray drying. Different techniques result in albumin NPs with different sizes. The coacervation method can be used to produce NPs

with mean diameters between 150 and 280nm [243]. In the process of simple coacervation, albumin is phase-separated by adding a desolvating agent such as ethanol to diminish the solubility of albumin in the aqueous phase. In order to obtain stable albumin nanoparticles, crosslinker such as glutaraldehyde, polyethyleneimine (PEI), methyl polyethylene glycol modified oxidized dextran (Dextranox-MPEG), formaldehyde, and 1-ethyl-3-(3-dimethylaminopropyl) carbodiimide (EDC) is then used as a to harden the coacervates [244, 245].

**Biomarkers for AAA targeting**

Targeting of NPs can be achieved either passively or actively. Passive targeting mainly relies on inflammation/hypoxia-induced increase of vascular endothelium permeability. It is the concept that was commonly used for targeting tumors because of their enhanced permeability and retention (EPR) effect [246, 247]. The leaky vessels and the absence of normal lymphatic drainage in tumors contribute to the local accumulation of macromolecules larger than 40kDa and NPs [248]. The circulation time of the NPs in the blood pool plays an important role in passive targeting. The prolongation of the circulation time can be achieved by NPs surface coating, for example, PEGylation [249].

Active targeting, on the other hand, depends on molecular recognition such as ligand/receptor and antigen/antibody interactions. Surface modification with molecules that target disease-related biomarkers is essential for NPs active targeting. Comparing to free drug delivery or passive targeting, active targeting can significantly increase the quantity of drug delivered to the tissue of interest [250, 251]. Moreover, the active targeting of AAAs can be achieved by a combination usage of NPs and external medical device.

Magnetic NPs can be guided to the location of the AAA under the influence of an applied external magnetic field. Superparamagnetic iron oxide (SPIO) nanoparticles, along with doxycycline were encapsulated in poly(lactic-co-glycolic acid) (PLGA) NPs and were successfully delivered to the aneurysmal tissue owing to the magnetic properties of SPIO [252].

The physiological abnormalities in aneurysmal tissues can generate local biomarkers for AAA targeting imaging and drug delivery. Overproduced ROS in the AAA wall provides targeting possibility for NPs made out of ROS responsive materials. An oxidation-responsive β-cyclodextrin (OxbCD) material based nanocarriers have been reported to successfully release loaded rapamycin upon triggering by a high level of ROS in a $CaCl_2$ induced rat AAA model [253]. The inflammatory response can also produce biomarkers for targeting, such as macrophage infiltration and upregulation of inflammatory molecules. The macrophage infiltration has been labeled by USPIO and was enhanced in MRI imaging for inflammation assessment in an ApoE -/- mice AAA study carried out by Turner, G.H. et al. [220]. The αvβ3 integrin, a cell surface glycoprotein receptor, has been shown to be upregulated in neovessel endothelial cells and atherosclerotic macrophages and has been used as a AAA target [254]. By using Arg-Gly-Asp (RGD), an extensively studied short amino acid sequence binder of the αvβ3 integrin, both macrophages and angiogenesis within AAA lesions in ApoE -/- mice can be targeted [255]. Cathepsin K, a lysosomal protease that is highly overexpressed within AAA tissue, was targeted with antibody conjugated cationic amphiphile (DMAB)-modified submicron particles [256].

The pathological structural changes in the aneurysmal tissue result from ECM degradation can be also used as targets for localized delivery. The microstructural defects in the aneurysmal wall have been successfully targeted in an elastase-induced rat AAA model using rapamycin loaded poly (γ-benzyl L-glutamate) (PBLG) NPs [257]. Degraded elastin fibers have been targeted using elastin antibody-conjugated PLA NPs loaded with BB-94 in a $CaCl_2$ induced rat AAA model [169]. The remodeling of the ECM causes abnormal deposition of collagen in the aneurysmal wall, which can also be used as a target. CNA-35 functionalized paramagnetic/fluorescent micellar nanoparticles target type I collagen in the AAA and result in a significantly higher magnetic resonance signal enhancement in the aneurysmal wall that can be used to predict the rupture risk [258]. The formation of AAAs and ILTs is associated with endothelial dysfunction and injury as animal models of endothelial dysfunction and endothelial nitric oxide synthase (eNOS) uncoupling had a very high rate of AAA formation [259]. The damaged endothelial cells on the surface of the AAA wall can be targeted with microbubbles conjugated with molecules that have affinities to specific endothelial determinants such as P-selectin [260].

# 3. PROJECT RATIONALE AND SPECIFIC AIMS

As described in the previous chapter, AAA patients can be currently treated with either conservative methods or surgical interventions depending on the extent of disease progression. Up to 90% of detected AAAs are small enough that they do not require surgery. However, for patients who do not meet the surgical criteria, their AAAs can still rupture unpredictably. Patients diagnosed with smaller AAAs are under a life-threatening situation since about 13% of AAAs cause death in patients before they are recommended for surgery [96]. This could be a result of the limitations of current imaging modality and the lack of pharmacotherapies. On the one hand, current imaging methods are excellent to look at the overall growth of aneurysms, while focal aortic wall weakening is generally not precisely detected. Such weak spots are usually the repercussions of severe elastin degradation in the aneurysmal tissue and can increase the risk of rupture. On the other hand, the small AAAs or AAAs that cannot be surgically replaced are also not treated effectively because there are no current pharmacological treatments to prevent AAA expansion approved by the FDA.

An imaging modality that can provide progression information other than diameter change of the AAAs is necessary to identify the patients with higher rupture risks, even if the sizes of their aneurysms were still small. To date, there is no satisfying imaging method that could be used to predict the rupture risk of AAAs. Current clinical diagnostic imaging modalities such as abdominal ultrasound imaging or contrast-enhanced CT provides mostly geometrical information of the AAAs but little insight on these factors that precede rupture

in AAAs. Moreover, in order to visualize the vascular system, a large dose of contrast agent is required for performing contrast-enhanced CT, the toxicity of which may raise concerns among the patients and place it at a disadvantage [141, 261]. Thus, it is desired to develop a more biocompatible and efficient contrast agent for CT imaging that can reveal the mechanical properties of the AAAs.

AAA treatment strategies are usually chosen based on the criteria that the treatment should bring more benefits than risks to the patient. With a well-established imaging modality that provides information about AAA rupture risks, clinical decisions will no longer be made simply contingent on the AAA sizes. For the patients with small AAAs who are left to wait until their AAA grows large enough to require surgery, or the patients whose peri and post-operatory risks are too high to receive surgical intervention, pharmacological management of aneurysms would be an attractive option. During the last decade, several pharmacological therapies to stop ECM degradation showed promising results in animal studies, as mentioned in the previous chapter. However, the high required dose and related off-target systemic side effects of these drugs limited the translating of these drugs into clinical application.

Among all the drugs that have been studied to reduce the inflammatory response, halt ECM degradation and suppress the ARS activities, PGG is highly promising for clinical use because of its relatively low cytotoxicity and ability to bind to stabilize the ECM to prevent AAA progression and improve the mechanical properties of the damaged aortic wall [262]. Although PGG is usually considered safe or even beneficial at low levels, few studies report on the acute toxicity of the use of a high dose of PGG in animals such

as a precipitous and lethal drop of blood pressure and a significant reduction in blood urea nitrogen level [263]. It is important to lower the required PGG dose for treating AAAs *in vivo* to achieve long-term treatment safety. A local drug delivery system with a controlled drug releasing profile can greatly increase the efficiency of the drug. Surface modified nanocarriers are great candidates for developing a target-oriented and controlled delivery system for precise medicines owing to their customizable characteristics. It can achieve the same therapeutic effect as systemic drug delivery while administrating drugs at a much lower total dosage.

The innovation strategy of this research is to develop a targeted CT imaging contrast agent using surface modified AuNPs, as well as a therapeutic local drug delivery system that delivers PGG to the degraded matrix in the aneurysmal tissue. We hypothesize that elastic lamina degradation can be measured by site-specific targeting of AuNPs to the degraded elastic laminae and that the spatial distribution of AuNP binding will correlate with wall weakness. Thus, these AuNPs could prove useful as a non-invasive surrogate marker of AAA rupture potential. We further hypothesize that the targeted delivery of pharmacological agents will prevent expansion and the ultimate rupture of AAA. The potential of targeting PGG loaded albumin NPs to be used as a novel local pharmacological treatment to stop and reverse the progression of AAAs by preserving and regenerating elastin in the aneurysmal aorta without severe systemic side effects would be studied in this research.

**Specific aim 1: To synthesize and characterize AuNPs that can target degraded elastin and create distinguishable CT contrast in the vascular wall.**

Sub aim 1: To synthesize, characterize and functionalize AuNPs.

*Approach:* We will firstly synthesize citrate-capped AuNPs with a size of ~150nm using a kinetically controlled seeded growth method [264]. Then after we replace the citrate cap on the surface of the AuNPs with PEG, the AuNPs will be conjugated with custom made elastin antibodies that can target the degraded elastin. The size and zeta-potential of both bare and antibody-conjugated AuNPs (EL-AuNPs) will be measured for characterization.

Sub aim 2: To investigate the toxicity and in-vitro targeting of EL-AuNPs.

*Approach:* We will use human smooth muscle cells (hSMCs) to evaluate the cytotoxicity of the EL-AuNPs. EL-AuNP uptake will be evaluated in both hSMCs and mouse macrophages. We will optimize the targeting performance of EL-AuNPs by trying out different combinations of PEG to AuNP ratios and incubating conditions. PPE treated porcine carotids will be used to study the *in-vitro* targeting and imaging capability of EL-AuNPs.

**Specific aim 2: To investigate whether EL-AuNPs can be targeted to AAAs *in-vivo* and to build a correlation between the micro-CT signal intensity of the targeted EL-AuNPs and the mechanical properties of the aneurysm in a clinically relevant AAA animal model.**

Sub aim 1: To build an *ex-vivo* correlation between the micro-CT signal intensity of targeted EL-AuNPs and mechanical properties of the aneurysmal tissue.

*Approach:* We will use the AngII infused mice model of AAA for these studies. We will inject EL-AuNPs intravenously to target the AAA *in-vivo.* Then the entire mouse

aorta will be explanted and imaged using micro-CT. We will quantify the micro-CT signal intensities of EL-AuNPs accumulated within the aneurysms from the *ex-vivo* scans and correlate them with the corresponding burst pressures. We will perform histological analysis on the targeted aneurysms to reveal the targeting site of the EL-AuNPs.

Sub aim 2: To visualize AAAs *in-vivo* with micro-CT using EL-AuNPs as a contrast agent and build a correlation between the targeted micro-CT signal intensity and mechanical properties of the aneurysmal tissue.

*Approach:* We will still use the AngII infused mice model of AAA for these studies. We will first, inject EL-AuNPs intravenously to visualize the AAAs distinctively *in-vivo* with micro-CT. Secondly, we will quantify the *in-vivo* micro-CT signal intensity of EL-AuNPs accumulated in the suprarenal aortic region since it is where the aneurysm usually develops in this animal model. And we will correlate the obtained signal intensity with the corresponding aortic burst pressure which represents AAA rupture risk, to investigate the potential of EL-AuNPs in predicting the progression of AAAs. We will perform histological analysis on the targeted aneurysms to reveal the targeting site of the EL-AuNPs.

**Specific aim 3: To investigate whether PGG loaded albumin NPs that are conjugated with antibodies can be targeted to AAAs in an AngII model and whether they stop the disease progression and restore the healthy function of the aortic wall by repairing elastin matrix.**

*Approach:* PGG loaded NPs will be synthesized and conjugated to anti-elastin antibodies. In AngII infused mice, we will investigate whether systemic injection with

PGG loaded NPs can target and reverse already developed AAA by monitoring the diameter changes of the aneurysms with an ultrasound system. We will also study the change in biomechanical properties of the aneurysmal tissue, such as biaxial mechanical properties, circumferential strain, and PWV. We will study the effect PGG has on the systemic and local status of inflammation, the local genetic expression, and the structure of ECM in the aneurysmal tissue.

Each specific aim research is described in separate chapters below.

# 4. SPECIFIC AIM 1: TO SYNTHESIZE AND CHARACTERIZE AuNPS THAT CAN TARGET DEGRADED ELASTIN AND CREATE DISTINGUISHABLE CT CONTRAST IN THE VASCULAR WALL

## 4.1 Introduction

Gold in nanoscale has been studied as an ideal radiopaque CT contrast agent for its high density, high atomic number, high X-ray absorption coefficient, and low toxicity [141]. The shape and size of the nanosized gold can be easily controlled during the synthesis. And the availability of different kinds of surface modification methods for AuNP renders it the potential to be a safe and effective contrast agent that can be applied both systemically and locally. PEGylated AuNPs with prolonged blood circulation times have the potential to be used to create contrast for the imaging of the cardiovascular system with aneurysms [265]. Moreover, surface modified AuNPs with a size of about 15nm have been targeted delivered to enhance the contrast of tumors, lymph nodes, and micro-calcifications *in-vivo* [266-268].

However, AuNPs with small sizes are not suitable for targeting vascular wall because of a large amount of unspecific cellular uptake and clearance by the host immune system. Moreover, a few studies have shown *in-vivo* toxicity of small AuNPs including acute inflammation and apoptosis in the liver, loss of structural integrity in the lungs, and diffusion of white pulp in the spleen, accompanied by gene expression changes [269-271]. AuNPs with a particle size of ~150nm show better biocompatibility and increased circulation time owing to their ability to escape the endothelium uptake and phagocytosis

by macrophages, thus, have a better potential to be used as a AAA targeting contrast agent for CT scan.

AuNPs are usually synthesized by a standard single phased water-based reduction of a gold salt with citrate as the initiator as described by Turkevich, J. et al and refined by Frens, G. [272, 273]. Briefly, $HAuCl_4$ solution was brought to boil and then the sodium citrate solution was added. An immediate color change of the solution was observed indicating the nucleation and formation of monodispersed spherical particles. The mixture was then kept boiling till the reduction of gold chloride was complete. However, this method was usually used to produce AuNPs with a size smaller than 100nm. In order to get monodisperse citrate-stabilized AuNPs with sizes larger than 150nm and uniform quasi-spherical shapes that are preferable in AAA targeted imaging, we adapted an improved seed growing AuNP synthesizing method reported by Bastus, N. G. et al for this research [264].

Surface modification for AuNPs also plays an essential role in AAA targeting. *In-vivo* targeting of AuNPs is achieved through either passive or active targeting. Passive targeting depends on the homing of the vectors in unhealthy tissues due to extravasation through the leaky blood vessel, while active targeting presents ligands on the AuNP surface for specific recognition [274]. In this study, the elastin antibodies that only bind to degraded elastin will be conjugated to the AuNP surface to actively targeting degraded elastin fibers presented in aneurysmal aortic walls. The quality of the conjugation will affect the number of antibodies attached to the AuNPs surface, thus, influence the targeting efficiency of EL-AuNPs. The accumulated EL-AuNPs at the aneurysmal site will

eventually be visualized in the CT scan by generating contrast against surrounding soft tissues. When the targeting efficiency is high, the dose of systemically administrated EL-AuNPs to generate enough contrast in AAAs would be lower. Thus, the conjugation process should be optimized to reduce the required EL-AuNPs dose while still allow the production of acquiring high-quality CT images that provide accurate information about the rupture risks of AAAs.

## 4.2 Materials and Methods

### Synthesis of ~150nm AuNPs

Citrate-stabilized AuNPs with a size of ~150nm were synthesized using a kinetically controlled seeded growth method (Figure 4-1) [264]. Briefly, the reduction of a gold hydrochloride solution was initiated by injecting 1 mL of 25mM $HAuCl_4 \bullet 3H_2O$ (Sigma Aldrich, St. Louis, MO) into 150 mL of 2.2 mM sodium citrate (Sigma Aldrich, St. Louis, MO) in a three-necked round-bottomed flask at boiling temperature for 10 min under vigorous stirring to form Au seeds with a diameter of ~10nm. Immediately after the synthesis of the Au seeds, the reaction was cooled to 90 °C in the same reaction vessel to avoid the secondary nucleation.

Then, 1 mL of 25 mM $HAuCl_4$ solution was injected into the reaction vessel and allowed to react for 30 mins. This process was repeated twice before the sample was diluted by extracting 55 mL of sample and adding 55 mL of 2.2mM sodium citrate. This diluted solution was then used as a seed solution, and the growing process was repeated. In order to control the growing speed and maintain the homogeneous growth of the AuNPs, the gold precursor to seed particle concentration was carefully controlled. The sizes of the AuNPs

were monitored after each growth step and the growth step was repeated until the AuNPs reaches the desired size. AuNPs solution was allowed to cool down and stored at 4°C for further usage. The sizes of three different batches of AuNPs were measured to evaluate the reproductivity of this method.

**Preparation of EL-AuNPs under different conjugation conditions**

The citrate-capped AuNPs were then conjugated with degraded elastin targeted antibodies using a three-step method (Fig 4-2). Three different batches of EL-AuNPs were produced under different conjugating conditions (Table 4-1). For the first batch of EL-AuNPs, a heterobifunctional thiol-PEG-acid (SH-PEG-COOH, 2000MW, Nanocs, NY) was firstly added to the AuNPs at a weight ratio of 1:4 (PEG: AuNPs) to replace the citrate cap of the AuNPs. The SH-PEG-COOH can not only stabilize the AuNPs but also provided carboxylic groups for further modifying reaction. The PEGylation process was finished at 25ºC for 4 hours. Secondly, a commonly used EDC (N-(3-Dimethylaminopropyl)-N-ethyl carbodiimide)/NHS (N-hydroxysulfosuccinimide) chemistry was applied to provide binding sites for antibodies on PEGylated AuNPs. EDC (Oakwood Chemical, Estill, SC) and NHS (Sigma Aldrich, St. Louis, MO) were added to the PEGylated AuNPs at a weight ratio of 1:2:1 (EDC: NHS: PEG) and incubated at 25ºC for 2 hours. Finally, the anti-elastin antibody (custom-made at Clemson University) was incubated with the surface modified AuNPs overnight to achieve the final conjugation.

For the second batch of EL-AuNPs, SH-PEG-COOH was added to the AuNPs at a weight ratio of 5:2 (PEG: AuNPs) and incubated at 25ºC for 8 hours. Then, EDC and NHS were added to the PEGylated AuNPs at a weight ratio of 1:2:1 (EDC: NHS: PEG) at 25ºC

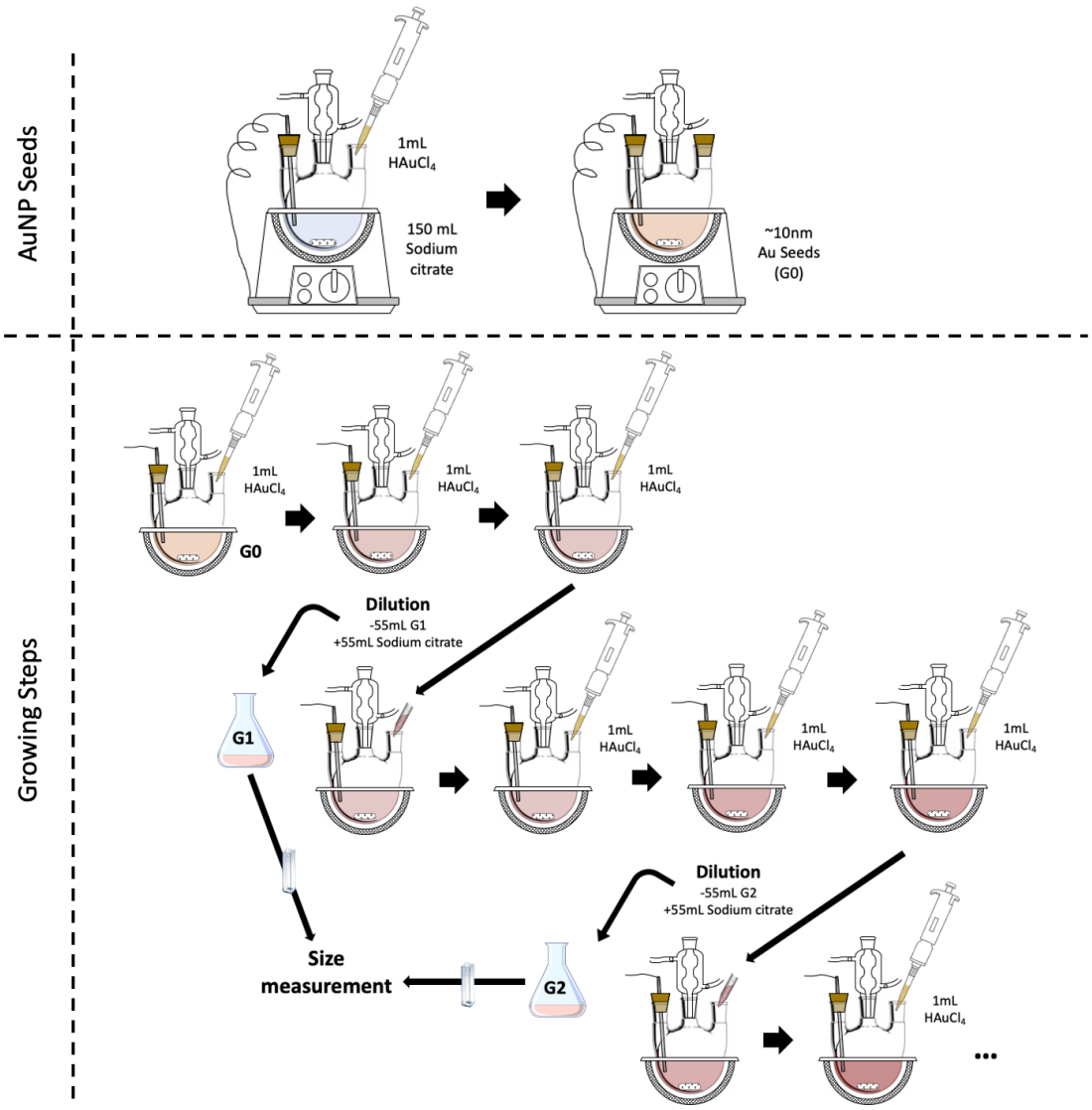


**Figure 4-1.** A schematic overview of the synthesis of AuNPs.

for 4 hours before antibodies were added and incubated overnight at 4ºC. And for the third batch of EL-AuNPs, AuNPs were incubated with the SH-PEG-COOH at a weight ratio of 4:1 (PEG: AuNPs) at 4ºC for 48 hours. Then, EDC and NHS were added to the PEGylated AuNPs at a weight ratio of 1:2:1 (EDC: NHS: PEG) and incubated at 25ºC for 6 hours before conjugating to the antibodies overnight at 4ºC.

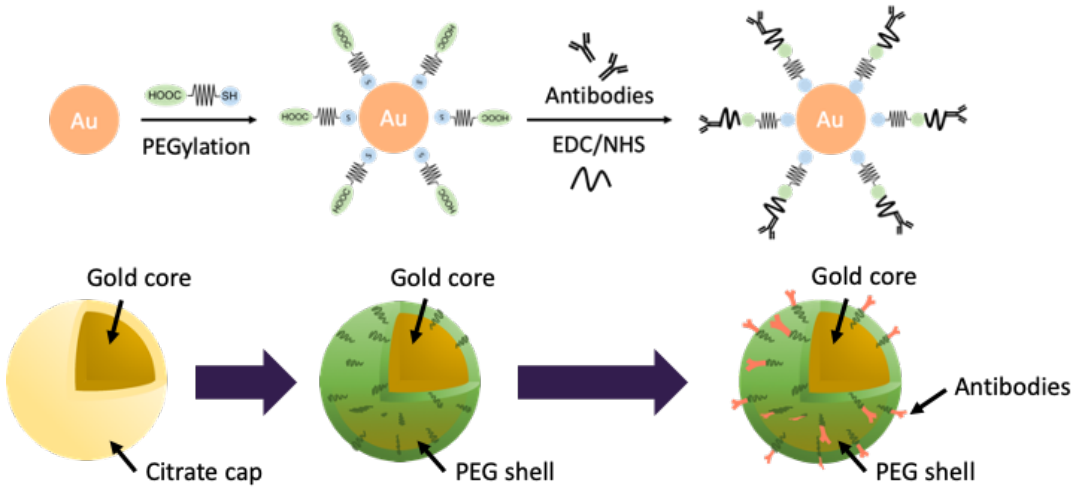


**Figure 4-2**. A schematic overview of the conjugation of elastin antibody to AuNPs.

**Table 4-1.** Different conjugation conditions for AuNPs

| | PEG: AuNP | PEGylation | EDC/NHS incubation |
|---|---|---|---|
| Batch 1 | 1:4 | 4 hours, 25°C | 2 hours, 25°C |
| Batch 2 | 5:2 | 8 hours, 25°C | 4 hours, 25°C |
| Batch 3 | 4:1 | 48 hours, 4°C | 6 hours, 25°C |

**Characterization of AuNPs and EL-AuNPs**

The hydrodynamic sizes of the AuNPs were measured after each diluting step and were also measured before and after the conjugation using a dynamic light scattering (DLS) system (Zetasizer Nano ZS, Malvern, Westborough, MA). Briefly, 40µL of each sample

was diluted in 1mL DI water and was then measured in disposable acrylic cuvettes under room temperature. Three measurements with at least twelve runs per measurement were performed for each sample with an absorption (k) of 3.32 and a refractive index (n) of 0.02. The zeta-potentials of AuNPs before and after the conjugation were measured using the same DLS system. Briefly, 40μL of each sample was diluted in 1mL DI water and was injected into the disposable folded capillary cells. Zeta potentials were measured under room temperature and three measurements with 100 runs per measurement were performed for each sample using the Smoluchowski model with an F(κa) value of 1.50.

To determine the concentration of the prepared AuNPs and EL-AuNPs, 1mL of each sample was firstly digested with 1mL of aqua regia in glass test tubes under room temperature for 1 hour. Then, the digested samples were dried under constant nitrogen flow until all the liquid was vaporized. The remaining solids were re-dissolved in 6mL of 0.1M hydrochloride acid and were sent to Agricultural Service Laboratory, Clemson University, for gold element quantification.

**Cytotoxicity of EL-AuNPs**

A standard live/dead assay was performed to evaluate the cytotoxicity of EL-AuNPs in hSMCs. Cells were seeded at a density of 10,000 cells/well in a 24-well tissue culture plate and incubated at 37ºC, 5% $CO_2$ overnight. 10μL of EL-AuNPs (to achieve a final concentration of 1.0, 2.0, and 5.0mg/mL) were then added into the seeded cells in triplicates and were incubated at 37ºC, 5% $CO_2$ for 1 hour. Then the cells were stained with Live/Dead cell staining kit II (PromoCell, Heidelberg, Germany) for 40 mins at room temperature and then imaged with a fluorescent microscope (Keyence, Itasca, IL). Live

cells were stained with the polyanionic dye calcein that produced an intense uniform green fluorescence with excitation of 495 nm and emission of 515 nm while dead cells were stained with EthD-III that produced a bright red fluorescence which was observed with excitation of 530 nm and emission of 635 nm.

The lactate dehydrogenase (LDH) assay (Thermo Scientific, Rockford, IL) is used to evaluate the cytotoxicity of EL-AuNPs in hSMCs in a quantified manner. Briefly, after determining the optimum cell number for LDH cytotoxicity assay, 10,000 cells/well were seeded in 100μL of media in a 96-well tissue culture plate, and the plate was incubated at 37ºC, 5% $CO_2$ overnight for the cells to attach. 10μL of EL-AuNPs (to achieve a final concentration of 1.0, 2.0 and 5.0mg/mL) were then added into the seeded cells in triplicates and were incubated at 37ºC, 5% $CO_2$ for 45 mins alone with a complete medium control without cells, and triplicates of both spontaneous LDH activity controls and maximum LDH activity controls. 50μL of each sample medium was transferred to another flat bottom 96 well-plate followed by adding 50μL of the reaction mixture to each sample well and incubating at room temperature for 30 mins protected from light. The reaction was stopped by applying 50μL of stop solution to each sample well and the absorbance of each sample at 490nm and 680nm was measured using a spectrophotometer (Epoch, BioTek, Winooski, VT). %Cytotoxicity was then calculated using the following two equations:

$$LDH\ activity = (Absorbance\ at\ 490nm) - (Absorbance\ at\ 680nm) \quad (1)$$

$$\%Cytotoxicity = \frac{Treated\ LDH\ acticity - Spontaneous\ LDH\ activity}{Maximum\ LDH\ activity - Spontaneous\ LDH\ activity} \times 100 \quad (2)$$

**Cellular uptake of EL-AuNPs**

Mouse macrophages were used as the cell line for *in-vitro* cellular uptake evaluation. Mouse macrophages were seeded in a 12-well plate with a density of 40,000 cells/well. Cells were then cultured in RPMI-1640 growth media that contains 10% fetal bovine serum at 37 °C with 5% $CO_2$ overnight for complete attachment. Macrophages were treated with 2mg/mL of EL-AuNPs for different periods (4 and 24 hours) in triplicates, after which the supernatant was removed, and cells were washed 3 times with PBS. Macrophages were gently scraped off the plate using cell scrapers, resuspended in 1mL of PBS, and collected by centrifugation at 1000 g for 4 minutes. Collected macrophages were further washed 3 more times with PBS and were lysed in an acid solution (2% HCl + 2% $HNO_3$) for 5 days for the quantification of gold by inductively coupled plasma mass spectrometry (ICP-MS).

The hSMCs were used for further *in-vitro* cellular uptake evaluation. hSMCs were plated at a density of 200,000 cells/well in a 12-well plate and cultured in complete growth media at 37 °C with 5% $CO_2$ overnight for complete attachment. hSMCs were treated with 2mg/mL of EL-AuNPs in triplicates for 4 and 24 hours, respectively. Trypsin/EDTA was used to release the hSMCs from the plate and the cell suspensions were centrifuged at 1000 g for 5 min. hSMCs were collected and washed for 3 more times with PBS then treated with an acid solution (2% HCl + 2% $HNO_3$) for 5 days to prepare lysates for the quantification of gold by ICP-MS.

***In-vitro* targeting of EL-AuNPs**

The targeting and imaging property of EL-AuNPs were tested using an *in-vitro* elastase treated porcine carotid model. Porcine carotids were bent into a U-shape and the middle part of each porcine carotid was immersed in 1mL of 20U/mL PPE (Tris buffered, pH= 7.8) for 90mins to induce limited elastin damage (Fig 4-3). After the PPE treatment, entire segments were immersed at 4 ºC overnight in three batches of 2mL of 3mg/mL EL-AuNPs that were conjugated differently. Samples were washed in phosphate-buffered saline (PBS) three times for 5 mins per time to remove the non-specifically bound EL-AuNPs and were scanned with micro-CT (0.2mm Al filter, 90kV, 250mA, 300ms) (Bruker, Billerica, MA) in corn oil. Reconstructions were carried out using the Skyscan NRecon software based on the Feldkamp algorithm. The distribution of the EL-AuNPs within the whole porcine carotids were visualized by building a 3D model using the maximum intensity projection (MIP) mode in the CT-Vox software.

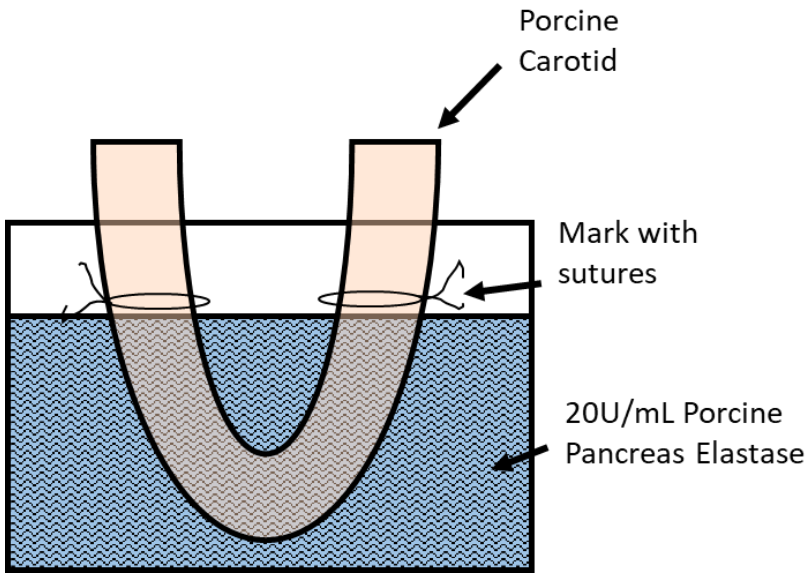


**Figure 4-3.** Schematic representation of the *in-vitro* PPE treatment of the middle part of porcine carotids that were used to test the targeting properties of EL-AuNPs.

Moreover, a quantitative *in-vitro* study has been performed on rat aortas to decide if there was a correlation between the EL-AuNPs accumulated in the tissue and the elastin damage level. The rat aorta segments with different elastin degradation levels were obtained by immersing the rat aorta segments in PPE for a different amount of time. Briefly, the rat abdominal aorta was firstly separated into suprarenal and infrarenal segments to minimize the influence of the intrinsic aortic elastin content difference. Then, the segments were immersed in 2 mL of 5U/mL PPE (Tris buffered, pH= 7.8) for 30, 60, and 90mins respectively to induce different levels of elastin damage. After PPE treatment, the segments were washed in PBS and immersed in 2 mL of 2mg/mL optimized EL-AuNPs overnight at 4 ºC under slow rocking. Samples were washed PBS three times for 5 mins per time to remove the non-specifically bound EL-AuNPs and were scanned with micro-CT (40kV, 600mAs, 300ms, no filter). The EL-AuNPs were separated from the aortic tissue and quantified using CT-An software and normalized to the volume of the sample. And 3D models of the aortic segments and the EL-AuNPs attached to the tissue were built using the same software and the models were visualized using the CT-Vol software.

**Histological analysis**

After being washed in deionized (DI) water, porcine carotid, and rat aorta segments from the treated middle and two untreated ends were embedded in optimal cutting temperature (OCT) compound (Sakura Finetek, Torrance, CA) and froze in -80ºC to form blocks. The blocks were then sectioned per standard procedures. Five-micrometer sections were mounted on positively charged glass slides. And slides were placed in 100% pre-cooled acetone (Fisher Science Education, Nazerath, PA) for 10 minutes to fix the sections.

Subsequently, the slides were rinsed with tap water for 5 minutes to remove the OCT compound and stained with Verhoeff-van Gieson (VVG) for elastic fibers.

### Desmosine quantification

Desmosine is a component of elastin that cross links with its isomer, isodesmosine, giving elasticity to the tissue [275]. Desmosine in the PPE treated aortic tissue was measured to be a marker for healthy elastin preserved in the tissue, representing the elastin damage level. Firstly, a small piece of tissue was cut off from each aortic sample and was lyophilized and the dry weights of which were weighed and recorded. The small aortic pieces were then homogenized to release the desmosine. The desmosine was measured using a mouse desmosine enzyme-linked immunosorbent assay (ELISA) kit (MyBiosource, San Diego, CA) and normalized using the dry weight of each tissue piece.

### Statistical analysis

All *in vitro* experiments including cell culture studies and tissue studies were done in triplicates. The data are reported as the mean ± standard deviation. Data from different groups were analyzed by one-way analysis of variance (ANOVA) followed by Tukey's HSD as a post-hoc test. Results were reported at three different significant levels: *** $p \leqslant 0.01$, ** $p \leqslant 0.05$, and * $p \leqslant 0.1$.

## 4.3 Results

### Characterization of AuNPs and EL-AuNPs

The sizes of the AuNPs increased gradually after each growth step and after 18 growth steps, the dynamic diameter of the AuNPs reached ~150 nm (Figure 4-4A and Table

4-1). The Z-average hydrodynamic size of the obtained AuNPs after 18 growth steps was 146 nm with a polydispersity index (PdI) of 0.060. According to the size distribution by volume, the peak of the diameters appeared at 169 nm with a standard deviation of 48 nm. These results indicated that we successfully synthesized monodispersed AuNPs most of which had a size of around 150 nm. The final Z-average sizes of the other two different batches of AuNPs were 143 nm (PdI: 0.050) and 154 nm (PdI:0.047)

**Table 4-2.** The Z-average diameters and volume distribution of AuNPs from each growth

| Growth step | Z-Average diameter (nm) | Volume distribution peak (nm) | St Dev (nm) |
|---|---|---|---|
| 1 | 24 | 13 | 5 |
| 2 | 26 | 16 | 6 |
| 3 | 26 | 19 | 7 |
| 4 | 28 | 23 | 7 |
| 5 | 31 | 26 | 9 |
| 6 | 34 | 30 | 10 |
| 7 | 36 | 32 | 11 |
| 8 | 41 | 39 | 12 |
| 9 | 44 | 43 | 14 |
| 10 | 51 | 48 | 16 |
| 11 | 60 | 54 | 22 |
| 12 | 62 | 58 | 24 |
| 13 | 73 | 63 | 30 |
| 14 | 99 | 93 | 52 |
| 15 | 100 | 97 | 50 |
| 16 | 113 | 127 | 39 |
| 17 | 131 | 150 | 49 |
| 18 | 146 | 169 | 48 |

respectively, with volume distributions of 168 ± 51 nm and 177 ± 47 nm respectively. The batch to batch variation of the AuNP size distribution was very small.

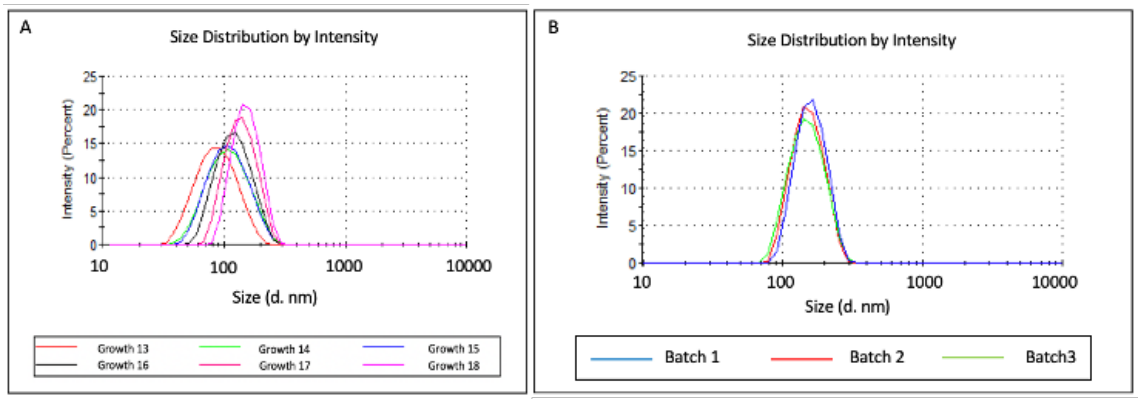


**Figure 4-4.** Size distribution by intensity measured using the DLS system. (A) Sizes of AuNPs from growth step 13 to 18. (B) Sizes of three different batches of AuNPs.

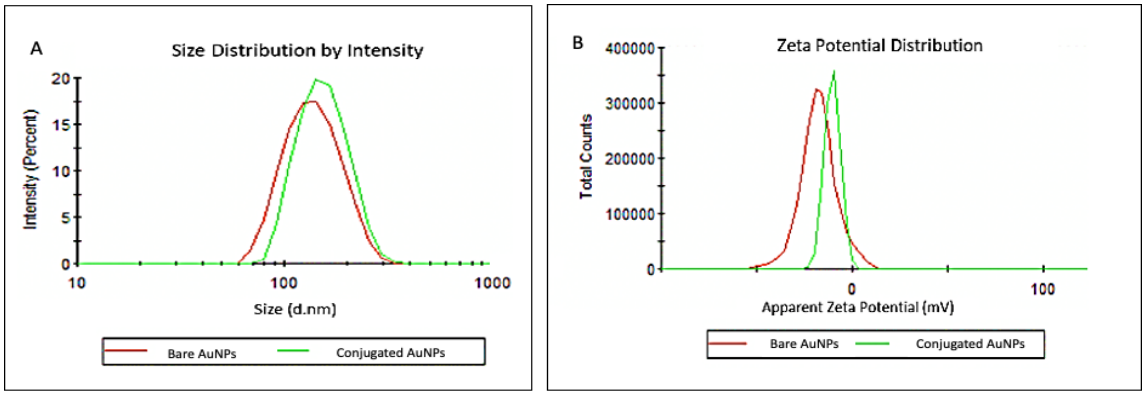


**Figure 4-5.** Size and zeta-potential characterization of AuNPs and EL-AuNPs. (A) Size distribution of AuNPs before and after conjugation; (B) Zeta-potential distribution of AuNPs before and after conjugation.

After the conjugation step, the intensity weighed hydrodynamic diameter of the AuNPs increased from 145 ± 46 nm to 157 ± 44 nm, and the volume weighed hydrodynamic diameter of the AuNPs increased from 156 ± 57 nm to 173 ± 53 nm,

indicating the formation of a PEG-EDC-NHS-Antibody shell surrounding the AuNPs in place of the original citrate cap (Figure 4-5A). The average zeta-potential of the AuNPs also increased from -17.6 ±9.4 mV to -10.4 ±4.2 mV after the conjugation, which also confirmed that the completion of the surface modification (Figure 4-5B).

**Cytotoxicity of EL-AuNPs in hSMCs**

The cytotoxicity of EL-AuNPs was tested at a concentration of 1, 2, and 5mg/mL. EL-AuNPs tested at all three concentrations were not found toxic to hSMCs in cell cultures

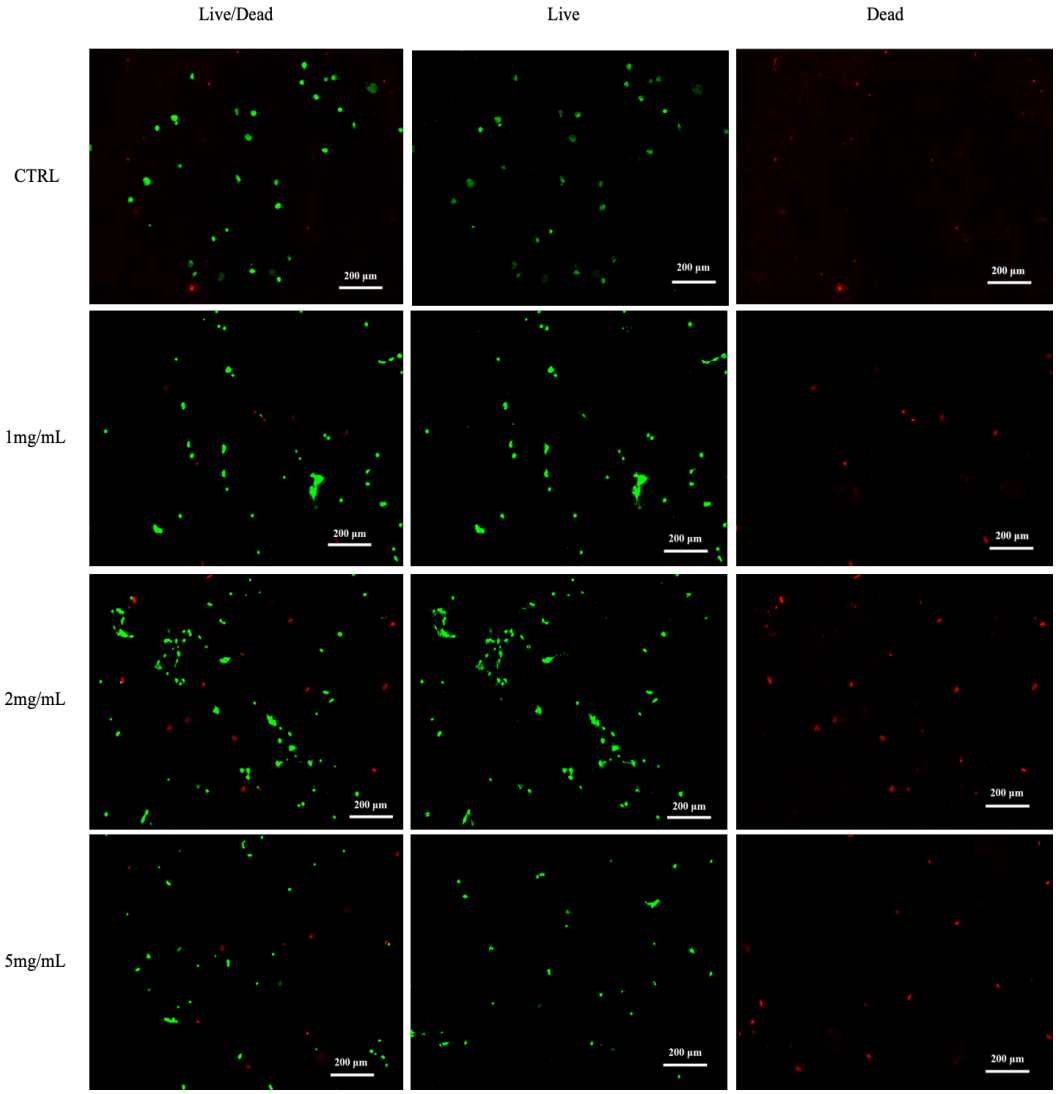

**Figure 4-6.** Live/dead assay for deciding cytotoxicity of EL-AuNPs with concentration of 1mg/mL, 2mg/mL and 5mg/mL.

according to both live/dead assay and LDH assay. Live/dead assay of hSMCs showed no abnormalities in morphology and a limited number of dead cells (Figure 4-6). The live and dead cells were identified and counted for each group from the images and the percentages of the dead cells were calculated. The cell viabilities for all three treated groups were similar to the control group (Table 4-3).

**Table 4-3.** Live/dead cell count and the percentage of dead cells

| | Total count | Live count | Dead count | Dead (%) |
|---|---|---|---|---|
| CTRL | 45 | 36 | 9 | 20.0% |
| 1mg/mL | 53 | 44 | 9 | 17.0% |
| 2mg/mL | 100 | 81 | 19 | 19.0% |
| 5mg/mL | 51 | 40 | 11 | 21.6% |

According to the LDH cytotoxicity assay, the average LDH activity of the spontaneous control is 0.232 and the average LDH activity of maximum control is 2.766. The average LDH activities for 1, 2 and 5mg/mL group are 0.229, 0.230, and 0.229, respectively. The LDH activities in EL-AuNPs treated group is not significantly different from the spontaneous control group and none of the calculated average percentages of cytotoxicity of the three treated groups were positive (Figure 4-7). It provided further

evidence to indicate that the treatment with EL-AuNPs at a concentration of 1, 2, and 5mg/mL shown no cytotoxicity to cultured hSMCs.

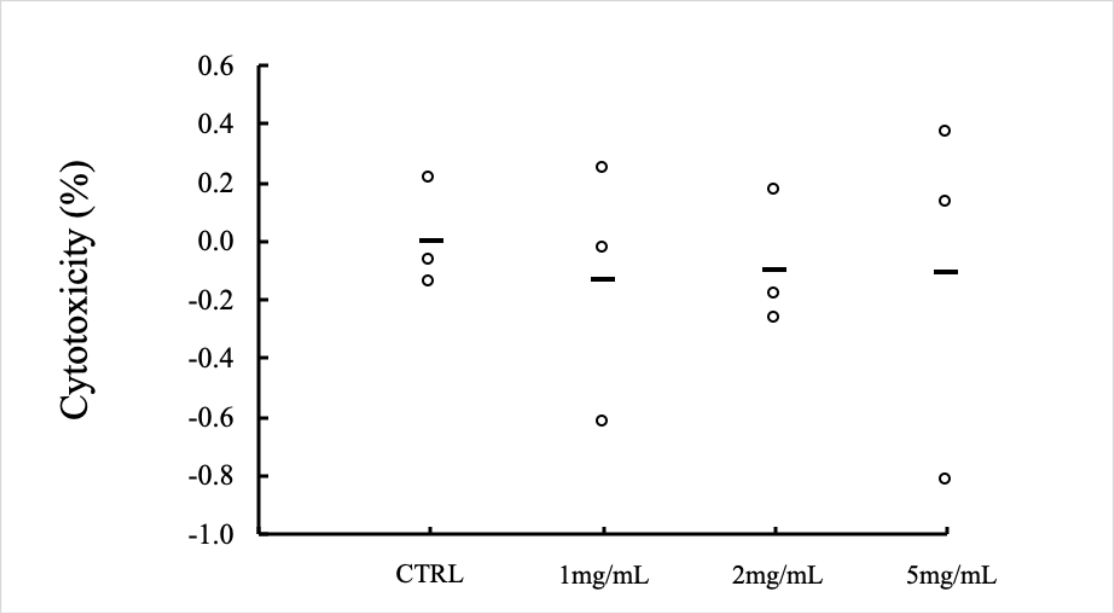


**Figure 4-7.** Cytotoxicity (%) calculated from LDH assay, the cytotoxicity percentage of individual sample was represented with a circle and the average result was represented with a bar.

**Cellular uptake of EL-AuNPs**

For mouse macrophages, the mass of the intracellular gold after incubation for four and twenty-four hours with the AuNPs were both below the detection limit of ICP-MS. For hSMCs, the average mass of the AuNPs taken by the cells after incubation for 4 h was 13.17μg. The percentage uptake from the total added gold was 0.687%. After incubation for 24 h, the average mass of gold in the cells incubated with AuNPs was 16.69μg and the percentage uptake from the total added gold was 0.834%. Thus, AuNPs as prepared for *in-*

*vivo* studies showed no significant uptake by hSMCs and mouse macrophages in cell cultures due to their size and negative surface charge.

### *In-vitro* targeting study for optimizing the conjugation condition

After PPE treatment of the porcine carotids, the elastin fibers in the middle segment of the porcine carotids were fragmented and degraded while the elastin fibers in the two ends remain intact, as shown in the VVG staining (Figure 4-8). It suggested that we successfully established a partially damaged *in-vitro* elastase model for studying the ability of the EL-AuNPs to target the degraded elastin in the vascular wall.

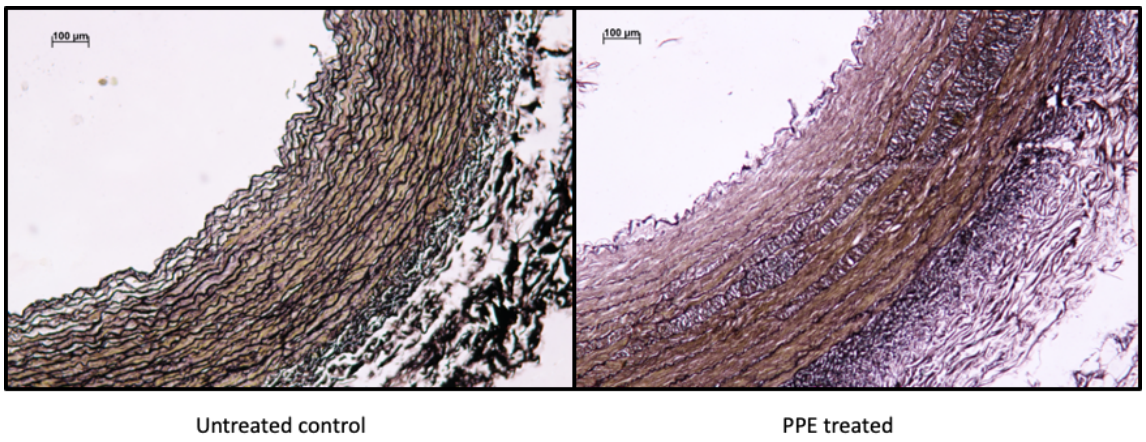


**Figure 4-8.** VVG stain for untreated and elastase treated porcine carotid sections.

In the 3D models that were reconstructed from the micro-CT scans, the EL-AuNPs showed a much higher contrast than the soft tissue because of its higher x-ray adsorption rate (Figure 4-9). EL-AuNPs accumulated exclusively at the PPE treated section while sparing the untreated healthy two ends of the carotids, indicating the targeting ability of the EL-AuNPs to degraded elastin. Also, different combinations of conjugation conditions resulted in different targeting efficiency of EL-AuNPs. For the porcine carotids treated

with batch one EL-AuNPs, the CT scan had not shown the accumulation of EL-AuNPs in the damaged tissue. Batch two EL-AuNPs showed some targeting signal at the damaged site in the CT scans, but the signal was still very weak. The third batch of EL-AuNPs provided strong and specific signals in the reconstructed micro-CT model in the PPE treated porcine carotid tissue. The third conjugation condition which showed the highest signal intensity of the EL-AuNPs at the damaged section was used for further studies.

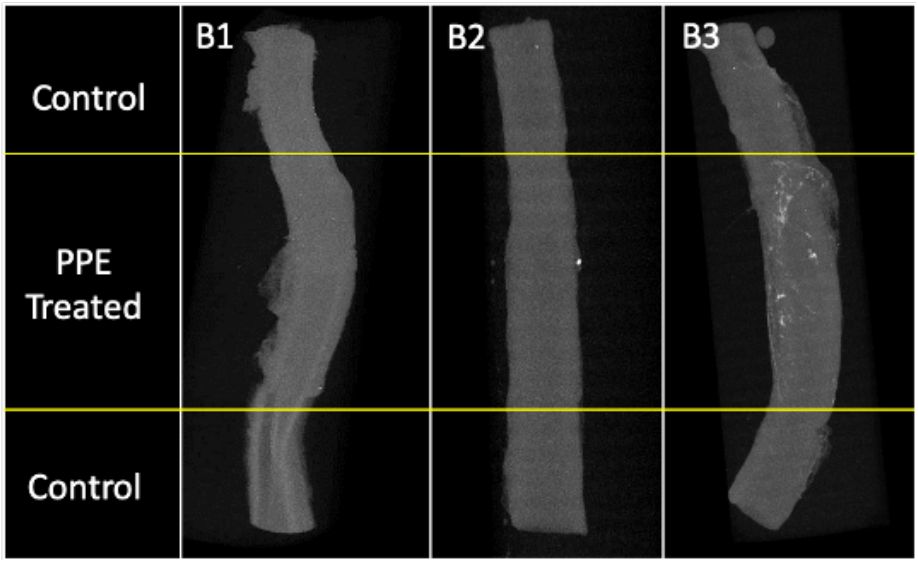


**Figure 4-9.** Signals for differently conjugated EL-AuNPs in the reconstructed porcine carotid MIP models. B1, B2, and B3 were the porcine carotids that were targeted with EL-AuNPs conjugated under the first, second, and third conditions mentioned in Table 4-1 respectively.

After PPE treatment of the rat aortic segments for 30, 60, and 90 mins respectively, different levels of elastin fiber fragmentation and degradation were observed in VVG staining (Figure 4-10). In the control group, the elastin fibers in the aortic wall were intact and well-aligned. As the PPE treatment time increased, the elastin laminae became more

disorganized and fragmented. The quantification of desmosine in the PPE treated tissues further confirmed different damage levels of the elastin content. All three treated groups

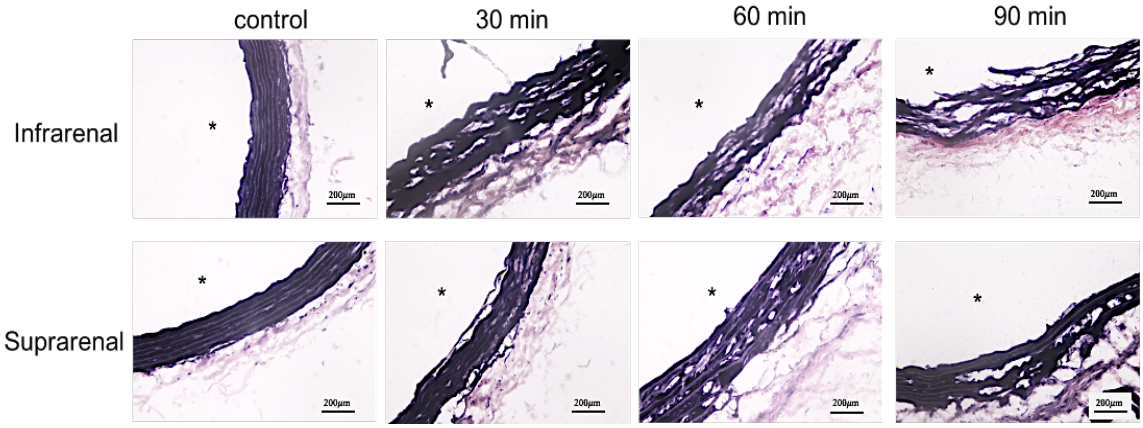


**Figure 4-10.** VVG staining of healthy control and rat aortic tissue after 30, 60, and 90 minutes of PPE treatment. The aortic lumen was indicated with *.

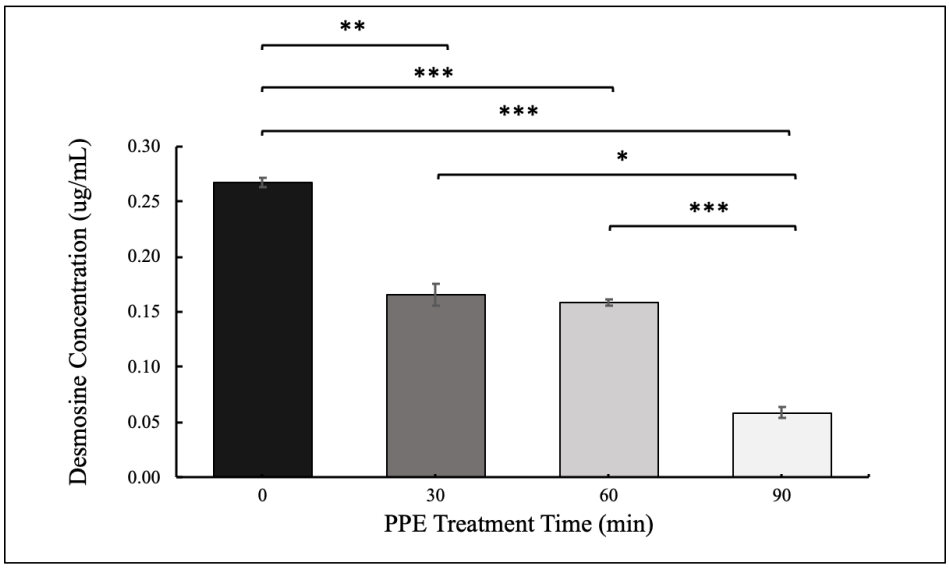


**Figure 4-11.** Quantification of desmosine extracted from damaged aortic tissue using ELISA assay, ***p<0.01, **p<0.05, *p<0.1.

had significantly lower desmosine concentration comparing to the control group. Moreover, the quantities of desmosine in the tissues decreased as the PPE treatment time increased (Figure 4-11). These results suggested that a longer PPE treatment time can induce a more severe elastin degradation in the rat aortic tissue. It provided us a model for studying the correlation between the quantity of targeted EL-AuNPs and the aortic elastin damage level *in-vitro*.

3D reconstructed Micro-CT model showed the distribution of the EL-AuNPs within

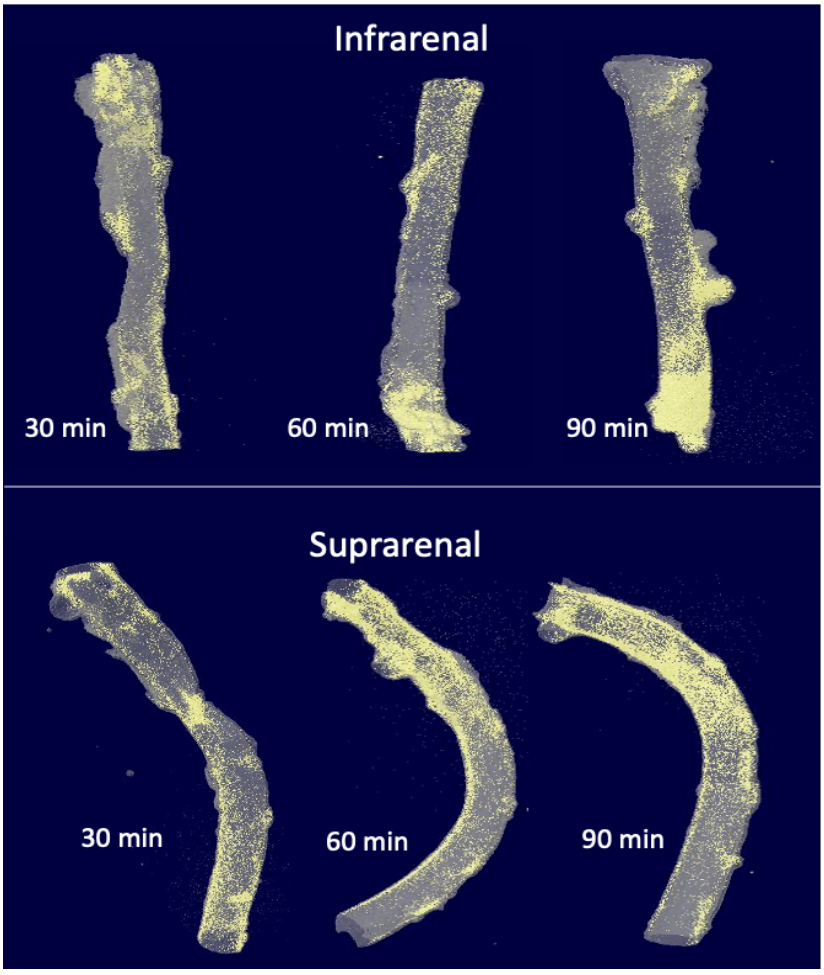


**Figure 4-12.** 3D models of the aortic tissue samples and the accumulated EL-AuNPs (highlighted in yellow) reconstructed from micro CT imaging.

the rat aortic tissues (Figure 4-12). The signal from EL-AuNPs was differentiated from the aortic tissue and highlighted yellow. More EL-AuNPs were found accumulating in the 90-minute PPE treated group comparing to the 30- and 60-minute group. And the 30- minute group showed the least EL-AuNP attachment to the tissue. Moreover, for quantitative analysis, the amount of the EL-AuNP signal was calculated and normalized to the total volume of the tissue. A negative correlation between the EL-AuNP to tissue ratio and the concentration of desmosine in the tissue has been built (Figure 4-13). As the desmosine level in the tissue decreased and the signal percentage of EL-AuNPs increased. Since a lower tissue desmosine concentration indicated more elastin degradation, the accumulation of the EL-AuNPs within the tissue could positively correlate to the degree of tissue elastin damage.

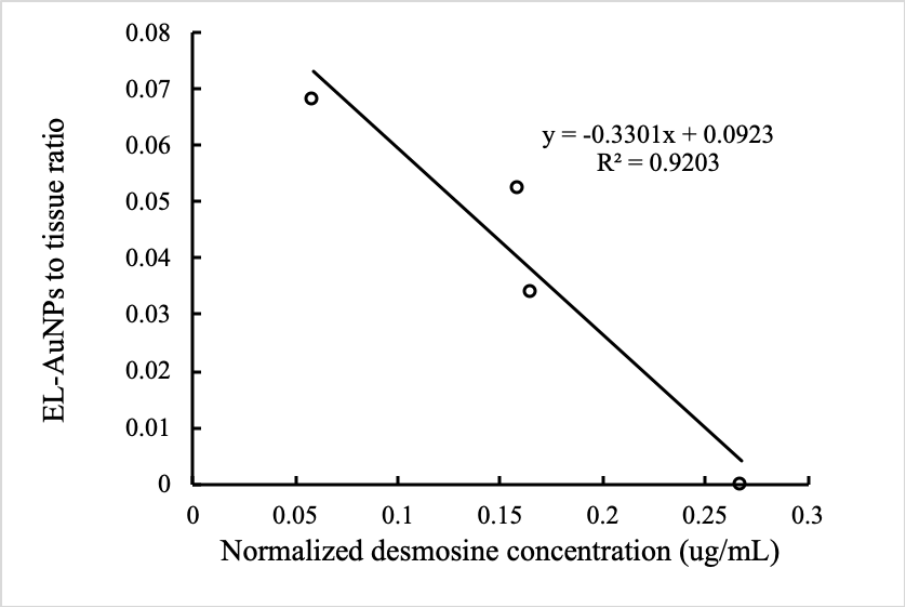


**Figure 4-13.** The correlation of the EL-AuNPs to tissue ratio with tissue desmosine concentration.

## 4.4 Discussion

Colloidal gold is wildly used in nanotechnology research as model particles. They can be synthesized in different shapes, such as spheres, rods, and stars, with various size ranges. And AuNPs with different shapes and sizes have different pharmacokinetic and biodistribution parameters [276]. In order to increase the efficacy of using AuNPs for biomedical purposes, the combination of shape and size has to be chosen carefully according to specific applications. For drug-delivery or imaging applications, spherical AuNPs suit the best since they can be easily synthesized with high monodispersity using highly labile stabilizing ligands that allow for facile, efficient, and high-density ligand exchange [277].

Besides, the size has been demonstrated to influence the blood half-time and the biodistribution of the AuNP, two parameters that play important roles in achieving desired biomedical effects when injected intravenously. A study of the size-dependent biodistribution of the AuNPs in rats performed by De Jong, W.H. et al. has demonstrated that small AuNPs had more widespread organ distribution while larger particles were only detected in blood, liver, and spleen [278]. In this study, in order to target AAAs, we synthesized spherical AuNPs with a hydrodynamic size of ~150 nm. The spherical shape was beneficial for attaching antibodies to the surface of AuNPs to achieve targeting. And the relatively large size could prevent the AuNPs from staying in organs like the brain and lungs while still allow them to circulate for enough time to ensure vascular targeting.

The cytotoxicity of the AuNPs was also reported to be size and shape dependent. Generally, the cytotoxicity of the AuNPs decrease as the size increase. Pan, Y. et al. have

demonstrated that AuNPs 1–2 nm in size have a much higher cytotoxicity and wilder distribution comparing to larger 15-nm gold colloids [279]. Mateo, D. et al. have reported that stronger cytotoxic effects were observed in 30 nm AuNPs treated human dermal fibroblasts than those obtained with the 50 and 90 nm NPs-treated cells [280]. Meanwhile, different shapes of AuNPs have different cytotoxic profiles. Lee, Y.J. et al. have reported that among chitosan capped nanorods, stars and spheres, nanorods showed the highest toxicity against AGS, HeLa, HepG2, and HT29, followed by nanostars and finally by nanospheres [281]. Furthermore, surface modification has been proved to help reduce the AuNPs cytotoxicity. Niidome, T. et al. suggested that surface modification of gold nanorods with PEG could reduce their *in-vitro* toxicity [282].

For our EL-AuNPs with a size of ~170 nm, Live/dead assay showed no difference in cell viabilities between EL-AuNPs treated group and untreated control. LDH leakage due to cell membrane damage was measured as another indicator of EL-AuNP-induced cytotoxicity. Cells that were treated with EL-AuNPs showed no higher LDH leakage in the short term comparing to the untreated control. These results suggested the low cytotoxicity of EL-AuNPs on hSMCs *in-vitro*. The good biocompatibility of the EL-AuNPs could be a result of the combination of their spherical shape, relatively large particle size, and PEG/antibodies coated surface. Thus, it is considered safe to use the AuNPs at the concentration designed for *in-vivo* studies.

Surface functionalized AuNPs have been regarded as an ideal contrast agent for diagnostic purposes because of their great imaging properties and biocompatibility. Not only their surface can be modified with PEG to achieve prolonged circulation time for

blood pool imaging, but also, the conjugation with molecules that target specifically to pathological biomarkers renders AuNPs the ability to selectively and effectively enhance the contrast of the tissue of interest. Passive targeting, active targeting, or a combination of both strategies can be used to achieve aneurysm-specific particle accumulation for imaging. For example, Kim, D. et al. reported that they have gained more than 4-fold greater CT intensity when imaging prostate cancer by using AuNPs that has been surface functionalized with a prostate-specific membrane antigen (PSMA) RNA aptamer that actively targeted prostate cancer cells that express the PSMA protein [283].

The amount of contrast that could be generated in CT scans depends on the mass/concentration of the contrast agent accumulated in the desired tissue. For blood pool imaging, a large dose of contrast agent is usually applied to visualize the vasculatures, which could result in side effects such as hepatoxicity and nephrotoxicity [284]. Thus, targeting efficiency of the EL-AuNPs could drastically influence the imaging quality and should be optimized to reduce the systemic dosage required. For a given size of nanoparticles, how NP surface modification was achieved would influence their surface charge and the number of conjugated surface antibodies. Thus, it would result in variable clearance rate *in-vivo* and different chances for the antibodies to interact with the desired ligands. In our study, we conjugated EL-AuNPs using different combinations of PEG to AuNPs ratio, PEGylation duration and temperature, and the incubation time for the EDC/NHS reaction. Moreover, the combination that showed a higher contrast at the elastase damaged area in an *in-vitro* porcine carotid model was considered to have a better targeting efficiency. The combination that has presented the highest targeted signal in the

CT scan has been chosen as the protocol to prepare the EL-AuNPs that were used in targeting studies.

However, surface coatings can change the charge of the nanoparticle and alter protein adsorption and cellular uptake during circulation [285]. Nanoparticles that are positively charged have higher rates of phagocytosis and shorter blood circulation half-life than neutral and negatively charged particles [286]. We successfully conjugated the AuNPs to be negatively charged according to the results of the zeta-potential measurement. It would help the NPs avoid being phagocytosed by macrophages and also uptake by any other cells like SMCs and make them applicable for effective vascular targeting. According to the cellular uptake study performed in hSMCs and mouse macrophages, an infinitesimal amount of the AuNPs was detected that entered the cells. The fact that most of the AuNPs stayed outside of both SMCs and macrophages rendered them the ability to achieve targeting to the aortic lesions. Moreover, our AuNPs were surface modified with antibodies that could specifically bind to the degraded elastin. It has been shown in our *in-vitro* study that these EL-AuNPs s could target to the tissues that presented elastin damage and specifically increased the local contrast in CT-scans. Since the degradation of elastin laminae is one of the key pathological features of AAAs, it is possible to use EL-AuNPs to target AAAs *in-vivo* for imaging purposes.

Based on the elastin targeting property of the EL-AuNPs, we investigated the correlation between the EL-AuNPs accumulation and the elastin damage using an *in-vitro* elastase model. Different elastin damage level could be induced by treating the aortic tissue for a different amount of time and the degradation of the elastin in this model were not

reversible. Since elastin is an important mechanical component in the aortic wall that provides strength and elasticity to endure the stress given by the blood flow [287], the decrease in elastin content could result in a weaker aortic wall with a higher rupture risk. Moreover, as more elastin in the aortic wall degraded, it provided more binding sites for the elastin antibodies anchored on the surface of the EL-AuNPs. We have observed a positive correlation between the gold to tissue volume ratio and the duration of elastase treatment, which indicated that more EL-AuNPs have accumulated in the samples with more degraded elastin. This observation suggested that our EL-AuNPs had the potential to be used as an indicator of elastin damage and a novel tool for evaluating the rupture risk of the AAAs.

### 4.5 Conclusion

In this aim, we successfully produced degraded elastin antibodies conjugated AuNPs that had an average size of ~170 nm and were negatively charged. We have shown that these NPs are biocompatible with minimal cytotoxicity to SMCs and low cellular uptake by both SMCs and macrophages. After being tested in an elastase treated porcine carotid model, the EL-AuNPs presented the ability to actively target the tissue with elastin damage and can increase the contrast of the targeted area in CT scans. Moreover, the accumulated gold to tissue ratio decided by the CT analysis was positively correlated to the damage level of the elastase treated tissue. Thus, the EL-AuNPs could be used as a safe and efficient targeting CT contrast reagent for vascular diseases with the potential to reveal the local elastin damage.

# 5. SPECIFIC AIM 2: TO INVESTIGATE WHETHER EL-AuNPS CAN BE TARGETED TO AAAS IN-VIVO AND BUILD A CORRELATION BETWEEN THE MICRO-CT SIGNAL INTENSITY OF EL-AuNPS AND MECHANICAL PROOERTIES OF THE ANEURYSM IN AN ANGII INFUSION INDUCED MOUSE MODEL

## 5.1 Introduction

Ultrasonography is the gold standard tool for AAA screening and diagnostic due to its simplicity, safety, validity, cost-effectiveness, reproducibility, and public acceptance [288]. It can provide relatively precise AAA geometrical information such as the diameter and the growth rate of the aneurysm, which are commonly used as clinical interventional criteria. However, the potential risk of an aneurysm rupture is determined by its mechanical condition more than just AAA geometry. The intrinsic biomechanical properties and the environmental stress conditions of the aneurysm change all the time during the disease progression and decide the rupture risk of the AAAs.

Although large AAAs are statistically more prone to rupture, small AAAs can fail prior to meeting the surgical criteria. Patients with smaller AAAs can still be under a life-threatening situation since about 13% of AAAs cause death in patients before they are recommended for surgery [96]. Thus, geometrical information alone is insufficient as a universal predictor for AAA failure. Identification of localized vulnerabilities (i.e., weak points within the wall) would provide crucial diagnostic information to aid clinical strategies and decrease mortality in patients suffering from AAAs. A targeted nanoparticle

system can be ideal to serve the purpose of providing pathological information for AAAs when being used as an imaging contrast agent.

As described previously, key pathological processes occurring within AAAs such as increased ROS activity, inflammation, VSMCs apoptosis, and ECM remodeling have emerged as potential targets for nanoparticle-based diagnostics. Imaging agents and drugs have been successfully delivered to the AAAs by applying surface modified NPs that target these biomarkers as carriers. However, levels of inflammation and collagen remodeling that happen in the AAA vary with time and patients, and therefore cannot be used as a reliable surrogate for chronic aneurysmal rupture risk assessment. On the other hand, since there is rarely elastin synthesis in adults, the elastic lamina in the aortic wall does not remodel substantially within the timeline of aortic disease progression. The degradation of the aneurysmal wall is a consistent feature of AAAs making it an ideal target for delivering NPs.

Animal models are well established for studying AAAs *in-vivo*. Considering the complicated *in-vivo* environment, it is important to test imaging agents and treatments with AAAs that were developed in animal models to provide some insights about how they might interact with human bodies. Many models of AAAs have been developed that use a diverse array of methods for producing the disease, including but not limited to genetic manipulation and chemical induction [289]. The genetic approaches are spontaneous and engineered mutations and the chemical approaches include the intraluminal infusion of elastase, peri-aortic incubations of calcium chloride, and subcutaneous implantation of AngII osmotic pump.

Even though these models recapitulate some facets of the human disease including medial degeneration, inflammation, thrombus formation, and rupture, each animal model can only mimic some pathogenesis of the real disease. The AngII infusion induced AAA model in the LDLr −/− mice is ideal to be used in the studies that aim to understand the AAA mechanical properties because of the formation of the ILTs in this model. Moreover, the formation of AAAs in the systemic AngII infusion induced model resembles human disease in the setting of mild hypertension with an enhanced incidence in the presence of hyperlipidemia [290].

**5.2 Materials and methods**

The animal study of EL-AuNPs was performed in an established AngII infusion induced mouse AAA model. The EL-AuNPs that were accumulated in the AAA sack via active targeting were visualized using both *ex-vivo* and *in-vivo* micro CT imaging (Figure 5-1). Briefly, the animal study can be divided into three parts: development of AAAs in-vivo, micro CT imaging, and tissue analysis. The AAAs were firstly induced in mice by the application of high cholesterol diet and AngII from subcutaneously implanted osmotic pumps. And the pumps were explanted from the mice before imaging to eliminate the high imaging noise given by the metal core of the pump. EL-AuNPs were injected intravenously to achieve targeting and create contrast. In the imaging step, the aortas were explanted and cleaned after the euthanasia for *ex-vivo* imaging study and were imaged with the micro-CT when immersed in corn oil to prevent it from drying out, while a live abdominal micro CT scan was performed before euthanasia and organ harvesting for the *in-vivo* imaging study. The harvested aortas were then analyzed mechanically and histologically.

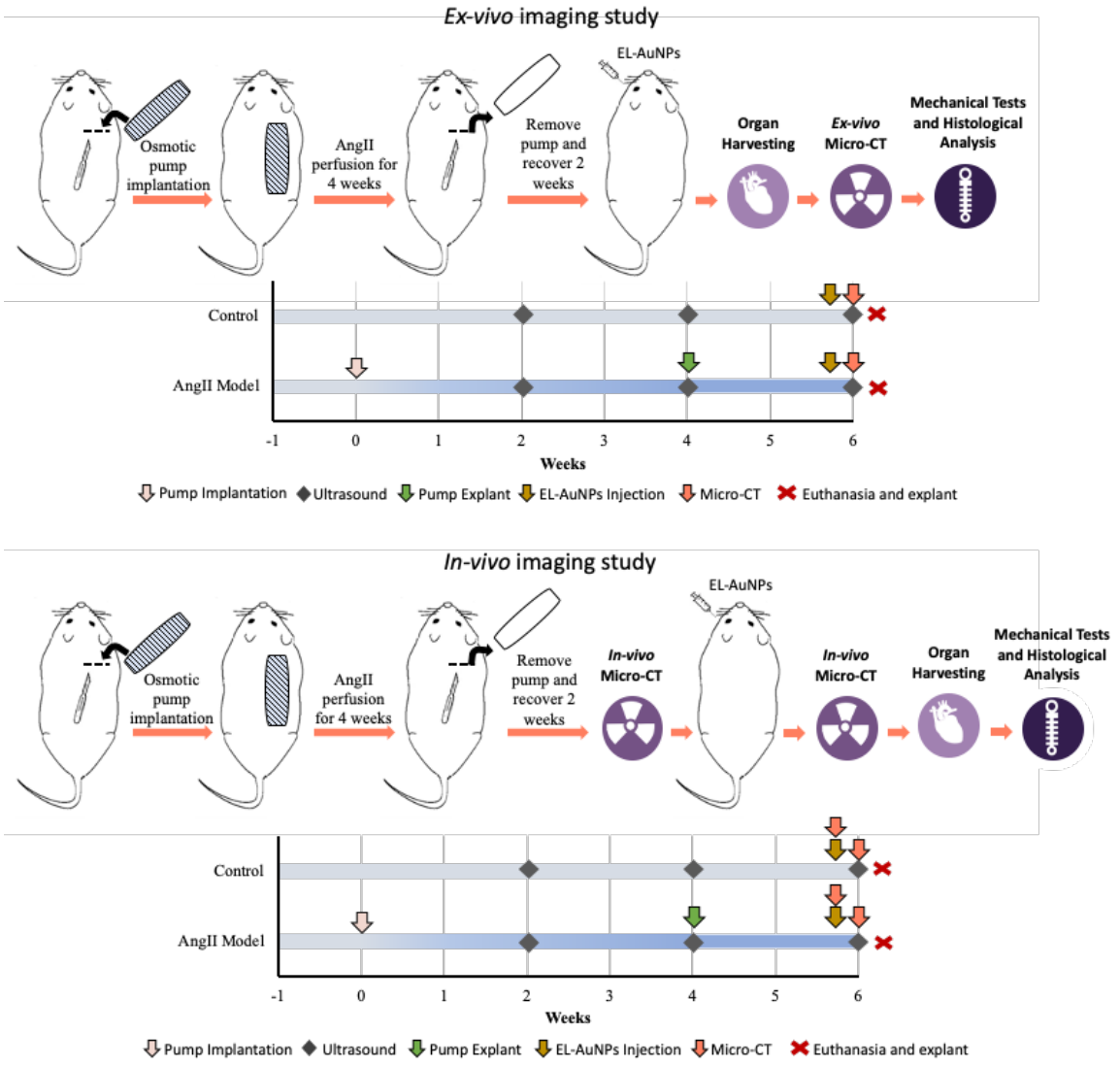


**Figure 5-1.** Schematic representation of the study design.

### Preparation of EL-AuNPs

For the *ex-vivo* imaging study, citrate capped AuNPs were purchased from Meliorum Technologies (Rochester, NY) with an average size of 150.0 ± 25.0 nm. And for the in-vivo imaging study, citrate capped AuNPs with an average size of 156.0 ± 57.4 nm were synthesized as described in the previous chapter. The conjugation process for both

types of AuNPs was the same. Briefly, a heterobifunctional thiol-PEG-acid (2000MW, Nanocs, New York, NY) was added to the AuNPs at a weight ratio of 4:1 and the mixture was incubated at 4°C for 48 hrs with gentle rocking to achieve PEGylation. PEGylated AuNPs were collected after centrifuging at 10,000 rpm for 20 minutes at room temperature and resuspended in 0.1M 2-(N-morpholino) ethanesulfonic acid buffer (MES, pH:5.5).

EDC/NHS chemistry was followed to conjugate the PEGylated AuNPs with the anti-elastin antibody. Briefly, EDC (Oakwood Chemical, Estill, SC) and Sulfo-NHS (Sigma Aldrich, St. Louis, MO) were added at a weight ratio of 2:1 and 4:1 to PEGylated AuNPs respectively. The mixture was incubated at room temperature for 6 hours with gentle vortexing. Resulting AuNPs were collected after centrifuging at 10,000 rpm for 20 minutes at room temperature and resuspended in 1mL of PBS (pH 7.8). 4μg anti-elastin antibody (custom-made at Clemson University) per mg AuNPs was added, and the mixture was incubated overnight at 4 °C under slow rocking. The excess antibodies were removed by centrifuging the resulting solution at 10,000 rpm for 20 minutes. EL-AuNPs were resuspended in saline to a concentration of 3mg/mL for *ex-vivo* imaging study injection and 20mg/mL for the *in-vivo* imaging study.

**Development of aneurysms with AngII in a mouse model**

For the *ex-vivo* imaging study, fifteen male LDLr (-/-) mice (2 months of age, on a C57BL/6 background) were obtained from the Jackson Laboratory (Bar Harbor, ME). Eleven mice were used for aneurysm studies while four other mice were used as healthy age-matched controls. Aneurysms were induced by systemic infusion of angiotensin II (AngII, Bachem Americas, Torrance, CA) in combination with a diet with saturated fat

(21% wt/wt) and cholesterol (0.2% wt/wt; catalog no. TD88137; Harlan Teklad) [92]. Briefly, mice were fed with a high-fat diet for one week before, and six weeks during AngII infusion. Osmotic pumps (model 2004; Alzet, Cupertino, CA) filled with AngII were implanted subcutaneously through an incision at the right back shoulder of the mice. 2% to 3% isoflurane was inhaled by the mice as anesthesia throughout the surgical process. The pumping rate for AngII was set to 1000ng/kg/min. Pumps were explanted four weeks after the implantation and mice were allowed to recover for two weeks. Disease progression was monitored with a high-frequency ultrasound machine, Fujifilm VisualSonics Vevo 2100 (Fujifilm VisualSonics, Toronto, ON, Canada), by utilizing a linear array probe (MS-550D, broadband frequency 22 MHz -55 MHz).

For the *in-vivo* imaging study, twenty male LDLr (-/-) mice (2 months of age, on a C57BL/6 background) were obtained from the Jackson Laboratory (Bar Harbor, ME). Seven mice were used for aneurysm studies among which one mouse was a healthy age-matched control. Aneurysms were induced monitored in the same way as in the *ex-vivo* imaging study. All animal use protocols for the study were approved by the Clemson University Animal Research Committee.

**Ultrasound analysis of AAAs**

The ultrasound system, Fujifilm VisualSonics Vevo 2100 (Fujifilm VisualSonics, Toronto, ON, Canada), was used for monitoring percent dilation and to assess the circumferential strain throughout the cardiac cycle and PWV of the aneurysm. The animals were placed in a supine position on the imaging table and were maintained under anesthesia by inhaling 2% to 3% isoflurane during imaging. Heart rate and body temperature of the

mice were carefully monitored during the imaging process. Suprarenal aortic inner diameters were measured using the built-in ultrasound software on the basic-mode ultrasound images.

Sagittal and transverse images for both healthy and aneurysmal aortas were obtained in motion mode. Systolic and diastolic diameters were measured and recorded at three different regions on each aneurysm or parent vessel using the built-in ultrasound software. The diastolic-to-systolic circumferential Green-LaGrange strains were calculated assuming axial symmetry using the two equations given below,

$$Circumferential\ Strain\ (\%) = \frac{1}{2}\left(\left(\frac{D_{sys}}{D_{dia}}\right)^2 - 1\right) * 100$$

where $D_{sys}$ represents the inner systolic aortic diameter and $D_{dia}$ represents the inner diastolic aortic diameter.

***Ex-vivo* Micro-CT imaging study**

EL-AuNPs were given to the mice (n=15) as a contrast agent through a retro-orbital injection at a dosage of 10 mg/kg animal weight under 2%-3% isoflurane anesthesia. Mice were euthanized 24 hours after the injections, and intact aortas (from ascending aorta to iliac bifurcation) were explanted. Surrounding connective tissue was cleaned before micro-CT scanning. Aortas were then immersed in corn oil and imaged (90kV, 250mAs, 300ms, 0.2mm Al filter) with a high-performance micro-CT system (Skyscan 1176, Bruker, Billerica, MA). Reconstructions were carried out using the Skyscan Nrecon software based on the Feldkamp algorithm. The reconstructed images of the aortas were visualized, and

the dimensions of the aneurysms measured using DataViewer and CT-Vox software. 3D maximum intensity projection (MIP) images were obtained to determine the distribution of EL-AuNPs within the aortas while attenuation images were acquired to study the intensity of the signals given by both EL-AuNPs and tissue. Signal intensity was further quantified using CT-An software.

### *In-vivo* Micro-CT imaging study

A baseline micro-CT scan (90kV, 250mAs, 200ms, 0.2mm Al filter) for each mouse was performed with a high-performance micro-CT system (Skyscan 1176, Bruker, Billerica, MA) to be used as control before the EL-AuNPs injection. EL-AuNPs were then administrated retro-orbitally to the mice (n=14) as a contrast agent at a dosage of 10 mg/kg animal weight under 2%-3% isoflurane anesthesia. The mice that received EL-AuNPs injection were fasted for 24 hours to clear out the feces and at the meantime EL-AuNPs were allowed to circulate for 24 hours to achieve targeting. Mice were scanned using the same micro-CT system and the same imaging settings as were used in baseline scan under 1.5% isoflurane anesthesia. Reconstructions were carried out using the Skyscan Nrecon software based on the Feldkamp algorithm. The reconstructed images of the aortas were visualized using DataViewer and CT-Vox software. And signal intensity was further quantified using CT-An software.

### EL-AuNPs biodistribution analysis

Ten mice were used for determining the biodistribution of EL-AuNPs *in-vivo*. EL-AuNPs were given to the mice (n=9) via retro-orbital injections at a dosage of 10 mg/kg animal weight under 2%-3% isoflurane anesthesia. Mice were euthanized at day 1, day 5,

and day 9 after the injections, and the entire livers, spleens, lungs and kidneys were explanted. 1 mm thick of sample from each harvested organ was embedded in OCT and sectioned for further darkfield imaging use. The rest of the samples were homogenized and lysed in an acid (2%HCl +2% $HNO_3$) overnight for gold extraction. The solution was then collected, and ICP-MS was performed for quantifying the concentration of the gold element in the samples.

**Aortic burst failure testing**

Burst pressure testing was performed on each suprarenal aortic segment within 24 hrs after explant to study the rupture potential and location of the failure. Aortas were shipped in EDTA-free-protease-inhibitor-cocktail on ice overnight to the University of South Carolina. Branches were ligated using 12/0 nylon suture and the aneurysm, including 1-2 mm distal and proximal to the necking region, were cannulated on shortened and roughed 26G needle tips with 7/0 silk suture and mounted to our custom-designed multi-axial murine artery mechanical testing device within an adventitial bath of PBS. The device enables temperature control, hydration, inflation, and extension capabilities while recording images at 45° intervals around the circumference of the tissue. All instruments are controlled via an integrated LabVIEW code. Samples reported here were first extended to an axial stretch ratio of 1.2 and then preconditioned through slow cyclic pressurization of luminal media using a syringe pump. Then the syringe pump was set to maintain an inflation rate of 1-3 mmHg/s until bursting was observed. PBS supplemented with phenol red was used as the luminal media to provide contrast capabilities to identify burst locations. During inflation, the vessels were closely monitored for

signs of failure, including dissection, and the pressure and location of failure were recorded. No tissue that failed at or around the mounting suture or hardware were included in the analysis.

**Aortic biaxial mechanical testing and data analysis**[1]

The mechanical properties of aortic aneurysmal tissues and controls were tested at the University of South Carolina (UofSC) within 24 hours of receiving tissues so that no more than 48 hours passed between animal sacrifice and mechanical testing. Aortas were mounted to a custom-designed biaxial testing rig. The details for this device and biaxial testing procedures can be found in Lane et al. 2020a and 2020b [291, 292]. Briefly, this test rig is equipped with a thin-beam loaded cell (LCL-113G; Omega Engineering), pressure transducer (PX409; Omega Engineering), RS-232 infuse/withdraw syringe pump (AL-1000; World Precision Instruments), motorized linear actuator (Z825B; Thorlabs), and K-Cube motor controller (KDC101; Thorlabs). All components had PC USB interface through a custom-written LabView code used to gather synchronous measurements while controlling pumps and actuators. The testing chamber was filled with warm PBS solution to maintain hydration throughout testing and PBS was flushed through the vessel lumen and device tubing to remove bubbles. The unloaded outer diameter ($D_o$) and length ($L$) were recorded using digital calipers. The artery then underwent five preconditioning cycles consisting of pressurization from 10 to 160 mmHg and axial stretching to a deformed length ($\ell$) at, and 5% above and below, the pressurization force-invariant axial stretch ratio, deemed the in vivo axial stretch.

[1] Section prepared by John F. Eberth, PhD, Shahd Hasanain, BS and Liya Du, BS

For data acquisition, the artery was extended to the three axial stretch ratios described previously before undergoing pressurization cycles (0–120 mmHg) with simultaneous force and outer diameter measurements at 10 mmHg pressure increments. Data was recorded in triplicate and the average and standard deviations of these tests reported. Primary continuous data collection consisted of pressure ($P$), deformed outer diameter at the peak bulge location ($d_o$), axial force ($f$), and axial stretch ratio ($\lambda_z$). Then vessels were pressure fixed by replacing luminal PBS with 4% paraformaldehyde solution and re-inflated to 100 mmHg in the axially extended state for 4 hours. In the deformed but fixed state, micro-Computed Tomography Imaging (Quantum GX Micro-CT Imaging System; PerkinElmer) was used to measure the deformed inner diameter. This step was necessary due to the lack of transparency of these calcified and heterogeneous tissues. Measurements consisted of an average of 4 locations along the circumference of the aneurysm bulge and were processed using Fiji-ImageJ.

Assuming axial symmetry and incompressibility, the inner diameter is calculated from,

$$d_i = 2\sqrt{\frac{d_o^2}{4} - \frac{V}{\pi \ell}} \tag{1}$$

where $V$ is the volume measured using a combination of micro-CT and biaxial testing.

From the primary data collection described above, the mid-wall circumferential and axial stretch ratios are calculated from

$$\lambda_\theta = \frac{d_i + d_o}{D_i + D_o}, \ \lambda_z = \frac{\ell}{L} \tag{2}$$

where $D_i$ is the unloaded inner diameter.

The mean circumferential and axial stresses are then calculated from

$$\sigma_\theta = P\frac{d_i}{d_o - d_i},\ \sigma_z = \frac{f}{\pi\left(d_0^2/4 - d_i^2/4\right)} \tag{3}$$

and the lumen area compliance from

$$c = \frac{\pi}{4}\frac{\Delta d_i^2}{\Delta P}, \tag{4}$$

where $\Delta P$ is the change from diastolic to systolic transmural pressures (80 to 120 mmHg) and $\Delta d$ the change in inner diameter at these pressures.

In general, discrete data were analyzed at a common pressure and in vivo axial stretch ratio unless otherwise noted.

**Morphological analysis of the explanted suprarenal abdominal aorta**

Morphological analysis was performed in the suprarenal area of the abdominal aorta. For the *ex-vivo* study, outer aortic diameters were measured on the abdominal ultrasound basic-mode-images at three different time points during a cardiac circle within the parent vessel and the lesion. For the *in-vivo* study, inner suprarenal aortic diameters at six different regions were measured using the built-in ultrasound software on the basic-mode ultrasound images. Mean values were then calculated for each. The dilation was calculated using the equation given below,

$$Dilation\ (\%) = \frac{\bar{D}_L - \bar{D}_H}{\bar{D}_L} \times 100$$

where $\overline{D}_H$ represents the mean diameter of the healthy aorta and $\overline{D}_L$ is the mean diameter of the pathological section.

**Histological analysis of the aneurysms**

Cryosections of both aneurysms and healthy aortas were used for histological analysis. Aortas were fixed in buffered formalin, embedded in optimal cutting temperature (OCT) compound (Sakura Finetek, Torrance, CA) after being washed in DI water and sectioned per standard procedures. Five-micrometer sections were obtained and mounted on positively charged glass slides. Slides were placed in 100% pre-chilled acetone (Fisher Science Education, Nazerath, PA) for 10 minutes to further fix the tissue sections. Subsequently, the slides were rinsed with tap water for 5 minutes to remove the OCT compound for further staining. Slides were then stained with Verhoeff-van Gieson (VVG) to visualize the elastin damage in different samples.

**Darkfield microscopy and hyperspectral mapping**

Cryosectioned histological samples (5μm) were examined with a CytoViva enhanced darkfield microscope optics system (CytoViva, Inc., Auburn, AL). The system (Olympus BX51) employs an immersion oil (Type A, nd> 1.515, Cargille Brand) ultra-dark-field condenser and a 40× air Plan-FL objective with an adjustable numerical aperture from 1.2 to 1.4. Illumination was provided by a Fiber-lite DC 950 regulated illuminator. Enhanced darkfield microscopy images were obtained using Exponent7 software with a gain setting of 2.8 and an exposure time of 53 ms to visualize the EL-AuNPs. A hyperspectral imager (mounted on a microscope and controlled by Environment for Visualization software from Exelis Visual Information Solutions, Inc.) was used to extract

spectral information for mapping the EL-AuNPs in the samples at an exposure time of 0.25ms with a full field of view (643 lines). Negative control samples (without AuNPs) were imaged and analyzed to create a spectral library as a reference. Gold mapping was achieved by applying a filtered spectral library by subtracting the negative control spectral library.

### Statistical analysis

All the results, including graphs in the figures, are given as mean± standard deviation. Statistical analysis was performed using a one-way ANOVA and Tukey's HSD as a post-hoc test. Results were considered significantly different when p-values $\leq 0.05$.

## 5.3 Results

### Characterization of EL-AuNPs

EL-AuNPs used the ex-vivo study were prepared by conjugating the custom-made antibody that recognizes degraded elastin with commercial gold nanoparticles. They were characterized by a DLS system for size and surface charge before and after the conjugation process. Before antibody conjugation, bare AuNPs had an average size of 150.00 ± 25.00nm and a zeta potential of -29.20 ± 3.91mV. EL-AuNPs had a final average size of 184.20 ± 18.09nm. The zeta potential of the NPs was measured as -5.06 ± 1.25mV. The EL-AuNPs used in the *in-vivo* study were homemade and the characteristics were described in the previous chapter. Briefly, the size of the AuNPs increased from 156.00 ± 57.40 nm to 173.40 ± 53.08 nm and the zeta potential also increased from -17.6 ± 9.36 mV to -10.4 ± 4.16 mV.

**Systemic AngII infusion-induced aneurysm mouse model**

After the infusion of the AngII, severe aortic dilation (> 1.5-fold) as well as moderate aortic dilation was observed at the suprarenal abdominal aorta in most of the mice (Figure 5-2a). 2D transverse *ex-vivo* micro-CT images revealed an increase of aortic outer

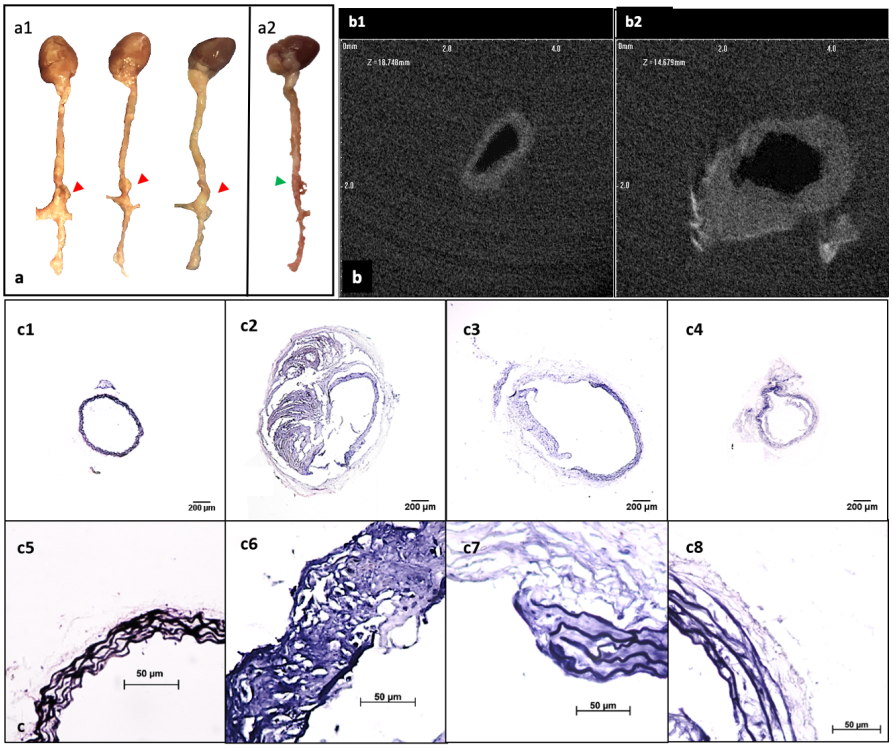


**Figure 5-2.** Development of suprarenal aortic aneurysms with various properties, **a.** Representative pictures showing the morphology of the whole explanted aortas. Various levels of dilations (indicated by arrows) were found at the suprarenal abdominal aortic regions in most of the AngII pump-implanted mice; **b.** *Ex-vivo* micro CT image showing the cross-sections of aortas at the healthy region (c1) and the aneurysmal region (c2); **c.** VVG staining shows different levels of elastin degradation amongst aneurysmal tissues (4x, c2-c4, 40x, c6-c8) compared to the healthy aortic control with only intact elastin (4x, c1, 40x, c5).

diameters and thickening of the aortic wall in the lesions compared to the normal aorta (Figure 5-2b). The enlargement of the suprarenal aortic diameters resulting from the systemic infusion of AngII varied from 9.08%-193.25% of the normal size (Table 5-1). VVG staining of the aneurysmal aorta demonstrated the degradation of elastin laminae inside the aortic wall. Lesion development in mice corresponded with the extent of elastic lamina degradation (Figure 5-2c). In fact, samples did not meet the 1.5-fold threshold but still presented with elastin damage (Figure 5-3).

**Table 5-1.** Diameter and dilation percentages of suprarenal abdominal aortas

| Sample | Healthy (mm) | Aneurysmal (mm) | Diameter Measurements | |
|---|---|---|---|---|
| | | | Dilation Percentages | Fold Increase |
| **MS#1** | 1.18±0.01 | 2.27±0.04 | 92.67% | 1.93 |
| **MS#2** | 1.12±0.02 | 2.31±0.04 | 106.62% | 2.07 |
| **MS#3** | 1.03±0.05 | 2.35±0.01 | 127.97% | 2.28 |
| **MS#4** | 1.30±0.05 | 2.83±0.08 | 117.64% | 2.18 |
| **MS#5** | 1.17±0.01 | 2.25±0.01 | 92.20% | 1.92 |
| **MS#6** | 0.93±0.04 | 1.55±0.04 | 66.39% | 1.66 |
| **MS#7** | 0.88±0.06 | 2.15±0.08 | 144.83% | 2.45 |
| **MS#8** | 1.03±0.07 | 1.84±0.10 | 79.15% | 1.79 |
| **MS#9** | 1.02±0.05 | 1.40±0.08 | 38.23% | 1.38 |
| **MS#10** | 1.23±0.02 | 1.39±0.06 | 12.18% | 1.12 |
| **MS#11** | 1.30±0.03 | 2.51±0.03 | 92.45% | 1.92 |
| **MS#12** | 0.92±0.03 | 2.18±0.26 | 137.39% | 2.37 |
| **MS#13** | 1.15±0.05 | 1.69±0.06 | 47.00% | 1.47 |
| **MS#14** | 1.14±0.03 | 1.25±0.13 | 9.22% | 1.09 |
| **MS#15** | 1.03±0.12 | 2.04±0.09 | 97.87% | 1.98 |
| **MS#16** | 0.85±0.08 | 1.24±0.06 | 45.63% | 1.46 |
| **MS#17** | 1.06±0.14 | 2.30±0.10 | 117.92% | 2.18 |

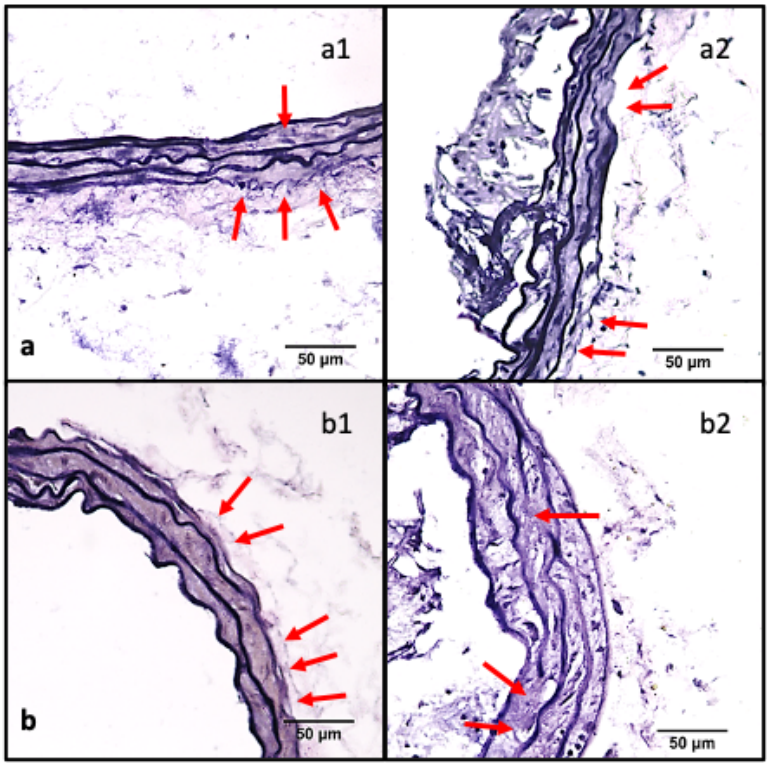


**Figure 5-3.** Elastin damage in aortic walls indicated by the red arrows for samples did not meet the 1.5-fold threshold.

**EL-AuNPs targeting to degraded elastin in the damaged aorta**

3D reconstructed micro-CT models from both *ex-vivo* (Figure 5-4a) and *in-vivo* scan (Figure 5-4b) presented stronger signals in the aneurysmal aortic segment than the healthy aortic segment. This suggested that a much higher concentration of EL-AuNPs accumulated at the aneurysmal area, which indicated their ability to target the aneurysms within 24 hours while sparing the healthy regions of the aorta. Enhanced darkfield microscopy (EDFM) in combination with VVG staining on the histological sections further confirmed the targeting sites of EL-AuNPs within the aneurysmal tissues. EL-AuNPs were found in darkfield microscopy images (Figure 5-4c) accumulating exclusively around the

degraded elastin as identified by VVG staining while sparing healthy and intact elastin fibers (Figure 5-4d). A stronger DFM signal was found in the section (Figure 5-4c1) which showed more elastin damage (Figure 5-4d1) than the control section (Figure 5-4c2) that contained only intact elastin fibers (Figure 5-4d2).

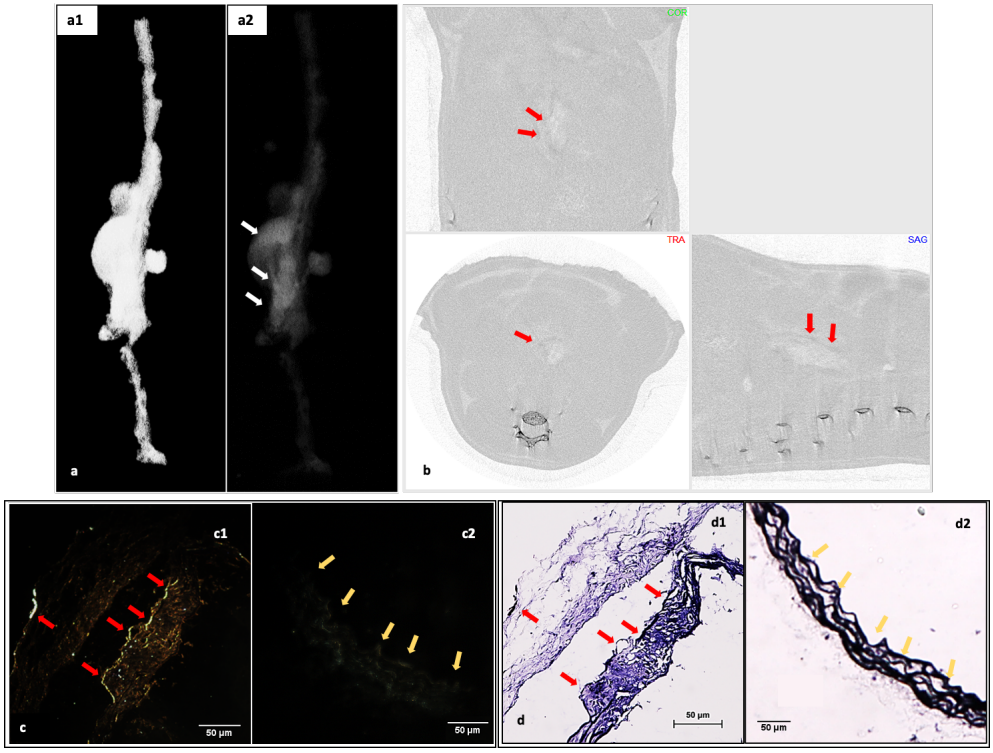


**Figure 5-4.** Localization of EL-AuNPs within aneurysmal tissues. **a.** An *ex-vivo* 3D model that visualizes the morphology of an aneurysmal aorta (a1) and corresponding attenuation mode that showed the distribution of EL-AuNPs (a2). **b.** An *in-vivo* 3D model showing EL-AuNPs targeting in transverse, longitudinal, and sagittal sections; **c.** Darkfield microscopy (DFM) of and **d.** corresponding histological analysis of elastin with VVG staining. The signal given by EL-AuNPs was found at the positions where degraded elastin was present, indicated by red arrows, while healthy and intact elastin fibers were devoid of signals as indicated by yellow arrows.

**EL-AuNP accumulation indicates elastin damage level**

Hyperspectral imaging (HSI), in conjunction with EDFM, provided spectral information for the aneurysmal tissue and the attached EL-AuNPs. Specific signatures of EL-AuNPs were mapped and separated from the noise given by the soft tissue according to their different spectral features. Bright field microscopy indicated different levels of elastin damage within different tissue samples by VVG staining (Figure 5-5a). EDFM and hyperspectral mapping of the counterparts demonstrated that the amount of EL-AuNPs that accumulated within the tissue samples varied with the elastin damage level (Figure 5-5b, c, d). The decreasing integrity of elastic fibers in the aortic wall increased local EL-AuNP accumulation. When extensive damage to elastin laminae was present in the bright field image (Figure 5-5a2), hyperspectral mapping identified a large quantity of EL-AuNPs in the tissue (Figure 5-5e2). Conversely, no EL-AuNP accumulation was mapped (Figure 5-5d1) in a control sample that showed no signs of elastin degradation (Figure 5-5a1).

**Biodistribution of AAAs**

HSI and EDFM were further used to visualize the distribution of EL-AuNPs in different organs at different time points after the injection (Figure 5-6). One day after the injection, EL-AuNPs were found in liver, spleen, lungs and kidneys in large quantities. Four days later, there were still EL-AuNPs found in all four organs. The quantities of EL-AuNPs slightly decreased in the liver, lungs and kidneys but increased in the spleen. On day 9 after the injection, a small number of EL-AuNPs were still in the liver and spleens. However, there was a significant decrease of the EL-AuNPs in all four organs. The images of lungs and kidneys barely showed differences from the control that had no EL-AuNPs injection.

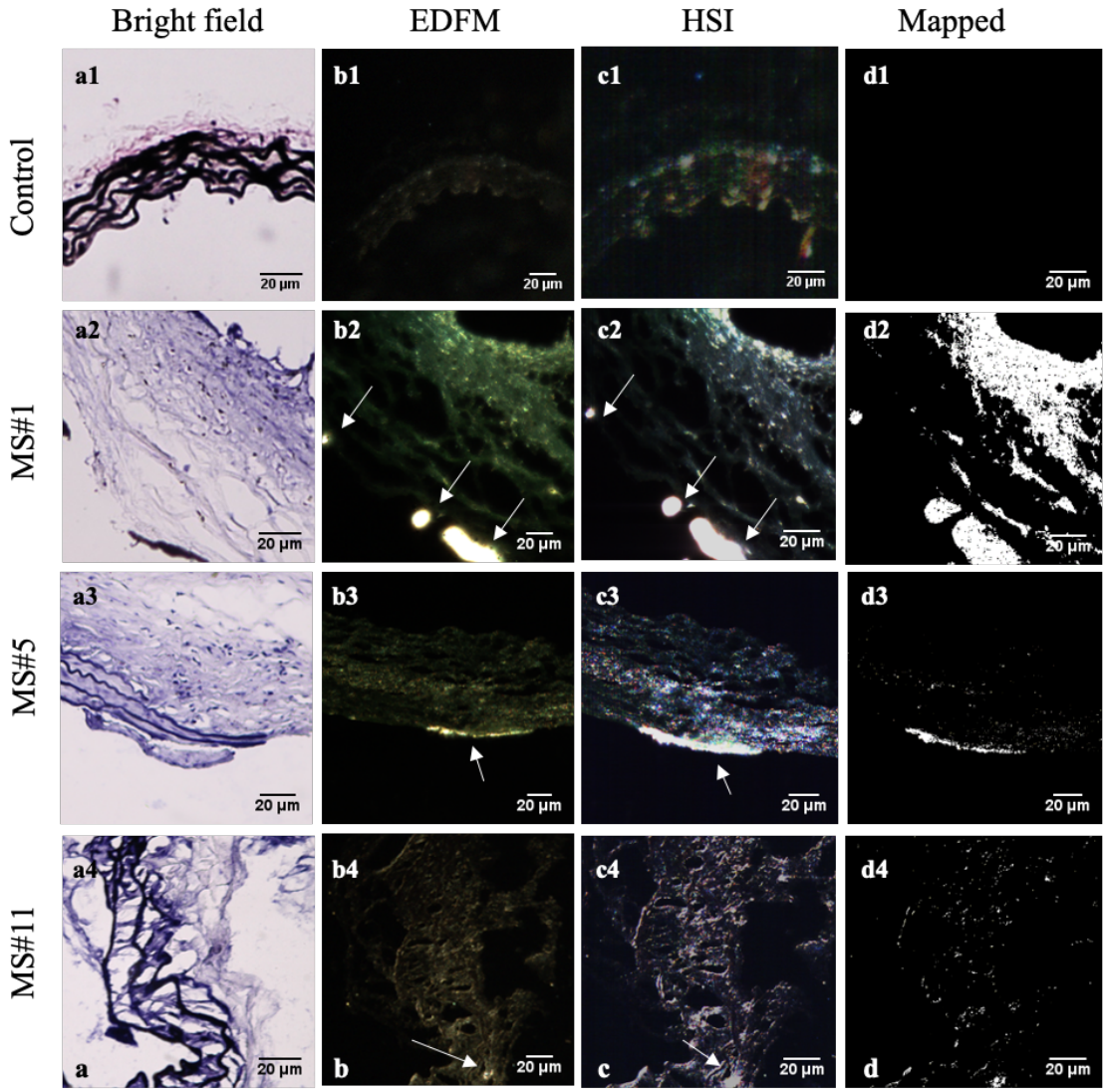


**Figure 5-5.** Hyperspectral mapping of suprarenal aorta tissue targeted by EL-AuNPs, rows from top to bottom correspond to suprarenal aortas with different levels of elastin damage within the aortic walls, from high to low, respectively. **a.** Different elastin degradation levels were found in the selected tissue samples; **b.** EDFM (40X) showed the existence of high contrast EL-AuNPs in the tissues denoted by the white arrows; **c.** HSI (40X) and **d.** Mapped images against their respective reference spectrum library generated with negative controls.

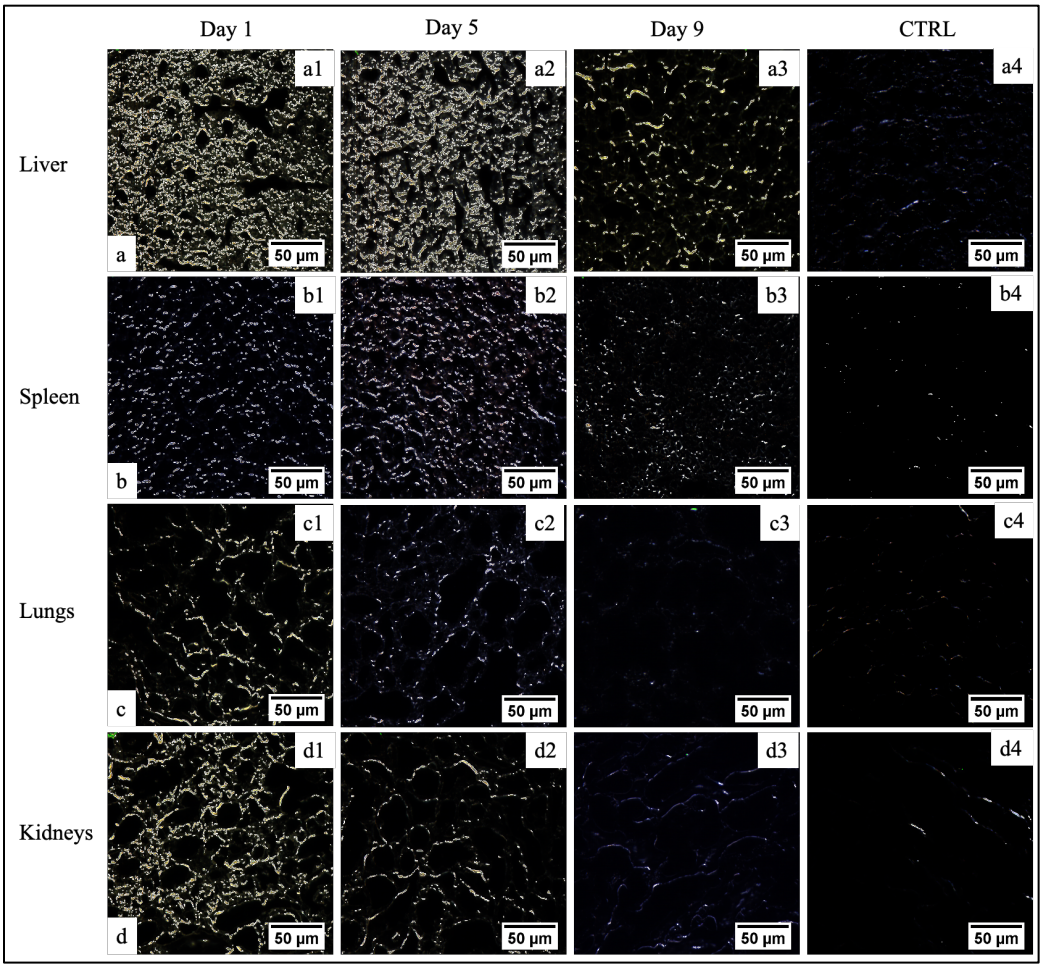


**Figure 5-6.** Hyperspectral mapping of liver, spleen, lungs, and kidneys visualizing the biodistribution of EL-AuNPs at day 1, 5 and 9 after the injection.

The biodistributions of the EL-AuNPs at day 1, 5 and 9 after the injection have been further quantified using ICP-MS. On day one, 1.70% of the given EL-AuNPs dose accumulated in the liver while 1.10%, 0.55% and 0.07% of the EL-AuNPs were found in spleen, lungs and kidneys, respectively. On day five, the EL-AuNPs in the liver was 0.59% of the given dose. There were 1.39%, 0.53%, and 0.07% of the given EL-AuNPs remained in the spleen, lungs, and kidneys, respectively. After 8 days of clearance, the number of the

EL-AuNPs in the liver and spleen decreased to 0.32% and 0.03 % respectively. The amount of the gold component in the lungs and kidneys were both below the detective limit.

**Ultrasound analysis of AAAs**

Ultrasound images of abdominal aortas were obtained before euthanasia. Healthy controls exhibited a relatively uniform inner diameter (Figure 5-7a1) while dilation in the AngII infused mice was most commonly observed at the suprarenal location (Figure 5-7a2-a4). Circumferential strains for all samples ranged from 3.44 to 12.82%. Circumferential strains of the healthy aortas were 16.08±2.40% (n=5) and were significantly decreased at the aneurysmal aortic regions of the AngII-infused mice. For aneurysms with a similar extent of dilation (MS#1, #5 and #11 with 92% dilation), the circumferential strains were 4.28±1.17%, 5.95±1.08%, and 9.60±1.05% respectively, suggesting the acute distensibility of the aneurysmal aortic wall was not necessarily related to the extent of chronic dilation (Figure 5-7b).

**Correlation of *ex-vivo* CT signal and burst pressure of the aorta**

The burst pressures for the samples harvested for *ex-vivo* study varied from 141.0 to 540.0 mmHg, while the burst pressure for healthy aortic controls was 566.5±30.4mmHg. The 3D micro-CT models of the aortas showed higher signal intensity at the suprarenal aortic regions of specimens having more server elastin damage and lower burst pressures, indicating that the accumulation of our EL-AuNPs was inversely correlated to the level of elastin damage and the load at failure (Figure 5-8a1-a3) while the age-matched control samples did not show any signs of EL-AuNPs accumulation (Figure 5-8a4). In order to establish a quantitative relationship between the signal and the ultimate burst pressure of

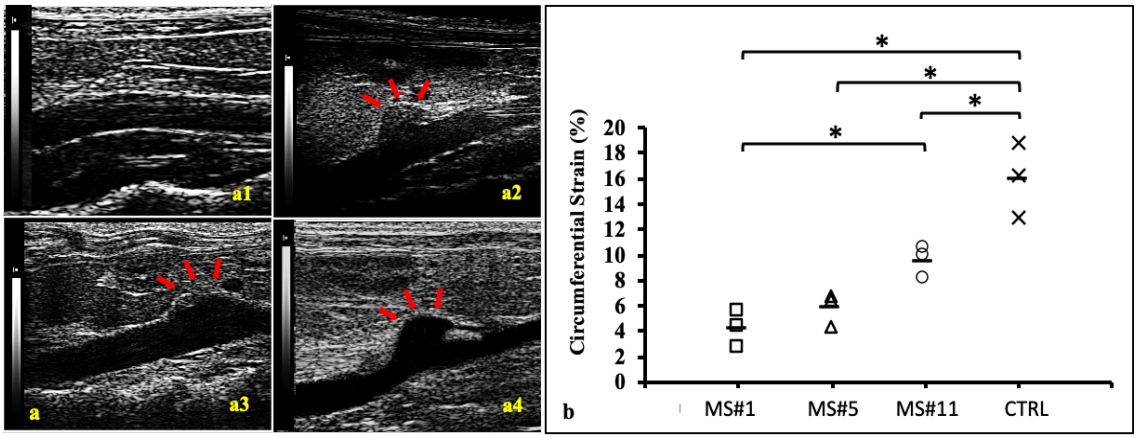


**Figure 5-7.** *In-vivo* ultrasound and circumferential strains. **a.** Representative B-mode in vivo ultrasound images of focalized aortic dilation indicated by red arrows; **b.** Circumferential Green-LaGrange strains throughout the cardiac cycle for three aneurysms with similar dilations (92%) but with different degrees of elastin damage. Ms#11 had minor aortic elastin damage and Ms#1 had severe aortic elastin damage. * $p<0.05$, solid line in each group represents the mean value.

the suprarenal aortas, the signals of the healthy aortic regions were used as negative controls and were subtracted from the total. For the age-matched control groups, the signal strength for all samples in the suprarenal region was 0. As the burst pressures of the suprarenal aorta decreased, indicating a weakening of the aorta, higher signals for EL-AuNPs were detected (Figure 5-8b). A power-law equation $y = 20+08x^{-3.586}$ was established with $R^2=0.9415$, where x represents the burst pressure and y represents the signal intensity, which demonstrated that the signal strengths given by EL-AuNPs had a strong negative correlation to the burst pressures of the aneurysmal tissues (Figure 5-8b)

whereas changes in aortic dilation ($R^2$=0.1932) or circumferential strain ($R^2$=0.3918) failed to show strong correlations to burst pressures (Figure 5-8c, 5-8d).

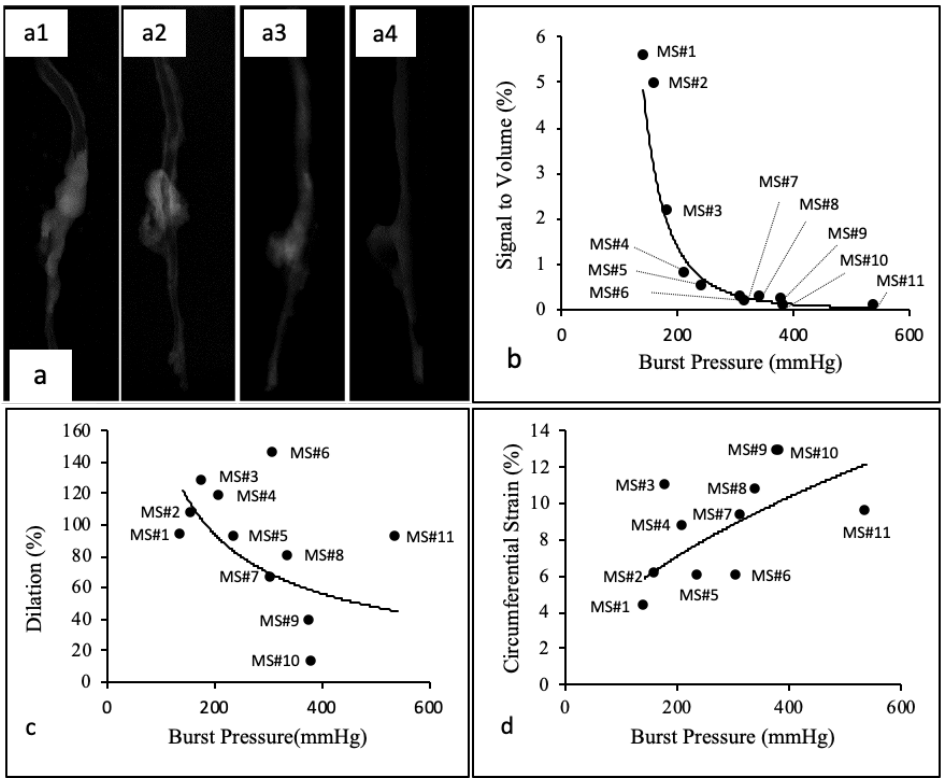


**Figure 5-8.** Representative reconstructed aorta models in attenuation mode and correlation between signal intensity, diameter increase, and burst pressure. **a.** 3D attenuation models for aneurysmal and control aortas with different elastin damage levels showing different suprarenal aortic signal intensity; **b.** A strong negative nonlinear correlation between signal intensity and burst pressure was found while **c.** dilation vs. burst pressure and **d.** the CSs vs. burst pressure was only weakly correlated with each other using the power-law.

### EL-AuNP distribution and the initial burst site defined in *ex-vivo* CT scans

The initial sites where suprarenal aortas started to rupture under pressurization were captured by a camera through visualization of the PBS supplemented with phenol red being

expelled at rupture site (Figure 5-9a arrows). 3D micro-CT data obtained from *ex-vivo* scans was displayed in the MIP mode, in which the lower-attenuation structures are not well visualized [293], in order to study the distribution of EL-AuNPs within the aneurysmal region (Figure 5-9b). Bright spots for EL-AuNPs in the reconstructed model could be correlated to where the first rupture occurred, suggesting that the weakest spots had the highest density of AuNP accumulation.

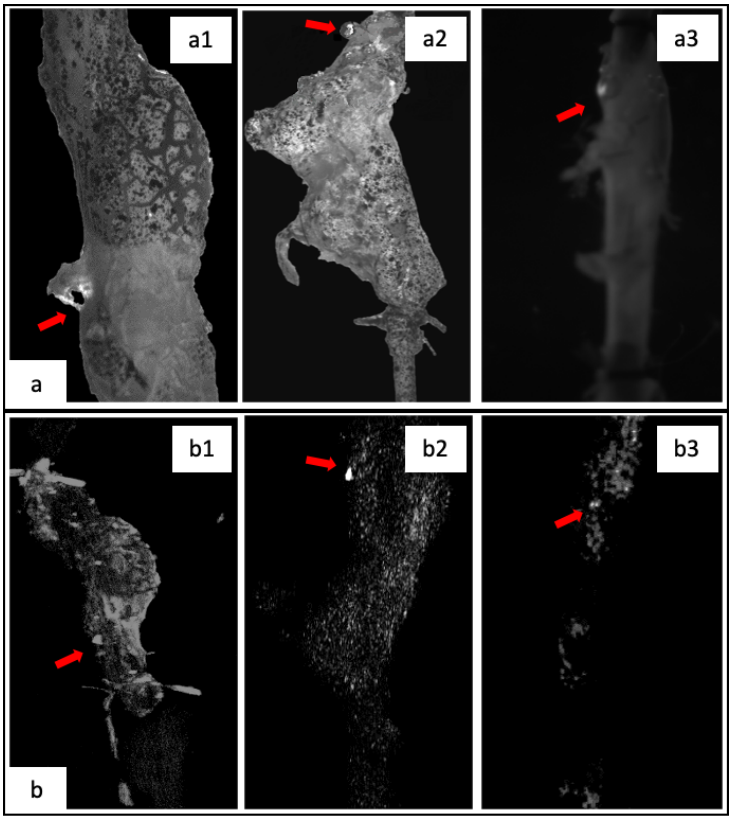


**Figure 5-9.** Representative burst pressure tests pictures and corresponding reconstructed aorta models in MIP mode. **a.** Burst pressure test showing the location on the aneurysmal wall where rupture is initiated under pressurization; **b.** For corresponding mouse aorta, the EL-AuNP induced signals were non-uniformly distributed within the aneurysmal segments. High-intensity spots correlate to the rupture sites.

**Correlation of *in-vivo* CT signal and biaxial mechanical properties of the aorta**

Two geometrical parameters, outer aortic diameter and aortic wall thickness, and two mechanical parameters, circumferential and axial stress, were measured and correlated to the AuNPs to tissue ratio using OLS regression (Figure 5-9). There was no correlation found between the outer aortic diameter and the AuNPs to tissue ratio while a slightly negative correlation was found between the aortic wall thickness and AuNPs to tissue ratio with $R^2$=0.5602. Strong positive correlations with AuNPs to tissue ratio were found in both circumferential stress ($R^2$=0.9375) and axial stress ($R^2$=0.7469).

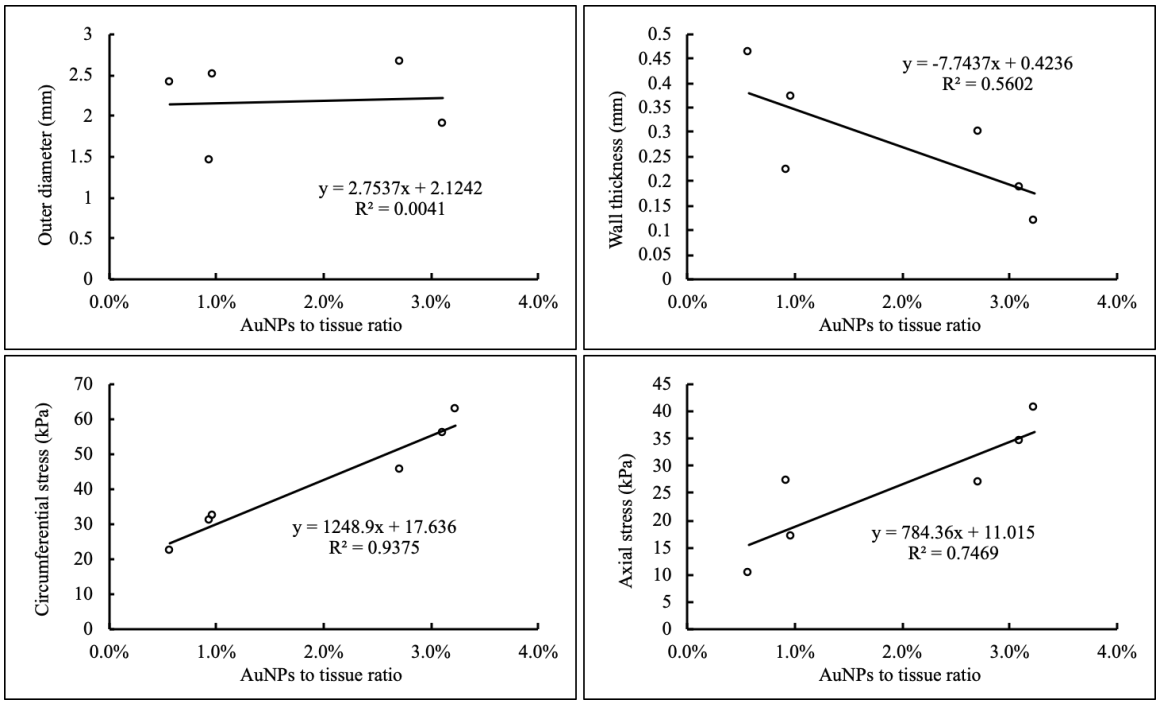


**Figure 5-9.** Correlations between different parameters measured and calculated from the biaxial mechanical testing and the AuNPs to tissue ratio.

## 5.4 Discussion

In this aim, we tried to develop a potential targeted contrast agent for CT imaging which will provide morphological information along with a better assessment of the rupture risk of AAAs. Nanoparticles have been used for the development of enhanced molecular imaging technologies targeting cancer cells [294]. AuNPs are commonly used due to their outstanding properties such as noncytotoxicity, excellent biocompatibility, ease of surface functionalization, strong light absorption, and scattering effects [294, 295]. Gehrmann, M. K. et al. reported using 50nm cmHsp70.1-conjugated AuNPs for imaging Hsp70 membrane-positive mouse tumor cells *in-vivo* [296]. Here, we used spherical gold nanoparticles with a final diameter of around 180 nm to target the AAAs. The increase in gold particle size from ~150nm to ~180nm after the antibody conjugation process indicated that we successfully conjugated the elastin antibody to the surface of the gold nanoparticles for achieving targeted delivery.

Suprarenal aortic aneurysms were then successfully initiated by systemically delivering AngII into LDLr (-/-) mice. AAAs were considered significant when the dilation of the aorta exceeded 1.5 times (i.e., 50% dilation) its normal external diameter [297]. Based on this criterion, some of the aortic dilations we found in the mice were not considered AAAs but at the initiating stage of AAAs. As reported by Trachet, B. et al., the incidence rate of AAAs in AngII infused mice was 56% [298]. Pathological features such as degradation of the elastic lamina and atherosclerosis were demonstrated by the histological study results. These features are consistent with what has been reported in the AngII infusion-induced AAA in the ApoE(-/-) mouse model [299], as well as in human

AAAs [300]. And our results showed that the diameter increase, elastin degradation level, and intraluminal atherosclerotic plaque formation in the suprarenal aortas vary among animals. Such variability was advantageous in this study because it enabled a wider spectrum fragmentation for correlation with AuNP accumulation.

To date, the targeting of AAAs for therapeutic and imaging purposes remains significantly challenging because of the limited number of viable targets and a relatively low hemodynamic residence time in the diseased aorta. Key pathological processes occurring within AAAs such as inflammation, vascular smooth muscle cell apoptosis, and even ECM remodeling have emerged as potential targets for nanoparticle-based diagnostics [215]. Shirasu, T. et al. reported a passive AAA targeting system using rapamycin nanoparticles. It was hypothesized in their study that the accumulation of nanoparticles was a result of micro-defects caused by inflammatory cell infiltration and ECM fragmentation [257]. For active targeting, macrophage targeting was reported for an MRI imaging with ultra-small superparamagnetic iron oxide (USPIO) and fluorine 18-labeled cross-linked iron oxide ($^{18}$F-CLOF) in AngII-infused ApoE (-/-) mouse model [220, 221, 223]. Klink, A. et al. [258] described the targeting of aortic adventitial ECM remodeling-related collagen in AngII-infused and TGFβ-neutralized C57BL/6 mice using paramagnetic/fluorescent micellar nanoparticles functionalized with a collagen-binding protein (CNA-35). All these previous targeting efforts focused on either inflammatory cells or collagen. Levels of inflammation and collagen remodeling vary with time and therefore cannot be used as a reliable surrogate for chronic aneurysmal rupture risk assessment.

On the other hand, the metabolic turnover of elastin is slow, with a half-life comparable to the human lifespan. Thus, unlike collagen fibers, the function of elastic fibers is not thought to depend on constant remodeling and turnover [301]. The adult elastic lamina does not remodel substantially within the timeline of aortic disease progression and the degradation of in the aneurysmal wall is a consistent feature of AAAs making it an ideal target for delivering nanoparticles. In this study, we successfully targeted gold nanoparticles to the aneurysmal site in AngII-infused LDLr (-/-) mice by conjugating them with antibodies that target only degraded-elastin as described previously [229]. Our results suggested that the targeting of our EL-AuNPs was both elastin-specific and damage-dependent as most of the EL-AuNPs were found attached to degraded elastin while sparing the healthy unimpaired aorta. Furthermore, the quantity of EL-AuNPs accumulated in the aneurysmal tissue was related to the extent of local elastin degradation which highlights altered biomechanical properties of the aortic wall leading to further disease progression and failure [45]. Thus, we tested if EL-AuNPs targeting could improve imaging and could be used as a potential non-invasive AAA rupture risk stratification tool.

Non-invasive abdominal ultrasound is commonly used in the diagnosis and monitoring of AAAs, mainly providing morphological information to evaluate disease progression. Others reported that high-frequency ultrasound could be used to assess aortic wall strain as part of biomechanical analysis in murine models [302, 303]. Our *in-vivo* abdominal ultrasound results indicated a reduction of circumferential wall strain throughout the cardiac cycle in the aneurysmal suprarenal aorta compared to the healthy aorta and these findings are consistent with the results from previous studies. An increasing

trend of EL-AuNP accumulation was found while the wall strain decreased. Our results demonstrate that there could be a correlation between EL-AuNP accumulation and overall biomechanics of the aneurysmal tissue.

Burst testing, a direct method of identifying rupture pressure and location, supported the correlation between the signal given by targeted EL-AuNP and the rupture potential of aneurysms [304]. We have used a well-established AngII model to assess AAAs. Aneurysms in this model, however, do not spontaneously rupture, so all burst pressure testing was performed on explanted aortas for correlation of rupture risk. Using a power model, a strong negative correlation was found between EL-AuNPs in the *ex-vivo* CT scans and the pressures at which a AAA will burst. Since the aortic diameter is the primary clinical criteria used for surgical intervention, it was interesting to note that no immediate pattern emerged correlating burst pressure to the extent of dilation in our AAAs. Although many large AAAs failed at lower pressures, others withstood much higher pressures. Incidentally, most AAAs in our study failed at or around the necking region and a few failed at the site of the branches. Likewise, aneurysms with similar dilation were shown to experience varying levels of circumferential strain throughout the cardiac cycle. Thus, the signal intensity of EL-AuNPs measured by *ex-vivo* CT shows a more meaningful relationship with the rupture risk of AAAs than does the increase in diameter or a decrease in circumferential strain.

This finding was further confirmed in the *in-vivo* imaging study. Targeted *in-vivo* imaging is more challenging because the AAAs usually locate deeply in the body covered with connective tissues. Also, the unbonded EL-AuNPs in the blood pool can influence the

targeted signal quantification. In order to minimize the influence of the non-specific signal from the blood pool, we allowed the EL-AuNPs to circulate for 24 hours to achieve sufficient targeting while most of the untargeted nanoparticles would be cleared out from the blood. We found an increase of contrast at the suprarenal aortic area in the *in-vivo* CT scan which again confirmed the targeting of the EL-AuNPs to the aneurysmal site. Moreover, we found that the number of the AuNPs accumulated in the aneurysmal tissue is not correlated to size of the aneurysm but was slightly negatively correlated to the thickness of the aortic wall. AuNPs to tissue ratio was positively correlated to both circumferential and axial stress suggesting the accumulation of AuNPs could be used as an indicator of stresses in the aneurysmal tissue. Since the high stresses in the aneurysms make them more tend to rupture, the AuNPs have the potential to assess the rupture risk of AAAs from *in-vivo* CT imaging.

The variability of the animal model used in the current work provides a tremendous strength in assessing our micro CT-based EL-AuNPs approach to AAA rupture potential. Variations in EL-AuNP distribution were found not only among different suprarenal aortic segments but also within the same aorta, suggesting variable degrees of elastin damage within the aneurysm and the possible existence of a 'weak point' where the rupture of the aneurysm initiates. Thus, our data suggest that an extent ECM degradation could be a more meaningful way to look at which patients are more prone to rupture and need immediate attention.

Moreover, the biodistribution of the EL-AuNPs in the major organs was studied to assess their clearance rate. Contrast agents should be cleared out of the system within a

reasonable time to ensure the safe application for the patients. Sonavane, G. et al. have reported the biodistribution of AuNPs with different sizes in mice 24 hours after the injection [305]. For 200nm EL-AuNPs, they found the highest concentration of gold in the liver followed by spleen, lung, and kidneys. Similarly, according to our results, the EL-AuNPs (~170nm) were mainly found in the livers and spleens, followed by kidneys and lungs on all three time points after the injection. In general, the total number of EL-AuNPs in the system decreased as the time goes by. And most of the EL-AuNPs were cleared out of the system eight days after a working dose injection for imaging. The results indicated that the EL-AuNPs were successfully cleared out of the system even in an animal model that presented compromised liver functions [306]. Thus, our EL-AuNPs are promising to be translated into a safe clinical use.

### 5.5 Conclusion

An AngII infusion LDLr (-/-) mouse model provided us with AAAs at different stages and having different biological and biomechanical properties. Degradation of elastin led to a decrease in aortic wall strain and a decrease in burst pressures in the aneurysmal aorta. EL-AuNPs enabled visualization of the degraded elastin in AAA sites so that the quantity of AuNPs could be used as a marker to predict the rupture risk and rupture sites for AAAs. This approach is highly advantageous because small and pre-aneurysmal tissues would likely demonstrate elastin damage prior to ultrasound diagnostics. Thus, such degraded elastin-targeting nanoparticles have the diagnostic potential as a sensitive noninvasive AAA targeting contrast agent for CT imaging.

# 6. SPECIFIC AIM 3: TO INVESTIGATE WHETHER ELASTIN ANTIBODY CONJUGATED PGG LOADED NANOPARTICLES CAN BE TARGETED TO AAAS IN AN ANGII MOUSE MODEL AND WHETHER THEY STOP THE AAA PROGRESSION AND RESTORE THE HEALTHY FUNCTION OF THE AORTIC WALL BY REPAIRING ELASTIN

## 6.1 Introduction

AAA patients can be currently treated with surgical interventions or conservative methods depending on the AAA status evaluated by its geometrical information and the patient's condition. Although surgical repair can effectively help patients who have big or ruptured AAA, the risk of the operation process and post-operation complications keep the perioperative mortality high. Pharmacotherapy is an ideal choice for AAA patients who are not recommended to be treated surgically. Even though to date, there is no pharmacotherapy available on the market, potential pharmacotherapy for AAA that focused on how to inhibit the degradation of ECM and maintain the integrity of the aortic vascular wall has been wildly studied.

As described in chapter 2, many reported drugs are effective in preventing AAA progression by inhibiting the MMP activity, stabilizing and regenerating the damaged elastin lamina in the aneurysmal vascular wall in animal models. However, these drugs did not show effects on stopping nor reversing the human AAA progression [307-310]. In order to develop a pharmacotherapy that can effectively and safely work in AAA patients, it is important to understand human AAA pathology. Various inflammatory mediators that can

activate pro-inflammatory signaling pathways, such as TNF-α and MCP-1, are involved in the pathogenesis of AAA by causing and maintaining the inflammatory response. Proinflammatory signaling pathways, in turn, activate ECM degradation enzymes, such as MMP-9 and MMP-2, and simultaneously reduce the expression of ECM synthetic enzymes, such as LOX, thereby causing an overall loss of elastic fibers [180, 311]. It has been established that elastin degradation is a primary cause of AAA progression [312]. The regression of elastin fibers in the aortic wall and restoration of normal arterial architecture would be preferable for treating AAA patients regardless of the aneurysm size.

PGG is a tannic acid derivative that has gained a lot of scientific attention recently because of its inherent ability to stabilize elastin by establishing a strong cohesive bond with the elastin in the ECM of the blood vessel. It can be used to provide an enhancement in vascular biomechanical properties and increased enzymatic degradation resistance [313]. Although tannic acid was also reported to have the same elastin binding ability as PGG, PGG was found to be more stable and had less cytotoxicity; thus, it was more favorable as an elastin-stabilizing agent [314].

Medial lamellar degradation in AAAs due to a combined effect of VSMC apoptosis, increased inflammatory responses and oxidative stress, and disruption of tissue enzymatic homeostasis can result in a reduction in elastin content and crosslinking [315]. Therapeutic traits of PGG such as elastin stabilization, inhibition of MMPs, and antioxidant capacity make it an attractive pharmacological option for AAA patients. *In-vivo* stabilization of infrarenal aortic elastin by periadventitial PGG application or systemic PGG-NPs administration in $CaCl_2$-mediated rat AAA model has shown to preserve the integrity of

the elastic lamellae, thus, prevent early AAA formation [200, 313]. Moreover, immediately after a localized elastase infusion in the porcine aorta, the intraluminal application of PGG in the elastase treated aortic segment was also reported to inhibit early AAA formation [316]. PGG-NPs that can successfully target to degraded ECM will achieve the controlled release of PGG to the AAAs and be a potential pharmacotherapy to stop and reverse the AAA progression.

It is important to test the functionality of PGG in stabilizing the degraded ECM in an AngII infused mouse model. Comparing to the previously studied $CaCl_2$-mediated rat AAA model and elastase-mediated mouse AAA model, which were developed based on localized surgical aortic damage, the aneurysms in AngII infused mouse model were induced using a systemic method, which resembles human aneurysm formation. It will offer a fresh perspective on the functionalities of PGG-NPs as a novel AAA treatment.

## 6.2 Materials and methods

### Preparation of blank, DiR loaded and PGG loaded BSA NPs

Blank BSA NPs (BLN-NPs) were prepared to be used as a control for the study by using a coacervation method described previously [19]. Briefly, 250 mg of BSA (Seracare, Milford, MA) was dissolved in 4 mL of DI water. 3mg glutaraldehyde (EM grade 70%, EMS, PA) was added into the BSA solution during stirring as a crosslinker. After an hour of stirring under room temperature, the mixture was added dropwise to 24 mL of ethanol under continuous sonication (Omni Ruptor 400 Ultrasonic Homogenizer, Omni International Inc, Kennesaw, GA) on ice for 30 minutes. The obtained BLN-NPs were

obtained by centrifugation at 6,000 rpm for 10 minutes and washed with water for three times by resuspension.

1, 1-dioctadecyl-3, 3, 3, 3- tetramethylindotricarbocyanine iodide (DiR) dye (PromoCell GmbH, Heidelberg, Germany) loaded BSA NPs (DiR-NPs) were obtained for studying *in-vivo* targeting using the procedure described above with modifications. 250 mg of BSA was dissolved in 4ml of DI water. 2.5 mg of DiR dye was dissolved in acetone first and was then added to the BSA solution. 10.5 mg glutaraldehyde was added as a crosslinker during stirring. After an hour of stirring under room temperature, the mixture was added dropwise to 24 mL of ethanol under continuous sonication on ice for 30 minutes. The obtained DiR-NPs were obtained by centrifugation at 4,000 rpm for 10 minutes and washed with water for three times by resuspension.

PGG-loaded NPs (PGG-NPs) were prepared for the treatment study using the modified version of the procedure described above. 250 mg of BSA was dissolved in 4 mL of DI water. 125mg PGG was dissolved in 400 µl of dimethyl sulfoxide and added slowly to the BSA solution under stirring. 3mg glutaraldehyde was then added as a crosslinker. After an hour of stirring at room temperature, the mixture was added dropwise to 24 mL of ethanol under continuous on ice for 30 minutes. PGG-NPs were obtained by centrifugation at 6,000 rpm for 10 minutes and washed with water by resuspension.

**Conjugation of NPs with degraded elastin antibodies**

All NPs were conjugated with homemade degraded elastin antibodies before being used in the animal study as described previously [19]. Briefly, 10 mg of NPs (blank, DiR

loaded, or PGG loaded) were PEGylated with 2.5 mg α-maleimide-ω-N-hydroxysuccinimide ester poly (ethylene glycol) (mPEG-NHS, M.W. 2000, Nanocs, NY, U.S.A.) at room temperature for one hour under gentle vortexing. 68 μg of Traut's reagent (G-Biosciences, Saint Louis, MO) was used for thiolation of 20 μg of a homemade elastin antibody, and the mixture was incubated in PBS for an hour at room temperature under gentle vortexing. Thiolated antibodies were added to the PEGylated NPs and incubated overnight at 4 ºC on a slow rocker for conjugation.

***In-vivo* study in an AngII infusion induced mouse model**

Forty-two male LDLr -/- mice (2 months of age, on a C57BL/6 background) were obtained from the Jackson Laboratory (Bar Harbor, ME) for investigating the effects of the NP treatment on the aneurysms. Aneurysms were induced by systemic infusion of AngII (Bachem Americas, Torrance, CA) in combination with a diet with saturated fat (21% wt/wt) and cholesterol (0.2% wt/wt; catalog no. TD88137; Harlan Teklad) throughout the whole study. Osmotic pumps (model 2004; Alzet, Cupertino, CA) filled with AngII were implanted subcutaneously to the mice. 2% to 3% isoflurane inhalation was used as anesthesia during the surgery. The osmotic pump released AngII consistently for 4 weeks at a rate of 1500ng/kg/min. Disease progression was monitored with Fujifilm VisualSonics Vevo 2100 ultrasound machine (Fujifilm VisualSonics, Toronto, ON, Canada) by utilizing a linear array probe (MS-550D, broadband frequency 22 MHz -55 MHz).

For the targeting study, 10mg/kg animal weight of anti-elastin antibody (EL) conjugated DiR-NPs were injected intravenously to three mice after the 4-week infusion of AngII. These mice were euthanized 24 hours later, and the aortas were harvested for

further analysis. For treatment study, twelve mice were treated with EL conjugated BLN-NPs while another twelve mice received EL conjugated PGG-NPs, both at a dose of 10mg/kg animal weight, biweekly on week 4 and week 6 via the tail vein. Fifteen mice that did not receive any kind of treatment were used as control. Three of the control mice were euthanized at week 4; All other mice were euthanized at week 8 as shown in the timeline graph (Figure 6-1). Blood was collected via a heart puncture and organs were harvested after being perfused with saline for further analysis. All animal use protocols for the study were approved by the Institutional Animal Care and Use Committee (IACUC) at Clemson University.

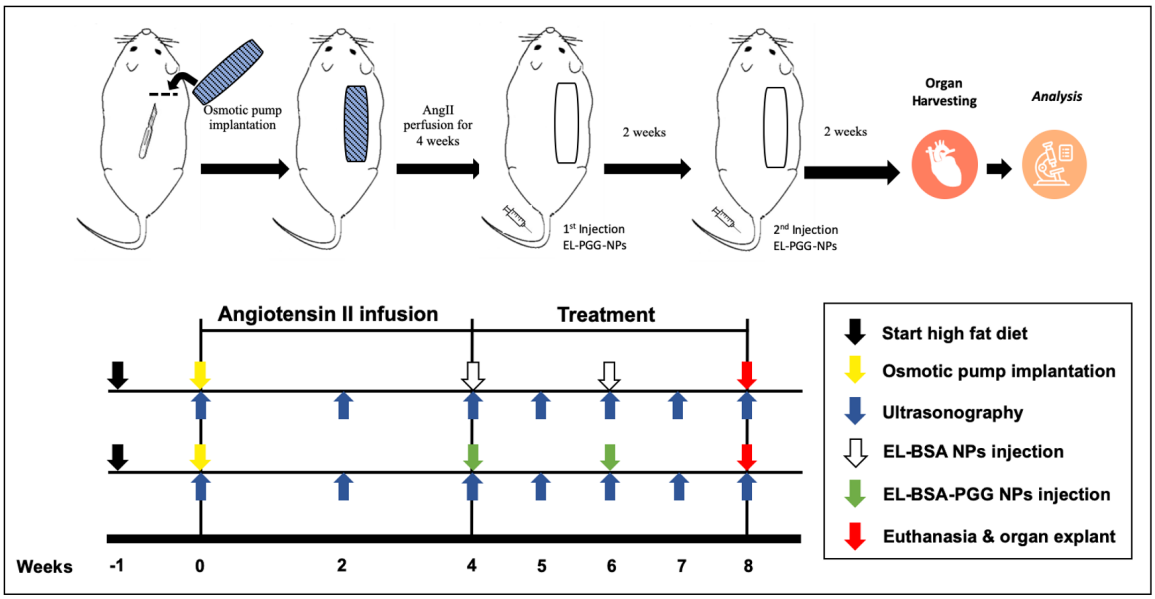


**Figure 6-1.** Schematic representation of the study design.

### Ultrasound analysis of AAAs

The ultrasound system, Fujifilm VisualSonics Vevo 2100 (Fujifilm VisualSonics, Toronto, ON, Canada), was used for monitoring percent dilation and to assess the

circumferential strain throughout the cardiac cycle and PWV of the aneurysm. The animals were placed in a supine position on the imaging table and were maintained under anesthesia by inhaling 2% to 3% isoflurane during imaging. Heart rate and body temperature of the mice were carefully monitored during the imaging process. Suprarenal aortic inner diameters were measured using the built-in ultrasound software on the basic-mode ultrasound images. The dilation was calculated using the equation given below,

$$Dilation\ (\%) = (\overline{D}_L - \overline{D}_H)/\overline{D}_L \times 100$$

where $\overline{D}_H$ represents the mean inner diameter of the suprarenal aorta before the surgery and $\overline{D}_L$ is the mean inner diameter after surgery at the time points mentioned above.

Sagittal and transverse images for both healthy and aneurysmal aortas were obtained in motion mode. Systolic and diastolic diameters were measured and recorded at three different regions on each aneurysm or parent vessel using the built-in ultrasound software. The diastolic-to-systolic circumferential Green-LaGrange strains and the percentage change of the circumferential strains throughout the study were calculated assuming axial symmetry using the two equations given below,

$$CS\ (\%) = (1/2)((\overline{D}_{sys}/\overline{D}_{dia})2 - 1) \times 100 \quad (1)$$

$$CS\ (\%) = (CS_L - CS_H)/CS_L \times 100 \quad (2)$$

where $\overline{D}_{sys}$ represents the inner systolic aortic diameter, $\overline{D}_{dia}$ represents the inner diastolic aortic diameter, $CS_H$ represents the circumferential strain of the suprarenal aorta before the surgery and $CS_L$ is the circumferential strain after surgery at the time points mentioned above.

PW Doppler mode was used to measure the blood flow at the beginning and the end of the suprarenal aortic lumen prior to each PWV acquisition. All PW Doppler measurements were performed at a PRF of 20 kHz and a 45° incidence angle. Throughout the acquisition, the ECG for each mouse was monitored and recorded. PWV at each time point and the change of PWV throughout the study were then calculated with the two equations below,

$$PWV = d/(t_2 - t_1) \quad (1)$$

$$PWV\ Change\ (\%) = (PWV_L - PWV_H)/PWV_L \times 100 \quad (2)$$

where d represents the distance between the beginning and end of the suprarenal aorta, $t_1$ is the time when pressure wave arrives at the beginning point and $t_2$ is the time when pressure wave arrives at the endpoint referenced to the R wave of the ECG, and $PWV_L$ represents the PWV of the suprarenal aorta before the surgery and $PWV_H$ is the PWV after surgery at the time points mentioned above.

**Systemic interferon-gamma (IFN-γ) levels**

Blood was drawn via a heart stick with a 1 mL syringe. After allowing 30 min for clotting, the blood was centrifuged at 14,000 rpm for 10 min and the serum was collected. Mouse serum was examined for IFN-γ using a commercial mouse ELISA kit (Invitrogen, Carlsbad, CA) per manufactural protocol.

**Histological analysis of the aneurysms**

Frozen aortas were embedded in OCT compound (Sakura Finetek, Torrance, CA) after being washed in DI water. The blocks were allowed to stay in -80ºC for overnight and

then sectioned per standard procedures. Five-micrometer sections were mounted on positively charged glass slides. Slides were placed in 100% pre-cooled acetone (Fisher Science Education, Nazerath, PA) for 10 minutes to fix the sections. Subsequently, the slides were rinsed with tap water for 5 minutes to remove the OCT compound and stained with hematoxylin and eosin (H&E) for tissue morphology and VVG for elastic fibers. Some fresh samples were imaged directly after removing the OCT compound and imaged with a fluorescent microscope to visualize the DiR-NPs targeting within the tissue.

### *In-situ* zymography

*In-situ* zymography was performed on 5μm cryosections to evaluate MMP activity in the suprarenal aortic tissue samples. All the cryosections were rinsed with tap water for 5 minutes to remove the OCT. Each section was treated with 200μL of the mixture of 0.2mg/mL DQ-Gelatin (Invitrogen, Eugene, OR) in developing buffer and then incubated at 37°C for two hours. After being washed in DI water for 5 minutes, all sections were stained with DAPI (Life Technologies, Carlsbad, CA) for 5 mins and an EVOS$^{TM}$ XL cell imaging system (Invitrogen, Bothell, WA) was used to capture images of the samples.

### Immunohistochemistry (IHC) for macrophages

All the cryosections were rinsed with PBS 3 times for 5 minutes per time to remove the OCT compound. The sections were firstly treated with 3% hydrogen peroxide under room temperature for 10 minutes to block the endogenous peroxidase activity. Then, the unspecific binding sites on the sections were blocked with background buster (Innovex Biosciences, Richmond, CA) under room temperature for 30 minutes. The sections were

incubated with the primary antibodies (anti-CD68 and anti-CD80) at 4°C overnight. An avidin-biotin complex method (Vector, Burlingame, CA) was used to detect and amplify the target signal and the staining was completed using a DAB kit (Vector, Burlingame, CA). Slides were counterstained with hematoxylin.

**Flow cytometry**

The spleens and thymus of the mice from BLN-NPs, PGG-NPs, and control groups were collected, minced, and meshed on 70 μm filters. Immunofluorescence staining was performed as described in previous studies [201, 317]. Briefly, cells were incubated with Fc block solution (purified anti-mouse CD16/CD32, clone 2.4G2, BD Biosciences) for 15 minutes at room temperature to prevent non-specific binding. For cell surface markers, cells were incubated with the fluorescently conjugated antibody with CD68, APC anti-CD68 (clone FA-11) (BioLegend, San Diego, CA) in the dark for 30 minutes at 4ºC. For intracellular cytokine TGFβ-1 staining, cells were permeabilized with fix/permeabilization buffer (eBiosciences, San Diego, CA) for 15 minutes before antibody PE anti-TGFβ1 (clone TW7-2089) (BioLegend, San Diego, CA) staining. After the extensive washing of cells in FACS buffer, the cytometric acquisition was performed using the Attune NxT flow cytometer (Thermo Fisher Scientific, Waltham, MA). Data analysis was performed using FlowJo (TreeStar, Ashland, OR) software. For gating, lymphocytes were identified using FSC and SSC gating, and signals were selected based on SSC-A/H and FSC-A/H characteristics. Then $CD68^{+}$ or $TGF\beta1^{+}$ cells were selected on the base of their expression level. Data are the representative of triplicate of repetition twice.

**Quantitative polymerase chain reaction (qPCR)**

Suprarenal aortas were homogenized and lysed in TRIzol™ (Invitrogen, Carlsbad, CA) for mRNA extraction. mRNAs were isolated per manufacturer's protocol. The quality of the mRNA extracted was confirmed with the A260/A280 ratio as measured by a BioTek Synergy 2 plate reader (BioTek, Winooski, VT). Primers were designed for obtaining cDNA copies of MMP-2, TIMP-1, TIMP-2, LOX, elastin (ELN), and housekeeping genes actin-beta (ACTB) and peptidylprolyl isomerase A (PPIA) (sequences are shown in Table 6-1) and obtained from Integrated DNA Technologies™ (Coralville, IA). cDNA was obtained via reverse transcriptase (RT)-PCR using an OneStep RT-PCR kit (Qiagen, Valencia, CA) as per manufacturer's protocol. The qPCR was performed in the following sequence using a Rotor gene qPCR machine (Qiagen, Valencia, CA): 15 secondes at 94ºC, 30 seconds at 60ºC, and 30 seconds at 72ºC for 40 circles. Gene expression in each sample was normalized to the expression of the housekeeping genes and compared to the control group using the $2^{-(\Delta\Delta T)}$ cycle threshold (Ct) analysis as follow:

$$\Delta\Delta Ct = (Ct_{\text{Target gene}} - Ct_{\text{Reference gene}})_{\text{Experimental}} - (Ct_{\text{Target gene}} - Ct_{\text{Reference gene}})_{\text{Control}}$$

**Aortic biaxial mechanical testing and data analysis**[2]

The mechanical properties of aortic aneurysmal tissues and controls were tested at the University of South Carolina (UofSC) as described in Chapter 5. No more than 48 hours passed between animal sacrifice and mechanical testing. Aortas were mounted to a custom-

[2] Section prepared by John F. Eberth, PhD and Shahd Hasanain, BS

**Table 6-1.** Primers designed for qPCR

| | | |
|---|---|---|
| MMP-2 | Mouse MMP2_FWD | AACGGTCGGGAATACAGCAG |
| | Mouse MMP2_REV | GTAAACAAGGCTTCATGGGGG |
| TIMP-1 | Mouse TIMP1_FWD | GGCATCTGGCATCCTCTTGT |
| | Mouse TIMP1_REV | TTAGCATCCAGGTCCGAGTTG |
| TIMP-2 | Mouse TIMP2_FWD | TATCTACACGGCCCCCTCTT |
| | Mouse TIMP2_REV | TCCCAGGGCACAATGAAGTC |
| ELN | Mouse ELN_FWD | CCACCTCTTTGTGTTTCGCTG |
| | Mouse ELN_REV | ACCCAAAGAGCACACCAACAAT |
| LOX | Mouse LOX_FWD | ACGGCTTGTGTAACTGCAAAC |
| | Mouse LOX_REV | TCTGGGAAAGCGCACAGAG |

designed biaxial testing rig. The details for this device and biaxial testing procedures can be found in Lane et al. 2020a and 2020b [291, 292]. Briefly, this test rig is equipped with a thin-beam loaded cell (LCL-113G; Omega Engineering), pressure transducer (PX409; Omega Engineering), RS-232 infuse/withdraw syringe pump (AL-1000; World Precision Instruments), motorized linear actuator (Z825B; Thorlabs), and K-Cube motor controller (KDC101; Thorlabs). All components had PC USB interface through a custom-written LabView code used to gather synchronous measurements while controlling pumps and

actuators. The testing chamber was filled with warm PBS solution to maintain hydration throughout testing and PBS was flushed through the vessel lumen and device tubing to remove bubbles. The unloaded outer diameter ($D_o$) and length ($L$) were recorded using digital calipers. The artery then underwent five preconditioning cycles consisting of pressurization from 10 to 160 mmHg and axial stretching to a deformed length ($\ell$) at, and 5% above and below, the pressurization force-invariant axial stretch ratio, deemed the *in-vivo* axial stretch.

For data acquisition, the artery was extended to the three axial stretch ratios described previously before undergoing pressurization cycles (0–120 mmHg) with simultaneous force and outer diameter measurements at 10 mmHg pressure increments. Data was recorded in triplicate and the average and standard deviations of these tests reported. Primary continuous data collection consisted of pressure ($P$), deformed outer diameter at the peak bulge location ($d_o$), axial force ($f$), and axial stretch ratio ($\lambda_z$). Then vessels were pressure fixed by replacing luminal PBS with 4% paraformaldehyde solution and re-inflated to 100 mmHg in the axially extended state for 4 hours. In the deformed but fixed state, micro-Computed Tomography Imaging (Quantum GX Micro-CT Imaging System; PerkinElmer) was used to measure the deformed inner diameter. This step was necessary due to the lack of transparency of these calcified and heterogeneous tissues. Measurements consisted of an average of 4 locations along the circumference of the aneurysm bulge and were processed using Fiji-ImageJ.

Assuming axial symmetry and incompressibility, the inner diameter is calculated from,

$$d_i = 2\sqrt{\frac{d_o^2}{4} - \frac{V}{\pi \ell}} \tag{5}$$

where $V$ is the volume measured using a combination of micro-CT and biaxial testing.

From the primary data collection described above, the mid-wall circumferential and axial stretch ratios are calculated from

$$\lambda_\theta = \frac{d_i + d_o}{D_i + D_o}, \quad \lambda_z = \frac{\ell}{L} \tag{6}$$

where $D_i$ is the unloaded inner diameter.

The mean circumferential and axial stresses are then calculated from

$$\sigma_\theta = P\frac{d_i}{d_o - d_i}, \ \sigma_z = \frac{f}{\pi\left(d_0^2/4 - d_i^2/4\right)} \tag{7}$$

and the lumen area compliance from

$$c = \frac{\pi}{4}\frac{\Delta d_i^2}{\Delta P}, \tag{8}$$

where $\Delta P$ is the change from diastolic to systolic transmural pressures (80 to 120 mmHg) and $\Delta d$ the change in inner diameter at these pressures.

In general, discrete data were analyzed at a common pressure and in vivo axial stretch ratio unless otherwise noted.

### Statistical analysis

The data are reported as the mean ± standard deviation. Data from the same group at different time points were analyzed by paired T-test. Data from different groups were analyzed by one-way ANOVA followed by Tukey's HSD as a post-hoc test.

## 6.3 Results

### AngII infusion induced mouse model and in-vivo targeting study

After four weeks of AngII infusion, aneurysms with different sizes were found at the suprarenal region of the mice. According to the ultrasound diameter measurements on week four, some aortic dilations were less than 50%, which didn't meet the diagnostic standard for AAAs (part of the data presented). To bestow the study more clinical significance, we focused on mice with dilation of more than 50% at the suprarenal aorta for further study.

For studying the *in-vivo* targeting of the nanoparticle carrier, DiR-NPs were delivered systemically via tail vail and allowed to circulate for 24 hours. The aortas of the mice were explanted and imaged *ex-vivo* using the IVIS Lumina imaging system (PerkinElmer, Branford, CT) to visualize the DiR-NPs signal (Figure 6-2). According to the IVIS images (Figure 6-2 a2 and a3), the suprarenal region of the mice aortas where the aneurysms were found (Figure 6-2 a1) showed high fluorescent signal exclusively, indicating the accumulation of the DiR-NPs in the aneurysmal tissue. Further histological analysis showed that the DiR-NPs appeared at the sites where degraded elastin was displayed in the VVG staining (Figure 6-2 b and c). These results confirmed that our nanoparticle carrier could successfully reach and accumulate in the aneurysmal tissue by

targeting the degraded elastin in the ECM. These nanocarriers could be used for targeted drug delivery to stabilize the ECM and stop the progression of the aneurysm.

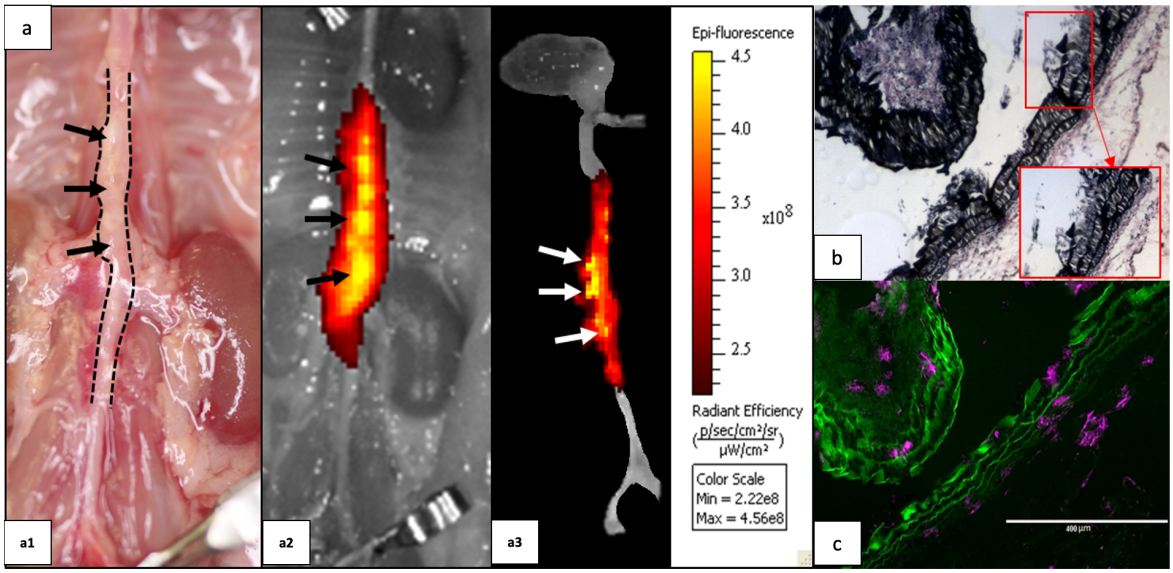


**Figure 6-2.** DiR-NPs targeting in AngII mice model. **a.** Overall targeting in the aorta; **b.** VVG staining indicating sites of degraded elastin; **c.** Fluorescent imaging of the counterpart visualizing DiR-NPs distribution within the tissue.

**The influence of PGG treatment in aortic dilation percentage**

All the mice that were used in the treatment study showed similar percentages of dilation when the AngII infusion was finished. According to the average inner diameters of aneurysms at week four measured and calculated from *in-vivo* abdominal ultrasound, all three groups (n=5) had a more than 100% diametric increase during the AngII infusion. After four more weeks (2 injections) of treatment, only in the PGG-NPs group, it has been found that the size of the aneurysms became smaller. The dilation percentages for aneurysms in the BLN-NPs group and the control group kept increasing even without the

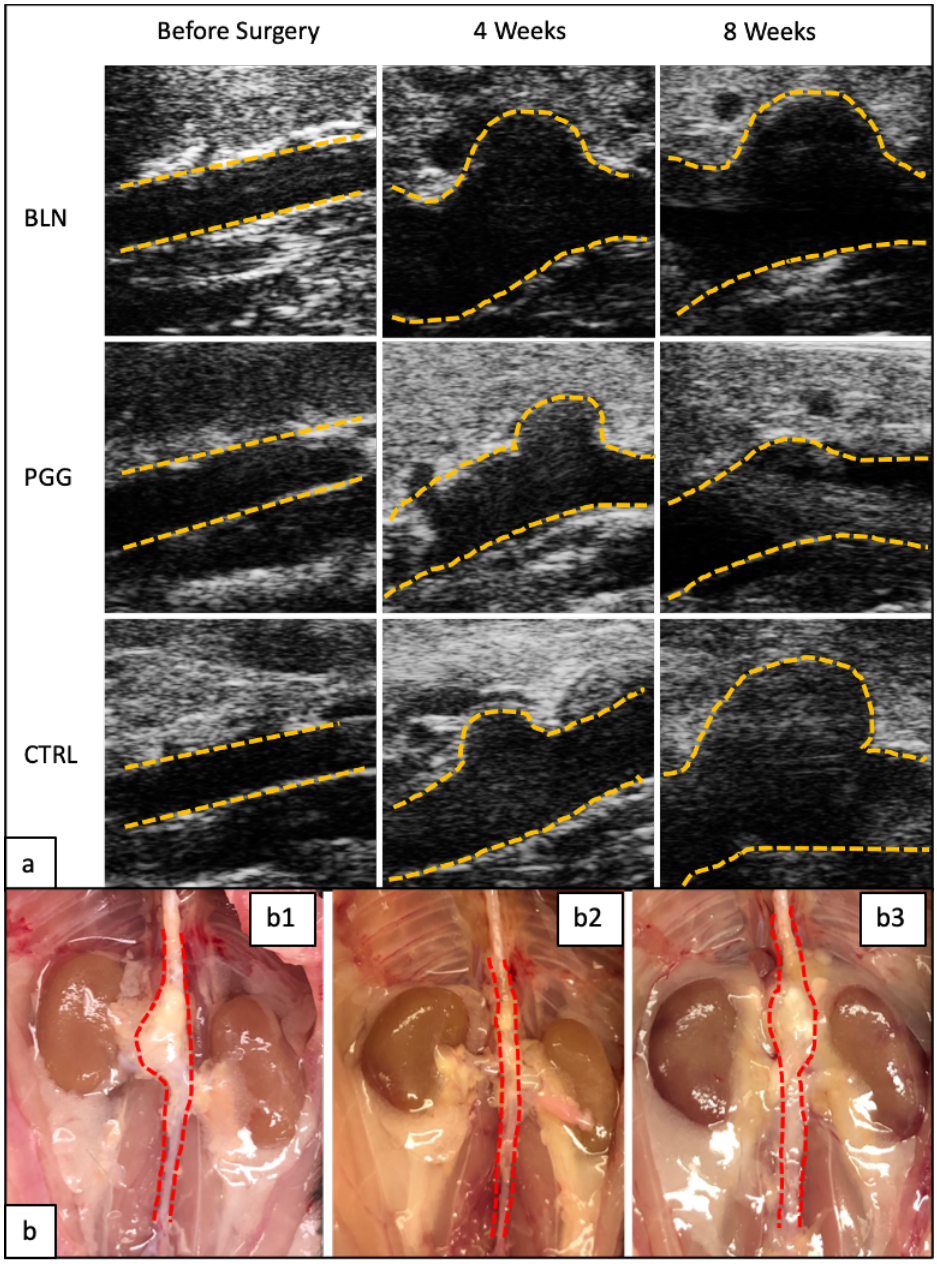


**Figure 6-3.** *In-vivo* ultrasound and percentage of dilation change in all three groups. **a.** Representative B-mode *in-vivo* ultrasound images of abdominal aortas before pump implantation, at 4 weeks when the infusion of the Ang II was finished, and 8 weeks when the treatment was finished; **b.** Gross view of the aortas from BLN-NPs (b1), PGG-NPs (b2), and control group (b3) at the endpoint.

AngII infusion (Figure 6-3a). The gross views of the explanted aortas also presented smaller outer aortic diameters of the suprarenal area in the PGG-NPs group comparing to the BLN-NPs and the control group (Figure 6-3b).

Precisely, after the treatment, the PGG-NPs group showed a decrease ($p=0.07$) in aortic dilation percentage from 139.16±49.14% at week four to 97.75±49.77% at week eight. However, for the BLN-NPs group, the aortic diameter kept increasing to a significant level ($p<0.01$) from 104.10±34.14% at week four to 182.44±46.55% at week eight. And the aortic diameter significantly increased ($p=0.03$) from 109.38±27.13% at week four to 188.11±84.92% at week eight for the control group. (Figure 6-4).

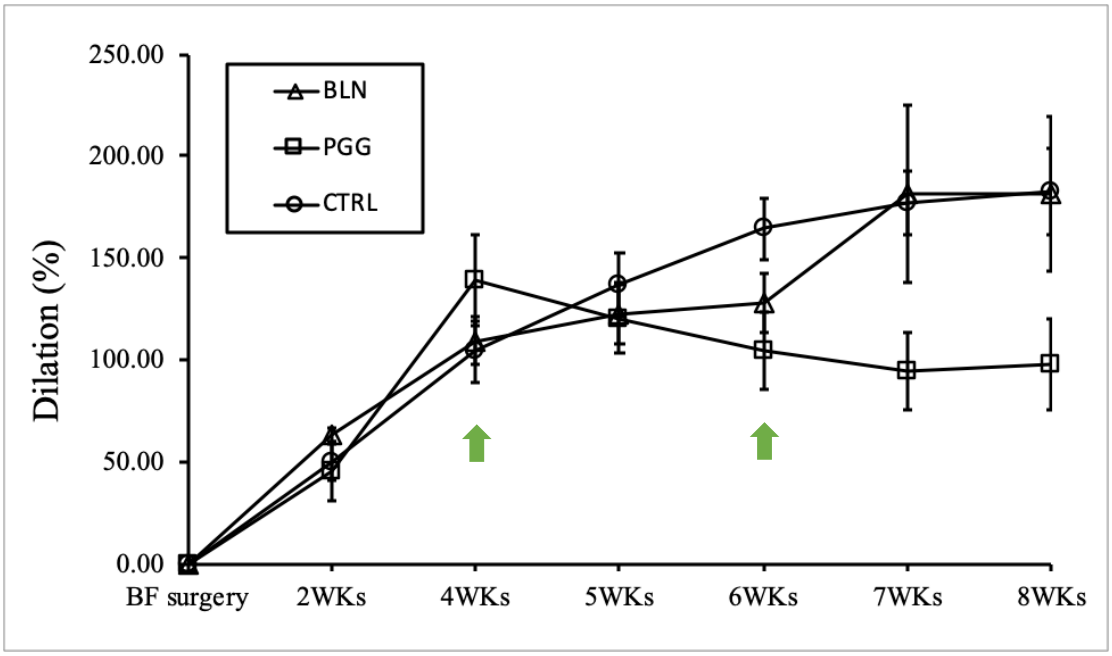


**Figure 6-4.** Dilation percentage (> 50% at week 4) of BLN-NPs group, PGG-NPs group, and control group before the treatment at week 2 and 4, and during the treatment at week 5, 6, 7 and 8, green arrows indicated the timepoints when the injection happened.

The same trend has also been observed in the suprarenal aortas with a dilation percentage smaller than 50% (Figure 6-5). By the end of the AngII infusion, these mice only presented moderate enlargement of the suprarenal aorta. After the treatment, the PGG-NPs group still showed a significant decrease ($p=0.02$) in aortic dilation percentage from 22.09±5.24% at week four to 7.82±8.26% at week eight. As for the control group, the aortic diameter kept increasing from 21.01±18.71% at week four to 43.95±17.94% at week eight.

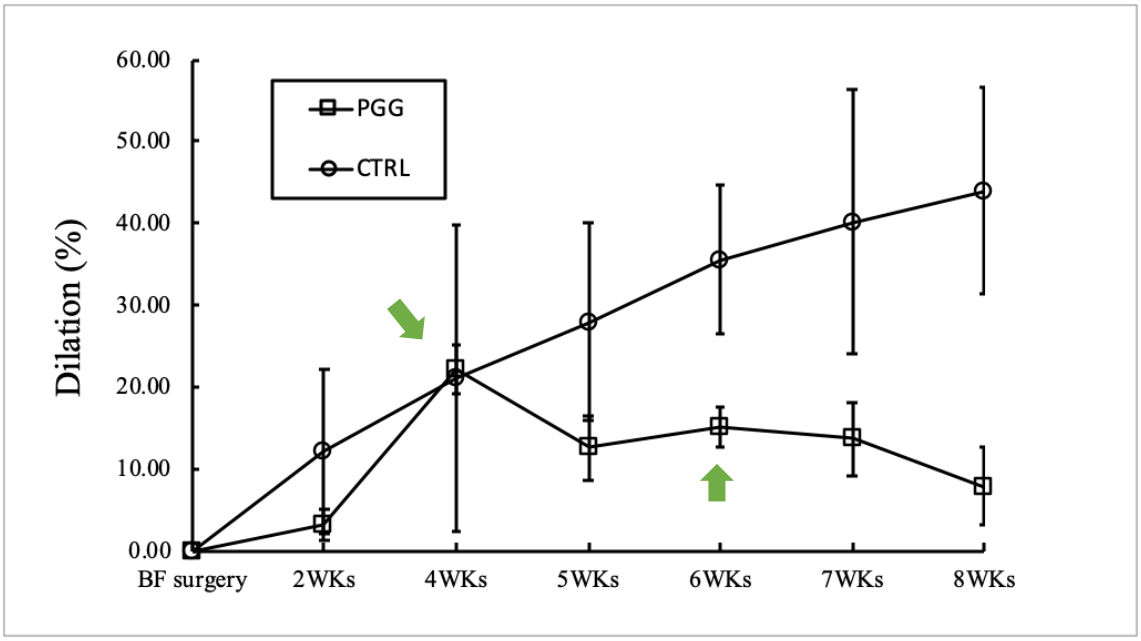


**Figure 6-5.** Dilation percentage (< 50% at week 4) of PGG-NPs group and control group before the treatment at week 2 and 4, and during the treatment at week 5, 6, 7, and 8. Green arrows indicated the timepoints when the injection happened.

**The influence of PGG treatment in CSs and PWVs**

All the mice used for the study had a decrease of the systolic diameter to diastolic diameter ratio at the end of the AngII infusion. During four weeks of the PGG-NPs

treatment, the mechanical behavior of the aortic walls during a cardiac cycle started returning to normal while in the BLN-NPs and the control group, the ratios kept decreasing

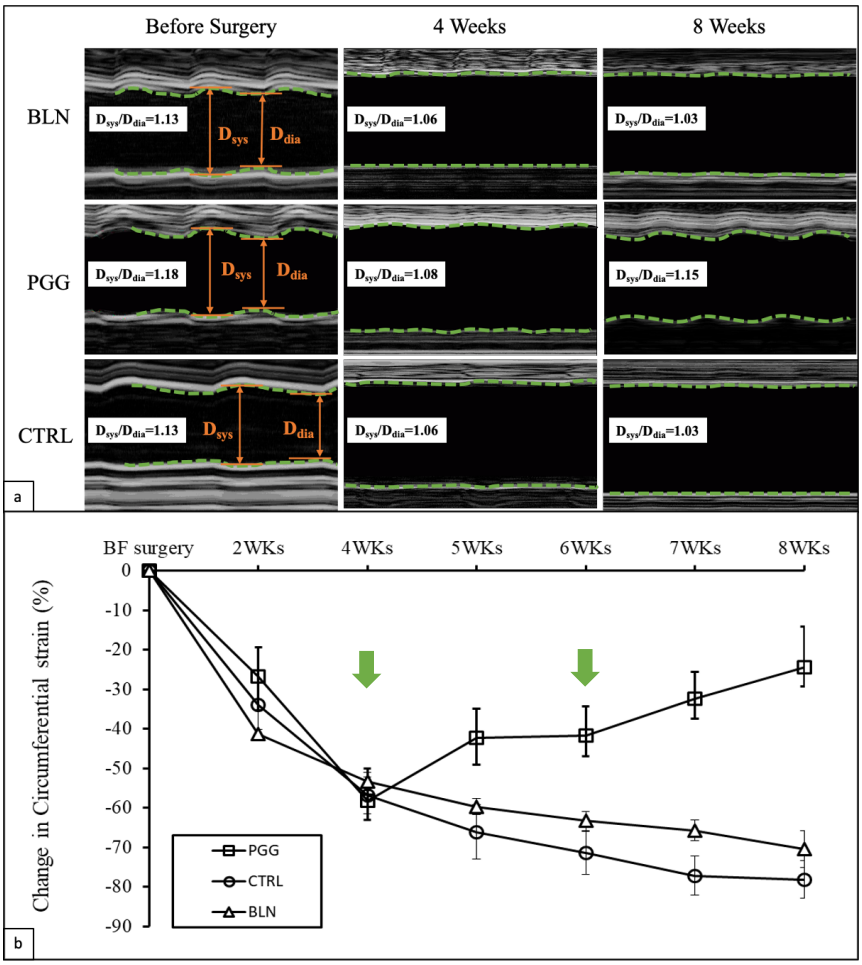


**Figure 6-6.** Change in circumferential strains for PGG-NPs, BLN-NPs, and control groups. **a.** Representative M-mode *in-vivo* ultrasound images of abdominal aortas before pump implantation, at 4 weeks when the infusion of the Ang II was finished, and at 8 weeks when the treatment was finished, showing the mechanical behavior change in a cardiac cycle; **b.** (%) change of corresponding circumferential Green-LaGrange strains throughout the cardiac cycle at week 2 and 4, and during the treatment at week 5, 6, 7, and 8. Green arrows indicated the timepoints when the injection happened.

(Figure 6-6a). CSs were further calculated to evaluate the change in the distensibility of the aneurysmal aortic wall (Figure 6-6b). All aneurysmal aortas showed a reduction in the strain values after the formation of the aneurysms.

By the end of the AngII infusion, the CSs of PGG-NPs, BLN-NPs, and control groups have decreased by 58.25±8.25%, 53.30±2.36%, and 56.85±4.73%, respectively. And after 4 weeks of NPs treatment, the aortas treated with PGG-NPs started to regain their distensibility, showing only a 24.50±10.34% CS decrease comparing to the healthy aortas. However, the CSs for both BLN-NPs treated group and control group decreased even more to 70.42±4.73% and 78.14±4.77% respectively at the endpoint of the treatment.

PWVs were also calculated to evaluate the progression of the AAAs (Figure 6-7). Before the surgery, the PGG-NPs group, BLN-NPs group, and control group have PWVs of 2.28±0.27 mm/ms, 2.21±0.17 mm/ms, and 2.38±0.28 mm/ms respectively. All aneurysmal aortas showed a reduction in the PWV after the formation of the aneurysms. The PWVs for the PGG-NPs, BLN-NPs, and control group dropped to 1.35±0.33 mm/ms, 1.56±0.11 mm/ms, and 1.49±0.19 mm/ms, respectively, after the AngII infusion. With four weeks of treatment, the PWV of the PGG-NPs group increased back to 2.43±0.13 mm/ms while the PWV was 0.97±0.12 mm/ms for BLN-NPs group and 1.09±0.32 mm/ms for the control group.

The changes in CSs and the PWVs were also monitored for the suprarenal aortas that had a dilation percentage of less than 50% at different time points. Both of the parameters changed in the same pattern as bigger aneurysms reported above (Figure 6-8). The CSs on average dropped by 28.07% after the AngII infusion in the PGG treated group

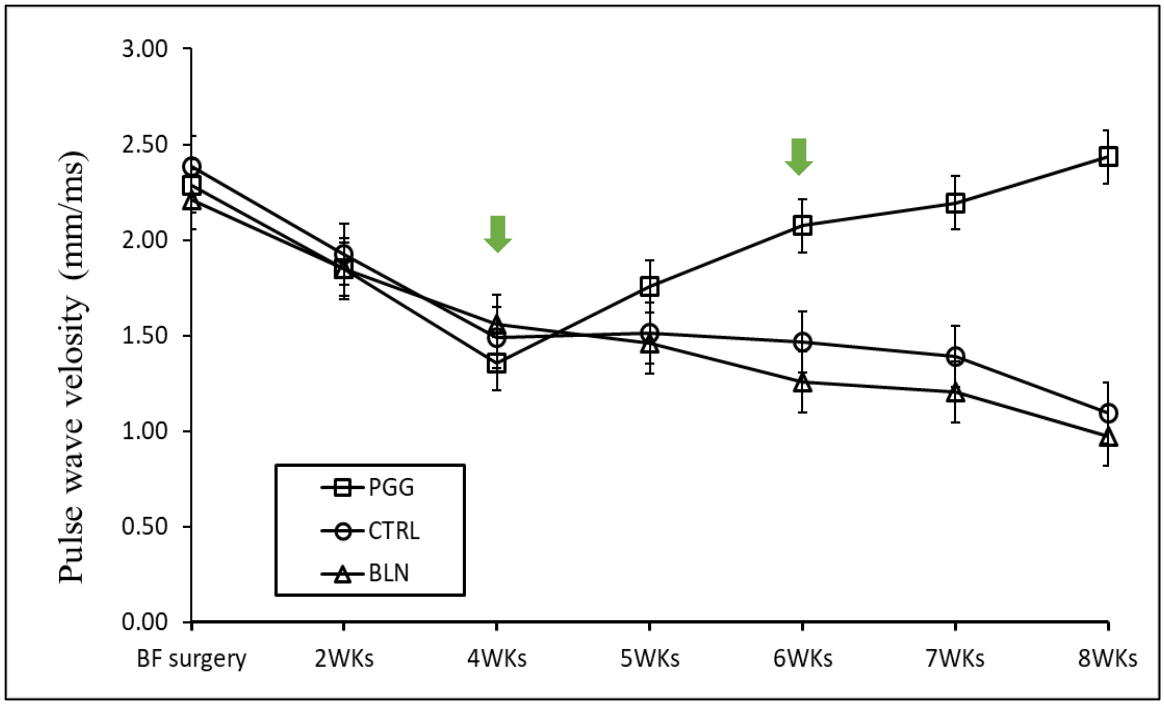


**Figure 6-7.** Change in pulse wave velocities for PGG-NPs, BLN-NPs, and control group at week 2 and 4, and during the treatment at week 5, 6, 7, and 8. Green arrows indicated the timepoints when the injection happened.

and by 8.32% in the control group. After four weeks of treatment, the average drop of CSs in the PGG treated group was only 6.89% comparing to 50.83% in the control group (Figure 6-8a). Moreover, the PWVs of the PGG group firstly decreased from 2.82±0.22 mm/ms to 1.32±0.31 mm/ms as the AAAs progress, and then increased to 2.34±0.22 mm/ms after PGG-NPs treatment. On the other hand, the PWVs of the control group firstly decreased from 2.12±0.23 mm/ms to 1.43±0.24 mm/ms as the AAAs progress, and then kept decreasing to 1.24±0.13 mm/ms without any treatment (Figure 6-8b).

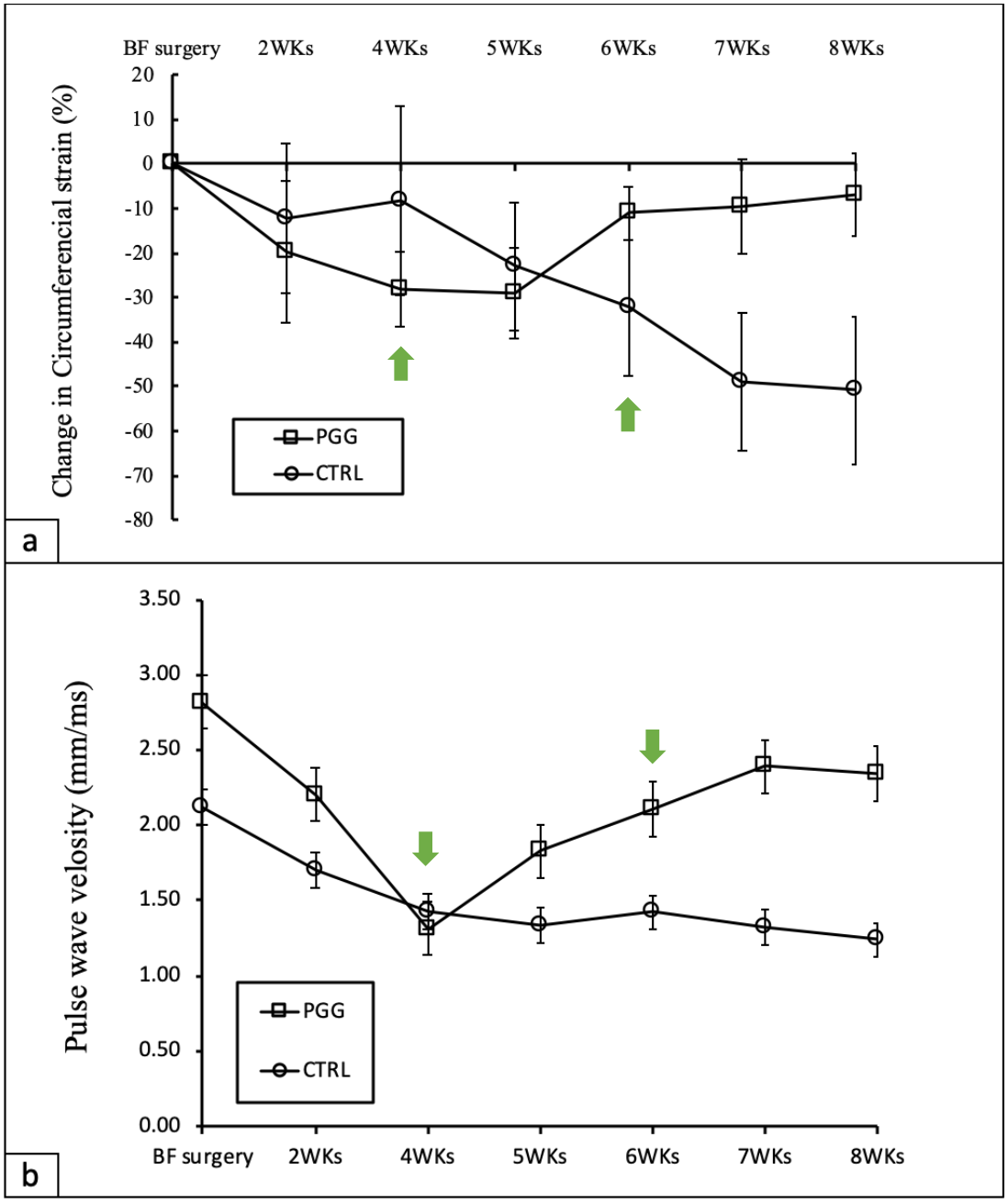


**Figure 6-8.** Change in **a.** circumferential strains and **b.** pulse wave velocities for suprarenal aortas that have <50% dilation in PGG-NPs and control group at week 2 and 4, and during the treatment at week 5, 6, 7, and 8. Green arrows indicated the timepoints when the injection happened.

**Histological analysis**

H&E and VVG staining of the suprarenal aortic sections from all three groups and aneurysms harvested at week 4 right after the AngII infusion provided information about the tissue morphology, cellular infiltration, and elastin degradation. The staining for the sections from the 4-week group exhibited the original status of the aneurysms before the

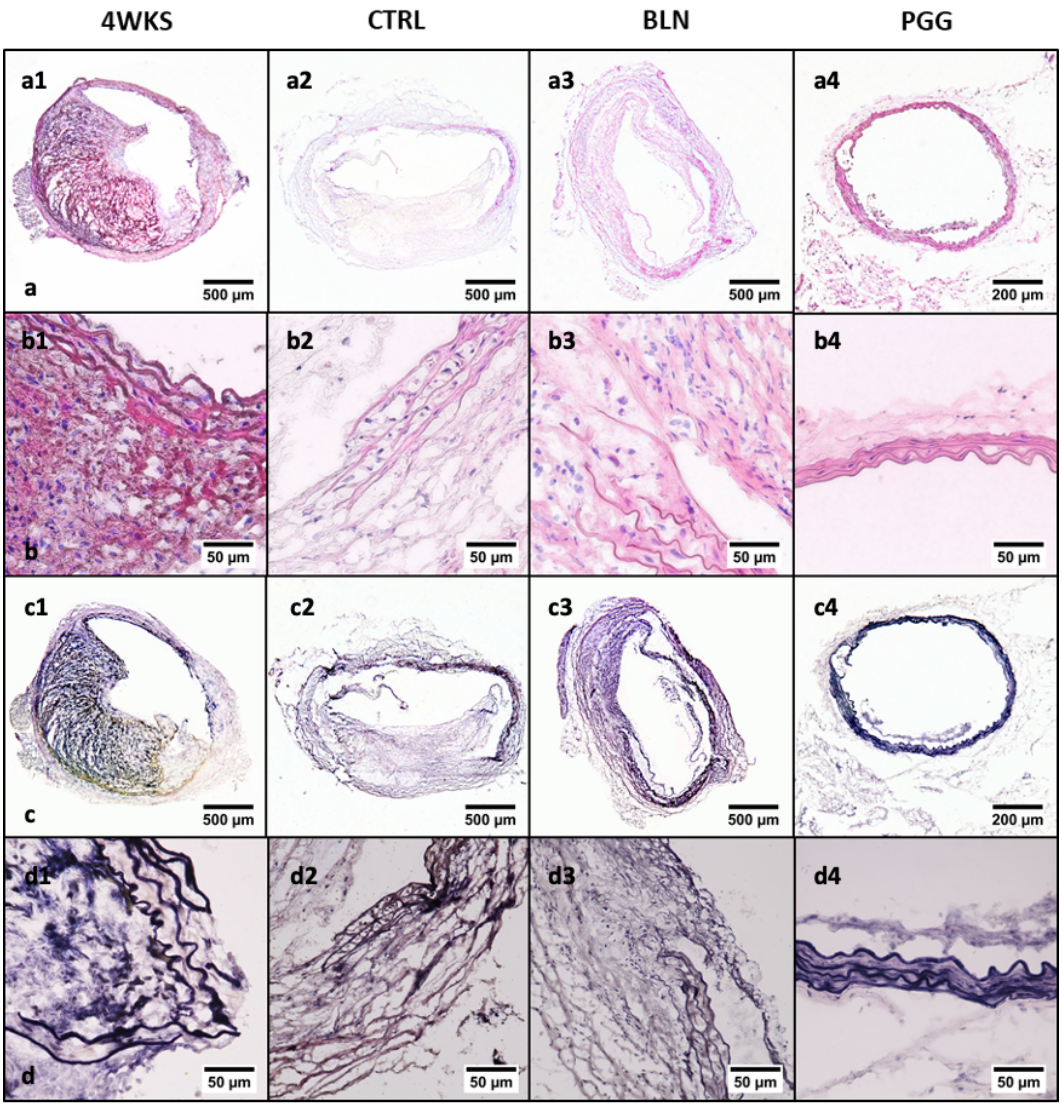


**Figure 6-9.** Histological images of tissue sections with H&E and VVG staining for 4-week, control, BLN-NPs, and PGG-NPs group at 4X and 40X.

treatment. An increase in aortic diameter was observed after the aneurysm formation. Massive inflammatory cells infiltrated the adventitial and medial layer of the aortas and severe elastin degradation in the aortic medial was also remarked. Comparing to the 4-week aneurysm and the sections from BLN-NPs and control group, the morphology of the tissues from PGG-NPs group were the closest to healthy with a relatively normal size and minimal infiltration of inflammatory cells (Figure 6-9a and 6-9b). Moreover, the VVG staining showed the most intact elastin laminae in the PGG-NPs group, while in the other three groups, there was severe degradation of elastin and formation of intraluminal plaques (Figure 6-9c and 6-9d).

**Assessment of systemic inflammation**

Serum IFN-γ levels were measured to evaluate the systemic inflammation. The control group had the highest amount of IFN-γ (49.94 ± 14.30 pg/ml) in the serum, followed by the BLN-NPs group (33.34 ±13.16 pg/ml). The PGG-NPs treated group has the lowest serum IFN- γ concentration (13.55 ± 8.09 pg/ml). The difference in IFN-γ concentration between the BLN-NPs and the control group was not significantly different at the 0.05 level. However, IFN-γ concentration in the PGG-NPs group was significantly lower than the control group ($p<0.01$) and BLN-NPs group ($p=0.04$) (Figure 6-10).

Flow cytometry showed a significant decrease of CD68 positive cells in the spleens ($p<0.058$) and a modest decrease in the thymuses from PGG-NPs treated mice comparing to the control group (Figure 6-11a). Similarly, the TGFβ-1 level significantly decreased after the treatment with PGG-NPs compared with the control group ($p<0.05$) in spleens (Figure 6-11b).

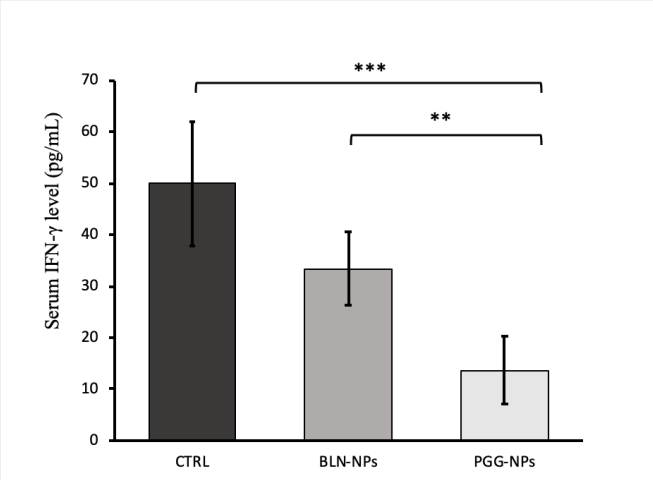


**Figure 6-10.** Serum IFN- γ concentrations of control, BLN-NPs, and PGG-NPs group.

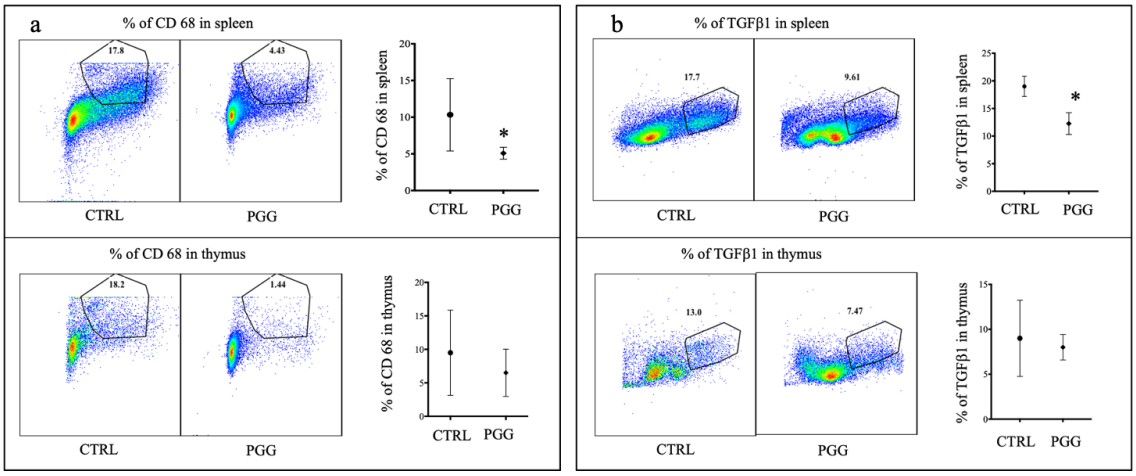


**Figure 6-11.** Flow cytometry dot plots and scatter plots for $CD68^+$ cells and $TGF\beta1^+$ expression in spleens and thymuses from the control group and PGG-NPs treated group. *$p<0.05$.

**Assessment of local inflammation**

IHC staining for CD68 and CD80 in suprarenal aortic sections from PGG-NPs, BLN-NPs, control, and 4-week group identified the infiltration of macrophages in the

aneurysmal tissue. The BLN-NPs, control and the 4-week group showed an intense pan-macrophage (CD68) staining (Figure 6-12 a1-a3). The PGG-NPs group was stained positive for CD68, but the staining only appeared in limited areas in the tissue and was less intense compared to the other three groups (Figure 6-12 a4). The BLN-NPs group, control group, and the 4 weeks group also showed intense M1 macrophage (CD80) staining (Figure 6-12 b1-b3) while the PGG-NPs group barely showed any staining (Figure 6-12 b4).

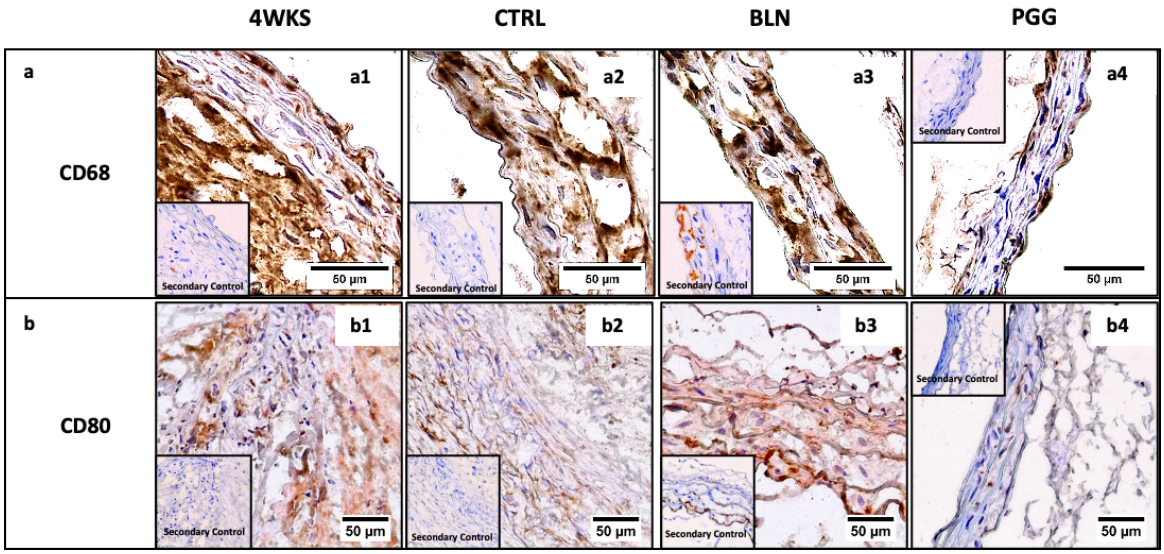


**Figure 6-12.** IHC results for CD68 (a1-a4), staining for the macrophage infiltration, and CD80 (b1-b4), staining for the M1 macrophages, in the suprarenal aortic tissue from the 4-week group, control group, BLN-NPs group, and PGG-NPs group.

*In-situ* zymography of the suprarenal aortic sections from PGG-NPs, BLN-NPs, control, and 4-week group visualized the MMP activities. The PGG-NPs group showed significant suppression of signal from MMP activities (Figure 6-13d) comparing to 4-week, control, and the BLN-NPs group (Figure 6-13 a, b, and c).

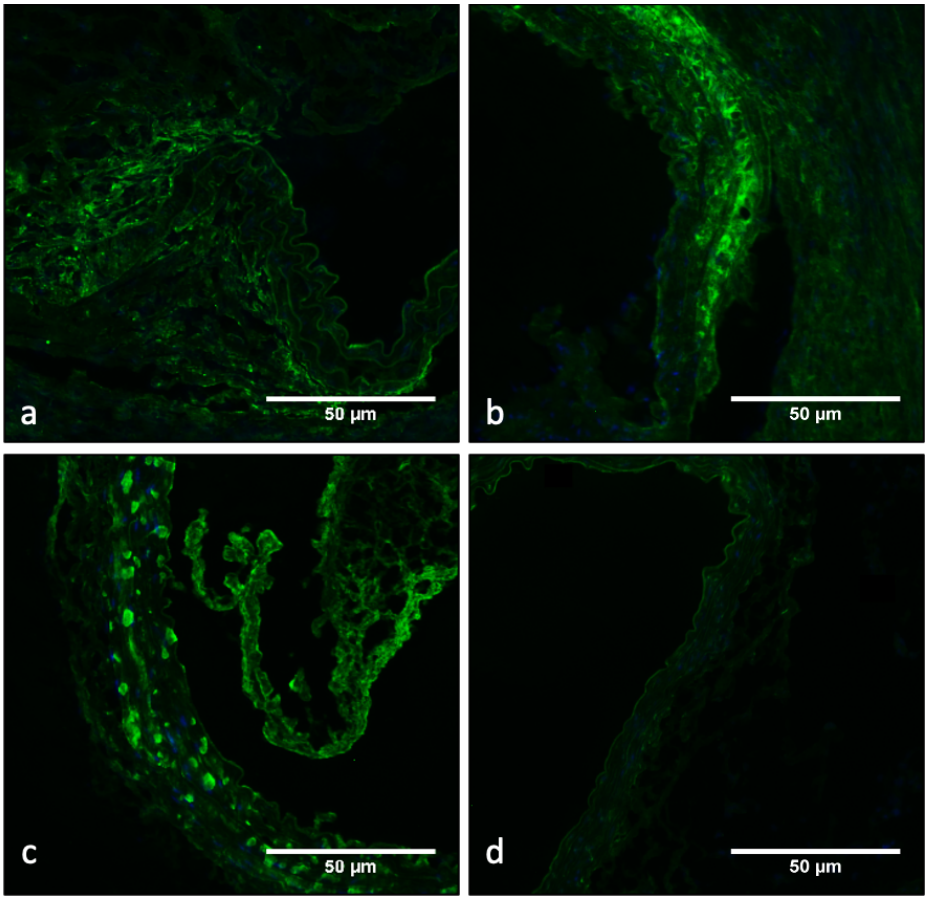


**Figure 6-13.** *In-situ* zymography showing MMPs activity in aneurysms harvested from the **a.** 4-week group, **b.** control group, **c.** BLN-NPs group, and **d.** PGG-NPs group.

qPCR analysis of the mRNA from the cells in the aneurysmal tissue showed that the BLN-NPs treatment did not seem to significantly affect all tested gene expressions. The MMP-2 expression in the PGG-NPs group was significantly lower compared to the control group ($p=0.04$) (1/5 of the control group expression) and modestly lower than the BLN-NPs group (1/4 of the BLN-NPs group expression) (Figure 6-14 a). TIMP-1 and TIMP-2 expression were both upregulated in the PGG-NPs group. PGG-NPs group showed a 2.2-fold upregulation of TIMP-1 and a significantly higher expression of TIMP-2 (2.8-fold

upregulation) comparing to the control group (p=0.07), and a 2-fold upregulation of TIMP-1 and 1.6-fold upregulation of TIMP-2 comparing to BLN-NPs group (Figure 6-14 b, c).

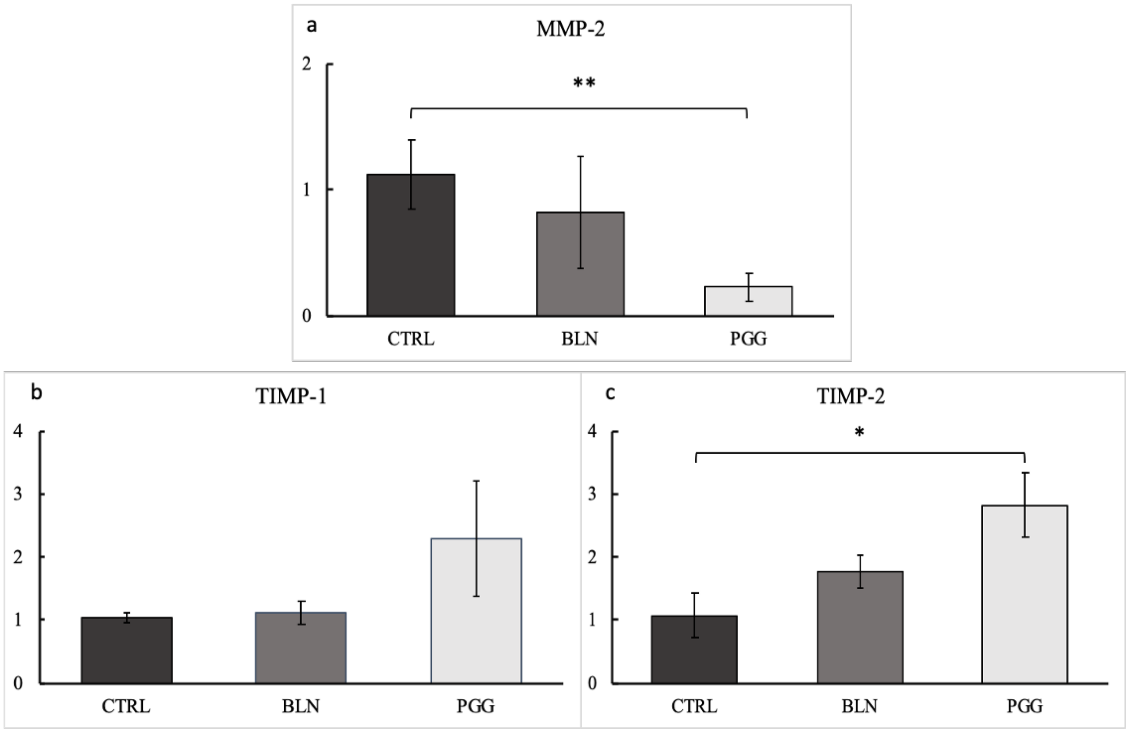


**Figure 6-14.** qPCR results of mRNA extracted from aneurysms harvested from the control group, BLN-NPs group, and PGG-NPs group for MMP-2, TIMP-1, and TIMP-2 expression. **p<0.05, *p<0.1.

**The effect of PGG treatment on elastin related genes**

qPCR analysis of the mRNA of ELN and LOX from the cells in the aneurysmal tissue showed a slightly increased ELN expression by 1.8-fold and 1.5-fold higher LOX expression in the PGG treated group. The BLN-NPs treatment again did not seem to change both ELN and LOX gene expressions comparing to the control group (Figure 6-15).

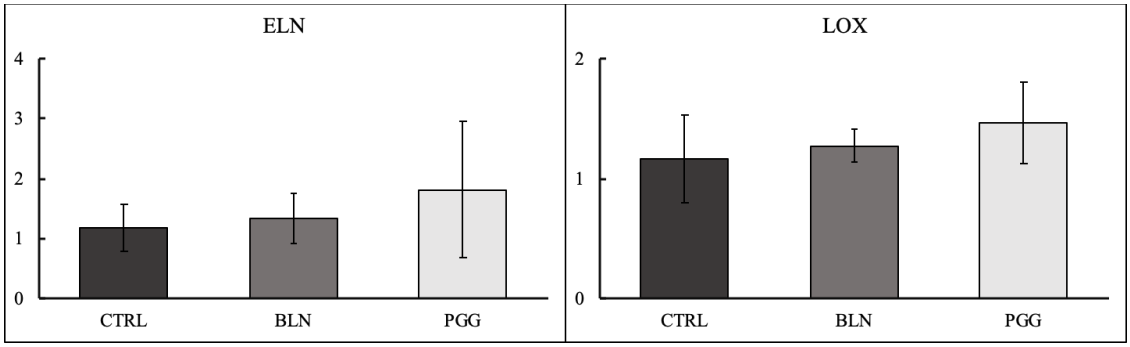


**Figure 6-15.** qPCR analysis of ELN and LOX for the control group, BLN-NPs group, and PGG-NPs group.

**Biaxial mechanical testing**

A leftward shift in the pressure-diameter curves indicated decreased dilation in the PGG treated group across the entire pressure range with a more prominent inflection point normally observed in elastic arteries of small animals (Figure 6-16 a). Accordingly, both unloaded and physiologically loaded outer diameters significantly decreased with elastase PGG-NP treatment. The direct observation of the force vs. pressure relationship showed an increasing value of force for PGG-NP group compared to the control group (Fig. 6-16 b). A significantly higher force was recorded for physiological pressures at these axial stretch ratios for the PGG-NPs group compared to the control group. A decrease in stiffness was observed in the circumferential direction in the PGG-NP group as indicated by the slope of the stretch-stress responses (Figure 6-16 c). A much lower circumferential stress in the control group was required to achieve the same circumferential as the PGG-NP treated group. Moreover, an increase in lumen area compliance was present in the PGG-NPs groups compared to the control group (Figure 6-16 d).

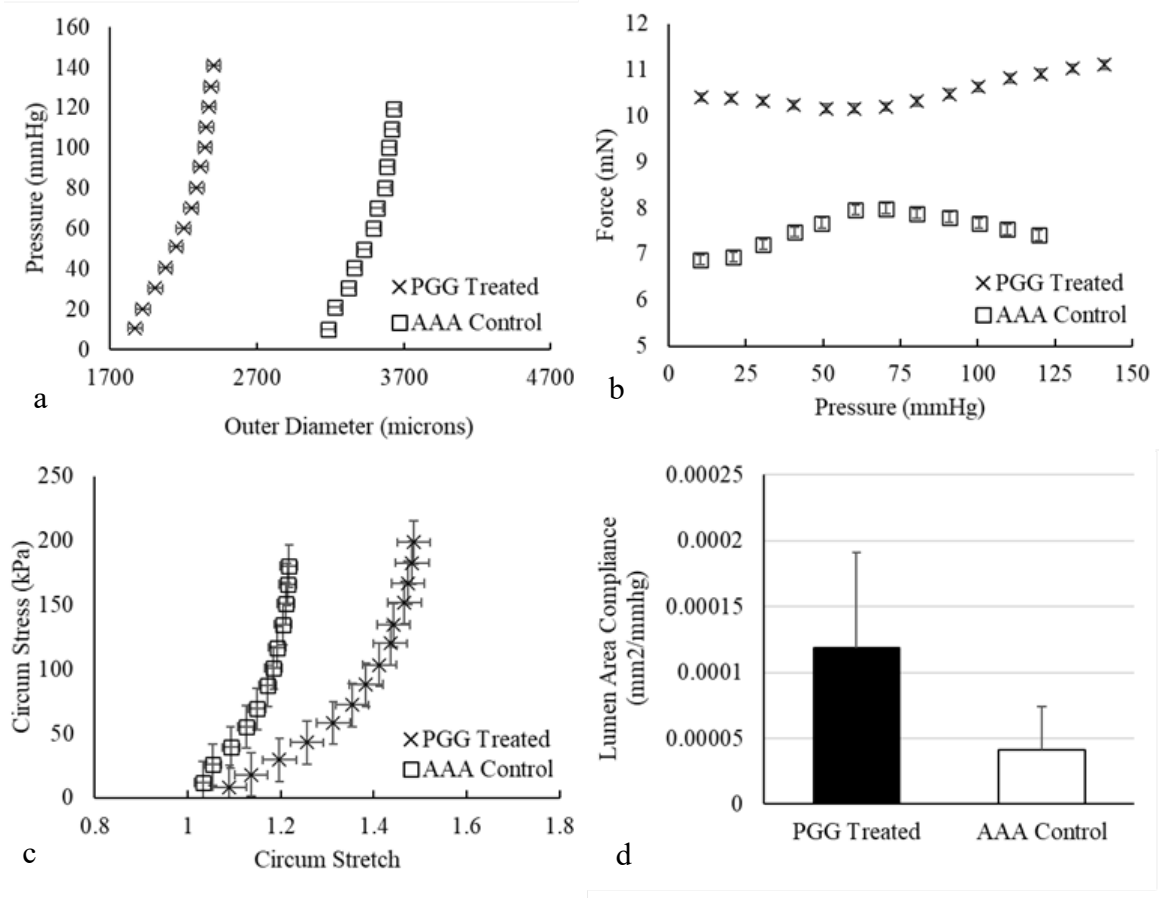


**Figure 6-16.** Biaxial test results for PGG-NPs and control group.

### 6.4 Discussion

Targeted drug delivery to AAAs possesses certain inherent challenges like hemodynamic conditions in the aorta and the complexity of pathophysiological markers expressed in the tissue. Much of the remodeling happens in the ECM of the aneurysmal tissue thus making it vital to design a vehicle that can reach and be retained in the ECM to maximize its effect. Being one of the most common animal models of AAA, we chose to work with the AngII model to stimulate spontaneous AAA formation in mice [289]. The formation of AAAs in this model resembles human disease in aspects that include male

gender preponderance, the setting of mild hypertension, and the presence of hyperlipidemia [290]. Moreover, the formation of intraluminal thromboses (ILT), which has been commonly seen in this model as well as in human AAAs, would limit the access to the aortic wall from the lumen for targeting drug delivery.

Owing to our group's documented publications that elastin degradation presents as a hallmark signal in AAAs, a novel targeting technique has been developed [318]. We have loaded BSA nanoparticles with DiR dye in order to quench autofluorescence from ECM proteins to test the targeting ability of these nanocarriers to degrading elastin *in-vivo* [319]. Concurring with the data shown by Nosoudi et al. [169], and Karamched et al. [242], we demonstrate the targeted delivery of nanoparticles to the aneurysmal site. More importantly, our histological results showed that the DiR-NPs accumulated at the medial layer of the aorta where the elastin was degrading. It indicated that the targeting of the NPs was achieved actively under the guidance of the conjugated antibodies regardless of the ILT. This finding was supported by our previous study suggesting the NPs targeted through the vasa vasorum rather than from the aortic lumen [169].

The change of aneurysmal aortic diameter is one of the most intuitional parameters that could be used to decide the efficacy of a AAA pharmacotherapy. We measured the inner diameter of the aneurysms at different timepoints throughout the study as a part of the evaluation for the status of aneurysms. Not all mice presented a more than 1.5-fold aortic enlargement, a clinical criterion for diagnosing AAAs, by the end of the AngII infusion. Then, we looked at two important biomechanical properties of aorta i.e., CS and PWV to further assess the development of the aneurysms. CS decreased significantly in

AngII infused mice developing aneurysms. It indicated that the aneurysmal aortic walls responded less to blood pressure variation after the aneurysm formation. Our observations coincide with other documented results, for example, by Favreau et al. [303], Trachet et al. [320], and Phillips et al. [321].

In contrast to the findings of increased PWVs [322-324], we noticed a significant decrease after 28 days of Ang-II infusion. This follows our hypothesis that increased local aortic diameter at the site of the aneurysm increases the time taken by the pulse to travel along the aneurysm. Moreover, the decrease of PWVs as a result of larger aortic diameters overweighed the increase of PWVs caused by the increase of aortic wall stiffness. Nandlall et al. also reported a decrease in PWV after AAA formation in an ApoE/TIMP-1 -/- murine model [325].

After 4 weeks of treatment, we observed a significant decrease in the size of PGG-NPs treated aneurysms. However, the aneurysm sizes in the BLN-NPs and untreated group kept increasing. The PGG-NPs treated aneurysms also restored part of their CSs and showed a significant increase in PWVs while the CSs and PWVs kept decreasing in the control groups. In coherence with the findings in a $CaCl_2$ induced rat model [169], we believe that the targeted delivery of PGG could restore the mechanical properties of the aneurysmal tissue and regress the aneurysms. This has been further confirmed by the observations from biaxial mechanical tests. The results from the biaxial mechanical tests indicated that PGG-NP treatment AAAs had better elasticity compared to the control group and presented higher strength against pressurization. Overall, our research demonstrated

the potential for the PGG-NP treatment to help aneurysmal tissue to regain better mechanical properties and decrease the rupture risk of the AAAs.

Then we looked into the mechanism of how PGG functioned both systemically and locally to halt and reverse the AAA progression. Inflammation in the aortic wall is a main trigger of AAA onset. Chronic inflammatory cell infiltration in the adventitial and medial aortic layers and the upregulation of the pro-inflammatory cytokine would result in the VSMCs apoptosis and ECM degradation, primarily elastic lamina degradation by proteolytic enzymes such as MMPs and cathepsins [35, 77, 78]. The progression of the local aortic inflammatory response requires the enhanced recruitment of inflammatory cells from the system [326]. Mellak et al. reported that the monocytes from the spleen could be mobilized by the presence of AngII and contribute to the development of AAA and the occurrence of rupture [327]. According to our flow cytometry results, a significant decrease in CD68 positive cells in the spleen was observed in PGG-NPs treated group compared with the control group. This indicated that PGG could reduce the available monocyte subsets in the system, thus, decrease the aortic macrophage accumulation and attenuate the inflammatory response in the local aneurysmal tissue.

The formation of AAAs also usually results in an altered systemic level of cytokines such as IFN-γ and TGFβ1. The expression of IFN-γ has been reported to be consistently upregulated in the circulation and tissues of patients with AAA [328], and has been shown to induce productions of MMP-9 in macrophages and MMP-2 in SMCs to promote AAA progression [329]. IFN-γ producing CD8 positive T cells were found to promote the development of aneurysm by increasing MMP producing macrophages [330]. It has been

reported that the inhibition of IFN-γ in the elastase AAA mouse model could abrogate the formation of aneurysms [329, 330]. We observed a significantly higher level of IFN-γ in the serum of the BLN-NPs treated group and the control group compared to the PGG-NPs treated group, indicating the systemic IFN-γ suppressing role of PGG-NPs in the AngII mouse model.

We further looked at how PGG treatment influenced the TGFβ1 level systemically. An overexpressed local level of TGFβ1 has been proved to be beneficial for stopping the progression of AAAs and stabilizing the already-formed aortic aneurysms [82, 331]. Here, interestingly, we found that the TGFβ1 cytokines level significantly decreased in the spleens. This could be evidence to support that the PGG-NPs reduced the systemic inflammatory responses in the AngII mouse model, but further studies are required to describe the role of the spleen TGF β1 level in the formation and progression of AAAs. Overall, our results suggested that PGG-NPs treatment could suppress the production of systemic inflammatory markers.

At the aneurysmal site, PGG can be thought to have two functions, one is to stabilize the ECM by inhibiting MMPs locally and two, to increase elastin fiber deposition. It is known that MMP-2 is one of the key players in AAA's pathophysiology. MMP-2 expression levels have been known to increase in AAA conditions in humans [332]. Activated macrophages are responsible for producing MMP-2, whose levels are not counter-balanced by the activity of their inhibitors (TIMPs) [333]. TIMPs play a crucial role in reducing aortic aneurysm formation. Results from Eskandari et al. [334] and Ikonomidis et al. [335] stressed the importance of TIMP-1 in protecting ECM against

aneurysm formation. The role of TIMP-2 is, however, controversial in the pathology of AAAs. Although TIMP-2 inhibits some MMPs it can also act as an MMP-2 activator. So, it can both promote and attenuate aneurysm formation. Xiong et al.[336] have reported that the absence of TIMP-2 led to protection against aneurysm formation probably by hampering MMP-2 production. However, Aoki et al. showed the protective effect of TIMP-2 in AAA formation by reducing the MMP-2 activity [337]. Putting all these facts aside, the imbalance of MMP and TIMP activity is primarily responsible for the degradation of collagen and elastin [85], which are the integral parts of the ECM.

Parasaram et al.[338] have reported that PGG could inhibit MMP activity *in-vitro* and even under acellular conditions (PGG added to development buffer during zymography rather than in cell culture medium). They have also shown that TIMP-1 levels were increased in rat pulmonary fibroblasts treated with PGG *in-vitro*. In our study, we showed that PGG inhibited MMP activity in the aneurysmal tissue by performing *in-situ* zymography on the aneurysmal sections. PGG-NPs treated aortas showed diminished MMP activity compared to the control and BLN-NP group. Moreover, we observed that PGG-NPs treatment significantly reduced the MMP-2 expression while upregulated the TIMP expression in the aneurysmal tissue compared with the control group. PGG-NP treatment was suggested to help achieve a protease/anti-protease balance in the aneurysmal tissue.

Sinha et al. [18] and Parasaram et al. [338] have further shown that PGG also helped in increasing elastin deposition in cell cultures, possibly by holding the tropoelastin molecules together. This helps LOX to finish crosslinking them before being “washed out”.

While the amount of tropoelastin produced by cells remained fairly similar in control and PGG treated cells, PGG treated cells have more elastic fibers laid down in the ECM. Our results of VVG staining indicated the replenishment of elastin fibers that were lost during the aneurysm development in the PGG-NP treated group. Restoration of elastin fibers at the aneurysmal site explained the changes observed in the biomechanical properties of aorta in this group. However, the expressions of ELN and LOX were not significantly enhanced in the PGG-NPs treated aneurysmal tissue. This could be a result of 1) the loaded PGG has been fully released from the nanocarrier after two weeks so the local genetic expressions returned to normal as shown in our previous cell culture study [338], and 2) the fact that most elastin fibers have already been repaired at the point of sample harvesting.

By stabilizing the elastin fibers in the ECM, PGG-NP treatment further ameliorated the inflammation in the AAAs. Some products of ECM degradation, such as elastin fragments (EFs) or elastin degradation products (EDPs), at the site of injury are chemotactic to macrophages [339]. Thus, suppression of elastin degradation may have further led to a suppression of macrophage activity in the area and significant suppression of MMP activity in the PGG-NP group. We have shown using IHC that the levels of CD68 stained macrophages decreased significantly with PGG treatment. Furthermore, CD80 staining reveals a complete absence of pro-inflammatory (M1) macrophages at the aneurysmal site. With the obtained results, one can arrive at the conclusion that PGG works by both inhibiting MMPs and restoring elastin in the aorta, which stops the recruitment of macrophages, thereby restoring a “normal” microenvironment at the aneurysmal site.

## 6.5 Conclusion

In this specific aim, we investigated the AAA treatment efficacy of PGG-NPs in the AngII infusion induced mice model. The PGG-NPs treated mice showed restoration of normalcy in the aorta with developed aneurysms in terms of aortic diameter, tissue morphology, elastin fibers in the ECM, inflammation scenario, and the mechanical properties. Targeted delivery of these PGG-NPs demonstrated a very promising therapeutic strategy for the reversal of already established AAAs.

# 7. CONCLUSION AND FUTURE RECOMMENDATIONS

## 7.1 Conclusions

AAA diagnosis and treatment have always been challenging owing to the complexity of the lesion location and AAA pathophysiology. Misdiagnosing of AAAs that tend to rupture can put the patients in a life-threatening situation. Even if the AAAs were successfully diagnosed with the current clinical diagnostic strategies, the mortality of the patients who received treatment remains high. In this research, we focused on targeting the degradation of elastin in the aneurysmal tissue, an essential protein that maintains the aortic elasticity and the degradation products of which mediates the local inflammation, in an attempt to develop a safe and efficient diagnostic tool as well as pharmacotherapy.

The first part of this research aimed to develop a targeted imaging contrast agent using AuNPs to provide details about aortic mechanical properties that could help generate a more accurate diagnosis. In this part of the research, we synthesized negatively charged 150nm AuNPs and modified their surfaces with antibodies that could target the degraded elastin. We have shown that these EL-AuNPs are not cytotoxic and also could be mostly clear out of the system within ten days. Moreover, we showed that optimized EL-AuNPs could enhance the CT imaging contrast of the tissue with elastin damage exclusively. And the contrast enhancements of signal in the CT-scans are positively correlated to the elastin damage level in the *in-vitro* arterial models. We further tested these EL-AuNPs in the AngII infusion induced mouse AAA model and showed targeting of the EL-AuNPs to the aneurysmal tissue in both *in-vivo* and *ex-vivo* CT scans. Correlations between the

accumulation of EL-AuNPs in the aneurysms and the mechanical properties (burst pressure and biaxial tests) have been built to render the EL-AuNPs potential to be used as a tool to assess the rupture risk of the AAAs.

The second part of the research focused on studying the therapeutic effects of PGG loaded BSA nanoparticles on AAAs in the same AngII model. Two injections of PGG-NPs within four weeks have shown to be effective in reducing the inflammatory response both locally and systemically. By stopping the inflammation in the aneurysmal tissue, PGG-NPs helped preserve the ECM and thus slowed down the AAA progression. Besides the anti-inflammatory effect, the treatment of PGG-NPs restored the elastin fibers in the aortic media, which improved the mechanical properties of the aneurysmal tissue and reduced their risks of rupture. Therefore, targeted delivery of PGG-NPs could be a promising pharmacotherapy for the AAA patients who are not recommended to undergo surgical interventions.

### 7.2 Recommendation for future work

- In this dissertation, we investigated the possibility of using EL-AuNPs as a targeted contrast agent to provide information about the micro defects in the aneurysmal tissue. We chose bursting tests and biaxial tests to assess the mechanical properties of the AAAs in order to find their correlation with the EL-AuNPs accumulated int the tissue. However, very limited parameters were tested in this study, and the accumulation of EL-AuNPs was correlated to each one of them independently. Considering the complication of the actual *in-vivo* environment, it is desired to develop a

scoring system that combines all the mechanical data into one total score, which will later be correlated to the EL-AuNPs. It will increase the overall accuracy of using EL-AuNPs accumulation to represent the AAA rupture potential.

- In our *ex-vivo* study, we observed the accumulation of EL-AuNPs in the weak spot within the aneurysmal sac. The areas that showed the highest signal intensity in the AAAs were found to rupture the first in the bursting tests. This indicated that we could use the EL-AuNPs to visualize the potential rupture sites in the AAAs. However, it was very challenging to apply this idea to the *in-vivo* study due to the limited quality of the CT imaging and the large amount of connective tissue around the AAAs. It would be essential to increase the imaging quality and visualize the weak spot of the AAAs in the *in-vivo* CT scans. The detailed EL-AuNPs maps that show the weak spot in the aneurysmal wall could be beneficial in assisting the clinical AAA repairing.
- It would be of interest to optimize the AuNP dose used in visualizing the AAAs *in-vivo.* In this dissertation, we only used one dose, 10mg/kg animal weight for both *in-vivo* and *ex-vivo* imaging studies. In the cell culture studies, we have shown very low toxicity of AuNPs at a dose that equaled to 100mg/kg animal dose in animal studies. An increased dose may increase the sensitivity of detecting the micro defects in the AAAs while remaining

non-toxic to the animals that receive the injection. Also, the optimization of the AuNPs dose can increase the CT imaging quality and accuracy.

- AuNPs could also be used as an imaging contrast agent for other elastin damage related diseases such as thoracic aortic aneurysms and chronic obstructive pulmonary disease. We have already shown in this research that the EL-AuNPs can achieve targeting in the aorta and can be distributed to the lungs.
- In this research, many aspects of how PGG-NPs helped stop and reverse the AAA progression has been studied. We revealed the anti-inflammatory and ECM regenerating role of the PGG-NPs. It would be interesting to study how PGG interacts with the aneurysmal tissue on the molecular level. It would provide us more insights into the AAA pathophysiology. This could also help us to optimize the dose of PGG-NPs injected to achieve the best treatment efficacy.
- Our *in-vivo* data showed that the treatment of PGG could restore the local elastin in the aneurysmal tissue. However, it didn't resolve the ILT that was commonly observed in this animal model as well as in the human AAAs. It would be useful to develop a combined treatment using PGG and drugs that could either resolve or stabilize the ILTs. On the one hand, the anti-inflammatory effect of PGG could help to slow down the formation of ILTs; on the other hand, the complementary drugs could resolve or stabilize the

existed ILT and prevent the formation of deadly embolus. It would help restore the normal functionality of the aneurysmal abdominal aorta.

- In this dissertation, we developed a diagnostic tool that could be used to assess AAA rupture potential as well as pharmacotherapy that has shown effectiveness in curing AAAs. It would be interesting to combine the use of AuNPs and PGG-NPs into one NP system to achieve theranostic purposes. By loading the BSA nanocarriers with both AuNPs and PGG, this novel nanoparticle system can not only be used as a contrast agent for visualizing the AAAs but also locally release PGG in a controlled manner that cures the disease.
- All the in-vivo studies we have performed in this study were performed in an AngII infusion induced mouse model. The targeting of NPs would be challenging in large animals. The dose of injection, the biodistribution and toxicity after injection can be totally different in larger animals as well as human. In order to translate all our findings into clinical use, it is important to perform further studies in larger animal models such as elastase induced porcine model.
- Here, in this research, the antibodies were designed to target the elastin degradation in rodents. In order to successfully target the AAAs in human for clinical use, the antibodies used for modifying the NPs should be customized to target the human elastin fragments. And the conjugation

conditions should be further optimized for the new antibodies to achieve better imaging or treating efficacy.

- We have developed a nanocarrier that could be used to deliver drugs locally to the AAAs. We could use this nanocarrier to load other drugs that have shown to reduce the inflammatory response in the cell culture studies or in animal studies but failed in clinical trials when they were delivered systemically, such as doxycycline, statins and coumaperine derivatives.

# REFERENCES

[1] A. Palazzuoli, M. Gallotta, G. Guerrieri, I. Quatrini, B. Franci, M.S. Campagna, E. Neri, A. Benvenuti, C. Sassi, R. Nuti, Prevalence of risk factors, coronary and systemic atherosclerosis in abdominal aortic aneurysm: comparison with high cardiovascular risk population, Vasc Health Risk Manag 4(4) (2008) 877-83.

[2] R.W. Thompson, B.T. Baxter, MMP inhibition in abdominal aortic aneurysms. Rationale for a prospective randomized clinical trial, Ann N Y Acad Sci 878 (1999) 159-78.

[3] H. Abdul-Hussien, R.G. Soekhoe, E. Weber, J.H. von der Thusen, R. Kleemann, A. Mulder, J.H. van Bockel, R. Hanemaaijer, J.H. Lindeman, Collagen degradation in the abdominal aneurysm: a conspiracy of matrix metalloproteinase and cysteine collagenases, Am J Pathol 170(3) (2007) 809-17.

[4] C.M. Brophy, J.M. Reilly, G.J. Smith, M.D. Tilson, The role of inflammation in nonspecific abdominal aortic aneurysm disease, Ann Vasc Surg 5(3) (1991) 229-33.

[5] F.M. Davis, D.L. Rateri, A. Daugherty, Mechanisms of aortic aneurysm formation: translating preclinical studies into clinical therapies, Heart 100(19) (2014) 1498-505.

[6] M.L. LeFevre, U.S.P.S.T. Force, Screening for abdominal aortic aneurysm: U.S. Preventive Services Task Force recommendation statement, Ann Intern Med 161(4) (2014) 281-90.

[7] E.J. Zucker, A.M. Prabhakar, Abdominal aortic aneurysm screening: concepts and controversies, Cardiovasc Diagn Ther 8(Suppl 1) (2018) S108-S117.

[8] A.R. Sparks, P.L. Johnson, M.C. Meyer, Imaging of abdominal aortic aneurysms, Am Fam Physician 65(8) (2002) 1565-1570.

[9] H. Hong, Y.A. Yang, B. Liu, W.B. Cai, Imaging of Abdominal Aortic Aneurysm: The Present and the Future, Curr Vasc Pharmacol 8(6) (2010) 808-819.

[10] H. Lusic, M.W. Grinstaff, X-ray-Computed Tomography Contrast Agents, Chem Rev 113(3) (2013) 1641-1666.

[11] D. Kim, S. Park, J.H. Lee, Y.Y. Jeong, S. Jon, Antibiofouling polymer-coated gold nanoparticles as a contrast agent for in vivo X-ray computed tomography imaging (vol 129, pg 7661, 2007), J Am Chem Soc 129(41) (2007) 12585-12585.

[12] A.N. Assar, C.K. Zarins, Ruptured abdominal aortic aneurysm: a surgical emergency with many clinical presentations, Postgrad Med J 85(1003) (2009) 268-73.

[13] J. Golledge, B. Cullen, C. Moran, C. Rush, Efficacy of simvastatin in reducing aortic dilatation in mouse models of abdominal aortic aneurysm, Cardiovasc Drugs Ther 24(5-6) (2010) 373-8.

[14] E.F. Steinmetz, C. Buckley, M.L. Shames, T.L. Ennis, S.J. Vanvickle-Chavez, D. Mao, L.A. Goeddel, C.J. Hawkins, R.W. Thompson, Treatment with simvastatin suppresses the development of experimental abdominal aortic aneurysms in normal and hypercholesterolemic mice, Ann Surg 241(1) (2005) 92-101.

[15] A.N. Sapadin, R. Fleischmajer, Tetracyclines: nonantibiotic properties and their clinical implications, J Am Acad Dermatol 54(2) (2006) 258-65.

[16] B.T. Baxter, J. Matsumura, J.A. Curci, R. McBride, L. Larson, W. Blackwelder, D. Lam, M. Wijesinha, M. Terrin, N.T.C. Investigators, Effect of Doxycycline on Aneurysm Growth Among Patients With Small Infrarenal Abdominal Aortic Aneurysms: A Randomized Clinical Trial, JAMA 323(20) (2020) 2029-2038.

[17] J.C. Isenburg, D.T. Simionescu, B.C. Starcher, N.R. Vyavahare, Elastin stabilization for treatment of abdominal aortic aneurysms, Circulation 115(13) (2007) 1729-37.

[18] A. Sinha, N. Nosoudi, N. Vyavahare, Elasto-regenerative properties of polyphenols, Biochem Biophys Res Commun 444(2) (2014) 205-11.

[19] N. Nosoudi, A. Chowdhury, S. Siclari, V. Parasaram, S. Karamched, N. Vyavahare, Systemic Delivery of Nanoparticles Loaded with Pentagalloyl Glucose Protects Elastic Lamina and Prevents Abdominal Aortic Aneurysm in Rats, J Cardiovasc Transl Res 9(5-6) (2016) 445-455.

[20] M.A.D. Humphrey J.D., The Cardiovascular System - Anatomy, Physiology and Cell Biology, Springer, Vienna, 2003.

[21] E.N. Marieb, K. Hoehn, Human anatomy & physiology, 8th ed., Benjamin Cummings, San Francisco, 2010.

[22] K.T. Patton, G.A. Thibodeau, C.P. Anthony, Anthony's textbook of anatomy & physiology, 20th edition. ed., Elsevier, St. Louis, Missouri, 2013.

[23] W.H. Organization, The top 10 causes of death, 2018. https://www.who.int/en/news-room/fact-sheets/detail/the-top-10-causes-of-death.

[24] S.S. Virani, A. Alonso, E.J. Benjamin, M.S. Bittencourt, C.W. Callaway, A.P. Carson, A.M. Chamberlain, A.R. Chang, S. Cheng, F.N. Delling, L. Djousse, M.S.V. Elkind, J.F. Ferguson, M. Fornage, S.S. Khan, B.M. Kissela, K.L. Knutson, T.W. Kwan, D.T. Lackland, T.T. Lewis, J.H. Lichtman, C.T. Longenecker, M.S. Loop, P.L. Lutsey, S.S. Martin, K. Matsushita, A.E. Moran, M.E. Mussolino, A.M. Perak, W.D. Rosamond, G.A. Roth, U.K.A. Sampson, G.M. Satou, E.B. Schroeder, S.H. Shah, C.M. Shay, N.L. Spartano, A. Stokes, D.L. Tirschwell, L.B. VanWagner, C.W. Tsao, E. American Heart Association Council on, C. Prevention Statistics, S. Stroke Statistics, Heart Disease and Stroke Statistics-2020 Update: A Report From the American Heart Association, Circulation 141(9) (2020) e139-e596.

[25] American College of Cardiology, AHA 2019 Heart Disease and Stroke Statistics. https://www.acc.org/latest-in-cardiology/ten-points-to-remember/2019/02/15/14/39/aha-2019-heart-disease-and-stroke-statistics. (Accessed 2019, February 19.

[26] T.O. University, Understanding cardiovascular diseases, 2016. https://www.open.edu/openlearn/ocw/mod/oucontent/view.php?printable=1&id=2613.

[27] C.P. Sharma, Biointegration of medical implant materials : science and design, CRC Press, Woodhead, Boca Raton, Oxford, 2010.

[28] A. Fortier, V. Gullapalli, R.A. Mirshams, Review of biomechanical studies of arteries and their effect on stent performance, IJC Heart & Vessels 4 (2014) 12-18.

[29] L.A. Martinez-Lemus, The dynamic structure of arterioles, Basic Clin Pharmacol Toxicol 110(1) (2012) 5-11.

[30] OpenStax, Structure and function of blood vessels, Anatomy & Physiology, OpenStax2016, p. 131.

[31] G.J. Tortora, B. Derrickson, Principles of anatomy and physiology, 12th ed., John Wiley & Sons, Hoboken, NJ, 2010.

[32] C. Lech, A. Swaminathan, Abdominal Aortic Emergencies, Emerg Med Clin North Am 35(4) (2017) 847-867.

[33] D.D. Heistad, M.L. Marcus, G.E. Larsen, M.L. Armstrong, Role of Vasa Vasorum in Nourishment of the Aortic-Wall, Am J Physiol 240(5) (1981) H781-H787.

[34] H. Wolinsky, S. Glagov, Comparison of abdominal and thoracic aortic medial structure in mammals. Deviation of man from the usual pattern, Circ Res 25(6) (1969) 677-86.

[35] H. Kuivaniemi, E.J. Ryer, J.R. Elmore, G. Tromp, Understanding the pathogenesis of abdominal aortic aneurysms, Expert Rev Cardiovasc Ther 13(9) (2015) 975-87.

[36] C.T. Tran, F. Lui, Anatomy, Abdomen and Pelvis, Abdominal Aorta, StatPearls, Treasure Island (FL), 2020.

[37] J. Rosenbloom, W.R. Abrams, R. Mecham, Extracellular matrix 4: the elastic fiber, FASEB J 7(13) (1993) 1208-18.

[38] S. Sugita, T. Matsumoto, Multiphoton microscopy observations of 3D elastin and collagen fiber microstructure changes during pressurization in aortic media, Biomech Model Mechanobiol 16(3) (2017) 763-773.

[39] M.J. Sherratt, Tissue elasticity and the ageing elastic fibre, Age (Dordr) 31(4) (2009) 305-25.

[40] R. Wang, J. Ozsvar, G.C. Yeo, A.S. Weiss, Hierarchical assembly of elastin materials, Current Opinion in Chemical Engineering 24 (2019) 54-60.

[41] A. Tsamis, J.T. Krawiec, D.A. Vorp, Elastin and collagen fibre microstructure of the human aorta in ageing and disease: a review, J R Soc Interface 10(83) (2013) 20121004.

[42] R.P. Mecham, L. Whitehouse, M. Hay, A. Hinek, M.P. Sheetz, Ligand affinity of the 67-kD elastin/laminin binding protein is modulated by the protein's lectin domain: visualization of elastin/laminin-receptor complexes with gold-tagged ligands, J Cell Biol 113(1) (1991) 187-94.

[43] K.H. Parker, A brief history of arterial wave mechanics, Med Biol Eng Comput 47(2) (2009) 111-8.

[44] Y.T.-B. Learning, Structure and Function of Connective Tissue and Bone. http://tbl.med.yale.edu/structure_and_function_of_connective_tissue_and_bone/reading.php.

[45] M.J. Collins, J.F. Eberth, E. Wilson, J.D. Humphrey, Acute mechanical effects of elastase on the infrarenal mouse aorta: implications for models of aneurysms, J Biomech 45(4) (2012) 660-5.

[46] M.J. Chow, J.R. Mondonedo, V.M. Johnson, Y. Zhang, Progressive structural and biomechanical changes in elastin degraded aorta, Biomech Model Mechanobiol 12(2) (2013) 361-72.

[47] S. Yolbas, N. Gozel, M.N. Dagli, S.S. Koca, E. Donder, Carotid artery stiffness in Behcet's disease, Eur J Rheumatol 4(2) (2017) 122-126.

[48] M. Sauvage, N. Hinglais, C. Mandet, C. Badier, F. Deslandes, J.B. Michel, M.P. Jacob, Localization of elastin mRNA and TGF-beta1 in rat aorta and caudal artery as a function of age, Cell Tissue Res 291(2) (1998) 305-14.

[49] A.J. Cocciolone, J.Z. Hawes, M.C. Staiculescu, E.O. Johnson, M. Murshed, J.E. Wagenseil, Elastin, arterial mechanics, and cardiovascular disease, Am J Physiol Heart Circ Physiol 315(2) (2018) H189-H205.

[50] S.K. Karnik, B.S. Brooke, A. Bayes-Genis, L. Sorensen, J.D. Wythe, R.S. Schwartz, M.T. Keating, D.Y. Li, A critical role for elastin signaling in vascular morphogenesis and disease, Development 130(2) (2003) 411-23.

[51] M. Gabriela Espinosa, W.S. Gardner, L. Bennett, B.A. Sather, H. Yanagisawa, J.E. Wagenseil, The effects of elastic fiber protein insufficiency and treatment on the modulus of arterial smooth muscle cells, J Biomech Eng 136(2) (2014) 021030.

[52] A. Wahart, T. Hocine, C. Albrecht, A. Henry, T. Sarazin, L. Martiny, H. El Btaouri, P. Maurice, A. Bennasroune, B. Romier-Crouzet, S. Blaise, L. Duca, Role of elastin peptides and elastin receptor complex in metabolic and cardiovascular diseases, FEBS J 286(15) (2019) 2980-2993.

[53] A. Le Page, A. Khalil, P. Vermette, E.H. Frost, A. Larbi, J.M. Witkowski, T. Fulop, The role of elastin-derived peptides in human physiology and diseases, Matrix Biol 84 (2019) 81-96.

[54] A. Hinek, A.V. Pshezhetsky, M. von Itzstein, B. Starcher, Lysosomal sialidase (neuraminidase-1) is targeted to the cell surface in a multiprotein complex that facilitates elastic fiber assembly, J Biol Chem 281(6) (2006) 3698-710.

[55] G. Faury, M.T. Ristori, J. Verdetti, M.P. Jacob, L. Robert, Effect of elastin peptides on vascular tone, J Vasc Res 32(2) (1995) 112-9.

[56] G. Faury, Y. Usson, M. Robert-Nicoud, L. Robert, J. Verdetti, Nuclear and cytoplasmic free calcium level changes induced by elastin peptides in human endothelial cells, Proc Natl Acad Sci U S A 95(6) (1998) 2967-72.

[57] K.A. Hance, M. Tataria, S.J. Ziporin, J.K. Lee, R.W. Thompson, Monocyte chemotactic activity in human abdominal aortic aneurysms: role of elastin degradation peptides and the 67-kD cell surface elastin receptor, J Vasc Surg 35(2) (2002) 254-61.

[58] G. Guo, P. Booms, M. Halushka, H.C. Dietz, A. Ney, S. Stricker, J. Hecht, S. Mundlos, P.N. Robinson, Induction of macrophage chemotaxis by aortic extracts of the mgR Marfan mouse model and a GxxPG-containing fibrillin-1 fragment, Circulation 114(17) (2006) 1855-62.

[59] M. Hauck, I. Seres, I. Kiss, J. Saulnier, A. Mohacsi, J. Wallach, T. Fulop, Jr., Effects of synthesized elastin peptides on human leukocytes, Biochem Mol Biol Int 37(1) (1995) 45-55.

[60] R.M. Senior, G.L. Griffin, R.P. Mecham, Chemotactic responses of fibroblasts to tropoelastin and elastin-derived peptides, J Clin Invest 70(3) (1982) 614-8.

[61] T. Ooyama, K. Fukuda, H. Oda, H. Nakamura, Y. Hikita, Substratum-bound elastin peptide inhibits aortic smooth muscle cell migration in vitro, Arteriosclerosis 7(6) (1987) 593-8.

[62] M.A. Dale, W. Xiong, J.S. Carson, M.K. Suh, A.D. Karpisek, T.M. Meisinger, G.P. Casale, B.T. Baxter, Elastin-Derived Peptides Promote Abdominal Aortic Aneurysm Formation by Modulating M1/M2 Macrophage Polarization, J Immunol 196(11) (2016) 4536-43.

[63] A. Chatron-Colliet, N. Lalun, C. Terryn, S. Kurdykowski, M. Lorenzato, A. Rusciani, D. Ploton, L. Duca, H. Bobichon, The elastin peptide (VGVAPG)3 induces the 3D reorganisation of PML-NBs and SC35 speckles architecture, and accelerates proliferation of fibroblasts and melanoma cells, Histochem Cell Biol 143(3) (2015) 245-58.

[64] S. Mochizuki, B. Brassart, A. Hinek, Signaling pathways transduced through the elastin receptor facilitate proliferation of arterial smooth muscle cells, J Biol Chem 277(47) (2002) 44854-63.

[65] E.H.M. Paiman, M. Louwerens, D. Bresters, J.J.M. Westenberg, Q. Tao, R.J. van der Geest, A.C. Lankester, A.A.W. Roest, H.J. Lamb, Late effects of pediatric hematopoietic stem cell transplantation on left ventricular function, aortic stiffness and myocardial tissue characteristics, J Cardiovasc Magn Reson 21(1) (2019) 6.

[66] C. Kropidlowski, M. Meier-Schroers, D. Kuetting, A. Sprinkart, H. Schild, D. Thomas, R. Homsi, CMR based measurement of aortic stiffness, epicardial fat, left ventricular myocardial strain and fibrosis in hypertensive patients, Int J Cardiol Heart Vasc 27 (2020) 100477.

[67] R. Homsi, D. Thomas, J. Gieseke, M. Meier-Schroers, D. Dabir, D. Kuetting, J.A. Luetkens, C. Marx, H.H. Schild, A. Sprinkart, Epicardial Fat Volume and Aortic Stiffness

in Healthy Individuals: A Quantitative Cardiac Magnetic Resonance Study, Rofo 188(9) (2016) 853-8.

[68] P. Lacolley, P. Boutouyrie, M. Glukhova, J.M. Daniel Lamaziere, P.F. Plouin, P. Bruneval, P. Vuong, P. Corvol, S. Laurent, Disruption of the elastin gene in adult Williams syndrome is accompanied by a paradoxical reduction in arterial stiffness, Clin Sci (Lond) 103(1) (2002) 21-9.

[69] J. Zhang, X. Zhao, D.E. Vatner, T. McNulty, S. Bishop, Z. Sun, Y.T. Shen, L. Chen, G.A. Meininger, S.F. Vatner, Extracellular Matrix Disarray as a Mechanism for Greater Abdominal Versus Thoracic Aortic Stiffness With Aging in Primates, Arterioscler Thromb Vasc Biol 36(4) (2016) 700-6.

[70] P. Lacolley, V. Regnault, P. Segers, S. Laurent, Vascular Smooth Muscle Cells and Arterial Stiffening: Relevance in Development, Aging, and Disease, Physiol Rev 97(4) (2017) 1555-1617.

[71] X. Li, G. Zhao, J. Zhang, Z.Q. Duan, S.J. Xin, Prevalence and Trends of the Abdominal Aortic Aneurysms Epidemic in General Population - A Meta-Analysis, Plos One 8(12) (2013).

[72] D. Mozaffarian, E.J. Benjamin, A.S. Go, D.K. Arnett, M.J. Blaha, M. Cushman, S.R. Das, S. de Ferranti, J.P. Despres, H.J. Fullerton, V.J. Howard, M.D. Huffman, C.R. Isasi, M.C. Jimenez, S.E. Judd, B.M. Kissela, J.H. Lichtman, L.D. Lisabeth, S.M. Liu, R.H. Mackey, D.J. Magid, D.K. McGuire, E.R. Mohler, C.S. Moy, P. Muntner, M.E. Mussolino, K. Nasir, R.W. Neumar, G. Nichol, L. Palaniappan, D.K. Pandey, M.J. Reeves, C.J. Rodriguez, W. Rosamond, P.D. Sorlie, J. Stein, A. Towfighi, T.N. Turan, S.S. Virani, D. Woo, R.W. Yeh, M.B. Turner, A.H.A.S.C. Stroke, Executive Summary: Heart Disease and Stroke Statistics-2016 Update A Report From the American Heart Association, Circulation 133(4) (2016) 447-454.

[73] S. Aggarwal, A. Qamar, V. Sharma, A. Sharma, Abdominal aortic aneurysm: A comprehensive review, Exp Clin Cardiol 16(1) (2011) 11-15.

[74] M.E. Lindsay, H.C. Dietz, Lessons on the pathogenesis of aneurysm from heritable conditions, Nature 473(7347) (2011) 308-316.

[75] A.R. Brady, L.C. Brown, E.G.R. Fowkes, R.M. Greenhalgh, J.T. Powell, C.V. Ruckley, S.G. Thompson, U.K.S.A. Tria, Long-term outcomes of immediate repair compared with surveillance of small abdominal aortic aneurysms., New Engl J Med 346(19) (2002) 1445-1452.

[76] A. Lee, M.D. Dake, Abdominal and Thoracic Aortic Aneurysms, Springer, Cham2018.

[77] Y.W. Qin, G.P. Shi, Cysteinyl cathepsins and mast cell proteases in the pathogenesis and therapeutics of cardiovascular diseases, Pharmacol Therapeut 131(3) (2011) 338-350.

[78] G.K. Sukhova, G.P. Shi, Do cathepsins play a role in abdominal aortic aneurysm pathogenesis?, Ann Ny Acad Sci 1085 (2006) 161-169.

[79] F.M. Davis, D.L. Rateri, A. Daugherty, Abdominal aortic aneurysm: novel mechanisms and therapies, Curr Opin Cardiol 30(6) (2015) 566-73.

[80] A. Furusho, H. Aoki, S. Ohno-Urabe, M. Nishihara, S. Hirakata, N. Nishida, S. Ito, M. Hayashi, T. Imaizumi, S. Hiromatsu, H. Akashi, H. Tanaka, Y. Fukumoto, Involvement of B Cells, Immunoglobulins, and Syk in the Pathogenesis of Abdominal Aortic Aneurysm, J Am Heart Assoc 7(6) (2018).

[81] H. Kugo, H. Tanaka, T. Moriyama, N. Zaima, Pathological Implication of Adipocytes in AAA Development and the Rupture, Ann Vasc Dis 11(2) (2018) 159-168.

[82] Y. Wang, S. Krishna, P.J. Walker, P. Norman, J. Golledge, Transforming growth factor-beta and abdominal aortic aneurysms, Cardiovasc Pathol 22(2) (2013) 126-32.

[83] M. Onoda, K. Yoshimura, H. Aoki, Y. Ikeda, N. Morikage, A. Furutani, M. Matsuzaki, K. Hamano, Lysyl oxidase resolves inflammation by reducing monocyte chemoattractant protein-1 in abdominal aortic aneurysm, Atherosclerosis 208(2) (2010) 366-9.

[84] R.W. Thompson, J.A. Curci, T.L. Ennis, D. Mao, M.B. Pagano, C.T. Pham, Pathophysiology of abdominal aortic aneurysms: insights from the elastase-induced model in mice with different genetic backgrounds, Ann N Y Acad Sci 1085 (2006) 59-73.

[85] G.M. Longo, W. Xiong, T.C. Greiner, Y. Zhao, N. Fiotti, B.T. Baxter, Matrix metalloproteinases 2 and 9 work in concert to produce aortic aneurysms, J Clin Invest 110(5) (2002) 625-32.

[86] H. Lu, D.L. Rateri, D. Bruemmer, L.A. Cassis, A. Daugherty, Novel mechanisms of abdominal aortic aneurysms, Curr Atheroscler Rep 14(5) (2012) 402-12.

[87] L. Maegdefessel, R.L. Dalman, P.S. Tsao, Pathogenesis of abdominal aortic aneurysms: microRNAs, proteases, genetic associations, Annu Rev Med 65 (2014) 49-62.

[88] D.M. Milewicz, MicroRNAs, fibrotic remodeling, and aortic aneurysms, J Clin Invest 122(2) (2012) 490-3.

[89] C.W. Kim, S. Kumar, D.J. Son, I.H. Jang, K.K. Griendling, H. Jo, Prevention of abdominal aortic aneurysm by anti-microRNA-712 or anti-microRNA-205 in angiotensin II-infused mice, Arterioscler Thromb Vasc Biol 34(7) (2014) 1412-21.

[90] K. Di Gregoli, N.N. Mohamad Anuar, R. Bianco, S.J. White, A.C. Newby, S.J. George, J.L. Johnson, MicroRNA-181b Controls Atherosclerosis and Aneurysms Through Regulation of TIMP-3 and Elastin, Circ Res 120(1) (2017) 49-65.

[91] L. Maegdefessel, J. Azuma, R. Toh, A. Deng, D.R. Merk, A. Raiesdana, N.J. Leeper, U. Raaz, A.M. Schoelmerich, M.V. McConnell, R.L. Dalman, J.M. Spin, P.S. Tsao, MicroRNA-21 blocks abdominal aortic aneurysm development and nicotine-augmented expansion, Sci Transl Med 4(122) (2012) 122ra22.

[92] L.A. Cassis, M. Gupte, S. Thayer, X. Zhang, R. Charnigo, D.A. Howatt, D.L. Rateri, A. Daugherty, ANG II infusion promotes abdominal aortic aneurysms independent of increased blood pressure in hypercholesterolemic mice, Am J Physiol Heart Circ Physiol 296(5) (2009) H1660-5.

[93] B.C. Tieu, C. Lee, H. Sun, W. Lejeune, A. Recinos, 3rd, X. Ju, H. Spratt, D.C. Guo, D. Milewicz, R.G. Tilton, A.R. Brasier, An adventitial IL-6/MCP1 amplification loop accelerates macrophage-mediated vascular inflammation leading to aortic dissection in mice, J Clin Invest 119(12) (2009) 3637-51.

[94] G. Martufi, A. Forneris, J.J. Appoo, E.S. Di Martino, Is There a Role for Biomechanical Engineering in Helping to Elucidate the Risk Profile of the Thoracic Aorta?, Ann Thorac Surg 101(1) (2016) 390-8.

[95] M.R. Roach, A.C. Burton, The effect of age on the elasticity of human iliac arteries, Can J Biochem Physiol 37(4) (1959) 557-70.

[96] D.A. Vorp, Biomechanics of abdominal aortic aneurysm, J Biomech 40(9) (2007) 1887-902.

[97] J. Tong, T. Cohnert, G.A. Holzapfel, Diameter-related variations of geometrical, mechanical, and mass fraction data in the anterior portion of abdominal aortic aneurysms, Eur J Vasc Endovasc Surg 49(3) (2015) 262-70.

[98] J.D. Humphrey, G.A. Holzapfel, Mechanics, mechanobiology, and modeling of human abdominal aorta and aneurysms, J Biomech 45(5) (2012) 805-14.

[99] S.J. Cameron, H.M. Russell, A.P. Owens, 3rd, Antithrombotic therapy in abdominal aortic aneurysm: beneficial or detrimental?, Blood 132(25) (2018) 2619-2628.

[100] S.L. Muluk, P.D. Muluk, J. Shum, E.A. Finol, On the Use of Geometric Modeling to Predict Aortic Aneurysm Rupture, Ann Vasc Surg 44 (2017) 190-196.

[101] S.S. Raut, S. Chandra, J. Shum, E.A. Finol, The role of geometric and biomechanical factors in abdominal aortic aneurysm rupture risk assessment, Ann Biomed Eng 41(7) (2013) 1459-77.

[102] J.D. HUMPHREY, K.R. RAJAGOPAL, A CONSTRAINED MIXTURE MODEL FOR GROWTH AND REMODELING OF SOFT TISSUES, Mathematical Models and Methods in Applied Sciences 12(03) (2002) 407-430.

[103] P. Erhart, J. Roy, J.P. de Vries, M.L. Liljeqvist, C. Grond-Ginsbach, A. Hyhlik-Durr, D. Bockler, Prediction of Rupture Sites in Abdominal Aortic Aneurysms After Finite Element Analysis, J Endovasc Ther 23(1) (2016) 115-20.

[104] H. Jalalzadeh, E.L. Leemans, R. Indrakusuma, R.N. Planken, M.J.W. Koelemay, C.J. Zeebregts, H.A. Marquering, M.J. van der Laan, R. Balm, Estimation of Abdominal Aortic Aneurysm Rupture Risk with Biomechanical Imaging Markers, J Vasc Interv Radiol 30(7) (2019) 987-994 e4.

[105] C.A. Figueroa, S. Baek, C.A. Taylor, J.D. Humphrey, A Computational Framework for Fluid-Solid-Growth Modeling in Cardiovascular Simulations, Comput Methods Appl Mech Eng 198(45-46) (2009) 3583-3602.

[106] A. Sheidaei, S.C. Hunley, S. Zeinali-Davarani, L.G. Raguin, S. Baek, Simulation of abdominal aortic aneurysm growth with updating hemodynamic loads using a realistic geometry, Med Eng Phys 33(1) (2011) 80-8.

[107] S. Zeinali-Davarani, L.G. Raguin, D.A. Vorp, S. Baek, Identification of in vivo material and geometric parameters of a human aorta: toward patient-specific modeling of abdominal aortic aneurysm, Biomech Model Mechanobiol 10(5) (2011) 689-99.

[108] S. Khosla, D.R. Morris, J.V. Moxon, P.J. Walker, T.C. Gasser, J. Golledge, Meta-analysis of peak wall stress in ruptured, symptomatic and intact abdominal aortic aneurysms, Br J Surg 101(11) (2014) 1350-7; discussion 1357.

[109] T.C. Gasser, Biomechanical Rupture Risk Assessment: A Consistent and Objective Decision-Making Tool for Abdominal Aortic Aneurysm Patients, Aorta (Stamford) 4(2) (2016) 42-60.

[110] M.E. Groeneveld, J.P. Meekel, S.M. Rubinstein, L.R. Merkestein, G.J. Tangelder, W. Wisselink, M. Truijers, K.K. Yeung, Systematic Review of Circulating, Biomechanical, and Genetic Markers for the Prediction of Abdominal Aortic Aneurysm Growth and Rupture, J Am Heart Assoc 7(13) (2018).

[111] J.S. Lindholt, L. Heickendorff, S. Vammen, H. Fasting, E.W. Henneberg, Five-year results of elastin and collagen markers as predictive tools in the management of small abdominal aortic aneurysms, Eur J Vasc Endovasc Surg 21(3) (2001) 235-40.

[112] O. Morel, D. Mandry, E. Micard, C. Kauffmann, Z. Lamiral, A. Verger, E. Chevalier-Mathias, J. Mathias, G. Karcher, B. Meneroux, P. Rossignol, P.Y. Marie, Evidence of Cyclic Changes in the Metabolism of Abdominal Aortic Aneurysms During Growth

Phases: (1)(8)F-FDG PET Sequential Observational Study, J Nucl Med 56(7) (2015) 1030-5.

[113] C.W. Kotze, A.M. Groves, L.J. Menezes, R. Harvey, R. Endozo, I.A. Kayani, P.J. Ell, S.W. Yusuf, What is the relationship between (1)(8)F-FDG aortic aneurysm uptake on PET/CT and future growth rate?, Eur J Nucl Med Mol Imaging 38(8) (2011) 1493-9.

[114] C.W. Kotze, J.H. Rudd, B. Ganeshan, L.J. Menezes, J. Brookes, O. Agu, S.W. Yusuf, A.M. Groves, CT signal heterogeneity of abdominal aortic aneurysm as a possible predictive biomarker for expansion, Atherosclerosis 233(2) (2014) 510-7.

[115] C. Reeps, M. Essler, J. Pelisek, S. Seidl, H.H. Eckstein, B.J. Krause, Increased 18F-fluorodeoxyglucose uptake in abdominal aortic aneurysms in positron emission/computed tomography is associated with inflammation, aortic wall instability, and acute symptoms, J Vasc Surg 48(2) (2008) 417-23; discussion 424.

[116] J.S. Wilson, L. Virag, P. Di Achille, I. Karsaj, J.D. Humphrey, Biochemomechanics of intraluminal thrombus in abdominal aortic aneurysms, J Biomech Eng 135(2) (2013) 021011.

[117] A. Piechota-Polanczyk, A. Jozkowicz, W. Nowak, W. Eilenberg, C. Neumayer, T. Malinski, I. Huk, C. Brostjan, The Abdominal Aortic Aneurysm and Intraluminal Thrombus: Current Concepts of Development and Treatment, Front Cardiovasc Med 2 (2015) 19.

[118] S.J. Haller, J.D. Crawford, K.M. Courchaine, C.J. Bohannan, G.J. Landry, G.L. Moneta, A.F. Azarbal, S. Rugonyi, Intraluminal thrombus is associated with early rupture of abdominal aortic aneurysm, J Vasc Surg 67(4) (2018) 1051-1058 e1.

[119] C.M. Bhamidipati, G.S. Mehta, G. Lu, C.W. Moehle, C. Barbery, P.D. DiMusto, A. Laser, I.L. Kron, G.R. Upchurch, Jr., G. Ailawadi, Development of a novel murine model of aortic aneurysms using peri-adventitial elastase, Surgery 152(2) (2012) 238-46.

[120] G. Lu, G. Su, J.P. Davis, B. Schaheen, E. Downs, R.J. Roy, G. Ailawadi, G.R. Upchurch, Jr., A novel chronic advanced stage abdominal aortic aneurysm murine model, J Vasc Surg 66(1) (2017) 232-242 e4.

[121] Q. Wang, T. Zhou, Z. Liu, J. Ren, N. Phan, K. Gupta, D.M. Stewart, S. Morgan, C. Assa, K.C. Kent, B. Liu, Inhibition of Receptor-Interacting Protein Kinase 1 with Necrostatin-1s ameliorates disease progression in elastase-induced mouse abdominal aortic aneurysm model, Sci Rep 7 (2017) 42159.

[122] D.M. Basalyga, D.T. Simionescu, W. Xiong, B.T. Baxter, B.C. Starcher, N.R. Vyavahare, Elastin degradation and calcification in an abdominal aorta injury model: role of matrix metalloproteinases, Circulation 110(22) (2004) 3480-7.

[123] A. Maier, M.W. Gee, C. Reeps, H.H. Eckstein, W.A. Wall, Impact of calcifications on patient-specific wall stress analysis of abdominal aortic aneurysms, Biomech Model Mechanobiol 9(5) (2010) 511-21.

[124] B.C. Berk, J. Haendeler, J. Sottile, Angiotensin II, atherosclerosis, and aortic aneurysms, J Clin Invest 105(11) (2000) 1525-6.

[125] K. Gopal, P. Nagarajan, J. Jedy, A.T. Raj, S.K. Gnanaselvi, P. Jahan, Y. Sharma, E.M. Shankar, J.M. Kumar, beta-Carotene Attenuates Angiotensin II-Induced Aortic Aneurysm by Alleviating Macrophage Recruitment in Apoe(-/-) Mice, Plos One 8(6) (2013) e67098.

[126] A. Daugherty, M.W. Manning, L.A. Cassis, Angiotensin II promotes atherosclerotic lesions and aneurysms in apolipoprotein E-deficient mice, J Clin Invest 105(11) (2000) 1605-12.

[127] J.L. Poulsen, J. Stubbe, J.S. Lindholt, Animal Models Used to Explore Abdominal Aortic Aneurysms: A Systemic Review, European Journal of Vascular and Endovascular Surgery 52(4) (2016) 487-499.

[128] E. Allaire, P. Bruneval, C. Mandet, J.P. Becquemin, J.B. Michel, The immunogenicity of the extracellular matrix in arterial xenografts, Surgery 122(1) (1997) 73-81.

[129] E. Allaire, R. Forough, M. Clowes, B. Starcher, A.W. Clowes, Local overexpression of TIMP-1 prevents aortic aneurysm degeneration and rupture in a rat model, J Clin Invest 102(7) (1998) 1413-20.

[130] M. Matsushita, H. Kobayashi, K. Oda, N. Nishikimi, T. Sakurai, Y. Nimura, A rabbit model of abdominal aortic aneurysm associated with intimal thickening, Eur Surg Res 31(4) (1999) 305-13.

[131] T. Freestone, R.J. Turner, D.J. Higman, M.J. Lever, J.T. Powell, Influence of hypercholesterolemia and adventitial inflammation on the development of aortic aneurysm in rabbits, Arterioscler Thromb Vasc Biol 17(1) (1997) 10-7.

[132] K. Furubayashi, S. Takai, D. Jin, M. Muramatsu, T. Ibaraki, M. Nishimoto, H. Fukumoto, T. Katsumata, M. Miyazaki, The significance of chymase in the progression of abdominal aortic aneurysms in dogs, Hypertens Res 30(4) (2007) 349-57.

[133] S. Lerouge, J. Raymond, I. Salazkin, Z. Qin, L. Gaboury, G. Cloutier, V.L. Oliva, G. Soulez, Endovascular aortic aneurysm repair with stent-grafts: experimental models can reproduce endoleaks, J Vasc Interv Radiol 15(9) (2004) 971-9.

[134] W.D. Jordan, Jr., L.K. Sampson, S. Iyer, P.G. Anderson, K. Lyle, R.J. Brown, J. Luo, G.S. Roubin, Abdominal aortic aneurysm repair via percutaneous endovascular stenting in the swine model, Am Surg 64(11) (1998) 1070-3.

[135] J.V. Moxon, A. Parr, T.I. Emeto, P. Walker, P.E. Norman, J. Golledge, Diagnosis and monitoring of abdominal aortic aneurysm: current status and future prospects, Curr Probl Cardiol 35(10) (2010) 512-48.

[136] L.J. Wang, A.M. Prabhakar, C.J. Kwolek, Current status of the treatment of infrarenal abdominal aortic aneurysms, Cardiovasc Diagn Ther 8(Suppl 1) (2018) S191-S199.

[137] A.R. Sparks, P.L. Johnson, M.C. Meyer, Imaging of abdominal aortic aneurysms, Am Fam Physician 65(8) (2002) 1565-70.

[138] A. Klink, F. Hyafil, J. Rudd, P. Faries, V. Fuster, Z. Mallat, O. Meilhac, W.J. Mulder, J.B. Michel, F. Ramirez, G. Storm, R. Thompson, I.C. Turnbull, J. Egido, J.L. Martin-Ventura, C. Zaragoza, D. Letourneur, Z.A. Fayad, Diagnostic and therapeutic strategies for small abdominal aortic aneurysms, Nat Rev Cardiol 8(6) (2011) 338-47.

[139] R.M. Summers, J. Andrasko-Bourgeois, I.M. Feuerstein, S.C. Hill, E.C. Jones, M.K. Busse, B. Wise, K.E. Bove, B.A. Rishforth, E. Tucker, T.L. Spray, J.M. Hoeg, Evaluation of the aortic root by MRI: insights from patients with homozygous familial hypercholesterolemia, Circulation 98(6) (1998) 509-18.

[140] J.W. van Keulen, J. van Prehn, M. Prokop, F.L. Moll, J.A. van Herwaarden, Dynamics of the aorta before and after endovascular aneurysm repair: a systematic review, Eur J Vasc Endovasc Surg 38(5) (2009) 586-96.

[141] H. Lusic, M.W. Grinstaff, X-ray-computed tomography contrast agents, Chem Rev 113(3) (2013) 1641-66.

[142] L. Caschera, A. Lazzara, L. Piergallini, D. Ricci, B. Tuscano, A. Vanzulli, Contrast agents in diagnostic imaging: Present and future, Pharmacol Res 110 (2016) 65-75.

[143] H. Katayama, K. Yamaguchi, T. Kozuka, T. Takashima, P. Seez, K. Matsuura, Adverse reactions to ionic and nonionic contrast media. A report from the Japanese Committee on the Safety of Contrast Media, Radiology 175(3) (1990) 621-8.

[144] F. Hallouard, N. Anton, P. Choquet, A. Constantinesco, T. Vandamme, Iodinated blood pool contrast media for preclinical X-ray imaging applications--a review, Biomaterials 31(24) (2010) 6249-68.

[145] R. Solomon, Contrast media: are there differences in nephrotoxicity among contrast media?, Biomed Res Int 2014 (2014) 934947.

[146] E.E. Coche, F.D. Hammer, P.P. Goffette, Demonstration of pulmonary embolism with gadolinium-enhanced spiral CT, Eur Radiol 11(11) (2001) 2306-9.

[147] L. Smadja, M. Remy-Jardin, P. Dupuis, V. Deken-Delannoy, P. Devos, A. Duhamel, J.J. Laffitte, P. Dequiedt, J. Remy, [Gadolinium-enhanced thoracic CTA: retrospective analysis of image quality and tolerability in 45 patients evaluated prior to the description of nephrogenic systemic fibrosis], J Radiol 90(3 Pt 1) (2009) 287-98.

[148] J.M. Idee, M. Port, C. Robic, C. Medina, M. Sabatou, C. Corot, Role of thermodynamic and kinetic parameters in gadolinium chelate stability, J Magn Reson Imaging 30(6) (2009) 1249-58.

[149] H. Schmitt-Willich, Stability of linear and macrocyclic gadolinium based contrast agents, Br J Radiol 80(955) (2007) 581-2; author reply 584-5.

[150] H. Akgun, G. Gonlusen, J. Cartwright, Jr., W.N. Suki, L.D. Truong, Are gadolinium-based contrast media nephrotoxic? A renal biopsy study, Arch Pathol Lab Med 130(9) (2006) 1354-7.

[151] H. Blasco-Perrin, B. Glaser, M. Pienkowski, J.M. Peron, J.L. Payen, Gadolinium induced recurrent acute pancreatitis, Pancreatology 13(1) (2013) 88-9.

[152] F.K. Hui, M. Mullins, Persistence of gadolinium contrast enhancement in CSF: a possible harbinger of gadolinium neurotoxicity?, AJNR Am J Neuroradiol 30(1) (2009) E1.

[153] Y. Liu, J. Liu, K. Ai, Q. Yuan, L. Lu, Recent advances in ytterbium-based contrast agents for in vivo X-ray computed tomography imaging: promises and prospects, Contrast Media Mol Imaging 9(1) (2014) 26-36.

[154] A. Jakhmola, N. Anton, T.F. Vandamme, Inorganic nanoparticles based contrast agents for X-ray computed tomography, Adv Healthc Mater 1(4) (2012) 413-31.

[155] Y.F. Li, C. Chen, Fate and toxicity of metallic and metal-containing nanoparticles for biomedical applications, Small 7(21) (2011) 2965-80.

[156] A. Silvestri, L. Polito, G. Bellani, V. Zambelli, R.P. Jumde, R. Psaro, C. Evangelisti, Gold nanoparticles obtained by aqueous digestive ripening: Their application as X-ray contrast agents, J Colloid Interface Sci 439 (2015) 28-33.

[157] L. Zu, L. Liu, Y. Qin, H. Liu, H. Yang, Multifunctional BSA-Au nanostars for photoacoustic imaging and X-ray computed tomography, Nanomedicine 12(7) (2016) 1805-1813.

[158] I.C. Sun, D.K. Eun, J.H. Na, S. Lee, I.J. Kim, I.C. Youn, C.Y. Ko, H.S. Kim, D. Lim, K. Choi, P.B. Messersmith, T.G. Park, S.Y. Kim, I.C. Kwon, K. Kim, C.H. Ahn, Heparin-coated gold nanoparticles for liver-specific CT imaging, Chemistry 15(48) (2009) 13341-7.

[159] B.M. Cullum, E.S. McLamore, SPIE (Society), Smart biomedical and physiological sensor technology VIII : 28 April 2011, Orlando, Florida, United States, SPIE, Bellingham, Washington, 2011.

[160] R. Popovtzer, A. Agrawal, N.A. Kotov, A. Popovtzer, J. Balter, T.E. Carey, R. Kopelman, Targeted gold nanoparticles enable molecular CT imaging of cancer, Nano Lett 8(12) (2008) 4593-6.

[161] J.F. Hainfeld, M.J. O'Connor, F.A. Dilmanian, D.N. Slatkin, D.J. Adams, H.M. Smilowitz, Micro-CT enables microlocalisation and quantification of Her2-targeted gold nanoparticles within tumour regions, Br J Radiol 84(1002) (2011) 526-33.

[162] M.H. Oh, N. Lee, H. Kim, S.P. Park, Y. Piao, J. Lee, S.W. Jun, W.K. Moon, S.H. Choi, T. Hyeon, Large-scale synthesis of bioinert tantalum oxide nanoparticles for X-ray computed tomography imaging and bimodal image-guided sentinel lymph node mapping, J Am Chem Soc 133(14) (2011) 5508-15.

[163] O. Rabin, J. Manuel Perez, J. Grimm, G. Wojtkiewicz, R. Weissleder, An X-ray computed tomography imaging agent based on long-circulating bismuth sulphide nanoparticles, Nat Mater 5(2) (2006) 118-22.

[164] P. Balaz, Over view of up to date treatment modalities of asymptomatic abdominal aortic aneurysm, Cor et Vasa 54 (2012) E253-E257.

[165] S.G. Thompson, L.C. Brown, M.J. Sweeting, M.J. Bown, L.G. Kim, M.J. Glover, M.J. Buxton, J.T. Powell, Systematic review and meta-analysis of the growth and rupture rates of small abdominal aortic aneurysms: implications for surveillance intervals and their cost-effectiveness, Health Technol Assess 17(41) (2013) 1-118.

[166] M.L. Schermerhorn, A.J. O'Malley, A. Jhaveri, P. Cotterill, F. Pomposelli, B.E. Landon, Endovascular vs. open repair of abdominal aortic aneurysms in the Medicare population, N Engl J Med 358(5) (2008) 464-74.

[167] P.A. Gordon, B. Toursarkissian, Treatment of abdominal aortic aneurysms: the role of endovascular repair, AORN J 100(3) (2014) 241-59.

[168] D. Singh, S.K. Srivastava, T.K. Chaudhuri, G. Upadhyay, Multifaceted role of matrix metalloproteinases (MMPs), Front Mol Biosci 2 (2015) 19.

[169] N. Nosoudi, P. Nahar-Gohad, A. Sinha, A. Chowdhury, P. Gerard, C.G. Carsten, B.H. Gray, N.R. Vyavahare, Prevention of abdominal aortic aneurysm progression by targeted inhibition of matrix metalloproteinase activity with batimastat-loaded nanoparticles, Circ Res 117(11) (2015) e80-9.

[170] G.N. Smith, Jr., K.D. Brandt, K.A. Hasty, Activation of recombinant human neutrophil procollagenase in the presence of doxycycline results in fragmentation of the enzyme and loss of enzyme activity, Arthritis Rheum 39(2) (1996) 235-44.

[171] H. Abu Ali, V.M. Dembitsky, M. Srebnik, Contemporary aspects of boron : chemistry and biological applications, 1st ed., Elsevier, Amsterdam ; Boston, 2005.

[172] R.E. Vandenbroucke, C. Libert, Is there new hope for therapeutic matrix metalloproteinase inhibition?, Nat Rev Drug Discov 13(12) (2014) 904-27.

[173] M.S. Hayden, S. Ghosh, Shared principles in NF-kappaB signaling, Cell 132(3) (2008) 344-62.

[174] T. Saito, Y. Hasegawa, Y. Ishigaki, T. Yamada, J. Gao, J. Imai, K. Uno, K. Kaneko, T. Ogihara, T. Shimosawa, T. Asano, T. Fujita, Y. Oka, H. Katagiri, Importance of endothelial NF-kappaB signalling in vascular remodelling and aortic aneurysm formation, Cardiovasc Res 97(1) (2013) 106-14.

[175] K.G. Daniel, D. Chen, S. Orlu, Q.C. Cui, F.R. Miller, Q.P. Dou, Clioquinol and pyrrolidine dithiocarbamate complex with copper to form proteasome inhibitors and apoptosis inducers in human breast cancer cells, Breast Cancer Res 7(6) (2005) R897-908.

[176] Y.J. Nai, Z.W. Jiang, Z.M. Wang, N. Li, J.S. Li, Prevention of cancer cachexia by pyrrolidine dithiocarbamate (PDTC) in colon 26 tumor-bearing mice, JPEN J Parenter Enteral Nutr 31(1) (2007) 18-25.

[177] A.B. Nathens, R. Bitar, C. Davreux, M. Bujard, J.C. Marshall, A.P. Dackiw, R.W. Watson, O.D. Rotstein, Pyrrolidine dithiocarbamate attenuates endotoxin-induced acute lung injury, Am J Respir Cell Mol Biol 17(5) (1997) 608-16.

[178] P. Lauzurica, S. Martinez-Martinez, M. Marazuela, P. Gomez del Arco, C. Martinez, F. Sanchez-Madrid, J.M. Redondo, Pyrrolidine dithiocarbamate protects mice from lethal shock induced by LPS or TNF-alpha, Eur J Immunol 29(6) (1999) 1890-900.

[179] E.H. Lee, S.S. Kim, S.R. Seo, Pyrrolidine dithiocarbamate (PDTC) inhibits inflammatory signaling via expression of regulator of calcineurin activity 1 (RCAN1): Anti-inflammatory mechanism of PDTC through RCAN1 induction, Biochem Pharmacol 143 (2017) 107-117.

[180] K. Yoshimura, H. Aoki, Recent advances in pharmacotherapy development for abdominal aortic aneurysm, Int J Vasc Med 2012 (2012) 648167.

[181] J. Cheng, S.N. Koenig, H.S. Kuivaniemi, V. Garg, C.P. Hans, Pharmacological inhibitor of notch signaling stabilizes the progression of small abdominal aortic aneurysm in a mouse model, J Am Heart Assoc 3(6) (2014) e001064.

[182] F.E. Parodi, D. Mao, T.L. Ennis, M.A. Bartoli, R.W. Thompson, Suppression of experimental abdominal aortic aneurysms in mice by treatment with pyrrolidine dithiocarbamate, an antioxidant inhibitor of nuclear factor-kappaB, J Vasc Surg 41(3) (2005) 479-89.

[183] M.K. Jain, P.M. Ridker, Anti-inflammatory effects of statins: clinical evidence and basic mechanisms, Nat Rev Drug Discov 4(12) (2005) 977-87.

[184] U. Schonbeck, P. Libby, Inflammation, immunity, and HMG-CoA reductase inhibitors: statins as antiinflammatory agents?, Circulation 109(21 Suppl 1) (2004) II18-26.

[185] M. Takemoto, J.K. Liao, Pleiotropic effects of 3-hydroxy-3-methylglutaryl coenzyme a reductase inhibitors, Arterioscler Thromb Vasc Biol 21(11) (2001) 1712-9.

[186] K. Yoshimura, A. Nagasawa, J. Kudo, M. Onoda, N. Morikage, A. Furutani, H. Aoki, K. Hamano, Inhibitory effect of statins on inflammation-related pathways in human abdominal aortic aneurysm tissue, Int J Mol Sci 16(5) (2015) 11213-28.

[187] H. Nagashima, Y. Aoka, Y. Sakomura, A. Sakuta, S. Aomi, N. Ishizuka, N. Hagiwara, M. Kawana, H. Kasanuki, A 3-hydroxy-3-methylglutaryl coenzyme A reductase

inhibitor, cerivastatin, suppresses production of matrix metalloproteinase-9 in human abdominal aortic aneurysm wall, J Vasc Surg 36(1) (2002) 158-63.

[188] R. Sukhija, W.S. Aronow, R. Sandhu, P. Kakar, S. Babu, Mortality and size of abdominal aortic aneurysm at long-term follow-up of patients not treated surgically and treated with and without statins, Am J Cardiol 97(2) (2006) 279-80.

[189] B. Guzik, A. Sagan, D. Ludew, W. Mrowiecki, M. Chwala, B. Bujak-Gizycka, G. Filip, G. Grudzien, B. Kapelak, K. Zmudka, T. Mrowiecki, J. Sadowski, R. Korbut, T.J. Guzik, Mechanisms of oxidative stress in human aortic aneurysms--association with clinical risk factors for atherosclerosis and disease severity, Int J Cardiol 168(3) (2013) 2389-96.

[190] D. Gavrila, W.G. Li, M.L. McCormick, M. Thomas, A. Daugherty, L.A. Cassis, F.J. Miller, Jr., L.W. Oberley, K.C. Dellsperger, N.L. Weintraub, Vitamin E inhibits abdominal aortic aneurysm formation in angiotensin II-infused apolipoprotein E-deficient mice, Arterioscler Thromb Vasc Biol 25(8) (2005) 1671-7.

[191] K. Muttardi, A. Haydar, C.K. Phua, N. Chapman, M. Jenkins, N.J. Cheshire, C.D. Bicknell, An underused opportunity to introduce ACE inhibitors and influence prognosis: observational study of patients undergoing aortic surgery, JRSM Short Rep 4(6) (2013) 2042533313484145.

[192] F.H. Messerli, S. Bangalore, C. Bavishi, S.F. Rimoldi, Angiotensin-Converting Enzyme Inhibitors in Hypertension: To Use or Not to Use?, J Am Coll Cardiol 71(13) (2018) 1474-1482.

[193] K.E. Kortekaas, C.A. Meijer, J.W. Hinnen, R.L. Dalman, B. Xu, J.F. Hamming, J.H. Lindeman, ACE inhibitors potently reduce vascular inflammation, results of an open proof-of-concept study in the abdominal aortic aneurysm, Plos One 9(12) (2014) e111952.

[194] S. Liao, M. Miralles, B.J. Kelley, J.A. Curci, M. Borhani, R.W. Thompson, Suppression of experimental abdominal aortic aneurysms in the rat by treatment with angiotensin-converting enzyme inhibitors, J Vasc Surg 33(5) (2001) 1057-64.

[195] H. Xuan, B. Xu, W. Wang, H. Tanaka, N. Fujimura, M. Miyata, S.A. Michie, R.L. Dalman, Inhibition or deletion of angiotensin II type 1 receptor suppresses elastase-induced experimental abdominal aortic aneurysms, J Vasc Surg 67(2) (2018) 573-584 e2.

[196] Y. Fujiwara, S. Shiraya, T. Miyake, S. Yamakawa, M. Aoki, H. Makino, M. Nishimura, R. Morishita, Inhibition of experimental abdominal aortic aneurysm in a rat model by the angiotensin receptor blocker valsartan, Int J Mol Med 22(6) (2008) 703-8.

[197] H. Shan, S. Zhang, X. Li, K. Yu, X. Zhao, X. Chen, B. Jin, X. Bai, Valsartan ameliorates ageing-induced aorta degeneration via angiotensin II type 1 receptor-mediated ERK activity, J Cell Mol Med 18(6) (2014) 1071-80.

[198] Y. Pei, Y.F. Xiang, J.N. Chen, C.H. Lu, J. Hao, Q. Du, C.C. Lai, C. Qu, S. Li, H.Q. Ju, Z. Ren, Q.Y. Liu, S. Xiong, C.W. Qian, F.L. Zeng, P.Z. Zhang, C.R. Yang, Y.J. Zhang, J. Xu, K. Kitazato, Y.F. Wang, Pentagalloylglucose downregulates cofilin1 and inhibits HSV-1 infection, Antiviral Res 89(1) (2011) 98-108.

[199] C. Torres-León, J. Ventura-Sobrevilla, L. Serna-Cock, J.A. Ascacio-Valdés, J. Contreras-Esquivel, C.N. Aguilar, Pentagalloylglucose (PGG): A valuable phenolic compound with functional properties, Journal of Functional Foods 37 (2017) 176-189.

[200] J.C. Isenburg, D.T. Simionescu, B.C. Starcher, N.R. Vyavahare, Elastin stabilization for treatment of abdominal aortic aneurysms, Circulation 115(13) (2007) 1729-1737.

[201] S. Dhital, N.R. Vyavahare, Nanoparticle-based targeted delivery of pentagalloyl glucose reverses elastase-induced abdominal aortic aneurysm and restores aorta to the healthy state in mice, Plos One 15(3) (2020) e0227165.

[202] P. Hegde, P. Agrawal, P.K. Gupta, POLYPHENOLS -A USEFUL BIOMATERIAL : A REVIEW, Journal of Environmental Research And Development 10(03) (2016) 547-554.

[203] C.J. Epstein, R.P. Erickson, A.J. Wynshaw-Boris, Inborn errors of development : the molecular basis of clinical disorders of morphogenesis, Oxford University Press, Oxford ; New York, 2004.

[204] M. Au, T.I. Emeto, J. Power, V.N. Vangaveti, H.C. Lai, Emerging Therapeutic Potential of Nanoparticles in Pancreatic Cancer: A Systematic Review of Clinical Trials, Biomedicines 4(3) (2016).

[205] V.M. Tysseling-Mattiace, V. Sahni, K.L. Niece, D. Birch, C. Czeisler, M.G. Fehlings, S.I. Stupp, J.A. Kessler, Self-assembling nanofibers inhibit glial scar formation and promote axon elongation after spinal cord injury, J Neurosci 28(14) (2008) 3814-23.

[206] E.H. Jeong, G. Jung, C.A. Hong, H. Lee, Gold nanoparticle (AuNP)-based drug delivery and molecular imaging for biomedical applications, Arch Pharm Res 37(1) (2014) 53-9.

[207] X. Bai, F. Purcell-Milton, Y.K. Gun'ko, Optical Properties, Synthesis, and Potential Applications of Cu-Based Ternary or Quaternary Anisotropic Quantum Dots, Polytypic Nanocrystals, and Core/Shell Heterostructures, Nanomaterials (Basel) 9(1) (2019).

[208] L.M. Bauer, S.F. Situ, M.A. Griswold, A.C. Samia, High-performance iron oxide nanoparticles for magnetic particle imaging - guided hyperthermia (hMPI), Nanoscale 8(24) (2016) 12162-9.

[209] C.T. Matea, T. Mocan, F. Tabaran, T. Pop, O. Mosteanu, C. Puia, C. Iancu, L. Mocan, Quantum dots in imaging, drug delivery and sensor applications, Int J Nanomedicine 12 (2017) 5421-5431.

[210] K. El-Boubbou, Magnetic iron oxide nanoparticles as drug carriers: preparation, conjugation and delivery, Nanomedicine (Lond) 13(8) (2018) 929-952.

[211] H. Jahangirian, K. Kalantari, Z. Izadiyan, R. Rafiee-Moghaddam, K. Shameli, T.J. Webster, A review of small molecules and drug delivery applications using gold and iron nanoparticles, Int J Nanomedicine 14 (2019) 1633-1657.

[212] F. Dilnawaz, Polymeric Biomaterial and Lipid Based Nanoparticles for Oral Drug Delivery, Curr Med Chem 24(22) (2017) 2423-2438.

[213] J.Y. Yhee, J. Lee, H. Chang, J. Lee, I.C. Kwon, K. Kim, Molecular imaging and targeted drug delivery using albumin-based nanoparticles, Curr Pharm Des 21(14) (2015) 1889-98.

[214] L. Palmerston Mendes, J. Pan, V.P. Torchilin, Dendrimers as Nanocarriers for Nucleic Acid and Drug Delivery in Cancer Therapy, Molecules 22(9) (2017).

[215] T.I. Emeto, F.O. Alele, A.M. Smith, F.M. Smith, T. Dougan, J. Golledge, Use of Nanoparticles As Contrast Agents for the Functional and Molecular Imaging of Abdominal Aortic Aneurysm, Front Cardiovasc Med 4 (2017) 16.

[216] D.E. Owens, 3rd, N.A. Peppas, Opsonization, biodistribution, and pharmacokinetics of polymeric nanoparticles, Int J Pharm 307(1) (2006) 93-102.

[217] S.K. Sahoo, V. Labhasetwar, Nanotech approaches to drug delivery and imaging, Drug Discovery Today 8(24) (2003) 1112-1120.

[218] S.R. Alam, C. Stirrat, J. Richards, S. Mirsadraee, S.I. Semple, G. Tse, P. Henriksen, D.E. Newby, Vascular and plaque imaging with ultrasmall superparamagnetic particles of iron oxide, J Cardiovasc Magn Reson 17 (2015) 83.

[219] M. Suzuki, L. Bachelet-Violette, F. Rouzet, A. Beilvert, G. Autret, M. Maire, C. Menager, L. Louedec, C. Choqueux, P. Sabboural, O. Haddad, C. Chauvierre, F. Chaubet, J.B. Michel, J.M. Serfaty, D. Letourneur, Ultrasmall superparamagnetic iron oxide nanoparticles coated with fucoidan for molecular MRI of intraluminal thrombus, Nanomedicine (Lond) 10(1) (2015) 73-87.

[220] G.H. Turner, A.R. Olzinski, R.E. Bernard, K. Aravindhan, R.J. Boyle, M.J. Newman, S.D. Gardner, R.N. Willette, P.J. Gough, B.M. Jucker, Assessment of macrophage infiltration in a murine model of abdominal aortic aneurysm, J Magn Reson Imaging 30(2) (2009) 455-60.

[221] Y. Yao, Y. Wang, Y. Zhang, Y. Li, Z. Sheng, S. Wen, G. Ma, N. Liu, F. Fang, G.J. Teng, In vivo imaging of macrophages during the early-stages of abdominal aortic aneurysm using high resolution MRI in ApoE mice, Plos One 7(3) (2012) e33523.

[222] U. Sadat, V. Taviani, A.J. Patterson, V.E. Young, M.J. Graves, Z. Teng, T.Y. Tang, J.H. Gillard, Ultrasmall superparamagnetic iron oxide-enhanced magnetic resonance imaging of abdominal aortic aneurysms--a feasibility study, Eur J Vasc Endovasc Surg 41(2) (2011) 167-74.

[223] M. Nahrendorf, E. Keliher, B. Marinelli, F. Leuschner, C.S. Robbins, R.E. Gerszten, M.J. Pittet, F.K. Swirski, R. Weissleder, Detection of macrophages in aortic aneurysms by nanoparticle positron emission tomography-computed tomography, Arterioscler Thromb Vasc Biol 31(4) (2011) 750-7.

[224] J.F. Coelho, P.C. Ferreira, P. Alves, R. Cordeiro, A.C. Fonseca, J.R. Gois, M.H. Gil, Drug delivery systems: Advanced technologies potentially applicable in personalized treatments, EPMA J 1(1) (2010) 164-209.

[225] D. Bennet, S. Kim, Polymer Nanoparticles for Smart Drug Delivery, 2014.

[226] E. Agyare, K. Kandimalla, Delivery of Polymeric Nanoparticles to Target Vascular Diseases, J Biomol Res Ther 3(1) (2014).

[227] B. Tyler, D. Gullotti, A. Mangraviti, T. Utsuki, H. Brem, Polylactic acid (PLA) controlled delivery carriers for biomedical applications, Adv Drug Deliv Rev 107 (2016) 163-175.

[228] A. Mahapatro, D.K. Singh, Biodegradable nanoparticles are excellent vehicle for site directed in-vivo delivery of drugs and vaccines, J Nanobiotechnology 9 (2011) 55.

[229] A. Sinha, A. Shaporev, N. Nosoudi, Y. Lei, A. Vertegel, S. Lessner, N. Vyavahare, Nanoparticle targeting to diseased vasculature for imaging and therapy, Nanomedicine 10(5) (2014) 1003-12.

[230] P. Rafiei, A. Haddadi, Docetaxel-loaded PLGA and PLGA-PEG nanoparticles for intravenous application: pharmacokinetics and biodistribution profile, Int J Nanomedicine 12 (2017) 935-947.

[231] B. Sivaraman, A. Sylvester, A. Ramamurthi, Fibrinolytic PLGA nanoparticles for slow clot lysis within abdominal aortic aneurysms attenuate proteolytic loss of vascular elastic matrix, Mater Sci Eng C Mater Biol Appl 59 (2016) 145-156.

[232] A. Sylvester, B. Sivaraman, P. Deb, A. Ramamurthi, Nanoparticles for localized delivery of hyaluronan oligomers towards regenerative repair of elastic matrix, Acta Biomater 9(12) (2013) 9292-302.

[233] J. Liu, J. Xu, J. Zhou, Y. Zhang, D. Guo, Z. Wang, Fe3O4-based PLGA nanoparticles as MR contrast agents for the detection of thrombosis, Int J Nanomedicine 12 (2017) 1113-1126.

[234] Y. Zhang, J. Zhou, D. Guo, M. Ao, Y. Zheng, Z. Wang, Preparation and characterization of gadolinium-loaded PLGA particles surface modified with RGDS for the detection of thrombus, Int J Nanomedicine 8 (2013) 3745-56.

[235] F. Liu, J. Mu, B. Xing, Recent advances on the development of pharmacotherapeutic agents on the basis of human serum albumin, Curr Pharm Des 21(14) (2015) 1866-88.

[236] A.O. Elzoghby, W.M. Samy, N.A. Elgindy, Albumin-based nanoparticles as potential controlled release drug delivery systems, J Control Release 157(2) (2012) 168-82.

[237] B. Geny, B. Mettauer, B. Muan, P. Bischoff, E. Epailly, F. Piquard, B. Eisenmann, P. Haberey, Safety and efficacy of a new transpulmonary echo contrast agent in echocardiographic studies in patients, J Am Coll Cardiol 22(4) (1993) 1193-8.

[238] N.K. Ibrahim, N. Desai, S. Legha, P. Soon-Shiong, R.L. Theriault, E. Rivera, B. Esmaeli, S.E. Ring, A. Bedikian, G.N. Hortobagyi, J.A. Ellerhorst, Phase I and pharmacokinetic study of ABI-007, a Cremophor-free, protein-stabilized, nanoparticle formulation of paclitaxel, Clin Cancer Res 8(5) (2002) 1038-44.

[239] J.H. Jeong, H.K. Nguyen, J.E. Lee, W. Suh, Therapeutic effect of apatinib-loaded nanoparticles on diabetes-induced retinal vascular leakage, Int J Nanomedicine 11 (2016) 3101-9.

[240] Z. Wang, J. Li, J. Cho, A.B. Malik, Prevention of vascular inflammation by nanoparticle targeting of adherent neutrophils, Nat Nanotechnol 9(3) (2014) 204-10.

[241] J. Ji, J.A. Yang, X. He, W.P. Ling, X.L. Chen, Cardiac-targeting transfection of tissue-type plasminogen activator gene to prevent the graft thrombosis and vascular anastomotic restenosis after coronary bypass, Thromb Res 134(2) (2014) 440-8.

[242] S.R. Karamched, N. Nosoudi, H.E. Moreland, A. Chowdhury, N.R. Vyavahare, Site-specific chelation therapy with EDTA-loaded albumin nanoparticles reverses arterial calcification in a rat model of chronic kidney disease, Sci Rep 9(1) (2019) 2629.

[243] K. Langer, S. Balthasar, V. Vogel, N. Dinauer, H. von Briesen, D. Schubert, Optimization of the preparation process for human serum albumin (HSA) nanoparticles, Int J Pharm 257(1-2) (2003) 169-80.

[244] W. Lin, A.G. Coombes, M.C. Garnett, M.C. Davies, E. Schacht, S.S. Davis, L. Illum, Preparation of sterically stabilized human serum albumin nanospheres using a novel Dextranox-MPEG crosslinking agent, Pharm Res 11(11) (1994) 1588-92.

[245] H.M. Mansour, M. Sohn, A. Al-Ghananeem, P.P. Deluca, Materials for pharmaceutical dosage forms: molecular pharmaceutics and controlled release drug delivery aspects, Int J Mol Sci 11(9) (2010) 3298-322.

[246] V. Torchilin, Tumor delivery of macromolecular drugs based on the EPR effect, Adv Drug Deliv Rev 63(3) (2011) 131-5.

[247] J. Fang, H. Nakamura, H. Maeda, The EPR effect: Unique features of tumor blood vessels for drug delivery, factors involved, and limitations and augmentation of the effect, Adv Drug Deliv Rev 63(3) (2011) 136-51.

[248] M.F. Attia, N. Anton, J. Wallyn, Z. Omran, T.F. Vandamme, An overview of active and passive targeting strategies to improve the nanocarriers efficiency to tumour sites, J Pharm Pharmacol 71(8) (2019) 1185-1198.

[249] S. Sagnella, C. Drummond, Drug Delivery: A Nanomedicine Approach, Australian Biochemist 43(3) (2012) 5-8.

[250] P. Debbage, Targeted drugs and nanomedicine: present and future, Curr Pharm Des 15(2) (2009) 153-72.

[251] A.D. Friedman, S.E. Claypool, R. Liu, The smart targeting of nanoparticles, Curr Pharm Des 19(35) (2013) 6315-29.

[252] B. Sivaraman, G. Swaminathan, L. Moore, J. Fox, D. Seshadri, S. Dahal, I. Stoilov, M. Zborowski, R. Mecham, A. Ramamurthi, Magnetically-responsive, multifunctional drug delivery nanoparticles for elastic matrix regenerative repair, Acta Biomater 52 (2017) 171-186.

[253] J. Cheng, R. Zhang, C. Li, H. Tao, Y. Dou, Y. Wang, H. Hu, J. Zhang, A Targeting Nanotherapy for Abdominal Aortic Aneurysms, J Am Coll Cardiol 72(21) (2018) 2591-2605.

[254] T. Kitagawa, H. Kosuge, M. Uchida, Y. Iida, R.L. Dalman, T. Douglas, M.V. McConnell, RGD targeting of human ferritin iron oxide nanoparticles enhances in vivo MRI of vascular inflammation and angiogenesis in experimental carotid disease and abdominal aortic aneurysm, J Magn Reson Imaging 45(4) (2017) 1144-1153.

[255] T. Kitagawa, H. Kosuge, M. Uchida, M.M. Dua, Y. Iida, R.L. Dalman, T. Douglas, M.V. McConnell, RGD-conjugated human ferritin nanoparticles for imaging vascular inflammation and angiogenesis in experimental carotid and aortic disease, Mol Imaging Biol 14(3) (2012) 315-24.

[256] B. Jennewine, J. Fox, A. Ramamurthi, Cathepsin K-targeted sub-micron particles for regenerative repair of vascular elastic matrix, Acta Biomater 52 (2017) 60-73.

[257] T. Shirasu, H. Koyama, Y. Miura, K. Hoshina, K. Kataoka, T. Watanabe, Nanoparticles Effectively Target Rapamycin Delivery to Sites of Experimental Aortic Aneurysm in Rats, Plos One 11(6) (2016) e0157813.

[258] A. Klink, J. Heynens, B. Herranz, M.E. Lobatto, T. Arias, H.M. Sanders, G.J. Strijkers, M. Merkx, K. Nicolay, V. Fuster, A. Tedgui, Z. Mallat, W.J. Mulder, Z.A. Fayad, In vivo characterization of a new abdominal aortic aneurysm mouse model with conventional and molecular magnetic resonance imaging, J Am Coll Cardiol 58(24) (2011) 2522-30.

[259] J. Sun, H. Deng, Z. Zhou, X. Xiong, L. Gao, Endothelium as a Potential Target for Treatment of Abdominal Aortic Aneurysm, Oxid Med Cell Longev 2018 (2018) 6306542.

[260] A. Shamloo, S. Ebrahimi, A. Amani, F. Fallah, Targeted Drug Delivery of Microbubble to Arrest Abdominal Aortic Aneurysm Development: A Simulation Study Towards Optimized Microbubble Design, Sci Rep 10(1) (2020) 5393.

[261] H. Hong, Y. Yang, B. Liu, W. Cai, Imaging of Abdominal Aortic Aneurysm: the present and the future, Curr Vasc Pharmacol 8(6) (2010) 808-19.

[262] M.H. Lin, F.R. Chang, M.Y. Hua, Y.C. Wu, S.T. Liu, Inhibitory effects of 1,2,3,4,6-penta-O-galloyl-beta-D-glucopyranose on biofilm formation by Staphylococcus aureus, Antimicrob Agents Chemother 55(3) (2011) 1021-7.

[263] J. Zhang, L. Li, S.H. Kim, A.E. Hagerman, J. Lu, Anti-cancer, anti-diabetic and other pharmacologic and biological activities of penta-galloyl-glucose, Pharm Res 26(9) (2009) 2066-80.

[264] N.G. Bastus, J. Comenge, V. Puntes, Kinetically controlled seeded growth synthesis of citrate-stabilized gold nanoparticles of up to 200 nm: size focusing versus Ostwald ripening, Langmuir 27(17) (2011) 11098-105.

[265] D. Kim, S. Park, J.H. Lee, Y.Y. Jeong, S. Jon, Antibiofouling polymer-coated gold nanoparticles as a contrast agent for in vivo X-ray computed tomography imaging, J Am Chem Soc 129(24) (2007) 7661-5.

[266] L.E. Cole, T. Vargo-Gogola, R.K. Roeder, Contrast-enhanced X-ray detection of breast microcalcifications in a murine model using targeted gold nanoparticles, ACS Nano 8(7) (2014) 7486-96.

[267] W. Eck, A.I. Nicholson, H. Zentgraf, W. Semmler, S. Bartling, Anti-CD4-targeted gold nanoparticles induce specific contrast enhancement of peripheral lymph nodes in X-ray computed tomography of live mice, Nano Lett 10(7) (2010) 2318-22.

[268] T. Reuveni, M. Motiei, Z. Romman, A. Popovtzer, R. Popovtzer, Targeted gold nanoparticles enable molecular CT imaging of cancer: an in vivo study, Int J Nanomedicine 6 (2011) 2859-64.

[269] W.S. Cho, M. Cho, J. Jeong, M. Choi, H.Y. Cho, B.S. Han, S.H. Kim, H.O. Kim, Y.T. Lim, B.H. Chung, J. Jeong, Acute toxicity and pharmacokinetics of 13 nm-sized PEG-coated gold nanoparticles, Toxicol Appl Pharmacol 236(1) (2009) 16-24.

[270] Y.S. Chen, Y.C. Hung, I. Liau, G.S. Huang, Assessment of the In Vivo Toxicity of Gold Nanoparticles, Nanoscale Res Lett 4(8) (2009) 858-864.

[271] S.K. Balasubramanian, J. Jittiwat, J. Manikandan, C.N. Ong, L.E. Yu, W.Y. Ong, Biodistribution of gold nanoparticles and gene expression changes in the liver and spleen after intravenous administration in rats, Biomaterials 31(8) (2010) 2034-42.

[272] J. Turkevich, P.C. Stevenson, J. Hillier, A study of the nucleation and growth processes in the synthesis of colloidal gold, Discussions of the Faraday Society 11 (1951) 55-75.

[273] G. Frens, Controlled Nucleation for the Regulation of the Particle Size in Monodisperse Gold Suspensions, Nature Physical Science volume 241 (1973) 20-22.

[274] P. Ghosh, G. Han, M. De, C.K. Kim, V.M. Rotello, Gold nanoparticles in delivery applications, Adv Drug Deliv Rev 60(11) (2008) 1307-15.

[275] S. Ma, G.M. Turino, Y.Y. Lin, Quantitation of desmosine and isodesmosine in urine, plasma, and sputum by LC-MS/MS as biomarkers for elastin degradation, J Chromatogr B Analyt Technol Biomed Life Sci 879(21) (2011) 1893-8.

[276] N. Hoshyar, S. Gray, H. Han, G. Bao, The effect of nanoparticle size on in vivo pharmacokinetics and cellular interaction, Nanomedicine (Lond) 11(6) (2016) 673-92.

[277] E.C. Dreaden, L.A. Austin, M.A. Mackey, M.A. El-Sayed, Size matters: gold nanoparticles in targeted cancer drug delivery, Ther Deliv 3(4) (2012) 457-78.

[278] W.H. De Jong, W.I. Hagens, P. Krystek, M.C. Burger, A.J. Sips, R.E. Geertsma, Particle size-dependent organ distribution of gold nanoparticles after intravenous administration, Biomaterials 29(12) (2008) 1912-9.

[279] Y. Pan, S. Neuss, A. Leifert, M. Fischler, F. Wen, U. Simon, G. Schmid, W. Brandau, W. Jahnen-Dechent, Size-dependent cytotoxicity of gold nanoparticles, Small 3(11) (2007) 1941-9.

[280] D. Mateo, P. Morales, A. Ávalos, A.I. Haza, Comparative cytotoxicity evaluation of different size gold nanoparticles in human dermal fibroblasts, Journal of Experimental Nanoscience 10(18) (2015) 1401-1417.

[281] Y.J. Lee, E.Y. Ahn, Y. Park, Shape-dependent cytotoxicity and cellular uptake of gold nanoparticles synthesized using green tea extract, Nanoscale Res Lett 14(1) (2019) 129.

[282] T. Niidome, M. Yamagata, Y. Okamoto, Y. Akiyama, H. Takahashi, T. Kawano, Y. Katayama, Y. Niidome, PEG-modified gold nanorods with a stealth character for in vivo applications, J Control Release 114(3) (2006) 343-7.

[283] D. Kim, Y.Y. Jeong, S. Jon, A drug-loaded aptamer-gold nanoparticle bioconjugate for combined CT imaging and therapy of prostate cancer, ACS Nano 4(7) (2010) 3689-96.

[284] A.M. Levesque, C.D. Yang, C. Elchebly, M. Dore, Hepatotoxicity associated with iopamidol, Am J Health Syst Pharm 74(10) (2017) 636-640.

[285] C.C. Fleischer, C.K. Payne, Nanoparticle-cell interactions: molecular structure of the protein corona and cellular outcomes, Acc Chem Res 47(8) (2014) 2651-9.

[286] H. Valo, Biopolymer-Based Nanoparticles for Drug Delivery., Division of Pharmaceutical Technology, University of Helsinki, Finland, 2012.

[287] J.E. Wagenseil, R.P. Mecham, Vascular extracellular matrix and arterial mechanics, Physiol Rev 89(3) (2009) 957-89.

[288] A. Siso-Almirall, B. Kostov, M. Navarro Gonzalez, D. Cararach Salami, A. Perez Jimenez, R. Gilabert Sole, C. Bru Saumell, L. Donoso Bach, M. Villalta Marti, L. Gonzalez-de Paz, R. Ruiz Riera, V. Riambau Alonso, N. Acar-Denizli, M. Farre Almacellas, M. Ramos-Casals, J. Benavent Areu, Abdominal aortic aneurysm screening program using hand-held ultrasound in primary healthcare, Plos One 12(4) (2017) e0176877.

[289] A. Daugherty, L.A. Cassis, Mouse models of abdominal aortic aneurysms, Arterioscler Thromb Vasc Biol 24(3) (2004) 429-34.

[290] R.Y. Cao, T. Amand, M.D. Ford, U. Piomelli, C.D. Funk, The Murine Angiotensin II-Induced Abdominal Aortic Aneurysm Model: Rupture Risk and Inflammatory Progression Patterns, Front Pharmacol 1 (2010) 9.

[291] B.A. Lane, S.M. Lessner, N.R. Vyavahare, M.A. Sutton, J.F. Eberth, Null strain analysis of submerged aneurysm analogues using a novel 3D stereomicroscopy device, Comput Methods Biomech Biomed Engin 23(8) (2020) 332-344.

[292] B.A. Lane, X. Wang, S.M. Lessner, N.R. Vyavahare, J.F. Eberth, Targeted Gold Nanoparticles as an Indicator of Mechanical Damage in an Elastase Model of Aortic Aneurysm, Ann Biomed Eng (2020).

[293] S. Perandini, N. Faccioli, A. Zaccarella, T. Re, R.P. Mucelli, The diagnostic contribution of CT volumetric rendering techniques in routine practice, The Indian journal of radiology & imaging 20(2) (2010) 92-97.

[294] J. Gao, X.Y. Huang, H. Liu, F. Zan, J.C. Ren, Colloidal Stability of Gold Nanoparticles Modified with Thiol Compounds: Bioconjugation and Application in Cancer Cell Imaging, Langmuir 28(9) (2012) 4464-4471.

[295] C.D. Medley, J.E. Smith, Z. Tang, Y. Wu, S. Bamrungsap, W. Tan, Gold nanoparticle-based colorimetric assay for the direct detection of cancerous cells, Anal Chem 80(4) (2008) 1067-72.

[296] M.K. Gehrmann, M.A. Kimm, S. Stangl, T.E. Schmid, P.B. Noel, E.J. Rummeny, G. Multhoff, Imaging of Hsp70-positive tumors with cmHsp70.1 antibody-conjugated gold nanoparticles, Int J Nanomedicine 10 (2015) 5687-700.

[297] N. Kontopodis, D. Pantidis, A. Dedes, N. Daskalakis, C.V. Ioannou, The - Not So - Solid 5.5 cm Threshold for Abdominal Aortic Aneurysm Repair: Facts, Misinterpretations, and Future Directions, Front Surg 3 (2016) 1.

[298] B. Trachet, R.A. Fraga-Silva, P.A. Jacquet, N. Stergiopulos, P. Segers, Incidence, severity, mortality, and confounding factors for dissecting AAA detection in angiotensin II-infused mice: a meta-analysis, Cardiovasc Res 108(1) (2015) 159-70.

[299] J. Lysgaard Poulsen, J. Stubbe, J.S. Lindholt, Animal Models Used to Explore Abdominal Aortic Aneurysms: A Systematic Review, Eur J Vasc Endovasc Surg 52(4) (2016) 487-499.

[300] S. Aggarwal, A. Qamar, V. Sharma, A. Sharma, Abdominal aortic aneurysm: A comprehensive review, Exp Clin Cardiol 16(1) (2011) 11-5.

[301] J. Uitto, Q. Li, Z. Urban, The complexity of elastic fibre biogenesis in the skin--a perspective to the clinical heterogeneity of cutis laxa, Exp Dermatol 22(2) (2013) 88-92.

[302] C.J. Goergen, K.N. Barr, D.T. Huynh, J.R. Eastham-Anderson, G. Choi, M. Hedehus, R.L. Dalman, A.J. Connolly, C.A. Taylor, P.S. Tsao, J.M. Greve, In vivo quantification of murine aortic cyclic strain, motion, and curvature: implications for abdominal aortic aneurysm growth, J Magn Reson Imaging 32(4) (2010) 847-58.

[303] J.T. Favreau, B.T. Nguyen, I. Gao, P. Yu, M. Tao, J. Schneiderman, G.R. Gaudette, C.K. Ozaki, Murine ultrasound imaging for circumferential strain analyses in the angiotensin II abdominal aortic aneurysm model, J Vasc Surg 56(2) (2012) 462-9.

[304] V. Laterreur, J. Ruel, F.A. Auger, K. Vallieres, C. Tremblay, D. Lacroix, M. Tondreau, J.M. Bourget, L. Germain, Comparison of the direct burst pressure and the ring tensile test methods for mechanical characterization of tissue-engineered vascular substitutes, J Mech Behav Biomed Mater 34 (2014) 253-63.

[305] G. Sonavane, K. Tomoda, K. Makino, Biodistribution of colloidal gold nanoparticles after intravenous administration: effect of particle size, Colloids Surf B Biointerfaces 66(2) (2008) 274-80.

[306] V. Bieghs, P.J. Van Gorp, K. Wouters, T. Hendrikx, M.J. Gijbels, M. van Bilsen, J. Bakker, C.J. Binder, D. Lutjohann, B. Staels, M.H. Hofker, R. Shiri-Sverdlov, LDL receptor knock-out mice are a physiological model particularly vulnerable to study the onset of inflammation in non-alcoholic fatty liver disease, Plos One 7(1) (2012) e30668.

[307] M.E. Tornwall, J. Virtamo, J.K. Haukka, D. Albanes, J.K. Huttunen, Alpha-tocopherol (vitamin E) and beta-carotene supplementation does not affect the risk for large abdominal aortic aneurysm in a controlled trial, Atherosclerosis 157(1) (2001) 167-73.

[308] D.G. Hackam, D. Thiruchelvam, D.A. Redelmeier, Angiotensin-converting enzyme inhibitors and aortic rupture: a population-based case-control study, Lancet 368(9536) (2006) 659-65.

[309] M.J. Sweeting, S.G. Thompson, L.C. Brown, R.M. Greenhalgh, J.T. Powell, Use of angiotensin converting enzyme inhibitors is associated with increased growth rate of abdominal aortic aneurysms, J Vasc Surg 52(1) (2010) 1-4.

[310] A. Thompson, J.A. Cooper, M. Fabricius, S.E. Humphries, H.A. Ashton, H. Hafez, An analysis of drug modulation of abdominal aortic aneurysm growth through 25 years of surveillance, J Vasc Surg 52(1) (2010) 55-61 e2.

[311] A.N. Assar, Pharmacological therapy for patients with abdominal aortic aneurysm, Expert Rev Cardiovasc Ther 7(8) (2009) 999-1009.

[312] I. Wiernicki, M. Cnotliwy, I. Baranowska-Bosiacka, E. Urasinska, A. Kwas, J. Bober, P. Gutowski, Elastin degradation within the abdominal aortic aneurysm wall--relationship between intramural pH and adjacent thrombus formation, Eur J Clin Invest 38(12) (2008) 883-7.

[313] N. Nosoudi, A. Chowdhury, S. Siclari, S. Karamched, V. Parasaram, J. Parrish, P. Gerard, N. Vyavahare, Reversal of Vascular Calcification and Aneurysms in a Rat Model Using Dual Targeted Therapy with EDTA- and PGG-Loaded Nanoparticles, Theranostics 6(11) (2016) 1975-1987.

[314] J.C. Isenburg, N.V. Karamchandani, D.T. Simionescu, N.R. Vyavahare, Structural requirements for stabilization of vascular elastin by polyphenolic tannins, Biomaterials 27(19) (2006) 3645-51.

[315] M. Carmo, L. Colombo, A. Bruno, F.R. Corsi, L. Roncoroni, M.S. Cuttin, F. Radice, E. Mussini, P.G. Settembrini, Alteration of elastin, collagen and their cross-links in abdominal aortic aneurysms, Eur J Vasc Endovasc Surg 23(6) (2002) 543-9.

[316] B.O. Kloster, L. Lund, J.S. Lindholt, Inhibition of early AAA formation by aortic intraluminal pentagalloyl glucose (PGG) infusion in a novel porcine AAA model, Ann Med Surg (Lond) 7 (2016) 65-70.

[317] S. Dhital, J.V. Stokes, N. Park, K.S. Seo, B.L. Kaplan, Cannabidiol (CBD) induces functional Tregs in response to low-level T cell activation, Cell Immunol 312 (2017) 25-34.

[318] A. Sinha, A. Shaporev, N. Nosoudi, Y. Lei, A. Vertegel, S. Lessner, N. Vyavahare, Nanoparticle targeting to diseased vasculature for imaging and therapy, Nanomed-Nanotechnol 10(5) (2014) 1003-1012.

[319] M. Monici, Cell and tissue autofluorescence research and diagnostic applications, Biotechnol Annu Rev 11 (2005) 227-56.

[320] B. Trachet, A. Piersigilli, R.A. Fraga-Silva, L. Aslanidou, J. Sordet-Dessimoz, A. Astolfo, M.F. Stampanoni, P. Segers, N. Stergiopulos, Ascending Aortic Aneurysm in Angiotensin II-Infused Mice: Formation, Progression, and the Role of Focal Dissections, Arterioscler Thromb Vasc Biol 36(4) (2016) 673-81.

[321] E.H. Phillips, A.A. Yrineo, H.D. Schroeder, K.E. Wilson, J.X. Cheng, C.J. Goergen, Morphological and Biomechanical Differences in the Elastase and AngII apoE(-/-) Rodent Models of Abdominal Aortic Aneurysms, Biomed Res Int 2015 (2015) 413189.

[322] N. Sharma, R. Dev, J.D. Ruiz-Rosado, S. Partida-Sanchez, M. Guerau-de-Arellano, P. Dhakal, H. Kuivaniemi, C.P. Hans, Pharmacological inhibition of Notch signaling regresses pre-established abdominal aortic aneurysm, Sci Rep 9(1) (2019) 13458.

[323] B. Trachet, R.A. Fraga-Silva, F.J. Londono, A. Swillens, N. Stergiopulos, P. Segers, Performance comparison of ultrasound-based methods to assess aortic diameter and stiffness in normal and aneurysmal mice, Plos One 10(5) (2015) e0129007.

[324] D.M. Tham, B. Martin-McNulty, Y.X. Wang, V. Da Cunha, D.W. Wilson, C.N. Athanassious, A.F. Powers, M.E. Sullivan, J.C. Rutledge, Angiotensin II injures the arterial wall causing increased aortic stiffening in apolipoprotein E-deficient mice, Am J Physiol Regul Integr Comp Physiol 283(6) (2002) R1442-9.

[325] S.D. Nandlall, M.P. Goldklang, A. Kalashian, N.A. Dangra, J.M. D'Armiento, E.E. Konofagou, Monitoring and staging abdominal aortic aneurysm disease with pulse wave imaging, Ultrasound Med Biol 40(10) (2014) 2404-14.

[326] S.J. Jenkins, D. Ruckerl, P.C. Cook, L.H. Jones, F.D. Finkelman, N. van Rooijen, A.S. MacDonald, J.E. Allen, Local macrophage proliferation, rather than recruitment from the blood, is a signature of TH2 inflammation, Science 332(6035) (2011) 1284-8.

[327] S. Mellak, H. Ait-Oufella, B. Esposito, X. Loyer, M. Poirier, T.F. Tedder, A. Tedgui, Z. Mallat, S. Potteaux, Angiotensin II mobilizes spleen monocytes to promote the development of abdominal aortic aneurysm in Apoe-/- mice, Arterioscler Thromb Vasc Biol 35(2) (2015) 378-88.

[328] A.L. Golledge, P. Walker, P.E. Norman, J. Golledge, A systematic review of studies examining inflammation associated cytokines in human abdominal aortic aneurysm samples, Dis Markers 26(4) (2009) 181-8.

[329] W. Xiong, Y. Zhao, A. Prall, T.C. Greiner, B.T. Baxter, Key roles of CD4+ T cells and IFN-gamma in the development of abdominal aortic aneurysms in a murine model, J Immunol 172(4) (2004) 2607-12.

[330] H.F. Zhou, H.M. Yan, J.L. Cannon, L.E. Springer, J.M. Green, C.T.N. Pham, CD43-Mediated IFN-gamma Production by CD8(+) T Cells Promotes Abdominal Aortic Aneurysm in Mice, Journal of Immunology 190(10) (2013) 5078-5085.

[331] J. Dai, F. Losy, A.M. Guinault, C. Pages, I. Anegon, P. Desgranges, J.P. Becquemin, E. Allaire, Overexpression of transforming growth factor-beta1 stabilizes already-formed aortic aneurysms: a first approach to induction of functional healing by endovascular gene therapy, Circulation 112(7) (2005) 1008-15.

[332] C. Wang, Q. Chang, X. Qian, C. Tian, X. Sun, Angiotensin II induces an increase in MMP-2 expression in idiopathic ascending aortic aneurysm via AT1 receptor and JNK pathway, Acta Biochim Biophys Sin (Shanghai) 47(7) (2015) 539-47.

[333] C.M. Brophy, J.M. Reilly, G.W. Smith, M.D. Tilson, The role of inflammation in nonspecific abdominal aortic aneurysm disease, Annals of vascular surgery 5(3) (1991) 229-233.

[334] M.K. Eskandari, J.D. Vijungco, A. Flores, J. Borensztajn, V. Shively, W.H. Pearce, Enhanced abdominal aortic aneurysm in TIMP-1-deficient mice, J Surg Res 123(2) (2005) 289-93.

[335] J.S. Ikonomidis, W.C. Gibson, J.E. Butler, D.M. McClister, S.E. Sweterlitsch, R.P. Thompson, R. Mukherjee, F.G. Spinale, Effects of deletion of the tissue inhibitor of matrix metalloproteinases-1 gene on the progression of murine thoracic aortic aneurysms, Circulation 110(11 Suppl 1) (2004) II268-73.

[336] W. Xiong, R. Knispel, J. Mactaggart, B.T. Baxter, Effects of tissue inhibitor of metalloproteinase 2 deficiency on aneurysm formation, J Vasc Surg 44(5) (2006) 1061-6.

[337] T. Aoki, H. Kataoka, T. Moriwaki, K. Nozaki, N. Hashimoto, Role of TIMP-1 and TIMP-2 in the progression of cerebral aneurysms, Stroke 38(8) (2007) 2337-45.

[338] V. Parasaram, N. Nosoudi, A. Chowdhury, N. Vyavahare, Pentagalloyl glucose increases elastin deposition, decreases reactive oxygen species and matrix metalloproteinase activity in pulmonary fibroblasts under inflammatory conditions, Biochem Biophys Res Commun 499(1) (2018) 24-29.

[339] G. Guo, P. Gehle, S. Doelken, J.L. Martin-Ventura, Y. Von Kodolitsch, R. Hetzer, P.N. Robinson, Induction of macrophage chemotaxis by aortic extracts from patients with Marfan syndrome is related to elastin binding protein, PLoS One 6(5) (2011) e20138.